UNIVERSITY OF ROCHESTER
LABORATORY FOR LASER ENERGETICS

Volume 140
July–September 2014
DOE/NA/1944-1202

# LLE Review

## Quarterly Report

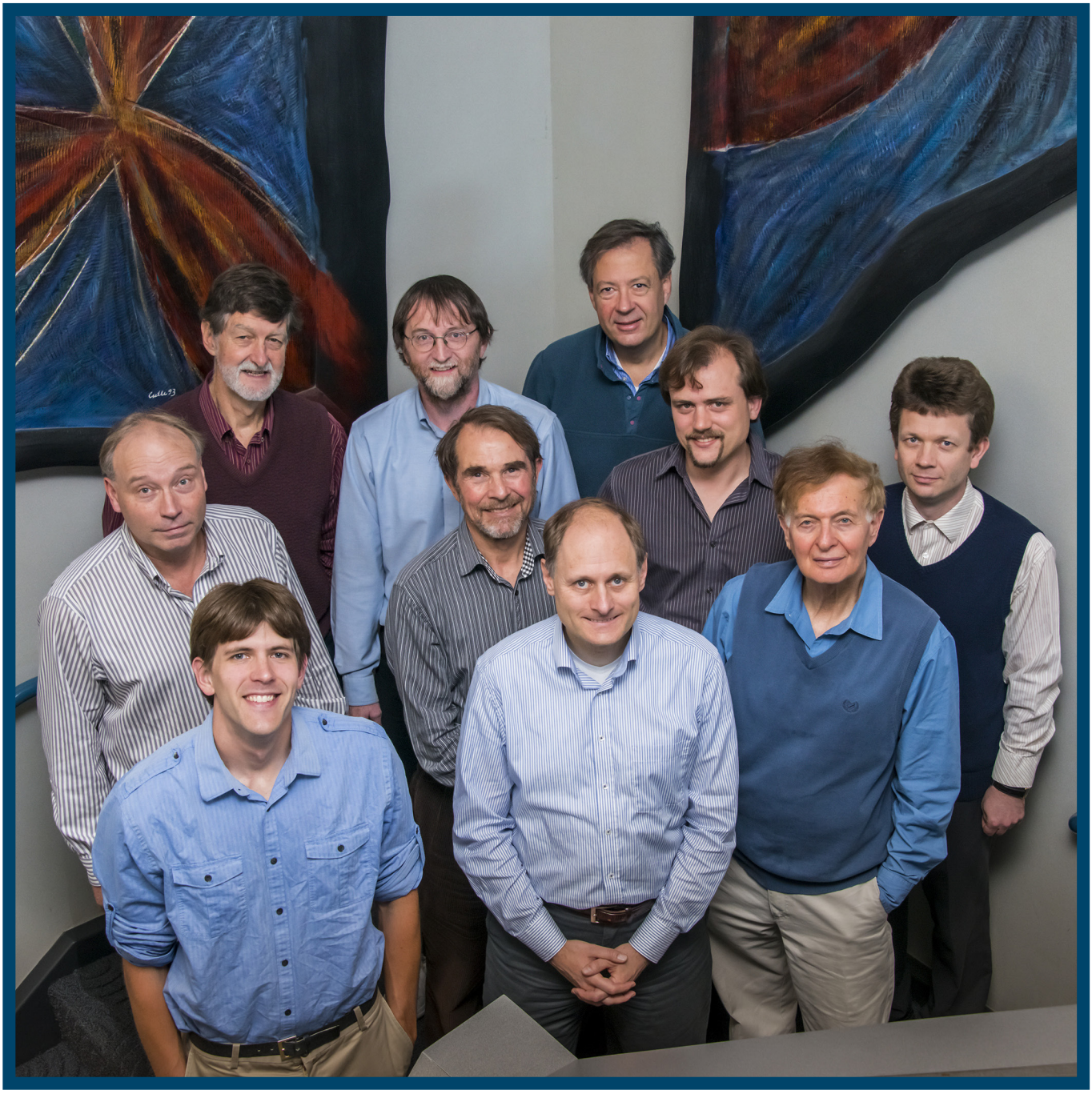

## About the Cover:

The photograph on the cover presents (left to right) R. Nora, W. Theobald, B. Yaakobi (front row), F. J. Marshall, W. Seka, D. T. Michel, A. A. Solodov (middle row), J. A. Delettrez, C. Stoeckl, and R. Betti (back row), who report on an experimental demonstration of gigabar spherical shock generation on the OMEGA laser, which is an important milestone for a shock-ignition scheme of inertial confinement fusion (p. 213). In shock ignition, a cryogenic deuterium–tritium fuel shell is first imploded by a nanosecond laser driver and then a strong shock wave is launched at the end of the laser pulse, initiating ignition in the center of the compressed shell. This work was performed in collaboration with M. Lafon, A. Casner, C. Reverdin, X. Ribeyre, A. Vallet, J. Peebles, F. N. Beg, and M. S. Wei (unavailable at the time when the photograph was taken).

The figure below shows [(a),(b)] x-ray framing-camera images capturing an x-ray flash at the time when the spherical strong shock converged in the target center and (c) scaling of the inferred maximum ablation pressure versus the maximum laser intensity that is absorbed at the critical surface (red solid circles and solid line). Large amounts of hot electrons were produced, which significantly enhanced the shock strength and scaling of effective maximum ablation pressure (without hot electrons) versus the maximum laser intensity is shown (blue open circles and dashed line).

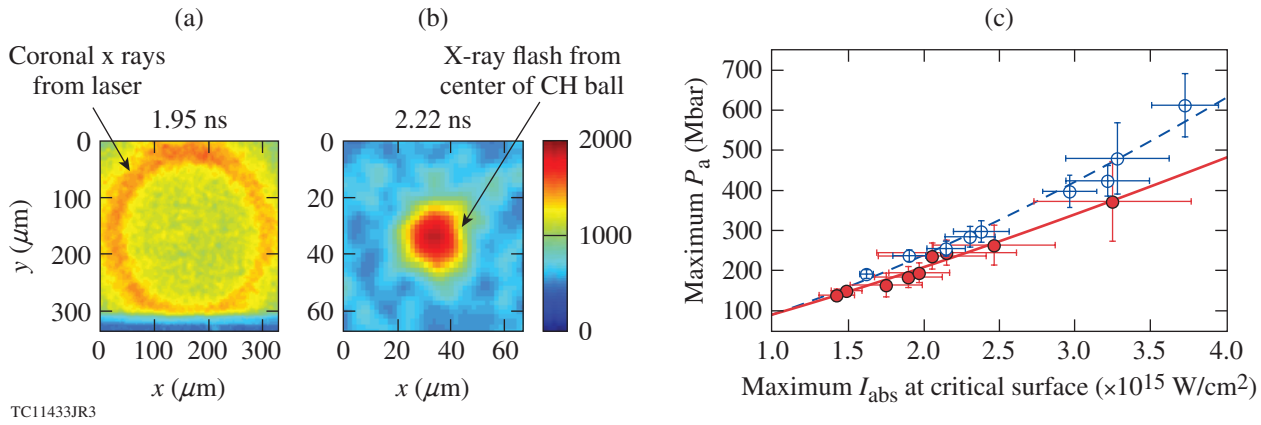




The work described in this volume includes current research at the Laboratory for Laser Energetics, which is supported by New York State Energy Research and Development Authority, the University of Rochester, the U.S. Department of Energy Office of Inertial Confinement Fusion under Cooperative Agreement No. DE-NA0001944, and other agencies.

Printed in the United States of America
Available from
National Technical Information Services
U.S. Department of Commerce
5285 Port Royal Road
Springfield, VA 22161
www.ntis.gov

For questions or comments, contact Andrey Solodov, Editor, Laboratory for Laser Energetics, 250 East River Road, Rochester, NY 14623-1299, (585) 273-3686.

Worldwide-Web Home Page: http://www.lle.rochester.edu/
(Color online)

UNIVERSITY OF ROCHESTER
LABORATORY FOR LASER ENERGETICS

Volume 140
July–September 2014
DE-NA0001944-1202

# LLE Review

## Quarterly Report

UR LLE

## Contents

# In Brief

This volume of the LLE Review, covering July–September 2014, features "Gigabar Spherical Shock Generation on the OMEGA Laser," by R. Nora and R. Betti (LLE and Fusion Science Center); W. Theobald, F. J. Marshall, D. T. Michel, W. Seka, B. Yaakobi, M. Lafon, C. Stoeckl, J. A. Delettrez, and A. A. Solodov (LLE); A. Casner and C. Reverdin (CEA, DAM, DIF); X. Ribeyre and A. Vallet (Universit de Bordeaux, CELIA); J. Peebles and F. N. Beg (University of California, La Jolla); and M. S. Wei (General Atomics). This article (p. 213) reports on the first experimental demonstration of the capability to launch shocks of several-hundred Mbars in spherical targets—a milestone for shock ignition. Using the temporal delay between launching the strong shock at the outer surface of the spherical target and the time when the shock converges at the center, the shock-launching pressure can be inferred using radiation–hydrodynamic simulations. Peak ablation pressures exceeding 300 Mbar are inferred at absorbed laser intensities of $\sim 3 \times 10^{15}$ W/cm$^2$. The shock strength is shown to be significantly enhanced by coupling suprathermal electrons with a total converted energy of up to 8% of the incident laser energy. At the end of the laser pulse, the shock pressure is estimated to exceed ~1 Gbar because of convergence effects.

Additional highlights of research presented in this issue include the following:

- M. Lafon and R. Betti (LLE and Fusion Science Center); and K. S. Anderson, T. J. B. Collins, R. Epstein, P. W. McKenty, J. F. Myatt, A. Shvydky, and S. Skupsky (LLE) present direct-drive–ignition designs with mid-*Z* ablators (p. 220). Ablator materials of moderate atomic number *Z* reduce the detrimental effects of laser–plasma instabilities in direct-drive implosions. To validate the physics of moderate-*Z* ablator materials for ignition target designs at the National Ignition Facility (NIF), hydro-equivalent targets are designed using pure plastic, high-density carbon, and glass ablators. The hydrodynamic stability of these targets is investigated through 2-D single-mode and multimode simulations. The overall stability of these targets to laser imprint perturbations and low-mode asymmetries allows for the development of high-gain target designs using uniform illumination. Designs using polar-drive illumination are developed within the NIF Laser System specifications. Mid-*Z* ablator targets are an attractive candidate for direct-drive–ignition designs since they present better overall performances than plastic ablators through reduced laser–plasma instabilities and a similar hydrodynamic stability.

- S. Ivancic, D. Haberberger, K. S. Anderson, R. S. Craxton, D. H. Froula, D. D. Meyerhofer, C. Stoeckl, and W. Theobald (LLE); and H. Habara, T. Iwawaki, and K. A. Tanaka (Graduate School of Engineering, Osaka University) report on channeling multikilojoule high-intensity laser beams in an inhomogeneous plasma (p. 233). Experiments have been performed that investigate the transport of high-intensity (>$10^{18}$ W/cm$^2$) laser light through a millimeter-sized, inhomogenous, kilojoule, laser-produced plasma up to overcritical density. The high-intensity light evacuates a conical-shaped cavity with a radial parabolic density profile that is observed using a novel optical probing technique—angular filter refractometery. The experiments showed that 100-ps infrared pulses with a peak intensity of $\sim 1 \times 10^{19}$ W/cm$^2$ produced a channel to plasma densities beyond critical, while 10-ps pulses with the same energy but higher intensity did not propagate as far. The plasma cavity forms in less than 100 ps, using a 20-TW laser pulse, and advances at a velocity of ~3 $\mu$m/ps, consistent with a ponderomotive hole-boring model.

- W. T. Shmayda, A. M. Boyce, R. Shea, and B. Petroski (LLE); M. Sharpe (LLE and Dept. of Nuclear Chemistry and Physics, University of Rochester); and W. U. Schröder (Dept. of Nuclear Chemistry and Physics, University of Rochester) study dependence of tritium release on temperature and water vapor from stainless steel (p. 238). In general, increasing either the sample temperature or the relative humidity causes an increased quantity of tritium to be removed. Increasing the temperature to 300°C in a dry gas stream results in a significant release of tritium and is, therefore, an effective means for reducing the tritium inventory in steel. For humid purges at 30°C, a sixfold increase in humidity results in a tenfold increase in the peak outgassing rate. Increasing the relative humidity from 0% to 20% when the sample temperature is 100°C causes a significant increase in the tritium outgassing rate. Finally, a simple calculation shows that more activity is available than is actually removed in an experiment, suggesting that the surface oxide acts as a barrier to tritium removal.

- R. D. Petrasso reports on the Sixth Omega Laser Facility Users Group Workshop on p. 243.

- This volume concludes with a summary of LLE's Summer High School Research Program (p. 248), the FY14 Laser Facility Report (p. 250), and the National Laser Users' Facility and External Users' Programs (p. 253).

Andrey Solodov
*Editor*

# Gigabar Spherical Shock Generation on the OMEGA Laser

Recently it has been shown[1–7] that the gain of an inertial confinement fusion implosion can be significantly enhanced by launching a strong spherically convergent shock at the end of the compression (or assembly) pulse. This two-step scheme is usually referred to as shock ignition (SI). Shock ignition has a distinct advantage over fast ignition[8] because it reduces the energy required for ignition as compared to conventional hot-spot ignition[9] while still using a single laser. Recent two-dimensional (2-D) simulations[3,10] have indicated the possibility of achieving ignition at submegajoule laser energies. While implosion experiments on the OMEGA laser[11]—using 60-beam symmetric implosions of CH shells filled with $D_2$—have demonstrated a fourfold increase in yield and a 40% increase in shell areal density for SI pulse shapes when compared to conventional implosions,[12] the final shock strength was much lower than the value required for ignition.

Demonstrating the capability to generate shocks of the order of $\gtrsim$300 Mbar at laser intensities in the range of $10^{15}$ to $10^{16}$ W/cm$^2$ is crucial to the long-term success of SI. Investigations to determine the shock strength in planar geometries have been completed at Laboratoire pour l'Utilisation des Lasers Intenses (LULI),[13] OMEGA,[14] and Prague Asterix Laser System (PALS),[15] where the largest shock pressure reported is ~90 Mbar at intensities <$10^{16}$ W/cm$^2$. Kritcher *et al.*[16] numerically investigated probing the equation of state of plastic under hundreds of megabar pressures in a spherical geometry using indirect-drive targets; however, current indirect-drive experiments at the National Ignition Facility (NIF)[17] limit the ablation pressure to ~130 Mbar (Ref. 18).

This article reports on the first shock and ablation pressures inferred in spherical geometry using an x-ray flash as the primary diagnostic. The targets were composed of 430- to 600-$\mu$m-outer-diam solid spheres of 5% titanium–doped plastic in which the outer 50 $\mu$m consisted of pure CH (see Fig. 140.1). The targets were illuminated by a 2-ns laser pulse with a 1-ns, low-intensity foot used to create a coronal plasma followed by a 1-ns, high-intensity square pulse with 22 to 27 kJ of laser energy. An assortment of small phase plates[19] were used to increase the on-target incident intensity up to ~$6 \times 10^{15}$ W/cm$^2$ at the initial target surface, both with and without smoothing by spectral dispersion (SSD).[20] The rapid rise in laser intensity by the high-intensity square pulse generated an inwardly propagating shock wave that converged at the center of the target, raising the temperature in a very small volume to hundreds of eV and resulting in the self-emission of x rays in the keV range. The seed shock pressure is inferred from hydrodynamic simulations constrained by the measured temporal occurrence of the x-ray flash.

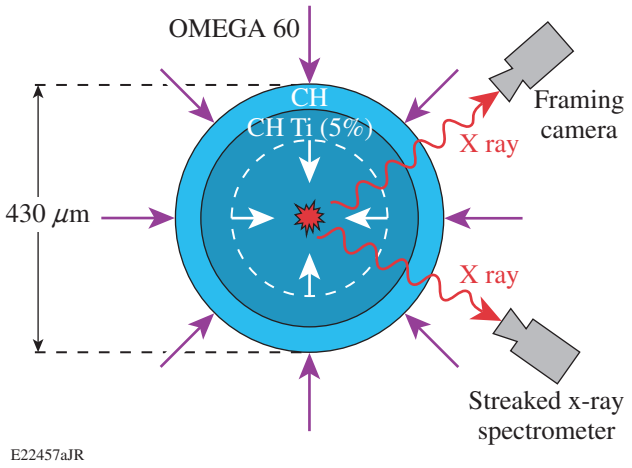


Figure 140.1
Experimental setup used to infer the shock and laser ablation pressure at shock-ignition (SI)–relevant intensities.

The x-ray emission from the center of the target was resolved temporally, spatially, and spectrally using an x-ray framing camera (XRFC)[21] and a streaked x-ray spectrometer (SXS).[22] The XRFC spatially and temporally resolved the x-ray emission, using a 4 × 4 pinhole array to produce 16 enlarged images of the target on a microchannel-plate (MCP) detector, which was covered with four strips of gold film. A 200-$\mu$m Be foil and a thin (12-$\mu$m) Ti foil placed in front of the detector, combined with the spectral response of the diagnostic, restricted the range of recorded x rays to ~3 to 7 keV. Figure 140.2 shows a portion of the raw data collected with the XRFC for a typical experi-

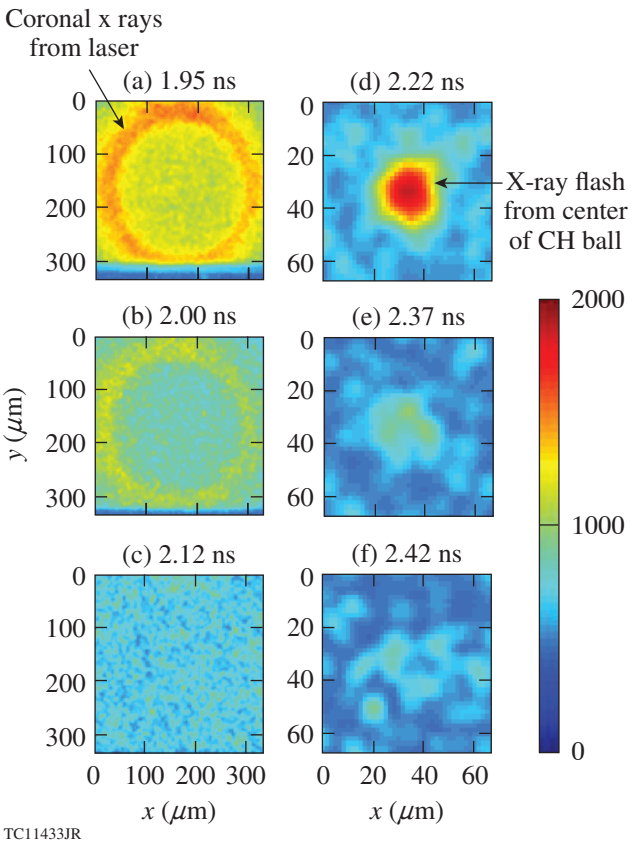


Figure 140.2
An x-ray framing camera (XRFC) captured a short x-ray flash at the time the shock converged in the center. The timing in each frame gives the peak time of the electrical gating pulse relative to the start of the laser pulse.

ment. At early times, the observed emission comes from the hot corona when the laser is still interacting with the target and, as time progresses, the laser shuts off and the corona cools. After a brief period of time, the appearance of a small but bright source of x rays originating from the center of the target is observed. The x ray emission was measured from a very small region with a diameter of less than ~15 $\mu$m [full width at half maximum (FWHM)]. The simultaneously operated SXS captured this line emission and determined the temporal width of the emitted intensity to be shorter than ~50 ps. The temporal occurrence of the x-ray flash between the two detectors is within the absolute timing error of each other.

The algorithm used to extract the x-ray flash times is based on Ref. 23. It translates the images formed onto the film or charge-coupled device (CCD) into an accurate time when the shock converged at the center of the target. To understand how the image is formed onto the film or a CCD camera, a brief description of the operation of the XRFC diagnostic and its MCP is provided. The XRFC consists of four independent strips that form an image onto a CCD camera when a voltage bias is applied to the MCP. X rays incident on the Au-coated photocathode ionize the atoms and if the voltage pulse is being applied, locally gates the photoelectrons down a single tube within the MCP, multiplying in number with a dependence on the applied voltage (which propagates across the strip). The electrons are accelerated by the applied voltage from the back of the MCP to the front of the phosphor plate and impact the phosphor plate, turning the electron energy back into visible light. This light is then imaged onto a film pack or CCD camera. Each strip contains its own voltage pulse that propagates across the length of the strip in ~200 ps. The bottom strip is triggered first, and subsequent strips (moving up) trigger once the voltage pulse has traversed the previous strip. This gives XRFC images that are both spatially resolved (via the pinhole array) and temporally gated (via the propagating voltage pulses).

The electrical gain of the photoelectrons as they travel down a single tube of the MCP is determined by the applied local voltage from the voltage pulse. As pointed out in Ref. 23, the gain scales with the voltage to the ninth power, $G \sim V^9$, for standard MCP setups. After discussions with many experimentalists, the exponent of the voltage dependence was changed to be as small as 5 or as large as 13, depending on the desired result. Figure 140.3 shows the gain of the voltage strip (red curve), shifted so the maximum occurs at 2.39 ns. The voltage pulse used in the model is the average of four pulse tests and is unique to each strip and framing camera; it has ~150-ps

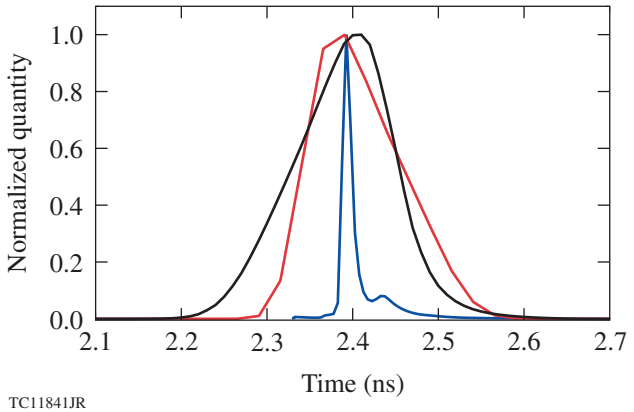


Figure 140.3
Temporal profiles of the simulated x-ray emission intensity when the ignitor shock reaches the center of the target (blue curve), voltage gain triggering the collection of photons (red curve), and convolution of the red and blue curves (black curve) versus time. The convolution is used to fit the experimentally integrated x-ray signal from the XRFC to accurately determine the flash time.

FWHM. Also shown in Fig. 140.3 is the simulated x-ray emission as a function of time for a typical experiment, delineated as the blue curve. The temporal dependence of the x-ray emission was obtained from a *Spect3D*[24] post-processed *LILAC*[25] simulation and is averaged over the entire emission time and spectral range of 3 to 7 keV. Details of the radiation–hydrodynamic simulations are provided later. In the simulation, the ignitor shock reaches the center of the target at 2.390±0.005 ns, resulting in the spike in x-ray emission. The emission decays after the shocked core cools and expands until a rebound shock causes a temporary increase in the emission. This secondary x-ray emission, however, is an order of magnitude weaker than the original x-ray emission; consequently, the FWHM of the simulated x-ray flash is ~15 ps. The convolution of the gain signal (red curve) and the simulated x-ray emission (blue curve) in Fig. 140.3 predicts the experimental intensity of the x-ray flash as a function of time (black curve). This indicates the x-ray emission would follow the shape of the convolution as a function of time and is used to translate the experimentally integrated pinhole images from XRFC into a specific x-ray flash time.

The signal gain of each strip (and camera) is convolved with the simulated x-ray emission, and its shape is compared to the experimentally measured intensity for each shot to determine the x-ray flash time. The intensity of the x-ray emission from each frame of the XRFC data is spatially integrated over the entire emission of a single pinhole image. The background emission from the cooling coronal plasma is subtracted from the integrated image and a low-pass filter is applied to the resulting data. The signal strength from each pinhole image is then fit to a Gaussian distribution and compared to the strength of the other images on the same strip. The relative values of these images are then compared to the simulated x-ray emission intensity to infer the x-ray flash time. Figure 140.4 shows the convolution of the voltage pulse gain from strips 2 and 3 (black and green curves, respectively) from XRFC4 for shot 72673 and compares it to the experimental intensity from that shot (circles). The spacing between each experimental point (circle) is determined by the time it takes the voltage pulse to propagate from one frame to another; it can be seen that the third and fourth frames of the second strip occur at roughly the same time as the first and second frames of the third strip. Because the voltage gain is unique to each strip, this analysis does not compare the signal strengths between strips but compares only the relative signal strength within the same strip. In Fig. 140.4, the convolutions have been adjusted in height and vertical offset to obtain the best fit of the experimental data to determine the x-ray flash time.

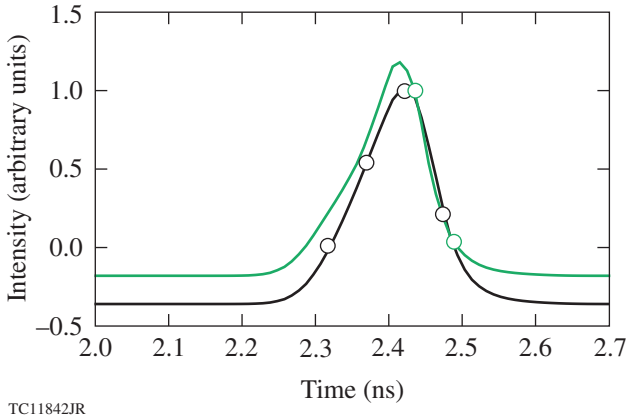


Figure 140.4
Best fit of the XRFC model used to extract the x-ray flash time from the data for shot 72673. The convolutions of the voltage pulse with the simulated x-ray emission are shown for strip 2 (black curve) and strip 3 (green curve) versus absolute time. The circles indicate the strip-normalized integrated intensity of the measured x-ray emission for each pinhole image.

The flash-time extraction analysis was applied to all of the experiments throughout the campaign, and the result of this analysis is shown in Fig. 140.5. A clear correlation between the size of the target and when the x-ray flash occurs is clearly observed, with smaller targets exhibiting earlier flash times. Also shown is the effect turning SSD on (blue) or off (red) has on the x-ray flash time. Generally, it is observed that experiments operating without SSD had earlier x-ray flash times because of the much larger amounts of generated suprathermal electrons.

Copious amounts of suprathermal electrons are generated when the thresholds for two-plasmon–decay (TPD) and stimu-

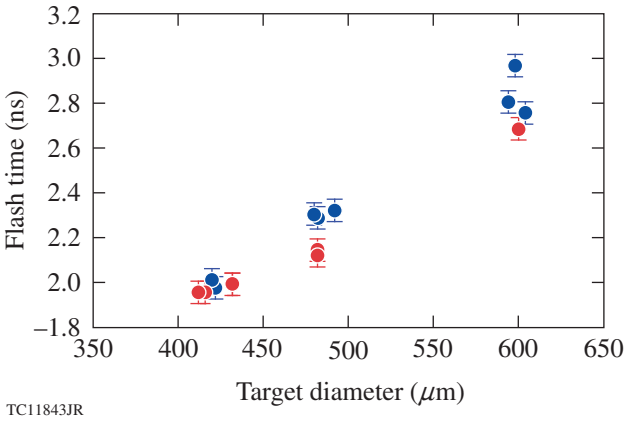


Figure 140.5
Experimental x-ray flash time versus target diameter for shots with SSD (blue) and without SSD (red). The error bars signify the ±50-ps accuracy in the absolute timing of the diagnostics.

lated Raman scattering (SRS) instabilities are exceeded early during the rise of the high-intensity square pulse.[26] The temperature of the suprathermal electrons and the temporal dependence were measured with a time-resolved, four-channel hard x-ray detector (HXRD)[27] and two time-integrated imaging-plate diagnostics—high-energy–radiography imager (HERIE)[28] and bremmstrahlung x-ray spectrometer (BMXS).[29] Typical temperatures measured for the suprathermal electrons can be fit to single-temperature Maxwellian distributions with central temperatures in the range of 50 to 100 keV. Up to 2 kJ (~8% of the total incident laser energy and 15% instantaneously) of suprathermal electrons were inferred to be deposited into the target by comparing the measured bremsstrahlung emission to Monte Carlo simulations, assuming that the suprathermal electrons were generated isotropically. Figure 140.6 shows that the measured total energy of the suprathermal electrons increased with the total laser energy and was dependent on whether or not SSD was functioning. The integrated intensity of the x-ray emission from shock convergence was measured with a gated microscope x-ray imager (GMXI)[30] and found to experience an ~25× increase when SSD was not operating (more suprathermal electrons) as compared to the case when SSD was turned on, indicating that the strength of the shock is greatly enhanced by the hot electrons. Measured time-resolved spectra for SRS, $\omega/2$, and $3\omega/2$ emissions show that both TPD and SRS are active. The observation of moderate suprathermal electron temperatures at these laser intensities has a significant impact on SI designs since they can enhance the ignitor shock[31] and improve the implosion performance.[10]

The shock and ablation pressures are inferred by constraining radiation–hydrodynamic simulations to the experimental observables: the temporal occurrence of the x-ray emission, the suprathermal electron energy and temperature distribution, and the temporal evolution of the hard x-ray emission (see Fig. 140.7). The simulations used the radiation–hydrodynamic code *LILAC* and were run with a multigroup radiation diffusion model, Thomas–Fermi[32] or *SESAME*[33,34] equations of state (EOS), flux-limited thermal transport,[35] and a suprathermal electron-transport package.[36] The suprathermal electron-transport package is a straight-line deposition model whereby a fraction of the laser energy reaching the quarter-critical surface is converted into suprathermal electrons with a single-temperature Maxwellian distribution and $2\pi$ forward divergence. The stopping range of the suprathermal electrons is modeled via collisional effects and is computed based on the work by Solodov and Betti.[37] The flux limiter, which is the only free parameter within the radiation–hydrodynamic simulations, is adjusted to match the experimentally measured x-ray flash time. Each simulation is, in principle, constrained by its own x-ray flash time and, therefore, has a unique flux limiter ranging from 5% to 8%; however, choosing 6.5% constrains all of the simulations within the experimental error bars. The ablation pressure is the pressure in the shell at the position where the

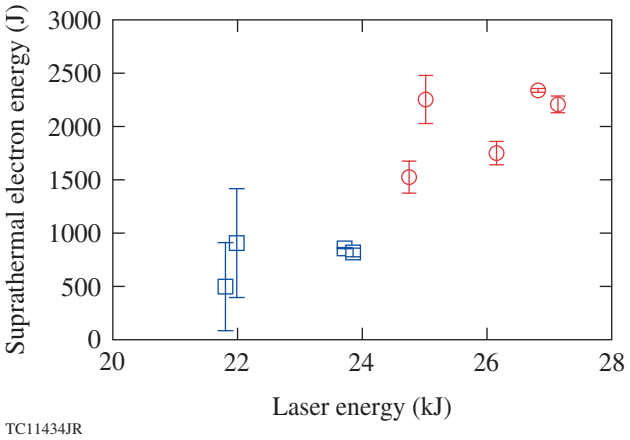


Figure 140.6
Total energy converted into suprathermal electrons versus laser energy. Up to ~8% of the total laser energy was converted into suprathermal electrons at moderate temperatures (50 to 100 keV). The error bars represent half the high-enery–radiography imager (HERIE) and bremsstrahlung x-ray spectrometer (BMXS) differences between the two time-integerated imaging-plate diagnostics.

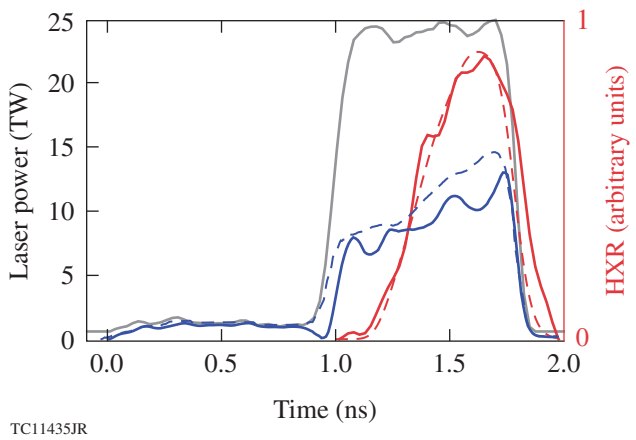


Figure 140.7
Comparison of a typical experimental (solid curves) and simulated (dashed curves) incident laser power (gray curves), laser absorption (blue curves), and hard x-ray emission (HXR, red curves) resulting from suprathermal electrons (in arbitrary units). The experimental hard x-ray emission was averaged over the three highest HXRD channels.

material velocity is zero in the lab frame, an accurate approximation for slowly imploding solid spheres.

Figure 140.8 illustrates the shock and ablation pressure inferred from a typical simulation that matches all of the experimental observables. The ablation pressure (blue curves) increases as a function of time, resulting from both thermal conduction of the absorbed laser energy and the energy deposition by suprathermal electrons, and decays soon after the laser is shut off. Meanwhile, the shock pressure (red curves) rapidly increases in time because of convergence effects.[38] For the particular shot shown in Fig. 140.8, the shock pressure is inferred to exceed 1 Gbar when the shock is ~25 $\mu$m from the center of the target. Additionally, simulations including suprathermal electrons (solid curves in Fig. 140.8) are observed to significantly enhance the ablation pressure by up to ~50% instantaneously over the case when the simulation is repeated in the absence of suprathermal electrons (dotted curves in Fig. 140.8). This result is corroborated with recent theoretical work showing ~300-Mbar shock pressures can be generated solely by suprathermal electrons.[39,40]

Inspection of Fig. 140.8 illustrates that a significant fraction of the energy carried by suprathermal electrons is deposited beyond the ablation front and contributes to the overall shock strength. In this specific example at 1.6 ns, only suprathermal electrons with temperatures less than 60 keV are stopped before

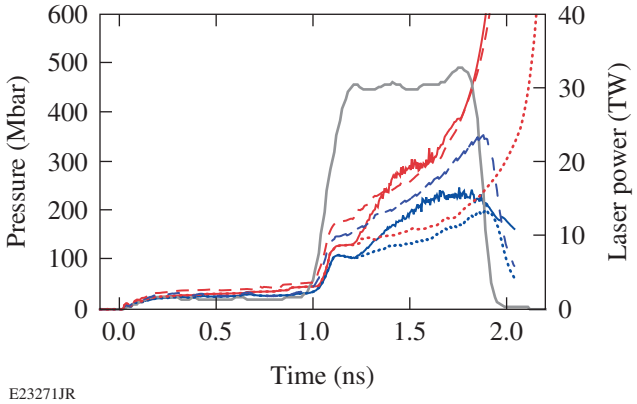


Figure 140.8
Simulated ablation pressure (blue curves) and shock pressure (red curves) as a function of time for shot 72679. The solid lines indicate a simulation that matches all experimentally observed quantities using a flux limiter of 5%. The dotted lines are the simulation results in the absence of suprathermal electrons (flux limiter of 5%). The dashed lines indicate a simulation that also matches the x-ray flash time but in the absence of suprathermal electrons (the flux limiter was increased to 8%). For reference, the solid gray line indicates the laser pulse.

the ablation surface, corresponding to ~12% of the total energy in a 70-keV Maxwellian distribution, while suprathermal electrons with temperatures from 60 to 200 keV are stopped between the ablation and shock front, corresponding to ~55% of the total suprathermal energy. Therefore, using the ablation pressure as a metric to describe the conversion of laser energy into a shock strength is no longer valid. A more-effective metric in this case would be to adjust the energy transport model to simulate the effect of suprathermal electrons on the shock strength and observe a new "effective ablation pressure." The effective ablation pressure (dashed curves in Fig. 140.8) drives the shock at the same velocity as when suprathermal electrons are included (solid curves in Fig. 140.8) but without the use of suprathermal electrons. This is achieved by increasing the flux limiter and is unique to each shot in the campaign. Physically, this can be explained by the fact that a shock must travel from the outside of the target to the center in the measured period of time regardless of how the energy is transferred. Therefore, whether the shock is solely driven by the rocket effect or by a combination of ablation pressure and suprathermal-electron energy deposition, the pressure behind the shock must be independent of the mechanism driving the shock and even insensitive of many physics details. Corroborating this point is the choice of equation of state (EOS); whether using Thomas–Fermi or *SESAME*, the resulting shock pressure required to match the experimental observables remains the same despite differences in post-shock mass density. The ambiguity in EOS could be solved by a direct measurement of the mass density (e.g., Ref. 16).

It was found that the maximum ablation pressure $P_a^{max}$ and effective maximum ablation pressure $P_a^{eff}$ for all of the experiments scale with the absorbed laser intensity at the critical surface, $I_{15\,abs}$, in units of $10^{15}$ W/cm$^2$ via the following formulas:

$$P_a^{max}\,(\text{Mbar}) \approx 90\, I_{15\,abs}^{1.2}, \tag{1}$$

$$P_a^{eff}\,(\text{Mbar}) \approx 90\, I_{15\,abs}^{1.4}, \tag{2}$$

and are shown in Fig. 140.9. The error bars in Fig. 140.9 are the result of adjusting the simulated x-ray flash time by ±50 ps as a result of the absolute error in the timing diagnostics, changing both the simulated absorbed intensity and ablation pressure. This scaling shows a significant departure from previous spherical ablation pressure scaling $P_a^{theory} \approx 100\, I_{15\,abs}^{7/9}$, derived for low intensities ($\leq 10^{15}$ W/cm$^2$) (Ref. 41). The differences are likely caused by the much larger laser intensities being used as well as the presence of copious amounts of

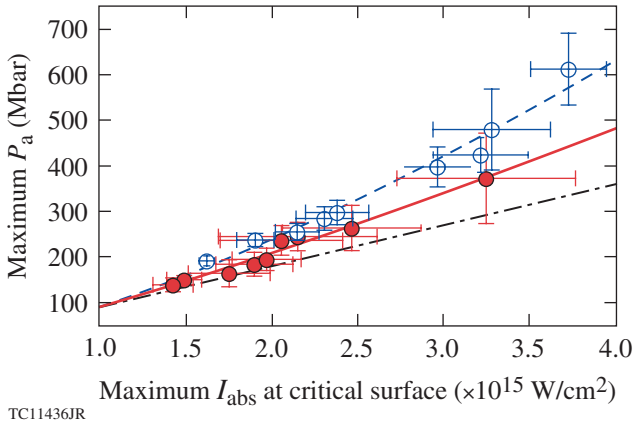


Figure 140.9
Scaling of the inferred maximum ablation pressure with suprathermal electrons (solid red circles and solid line) and effective maximum ablation pressure without suprathermal electrons (open blue circles and dashed line) versus the maximum laser intensity that is absorbed at the critical surface for simulations matching all of the experimental observables. The dashed–dotted line indicates the linear dependence of the ablation pressure on the absorbed laser intensity for unconstrained simulations with a flux limiter value of 6.5%.

suprathermal electrons that enhance the ablation pressure. An analysis of simulations in the absence of suprathermal electrons determined that the exponent of the ablation pressure scaling varies with the choice of flux limiter, e.g., choosing a value of 6.5% yields a linear dependence on the absorbed laser intensity (black dashed–dotted curve in Fig. 140.9). Comparing this curve with Eq. (1) demonstrates how suprathermal electrons enhance the ablation pressure.

Extrapolating Eqs. (1) and (2) to the absorbed laser intensities of ~$7 \times 10^{15}$ W/cm$^2$ used in the 700-kJ NIF SI point design of Ref. 10, one finds ablation pressures that significantly exceed the required ~600 Mbar (0.9 Gbar and 1.3 Gbar, respectively), indicating predicted ablation pressures to be high enough for robust ignition. However, NIF-scale ignition targets are much larger than those used in these OMEGA experiments, thereby leading to longer-scale-length plasmas at the time of shock launch. Higher levels of laser–plasma instabilities are expected, and a simple extrapolation of Eqs. (1) and (2) to NIF-scale plasmas may not be applicable. Therefore, despite these encouraging results obtained on OMEGA, an accurate extrapolation of the shock pressure to NIF requires experiments on NIF-scale targets.

In summary, this article reports on the first experimental ablation-pressure inferences in spherical geometries at SI-relevant laser intensities. Up to 8% of the laser energy was converted into suprathermal electrons that enhanced both the ablation pressure driving the shock and the shock itself, leading to an inferred effective ablation pressure scaling with the absorbed laser intensity of $P_a^{eff}$ (Mbar) ≈ 90 $I_{15\,abs}^{1.4}$. This result demonstrates the ability to launch several-hundred-Mbar shocks at SI-relevant laser intensities with the generation of moderate-temperature suprathermal electrons.

## ACKNOWLEDGMENT

This material is based upon work supported by the Department of Energy National Nuclear Security Administration under Award Number DE-NA0001944, the Office of Fusion Energy Sciences Number DE-FG02-04ER54786, the University of Rochester, and the New York State Energy Research and Development Authority. The support of DOE does not constitute an endorsement by DOE of the views expressed in this article.

## REFERENCES

1. R. Betti, C. D. Zhou, K. S. Anderson, L. J. Perkins, W. Theobald, and A. A. Solodov, Phys. Rev. Lett. **98**, 155001 (2007).
2. L. J. Perkins, R. Betti, K. N. LaFortune, and W. H. Williams, Phys. Rev. Lett. **103**, 045004 (2009).
3. X. Ribeyre, G. Schurtz, M. Lafon, S. Galera, and S. Weber, Plasma Phys. Control. Fusion **51**, 015013 (2009).
4. M. Lafon, X. Ribeyre, and G. Schurtz, Phys. Plasmas **20**, 022708 (2013).
5. A. J. Schmitt *et al.*, Phys. Plasmas **17**, 042701 (2010).
6. S. Atzeni, X. Ribeyre, G. Schurtz, A. J. Schmitt, B. Canaud, R. Betti, and L. J. Perkins, Nucl. Fusion **54**, 054008 (2014).
7. D. Batani, S. Baton, A. Casner, S. Depierreux, M. Hohenberger, O. Klimo, M. Koenig, C. Labaune, X. Ribeyre, C. Rousseaux, G. Schurtz, W. Theobald, and V. T. Tikhonchuk, Nucl. Fusion **54**, 054009 (2014).
8. M. Tabak *et al.*, Phys. Plasmas **1**, 1626 (1994).
9. J. Nuckolls *et al.*, Nature **239**, 139 (1972).
10. K. S. Anderson, R. Betti, P. W. McKenty, T. J. B. Collins, M. Hohenberger, W. Theobald, R. S. Craxton, J. A. Delettrez, M. Lafon, J. A. Marozas, R. Nora, S. Skupsky, and A. Shvydky, Phys. Plasmas **20**, 056312 (2013).
11. T. R. Boehly, D. L. Brown, R. S. Craxton, R. L. Keck, J. P. Knauer, J. H. Kelly, T. J. Kessler, S. A. Kumpan, S. J. Loucks, S. A. Letzring, F. J. Marshall, R. L. McCrory, S. F. B. Morse, W. Seka, J. M. Soures, and C. P. Verdon, Opt. Commun. **133**, 495 (1997).
12. W. Theobald, R. Betti, C. Stoeckl, K. S. Anderson, J. A. Delettrez, V. Yu. Glebov, V. N. Goncharov, F. J. Marshall, D. N. Maywar, R. L. McCrory, D. D. Meyerhofer, P. B. Radha, T. C. Sangster, W. Seka, D. Shvarts, V. A. Smalyuk, A. A. Solodov, B. Yaakobi, C. D. Zhou, J. A. Frenje, C. K. Li, F. H. Séguin, R. D. Petrasso, and L. J. Perkins, Phys. Plasmas **15**, 056306 (2008).

13. S. D. Baton *et al.*, Phys. Rev. Lett. **108**, 195002 (2012).

14. M. Hohenberger, W. Theobald, S. X. Hu, K. S. Anderson, R. Betti, T. R. Boehly, A. Casner, D. E. Fratanduono, M. Lafon, D. D. Meyerhofer, R. Nora, X. Ribeyre, T. C. Sangster, G. Schurtz, W. Seka, C. Stoeckl, and B. Yaakobi, Phys. Plasmas **21**, 022702 (2014).

15. D. Batani *et al.*, Phys. Plasmas **21**, 032710 (2014).

16. A. L. Kritcher *et al.*, High Energy Density Phys. **10**, 27 (2014).

17. G. H. Miller, E. I. Moses, and C. R. Wuest, Opt. Eng. **43**, 2841 (2004).

18. J. D. Lindl, Phys. Plasmas **2**, 3933 (1995).

19. S. P. Regan, T. C. Sangster, D. D. Meyerhofer, W. Seka, R. Epstein, S. J. Loucks, R. L. McCrory, C. Stoeckl, V. Yu. Glebov, O. S. Jones, D. A. Callahan, P. A. Amendt, N. B. Meezan, L. J. Suter, M. D. Rosen, O. L. Landen, E. L. DeWald, S. H. Glenzer, C. Sorce, S. Dixit, R. E. Turner, and B. MacGowan, J. Phys.: Conf. Ser. **112**, 022077 (2008).

20. S. Skupsky, R. W. Short, T. Kessler, R. S. Craxton, S. Letzring, and J. M. Soures, J. Appl. Phys. **66**, 3456 (1989).

21. D. K. Bradley, P. M. Bell, J. D. Kilkenny, R. Hanks, O. Landen, P. A. Jaanimagi, P. W. McKenty, and C. P. Verdon, Rev. Sci. Instrum. **63**, 4813 (1992).

22. M. Millecchia, S. P. Regan, R. E. Bahr, M. Romanofsky, and C. Sorce, Rev. Sci Instrum. **83**, 10E107 (2012).

23. D. K. Bradley, P. M. Bell, J. D. Kilkenny, R. Hanks, O. Landen, P. A. Jaanimagi, P. W. McKenty, and C. P. Verdon, Rev. Sci. Instrum. **63**, 4813 (1992).

24. J. J. MacFarlane *et al.*, in *Inertial Fusion Sciences and Applications 2003*, edited by B. A. Hammel, D. D. Meyerhofer, J. Meyer-ter-Vehn, and H. Azechi (American Nuclear Society, La Grange Park, IL, 2004), pp. 457–460.

25. E. Goldman, Laboratory for Laser Energetics, University of Rochester, Rochester, NY, LLE Report No. 16 (1973).

26. J. F. Myatt, J. Zhang, R. W. Short, A. V. Maximov, W. Seka, D. H. Froula, D. H. Edgell, D. T. Michel, I. V. Igumenshchev, D. E. Hinkel, P. Michel, and J. D. Moody, Phys. Plasmas **21**, 055501 (2014).

27. C. Stoeckl, V. Yu. Glebov, D. D. Meyerhofer, W. Seka, B. Yaakobi, R. P. J. Town, and J. D. Zuegel, Rev. Sci. Instrum. **72**, 1197 (2001).

28. R. Tommasini *et al.*, Rev. Sci. Instrum. **77**, 10E301 (2006).

29. C. D. Chen *et al.*, Rev. Sci. Instrum. **79**, 10E305 (2008).

30. F. J. Marshall and J. A. Oertel, Rev. Sci. Instrum. **68**, 735 (1997).

31. R. Betti, W. Theobald, C. D. Zhou, K. S. Anderson, P. W. McKenty, S. Skupsky, D. Shvarts, V. N. Goncharov, J. A. Delettrez, P. B. Radha, T. C. Sangster, C. Stoeckl, and D. D. Meyerhofer, J. Phys.: Conf. Ser. **112**, 022024 (2008).

32. A. R. Bell, Rutherford Appleton Laboratory, Chilton, Didcot, Oxon, England, Report RL-80-091 (1980).

33. G. I. Kerley, Phys. Earth Planet. Inter. **6**, 78 (1972).

34. G. I. Kerley, Sandia National Laboratory, Albuquerque, NM, Report SAND2003-3613 (2003).

35. R. C. Malone, R. L. McCrory, and R. L. Morse, Phys. Rev. Lett. **34**, 721 (1975).

36. J. Delettrez and E. B. Goldman, Laboratory for Laser Energetics, University of Rochester, Rochester, NY, LLE Report No. 36 (1976).

37. A. A. Solodov and R. Betti, Phys. Plasmas **15**, 042707 (2008).

38. Von G. Guderley, Luftfahrtforschung **19**, 302 (1942).

39. S. Gus'kov *et al.*, Phys. Rev. Lett. **109**, 255004 (2012).

40. X. Ribeyre *et al.*, Phys. Plasmas **20**, 062705 (2013).

41. S. Atzeni, Plasma Phys. Control. Fusion **42**, B143 (2000).

# Direct-Drive–Ignition Designs with Mid-*Z* Ablators

## Introduction

In laser-driven inertial confinement fusion (ICF),[1,2] a spherical capsule filled with deuterium–tritium (DT) is irradiated by direct laser illumination. Ablation of material from the target's outer surface generates a low-density coronal plasma and drives the implosion of the fuel shell through the rocket effect. To achieve ignition, the shell must be imploded at velocities >350 km/s to create a central hot spot enclosed within a cold and dense shell at stagnation. At the National Ignition Facility (NIF),[3] this implies that the hot spot of a capsule reaches both high areal density ($\rho R \sim 0.4$ g/cm$^2$) and high temperature ($T \sim 10$ keV) while the total target areal density exceeds 1.5 g/cm$^2$. The DT fuel entropy is characterized by the adiabat $\alpha$ defined as the ratio of the shell pressure to the Fermi pressure of a fully degenerate gas. To achieve such conditions, low-adiabat implosions ($\alpha \leq 3$) are required. The fuel adiabat is set during the first stage of the implosion, and it can be controlled by a precise tuning of the laser-induced, shock-wave timing. Low-adiabat implosions lead to higher areal densities and require less kinetic energy to achieve ignition conditions.

Shell preheat represents a major degradation mechanism for the fuel adiabat. Preheat is caused by the generation of hot electrons at densities below the critical density and results in degradation of the final compression. In the context of direct-drive implosions, the acceleration of electrons to high energies in the coronal plasma induced by the two-plasmon–decay (TPD)[4] instability can significantly reduce the target performance. Recent experiments on the OMEGA Laser System[5] have shown evidence of TPD-driven high-energy electrons during direct-drive implosions using $D_2$, DT, and plastic ablators.[6–8] Another critical area of concern to ICF is the unstable growth of target nonuniformitites resulting from hydrodynamic instabilities. During the implosion, the ablation surface between the expanding low-density coronal plasma and the high-density shell is subject to the Rayleigh–Taylor (RT) instability.[9,10] Therefore, perturbations imprinted on the target by nonuniform laser irradiation as well as modulations resulting from target fabrication will grow exponentially during the acceleration phase at a rate given by the modified Takabe formula[11,12] $\gamma(k) = \alpha\sqrt{kg/(1+kL)} - \beta k V_a$, where $\alpha$ and $\beta$ are coefficients depending on the ablation surface, $k$ is the wave number of the perturbation, $g$ is the acceleration, $L$ is the density scale length at the ablation surface, and $V_a$ is the ablation velocity. During the acceleration phase, the perturbation of the ablation surface feeds through to the inner shell surface, which becomes unstable when the shell is slowed down by the hot-spot gas. Excessive perturbation growth will reduce the total areal density level by raising the fuel adiabat and degrading the hot-spot conditions required for ignition. The unstable growth of these perturbations must be mitigated during the implosion to maintain the integrity of the shell at stagnation.

For ignition designs on the NIF, it is desirable to explore new ablators that mitigate both TPD and RT instabilities. Using materials of medium atomic number $Z$ as ablators presents some advantages and has recently gained interest for direct-drive implosions. In laser-driven ablation of low-$Z$ material, the optical laser radiation is absorbed around the critical density; the thermal energy is then transported by electrons from the absorption zone to the ablation surface. In the case of moderate-$Z$ materials, the thermal radiation is directly absorbed into the ablator material, resulting in a double-ablation-front (DAF) structure[13,14] (electron-conduction and radiation-driven ablation fronts). Such a structure leads to a higher ablation velocity $V_a$ and a longer density scale length $L$, thereby enhancing the ablative stabilization of RT growth at the electron front. Moreover, irradiation of mid-$Z$ materials results in a better absorption of laser energy by inverse bremsstrahlung than low-$Z$ ablators, leading to a higher electron temperature in the coronal plasma. The TPD instability gain is proportional to the inverse of the electron temperature[15] and will be increased for mid-$Z$ ablators compared to plastic for equal density scale length. Many experiments have been recently performed to investigate these effects. A significant reduction in the hard x-ray signal for mid-$Z$ ablators has been observed on OMEGA, suggesting the mitigation of the TPD-driven hot-electron generation.[16–19] Mid-$Z$ targets have also demonstrated a reduced laser-imprint efficiency as well as a lower overall RT growth rate[20–22] on OMEGA and OMEGA EP.[23] Using higher-$Z$ material ablators

is expected, however, to present some downsides. The electron-heat conduction is lower for higher-$Z$ materials, reducing the transport of the energy absorbed at subcritical densities to the ablation surface. The mass ablation rate and the resulting ablation pressure are consequently decreased, leading to a reduced hydrodynamic efficiency. Additionally, high-$Z$ materials present higher radiation losses in the hot coronal plasma as well as more radiation preheat of the fuel. Furthermore, at the radiation front, the ablation velocity and density-gradient scale length are reduced and the RT growth is enhanced. Simulations of the overall stability are, therefore, needed to correctly assess the conflicting behavior of the two ablation fronts.

The aim of this article is to evaluate the viability of these ablator materials as a path for ignition target designs on the NIF. The following sections (1) introduce the one-dimensional (1-D) design and performance of three targets using different mid-$Z$ ablators; (2) assess the linear stability of the TPD for these ablators; (3) explore the robustness to two-dimensional (2-D) single-mode and multimode perturbations under uniform drive; (4) display a polar-direct-drive beam configuration for each target; and, finally, (5) summarize the conclusions.

## One-Dimensional Target Design Using Mid-$Z$ Ablators

To investigate the viability of mid-$Z$ ablator materials for ignition targets, three hydro-equivalent targets (same implosion velocity and fuel adiabat) with average atomic number ranging from 3.5 to 10 were designed. The ignition designs use pure plastic (CH, $\langle Z \rangle = 3.5$), high-density carbon (HDC, $\langle Z \rangle = 6$), and glass ($SiO_2$, $\langle Z \rangle = 10$) ablators. The plastic target is a variant of the 1-D–equivalent NIF ignition target described by Collins *et al.*[24] Throughout this article, the conventional plastic ablator design is used as a reference target for comparison with the alternative carbon and glass ablators.

The 1-D radiation–hydrodynamic code *LILAC*[25] has been used to optimize the target design and carefully tune the laser pulse to obtain comparable implosion performance for all three targets. Figure 140.10 presents the target design as well as the laser pulse for each ablator material. The targets consist of a solid-DT fuel capsule filled with DT gas surrounded by a plastic layer coated with an ablator layer. The plastic and ablator layer thicknesses are precisely chosen to keep the fuel on a low adiabat during the implosion, avoiding radiation preheat of the DT fuel at the end of the laser pulse. Triple-picket laser pulses followed by a low-intensity foot and a Kidder-like[26] isentropic rise to the main drive are used to carefully tune the fuel adiabat at the beginning of the implosion as well as raise the ablation velocity at the outer surface to reduce the RT growth

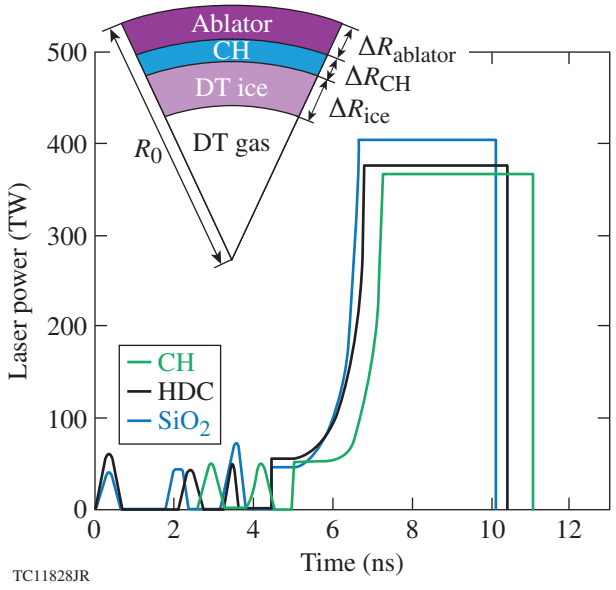


Figure 140.10
Schematic of the ignition target design and corresponding laser pulses for plastic (CH) (green curve), high-density carbon (HDC) (black curve), and glass ($SiO_2$) ablators (blue curve).

rate according to the modified Takabe formula in the **Introduction** (p. 220). Each picket along with the low-intensity foot has a 300-ps rise time. The laser beams use a super-Gaussian intensity profile focused at the initial target radius $R_0$ with an exponent $\sigma = 2.2$.

One-dimensional *LILAC* simulations of mid-$Z$ (HDC and $SiO_2$) ablators were performed using multigroup diffusion radiation transport; an average-ion model[27,28] in collisional radiative equilibrium (CRE)[29] for opacity tables; nonlocal thermodynamic equilibrium (non-LTE) tables for ionization; and a *SESAME*[30] equation of state (EOS). The low-$Z$ ablator (CH) was modeled using the Astrophysical Opacity Table (AOT)[31] and *SESAME* EOS. All simulations used electron thermal transport described in the classical Spitzer-Härm[32] approximation with a flux limiter $f = 0.06$. The structure of the DAF in higher-$Z$ materials strongly depends on the transport of radiation energy through the outer part of the shell. Although the plastic and carbon materials were properly modeled using 16 radiation groups, the glass ablator required 48 radiation groups to accurately describe the radiation transport and the resulting density and temperature profiles. We have found, however, that the results are relatively insensitive to details of the opacity tables. For instance, we compared simulations of the glass target using average-ion CRE tables and CRE tables generated by *PROPACEOS*[33] and found that the target gain changed by only 4%.

The target designs, laser parameters, and 1-D target performance for each ablator are summarized in Table 140.I. In this study, we consider plastic, high-density carbon, and glass with initial densities of 1.04, 3.5, and 2.32 g/cm$^3$, respectively. A plastic layer is introduced underneath the ablator in the mid-$Z$ designs as a protective layer for the DT fuel from possible radiation preheat produced by the mid-$Z$ ablator, as well as to reduce the density jump between the DT fuel and the ablator. The total energy in the pulses is 1.65 MJ, resulting in an implosion velocity of about 360 km/s for all three targets. The in-flight average fuel adiabat $\langle\alpha\rangle_{\text{fuel}}$ is kept at around 2. The ignition margin is determined by the level of multidimensional perturbations that the hot spot can tolerate to achieve marginal ignition. This parameter can be connected to a volume ratio described in 1-D by the minimal ratio of the clean volume at sub-ignition temperatures to the 1-D hot-spot volume[34,35] and is referred to as the minimum yield-over-clean (mYOC). The three targets have been designed to exhibit the same 1-D margin characterized by a mYOC ~ 40%. By doing so, all designs present a similar margin for ignition so that one can compare their robustness to ignition when the implosion is perturbed. Since mid-$Z$ ablators are significantly heavier than plastic and exhibit lower hydrodynamic efficiency, the high implosion velocities required for ignition can be achieved only by limiting the total mass, thereby making the shells thinner. All targets are irradiated with a laser intensity ~1.2 × 10$^{15}$ W/cm$^2$ and produce high gains. The glass target produces less thermonuclear energy because of a thinner DT layer. The in-flight aspect ratio (IFAR$_{2/3}$), defined as the ratio of the shell radius $R$ to the shell thickness $\Delta R$ (defined between the inner fuel interface and the radiation front) when the shell inner surface is two-thirds of the initial target radius, is 27 for CH and 24 for HDC. The glass design presents two different values for the IFAR$_{2/3}$, characterizing the aspect ratio of the target by including only the radiation front or both the radiation and electron fronts. As a result of a decompressed ablator caused by stronger radiation effects, the distance between the inner fuel surface and the electron ablation front is large, resulting in an IFAR$_{2/3}$ value of 14. If the shell thickness $\Delta R$ is defined as the full-width-at-half-maximum density and, therefore, does not account for the zone between the electron and the radiation ablation fronts, the value of IFAR$_{2/3}$ including only the radiation front reaches 35, which is higher than for the plastic and carbon ablators.

Table 140.I: Target design and performances for the different ablator materials.

| | CH | HDC | $SiO_2$ |
|---|---|---|---|
| $R_0$ ($\mu$m) | 1599 | 1550 | 1428 |
| $\Delta R_{\text{ice}}$ ($\mu$m) | 204 | 184 | 161 |
| $\Delta R_{\text{CH}}$ ($\mu$m) | – | 12 | 7 |
| $\Delta R_{\text{a}}$ ($\mu$m) | 43 | 13 | 23 |
| $E_{\text{L}}$ (MJ) | 1.65 | 1.65 | 1.65 |
| $V_{\text{imp}}$ (km/s) | 361 | 363 | 361 |
| $\langle\alpha\rangle_{\text{fuel}}$ | 2.2 | 2.1 | 2.0 |
| mYOC (%) | 41 | 40 | 41 |
| Gain | 74.6 | 72.0 | 53.0 |
| $I_{\text{L}}$ (×10$^{15}$ W/cm$^2$) | 1.2 | 1.3 | 1.5 |
| IFAR$_{2/3}$ | 27 | 24 | 35/14 |

At such laser intensities, the radiation effects induce strong modifications of the hydrodynamic profiles. Figure 140.11 shows profiles of the radial mass density (solid lines) and electron temperature (dashed lines) at the end of the laser pulse for the three targets. The laser energy is absorbed by inverse bremsstrahlung, with the cross-section scaled as $\langle Z^2\rangle/\langle Z\rangle$, and, therefore, enhances the absorption in mid-$Z$ materials. As a consequence, the temperature in the coronal plasma is higher for the carbon and glass ablators (5.3 and 6.2 keV, respectively) than for the plastic ablator (~4.9 keV). In the case of plastic targets, the absorbed laser energy is transferred to thermal electrons that drive the electron ablation front. For mid-$Z$ targets,

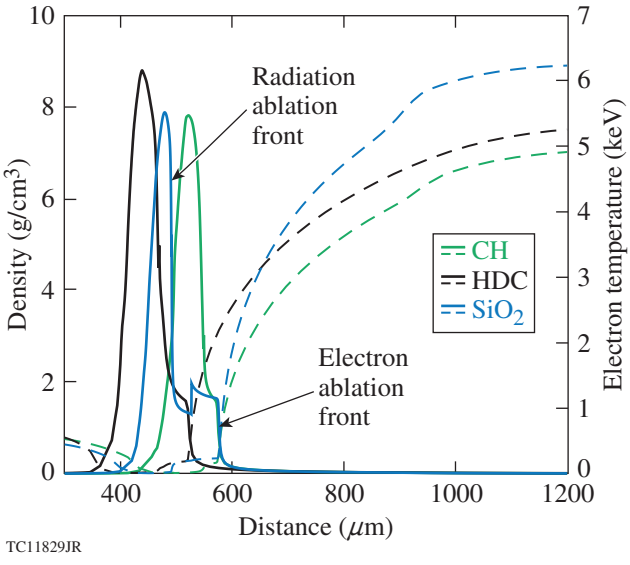


Figure 140.11
Profiles of radial mass density (solid curves) and electron temperature (dashed curves) at the end of the laser pulse for the plastic (11 ns) (green curve), carbon (10.4 ns) (black curve), and glass (10.1 ns) (blue curve) targets.

the high-temperature corona plasma emits strong radiation that deposits its energy in more-opaque regions of the target, where the temperature is lower and the density is higher, thereby driving the radiation ablation front. This DAF structure is clearly visible in Fig. 140.11.

Despite a better overall absorption, the hydroefficiency of ICF designs using mid-$Z$ ablators is expected to be altered in comparison with low-$Z$ material targets. The mass ablation rate and ablation pressure are decreased as the thermal conduction scales as $1/Z_{\text{eff}}$, where $Z_{\text{eff}} = \langle Z^2 \rangle / \langle Z \rangle$. As a result of less-effective heat transport and radiation losses in high-$Z$ coronal plasmas, the hydrodynamic efficiency is reduced. It has also been observed that the conduction zone is much shorter for mid-$Z$ materials than for plastic, which can have a compensating effect (that level depending on the material and its density) for the conduction losses.[17]

The three targets have been designed in 1-D to achieve similar implosion characteristics, high-gain performances, and ignition margins. The remaining sections compare mid-$Z$ to plastic ablators with respect to hot-electron generation and hydrodynamic instability growth.

**Mitigation of the Two-Plasmon–Decay Instability**

The performance of low-adiabat direct-drive implosions can be severely degraded by hot-electron preheating at laser intensities for which the quarter-critical electron density is above ~$5 \times 10^{14}$ W/cm$^2$. Recent experiments on OMEGA have shown that the hard x-ray signals generated by hot electrons from the TPD instability rise sharply at laser intensities above $5 \times 10^{14}$ W/cm$^2$ and then saturate for plastic ablator targets.[7,8,36] The measured hot-electron temperature is in the 50- to 100-keV range when the laser intensity increases from $5 \times 10^{14}$ to $10^{15}$ W/cm$^2$ and the fraction of total laser energy deposited into hot electrons saturates at a level of a few percent[18,37–39] at $10^{15}$ W/cm$^2$ in planar targets, which is sufficient to significantly raise the fuel adiabat. Implosions at adiabats relevant to the high-gain designs for the NIF require strategies to mitigate hot-electron preheat.

A straightforward path to preheat mitigation is to use different ablator materials to modify the hydrodynamic profiles and increase the instability threshold for the TPD instability. OMEGA experiments in the intensity range of 3 to $7 \times 10^{14}$ W/cm$^2$ have demonstrated lower hot-electron production for silicon, germanium, and chlorine-doped plastic ablators.[17–19] The reduction reaches a factor of 10 for an aluminum ablator,[17] which may be a result of a near-threshold effect. The hard x-ray signals caused by TPD-driven hot electrons were reduced by a factor of 40 in implosions using glass ablators compared to plastic[16] at an intensity of $10^{15}$ W/cm$^2$. The measured hot-electron temperature was reduced by a factor of 2 with the glass ablators, resulting in a reduction of the shell preheat by more than an order of magnitude.

The threshold[15] for triggering the absolute TPD instability of a plane electromagnetic (EM) wave in an inhomogenous plasma is given approximately by the parameter $\eta = L_n \times I_{14} / (230\, T_e) = 1$, where $L_n$ is the density scale length in $\mu$m, $I_{14}$ is the EM wave intensity in units of $10^{14}$ W/cm$^2$, and $T_e$ is the electron temperature in keV, with all these parameters being evaluated at quarter-critical density. According to this formula, ablators of moderate-$Z$ numbers exhibit several advantages over low-$Z$ materials: a higher electron temperature $T_e$; a better absorption in the corona, leading to a lower-intensity $I_{14}$ at quarter-critical density; and a shorter density scale length $L_n$ because of the slow expansion of the heavier fluid. However, the TPD instability presents a nonlinear behavior, leading to the saturation of the growth rate at high intensities.

The collisional damping of Langmuir waves (LW's) plays an important role in materials with a higher $Z_{\text{eff}}$ than plastic. The linear growth rate of the TPD instability obtained by Simon *et al.*[15] has been generalized to account for the LW collisional damping and can be expressed as

$$\hat{\gamma} = \frac{L_n I_{14}}{230\, T_e} - 1 - \frac{0.3\, Z_{\text{eff}} L_n \sqrt{I_{14}}}{230\, T_e^{5/2}}. \qquad (1)$$

The $Z_{\text{eff}}$ number of the three targets introduced in the previous section varies between 5.3 for CH, 6 for HDC, and 10.8 for $SiO_2$. Figure 140.12(a) shows the temporal evolution of the electron temperature at quarter-critical density, and Fig. 140.12(b) shows the generalized TPD growth rate introduced in Eq. (1) for the three designs. The temporal axis has been normalized to the beginning of the main drive for each target. The electron temperature has been increased by ~1500 eV and ~500 eV, respectively, for the glass and carbon targets compared to the plastic target (~4.0 keV). Because of a higher temperature and a shorter density scale length (~450 $\mu$m for $SiO_2$ and ~550 $\mu$m for CH), the first term of the right-hand side of Eq. (1) is decreased for mid-$Z$ materials. However, the effect of collisional damping on the TPD growth rate [represented by the last term of the right-hand side of Eq. (1)] is strongly dependent on the temperature and is also correlated to the effective atomic number. As a result, the carbon target and especially the glass target benefit from a higher collisional damping of LW than the

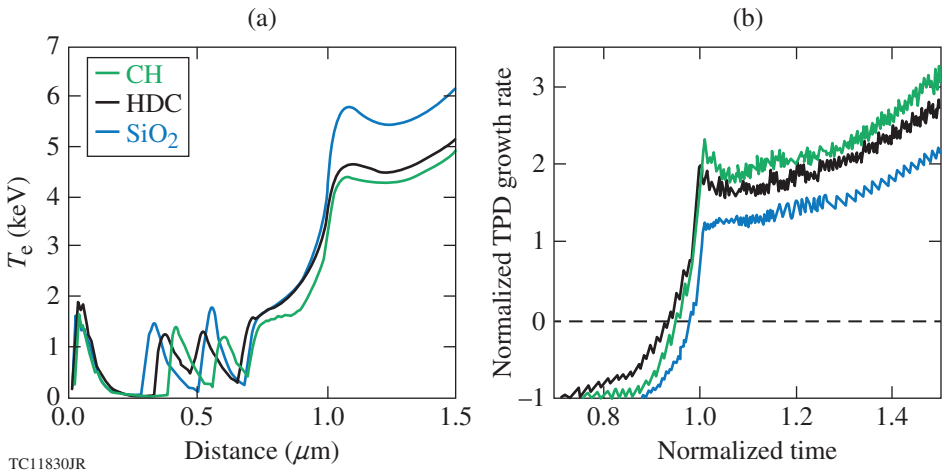


Figure 140.12
Temporal evolution of (a) the electron temperature at quarter-critical density and (b) the normalized two-plasmon–decay (TPD) growth rate for the plastic (green curve), high-density carbon (black curve), and glass ablators (blue curve).

plastic target. The absolute TPD instability is triggered when the generalized growth rate is positive $\hat{\gamma} > 0$. One can observe in Fig. 140.12(b) that the three targets will be affected by this instability. The growth rate is still lower, however, for mid-$Z$ than low-$Z$ ablators, presumably resulting in a saturation at a lower level of conversion fraction of energy into hot electrons.

Nonlinear effects such as the collisional damping of Langmuir waves (LW's) and the collisional damping of ion-acoustic waves (IAW's) can be accounted for by performing simulations[40] based on the Zakharov model of TPD.[41,42] These calculations describe the growth and the nonlinear saturation of the TPD instability. It has been shown that materials with a higher effective atomic number $Z_{\text{eff}} = \langle Z^2 \rangle / \langle Z \rangle$ lead to TPD saturation at similar intensities (~$10^{15}$ W/cm$^2$) but present a lower fraction of energy converted into hot electrons[43] (approximately half the level for glass material compared to plastic). On the basis of Ref. 43, mid-$Z$ materials appear to benefit from higher collisional damping of LW as well as from weaker damping of IAW.

For OMEGA implosions at intensities above $10^{15}$ W/cm$^2$, the stimulated Raman scattering (SRS) instability can also couple laser energy into hot electrons.[44] The laser-intensity threshold for excitation of SRS[45] is $I_{16} \simeq 10\left(T_e / L_n^{4/3}\right)$, where $I_{16}$ is in units of $10^{16}$ W/cm$^2$, $L_n$ is in $\mu$m, and $T_e$ is in keV at quarter-critical density for a laser wavelength of 0.351 $\mu$m. Another laser–plasma interaction (LPI) issue for coupling laser energy to the plasma is cross-beam energy transfer (CBET). The uniform illumination of targets with many overlapping laser beams creates favorable conditions to allow for the transfer of energy among beams, scattering the light outward and reducing laser coupling. Calculations have shown that CBET becomes an important factor in OMEGA implosions[46] at intensities above $5 \times 10^{14}$ W/cm$^2$. The dependence of the gain rate of CBET on atomic number $Z$ is complex but can be approximated[47] as $1/Z$. Consequently, the higher temperature and shorter density scale length exhibited in mid-$Z$ hydrodynamic profiles indicate a mitigation of SRS-driven hot electrons as well as a reduction of CBET.

### Hydrodynamic Stability of Moderate-Z Ablator Targets Under Uniform Drive

In this section, we investigate the hydrodynamic stability properties of mid-$Z$ ablators. Theoretical[14,48] and numerical studies[49] have shown that the DAF structure characteristic of mid-$Z$ materials can aid in the overall stabilization of the target. Reduced RT growth rates have been observed experimentally in bromine,[13,50] silicon, and germanium-doped plastic[20,21] compared to pure plastic. Therefore, the viability of mid-$Z$ ablators as a potential ICF direct-drive–ignition ablator is studied and compared to the hydrodynamic performance of plastic shells.

1. Single-Mode Simulations

The DAF structure of mid-$Z$ ablators affects the hydrodynamic stability. One-dimensional simulations are used to characterize the DAF properties. In Fig. 140.13, the 1-D *LILAC* simulations show the density profiles taken 500 ps after the beginning of the linear phase of the RT instability. The DAF structures are clearly visible for the $SiO_2$ and HDC targets, and a less-pronounced DAF can also be observed for the CH target. In ignition-scale targets, there is sufficient radiation generation and absorption to produce a DAF structure, even in CH ablators. The high ablation velocity caused by the small peak density (around 1 g/cm$^3$) at the electron front results in a strong ablative stabilization at the electron front in the DAF structure. As a consequence, the electron front is expected to be stable and only the RT instability at the radiation front must be considered. Unless otherwise indicated, the studies in the

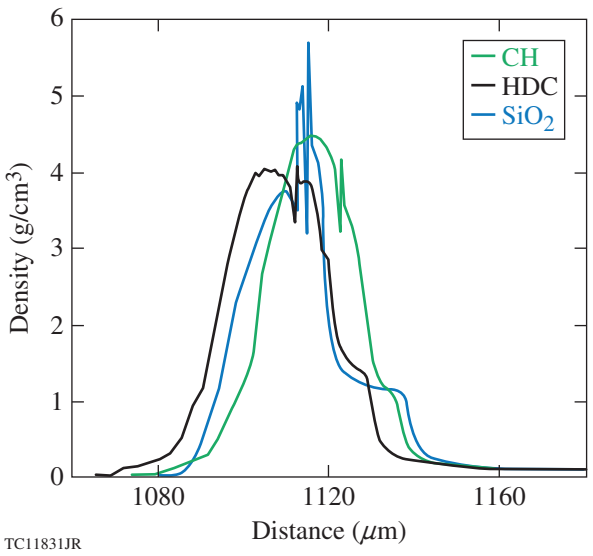


Figure 140.13
Radial mass-density profiles 500 ps after the beginning of the linear phase of the Rayleigh–Taylor (RT) instability for the plastic (8.6 ns) (green curve), carbon (8.0 ns) (black curve), and glass (7.5 ns) (blue curve) targets.

remainder of this article address the radiation front. The ablation velocity $V_a$, shell acceleration $g$, and density scale length $L$ have been extracted from the 1-D simulations at the radiation front for each target, and these values have been averaged over the linear phase of the RT growth. As one can observe in Fig. 140.13, the density scale length at the radiation front reduces when the atomic number increases with values of 3.8, 3.0, and 1.5 $\mu$m for CH, HDC, and $SiO_2$ ablators, respectively. The shell acceleration is slightly greater for the mid-$Z$ materials ($\sim 8.0 \times 10^{15}$ cm/s$^2$) than for plastic ($\sim 7.5 \times 10^{15}$ cm/s$^2$). The ablation velocity is also slightly increased for $SiO_2$ ($\sim 3.0 \times 10^5$ cm/s) compared to plastic ($\sim 2.8 \times 10^5$ cm/s), while the HDC target exhibits the higher value ($\sim 3.5 \times 10^5$ cm/s). According to the RT linear growth rate formula in the **Introduction** (p. 220), larger shell acceleration and smaller density scale length result in an increased growth of the classical RT instability at the radiation front for the mid-$Z$ targets. The higher mass ablation rate for the $SiO_2$ and especially for the HDC targets has, however, a stabilizing effect on the radiation ablation front. The slightly higher classical RT growth in the HDC target is, therefore, sufficiently compensated by the increase in the ablation velocity, while the $SiO_2$ target remains slightly more unstable than the CH target.

The RT growth in the DAF structure was investigated using the 2-D arbitrary Lagrangian–Eulerian radiation–hydrodynamics code *DRACO*.[51] This code has been recently benchmarked for single-mode linear growth against flat-foil experiments with mid-$Z$ ablators on OMEGA.[52] The *DRACO* simulations were performed using the same physical models used in the *LILAC* simulations presented in **One-Dimensional Target Design Using Mid-Z Ablators** (p. 221). The RT growth rate is calculated for several perturbation wave numbers during the linear phase of the instability by extracting the slope of a single perturbation-mode amplitude evolution in time at the radiation ablation front from the *LILAC* simulations. The RT growth is investigated for a single perturbation imposed on the target's outer surface of an initial amplitude chosen to keep the RT modes in the linear regime over the entire acceleration phase in the range of $20 < \ell < 200$. The 2-D simulations were performed using 20 azimuthal cells per half-wavelength of the perturbation and six radial cells in the interval outside the ablation surface defined by $1/k$ to ensure a good numerical resolution convergence and an accurate physical solution. The laser absorption was computed with sector ray tracing.

The amplitude of the perturbation grows exponentially as $\exp(\gamma t)$, where $\gamma$ is the linear growth rate during the acceleration phase, until it reaches the nonlinear phase when its amplitude exceeds $\sim 0.1\,\lambda$. At this point, more rapidly growing high harmonics appear and the nonlinearity of the perturbation begins. The initial amplitude for increasing mode numbers was decreased in order to keep the harmonic growth lower than 10% of the fundamental wavelength. The linear growth factor $\exp(\gamma t)$ is computed over the entire acceleration phase up to the time where the velocity reaches its peak value. Figure 140.14 shows the linear growth factor as a function of the mode number of the perturbation imposed on each target. In this figure, the initial amplitude of the mode is chosen right at the beginning of the acceleration phase, which is well past the phase inversions produced by shock propagation through the multiple interfaces occurring during the Richtmyer–Meshkov (RM) phase in the early stages of the illumination. The growth factor strongly increases with the mode number but remains similar for the three targets for low-mode numbers up to $\ell = 70$, while the glass target exhibits a larger growth than the plastic and carbon targets above $\ell = 70$. Furthermore, the growth factor depends on the perturbation wave number $k$ and is related to the mode number $\ell$ by $k = \ell/R$, where $R$ is the target's outer radius. Keeping in mind that the initial radius of the glass target is smaller than for the carbon and plastic targets, the wave number will be higher for $SiO_2$ for a specific mode number $\ell$, which will tend to increase the corresponding growth rate in comparison with HDC and CH. The most-damaging modes are those with wave numbers scaling as $k\Delta R \sim 1$, corresponding to $\ell \sim R\Delta R$. Longer wavelengths grow more slowly while shorter

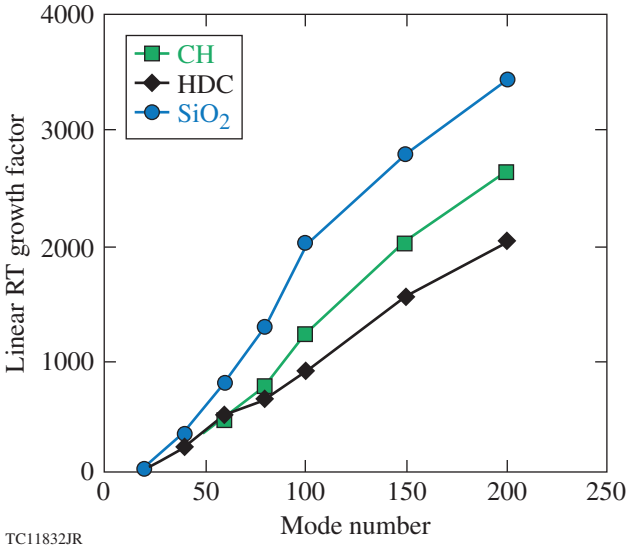


Figure 140.14
Linear growth factor of the Rayleigh–Taylor instability during the acceleration phase depending on the mode number of the perturbation for the plastic (green line with squares), high-density carbon (black line with diamonds), and glass ablators (blue line with circles).

wavelengths saturate at smaller amplitudes. Consequently, the integrity of the shell is mostly affected by $\ell$ modes in the range of $20 < \ell < 40$. Even when considering an uncertainty factor of 2, the linear growth factors in this range are similar for all three designs.

Carbon ablators exhibit lower growth than plastic for higher-mode numbers. The RT growth for the carbon target tends to saturate and enter the nonlinear phase earlier than the plastic target for higher-mode numbers. This could be an effect of the coupling between the perturbations growing at both the radiation and electron ablation fronts while no coupling occurs in the plastic target. According to Fig. 140.13, the standoff distance between the two fronts is small for the HDC target, which could lead to a more-effective coupling of the high-mode perturbations between the two fronts, while in comparison with the glass target where the large standoff distance reduces the coupling between the fronts.

Mid-*Z* ablators exhibit stability properties similar to those of plastic, especially for $\ell < 100$. A realistic implosion introduces, however, multiple sources of multimode perturbations that grow into the nonlinear regime (surface roughness, ice roughness, and laser imprint seeded by the multibeam laser irradiation). Therefore, multimode simulations must be performed to accurately assess the target performance.

2. Laser Drive and Capsule Nonuniformities

The stability of each target to multiple sources of nonuniformities is first investigated for uniform illumination. For these studies, the baseline configuration is the 1-D design, and the illumination pattern extracted from the 1-D simulation is used to irradiate the target. Several multimode simulations were performed in half-sphere geometry, using the code *DRACO*, to evaluate the overall hydrodynamic stability to capsule and single-beam nonuniformities. Capsule nonuniformities include inner-surface roughness of the DT ice layer and outer-surface roughness of the ablator. Laser nonuniformities are studied by including multimode laser imprint from single-beam irradiation. Each of these sources of perturbations is added individually to the baseline implosion for each target.

The effect of inner DT-ice roughness on the target performance is quantified by computing the gain normalized to the 1-D results while varying the amplitude of the perturbation. Perturbation modes up to $\ell = 50$ are included with the amplitude of the perturbation decaying as $\ell^{-1}$. The simulations are carried out using at least 12 azimuthal cells for the shortest wavelength. The NIF specification for the roughness of the inner DT-ice surface is set at 1-$\mu$m rms (root mean square). Figure 140.15(a) shows the target performance as a function of the initial amplitude of the inner DT-ice layer's roughness for each target. All three designs exhibit high target-gain reduction for ice roughness above 6-$\mu$m rms corresponding to 6× the NIF specification. Similarly, the capsule's sensitivity to the roughness of the ablator's outer surface is evaluated by imposing a multimode spectrum of perturbations of various amplitudes. Since the initial amplitude of the ice-roughness spectrum is set to scale as $\ell^{-1}$ in this study, the growth of high modes has a rather negligible effect on the overall stability so the ice-roughness power spectrum is chosen to include modes up to $\ell = 50$. The NIF specification for this source of perturbation is set at about 115-nm rms. Figure 140.15(b) shows the normalized target gain as a function of the surface roughness of the ablator's outer surface. All three targets achieve close to 1-D gains for up to 1-$\mu$m rms, corresponding to more than 8× the NIF specification. In conclusion, all three targets are robust to both the inner-ice-surface and outer-surface roughnesses well above NIF specifications.

The largest multimode perturbations in direct-drive ICF implosions are seeded by nonuniformities in the laser-beam intensity that imprint on the target early in the laser pulse and grow during the acceleration phase. Multimode simulations of laser imprinting using realistic single-beam laser nonuniformities, including even modes up to $\ell = 100$ to account for

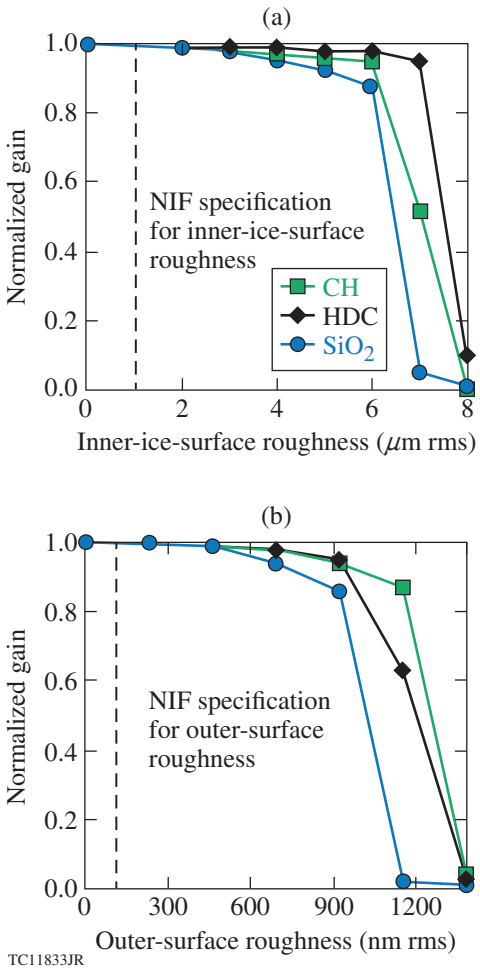


Figure 140.15
Normalized gain as a function of (a) ice roughness and (b) surface roughness for plastic (green curve), carbon (black curve), and glass (blue curve) targets in the uniform laser configuration.

the most-dangerous modes (see **Single-Mode Simulations**, p. 224), are performed for the three materials. These multimode illumination nonuniformities are modulated in time using 2-D smoothing by spectral dispersion (SSD)[53] as a method of temporal beam smoothing. Figure 140.16 shows the temporal evolution of the rms deviation of the density at the radiation ablation front extracted from half-sphere simulations of the three designs that included single-beam laser imprint. The RM-unstable phase can be observed for the three targets during the three-picket and the pre-foot laser pulses, while the RT-unstable phase starts at the beginning of the acceleration phase at 7.2 ns, 6.8 ns, and 6.6 ns for the CH, HDC, and $SiO_2$ targets, respectively. The RT growth rate at the radiation ablation front is slightly higher for the glass designs than for carbon and plastic designs, showing a comparable temporal growth of the rms deviation of density. This deviation saturates at the end of the acceleration phase and is not shown after the RT growth enters the nonlinear regime. The glass and plastic designs exhibit a smaller seed amplitude at the beginning of the RT-unstable phase (0.14 and 0.11 $\mu$m, respectively) about half the size of the carbon target (0.21-$\mu$m rms) because of phase inversions resulting from shock breakouts at the different interfaces during the RM-instability phase. Figure 140.17 shows

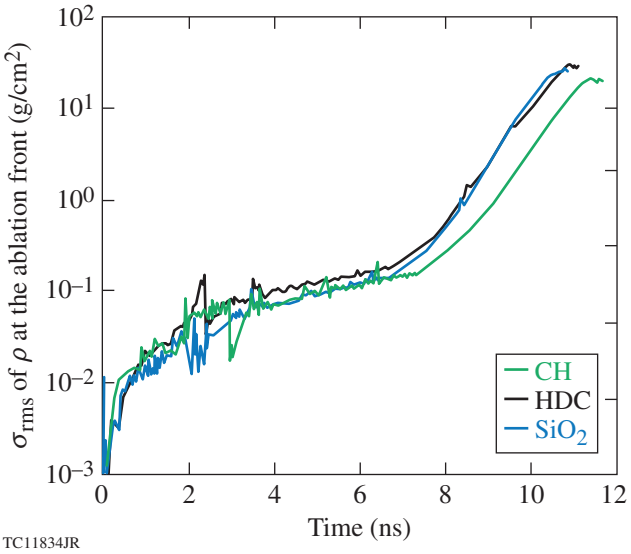


Figure 140.16
Temporal evolution of the $\sigma_{rms}$ of density at the radiation ablation front for the CH (green line), HDC (black line), and $SiO_2$ (blue line) targets.

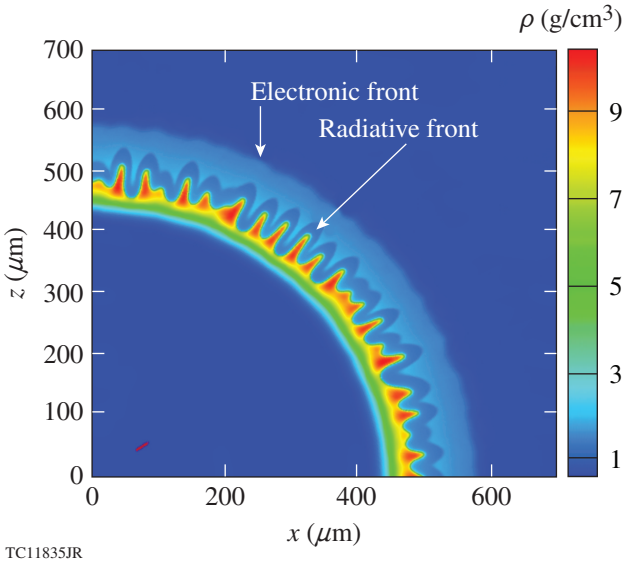


Figure 140.17
Simulated density contour plot of the uniform design subjected to laser imprint perturbations at the end of the pulse for the $SiO_2$ target.

the density contour plot of the simulation of laser imprint on the glass target at the end of the laser pulse. It clearly appears that the electron front remains stable during the acceleration phase while the RT instability has already strongly developed at the radiation front.

Perturbations at the unstable radiation ablation front are fed to the inner surface of the solid DT fuel during the acceleration phase. These perturbations seed the RT instability during the deceleration phase. The inner surface of the shell becomes unstable when the imploding material starts to decelerate because of the pressure exerted by the inner gas on the shell. When the amplitude of the final perturbation of the inner solid DT surface is comparable to the hot-spot radius, the ignition process can be severely compromised. Figure 140.18 displays the density contour plots for the (a) CH, (b) HDC, and (c) $SiO_2$ designs in the presence of laser imprinting with even modes up to $\ell = 100$ at time of ignition. The white solid lines indicate the ion temperature inside the hot spot in keV. The solid DT inner surface is more distorted for mid-*Z* ablators because of a thinner DT layer and more-effective feedthrough. The glass design exhibits a more-distorted shell than the other designs because of a higher in-flight aspect ratio. However, the overall stability of these targets to laser imprint perturbations exhibits enough margin to achieve ignition and produce high gains of 68 for CH, 62 for HDC, and 39 for $SiO_2$, corresponding to 91%, 86%, and 74%, respectively, of the nominal gain achieved for an unperturbed implosion.

Based on the above results, mid-*Z* ablator targets exhibit a performance similar to that of the conventional plastic ablator target under uniform laser irradiation. Mid-*Z* ablators do not mitigate the RT growth of perturbations seeded by either fabrication defects or laser-drive nonuniformities for ignition-scale target designs. The stabilizing effect observed at sub-ignition scale[13,20,21,50] does not significantly affect the growth at the radiation front because the radiation and electron ablation fronts are strongly decoupled during the acceleration phase. Nevertheless, mid-*Z* ablators for ignition targets mitigate the TPD instability while retaining stability properties similar to plastic ablators.

### Two-Dimensional Polar-Direct-Drive Configuration for Moderate-*Z* Ignition Targets

Because of its current indirect-drive laser configuration, standard direct-drive experiments using uniform illumination are not feasible on the NIF. To achieve the most-uniform target illumination for direct drive, repointing some of the beams from the x-ray drive configuration toward the equator should maintain enough symmetry in the drive pressure to achieve the ignition conditions [polar direct drive (PDD)[54]]. The oblique incidence of the repointed beams on the target decreases the coupling of the laser energy to the target, affecting its hydrodynamic efficiency and symmetry. Recent numerical[24,55–60] and experimental[55,61–64] studies have investigated direct-drive plastic target performances in a PDD configuration on both OMEGA and the NIF.

The 192 NIF beams are grouped into 48 clusters of four beams, with each cluster forming a quad. In the x-ray drive configuration, 24 *quads* from each hemisphere are pointed at different angles with respect to the polar axis, forming four

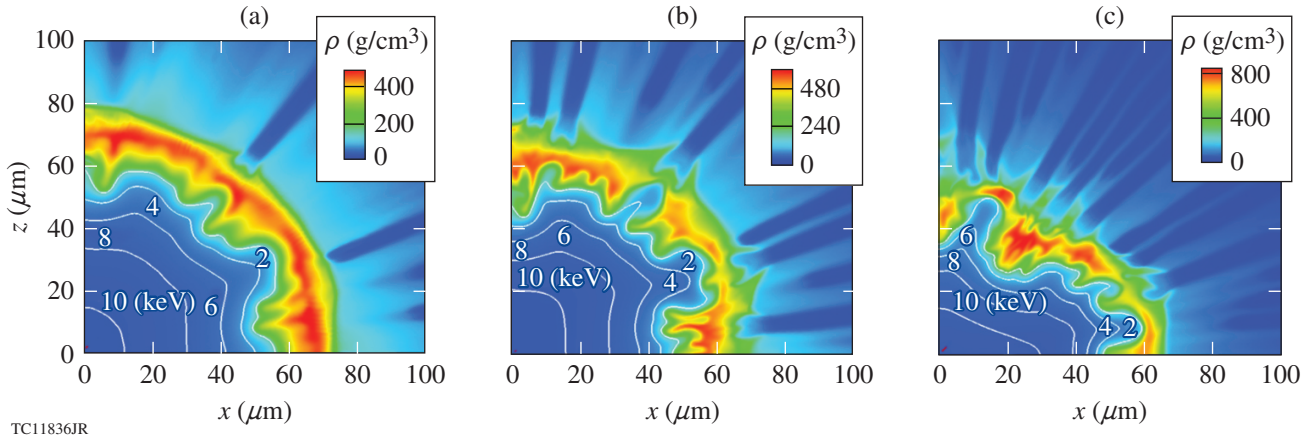


Figure 140.18
Simulated density contour plots of the 2-D uniform design subjected to laser-imprint perturbations at the onset of ignition for (a) the CH target at $t = 11.9$ ns, (b) the HDC target at $t = 11.4$ ns, and (c) the $SiO_2$ target at $t = 11.1$ ns. The white solid lines indicate (in keV) the ion temperature inside the hot spot.

*rings of beams*: four quads at 23.5°, four quads at 30°, eight quads at 44.5°, and eight quads at 50°. In the PDD configuration, the beams are repointed toward the equator: The four quads at 23.5° and 30° are repointed to 24.5° and 44°, respectively. The ring of beams at 44.5° is split into four quads repointed to 44° and four quads to 86°. The eight quads at an initial angle of 50° are all repointed to 86°. Therefore, the PDD configuration uses only three rings of beams at 24.5° (eight quads), 44° (16 quads), and 86° (24 quads) labeled, respectively, *polar*, *mid-latitude*, and *equatorial* beams to produce optimal results for drive uniformity.

Because the equatorial beams exhibit a greater obliquity to the target, they deposit their energy farther away from the ablation front than the polar beams, thereby lowering the laser absorption and reducing the drive efficiency. Therefore, the laser intensity must be increased near the equator relative to the pole to compensate for this effect. As the target implodes, time-dependent effects, as well as the multidimensional effects caused by lateral heat flow arising from temperature variations in the laser deposition region, must be considered. Furthermore, the absorption and hydrodynamic efficiency varies for different ablators. The irradiation strategy must also address the angular difference in hydrodynamic efficiency resulting from variations in density depending on the laser absorption around the target. The NIF can provide different laser pulses for each quad. To account for all these effects, different pulse shapes were used for the three rings of beams. In this study, each design required a dedicated beam-pointing strategy for the equatorial beams and time-dependent relative energy balance among the rings of beams, depending on the ablator. To illustrate this requirement, the laser pulses used to create the power balance between rings are presented in Fig. 140.19 for the $SiO_2$ design. Single-beam power for the polar (green curve), mid-latitude (blue curve), and equatorial (black curve) rings of beams is presented. To offset the reduction in laser drive, additional energy is required in the PDD configuration compared to the uniform illumination presented in **Hydrodynamic Stability of Moderate-*Z* Ablator Targets Under Uniform Drive** (p. 224). A total laser energy of 1.74 MJ, 1.75 MJ, and 1.76 MJ is used to achieve ignition of the CH, HDC, and $SiO_2$ designs, respectively.

Further optimization can be obtained by optimizing the laser-spot profiles compared to a uniform irradiation. It has been shown[24,59] that low super-Gaussian–order beam profiles are highly desirable for PDD laser-spot shapes since the energy on target can be efficiently redistributed by reducing the peaked illumination on the pole when using lower super-

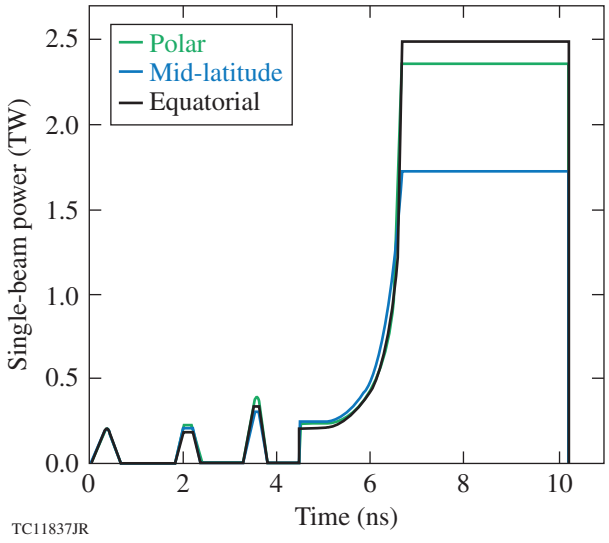


Figure 140.19
Single-beam power for the polar (green curve), mid-latitude (blue curve), and equatorial (black curve) rings of beams for the $SiO_2$ design.

Gaussian order. In this study, the on-target intensity is produced by a circular super-Gaussian profile using an order of 3.4 for the pole and 2.2 for the mid-latitude beams. To improve the absorption uniformity in the equatorial region, the laser-spot profile is obtained by adding an elliptical profile on the initial profile for the equatorial rings of beams. This ellipse is characterized by a super-Gaussian order of 2.2, a relative amplitude of 10% to 30% (depending on the ablator material) relative to the circular spot, an ellipticity of 3, and an offset of 15% of the initial target radius toward the equator relative to the center of the circular-spot profile. The focal-spot radius of the circular ellipse is set to the initial target radius for all rings of beams. Each irradiation region will require a different type of phase plate for each design presented in this article.

Polar-direct-drive simulations of the three designs were performed using the 2-D *DRACO* code including a three-dimensional (3-D) laser ray-trace modeling of the NIF beams and using a flux limiter of $f = 0.06$. The relative energy among the beams, the beam pointing, and the beam spot shapes were varied to find an optimal configuration of the target drive uniformity for each design. These calculations consider only the nonuniformities arising from beam pointing and energy balance in between rings of beams inherent to a PDD laser configuration. Simulated density contour plots along with ion temperatures (in keV) inside the hot spot (white solid lines) at the onset of ignition for the CH ($t = 12.03$ ns), HDC ($t = 11.33$ ns), and $SiO_2$ ($t = 11.15$ ns) targets are presented in Fig. 140.20.

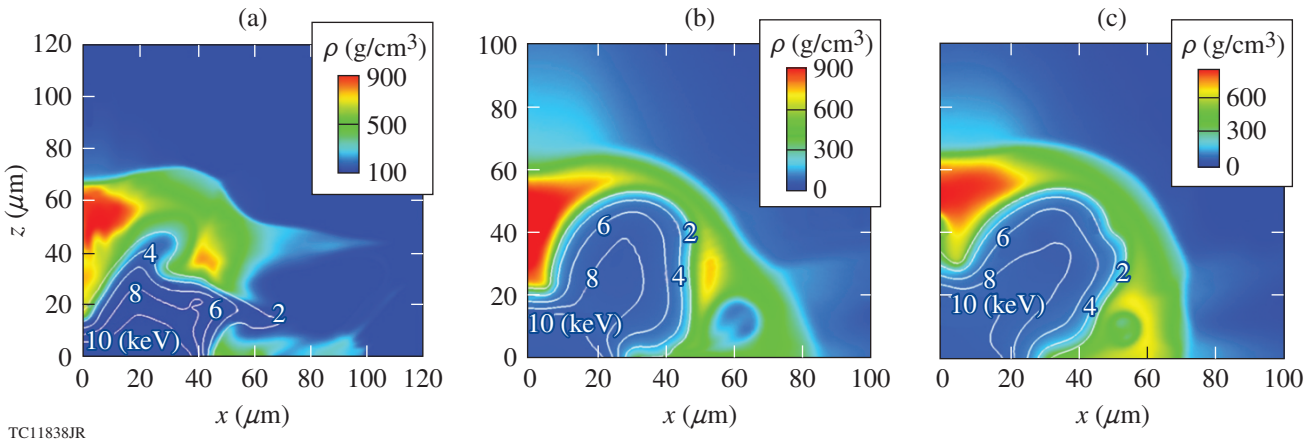


Figure 140.20
Simulated density contour plots at the onset of ignition of the (a) CH target at $t$ = 12.03 ns, (b) HDC target at $t$ = 11.33 ns, and (c) $SiO_2$ target at $t$ = 11.15 ns in the polar-direct-drive configuration. The white solid lines indicate the ion temperature inside the hot spot in keV.

All designs present a shell shape dominating $\ell = 4$ mode of nonuniformity characteristic of PDD implosions and exhibit similar shell integrity. All designs achieve high target gain using the PDD irradiation configuration. Values of 68 for CH, 65 for HDC, and 44 for $SiO_2$ are achieved corresponding to 91%, 90%, and 83%, respectively, of the nominal gain achieved for an unperturbed implosion under uniform illumination. Investigation of each design's robustness in this configuration is underway. The effects of laser imprinting and capsule nonuniformities on the PDD designs will be examined in future work. In addition, the recent developments in the *DRACO* code will allow us to investigate the nonlocal effects of heat transport[65,66] as well as the effects of CBET in laser coupling and absorption symmetry.

## Conclusions

The use of materials of medium atomic number $Z$ as ablators is considered as a possible path for direct-drive implosions to mitigate the detrimental effects of the TPD instability. Three hydro-equivalent ignition targets using pure plastic (CH), HDC, and glass ($SiO_2$) ablators have been designed to accelerate the DT fuel to the same implosion velocity and adiabat.

It has been shown that because of a higher temperature and a shorter density scale length, the threshold for the TPD instability is increased for mid-$Z$ materials. Moreover, the carbon target and especially the glass target benefit from a higher collisional damping effect on the TPD growth rate than for the plastic target. The growth rate is lower for mid-$Z$ than low-$Z$ ablators, resulting in reduced hot-electron energy and temperature. In addition, the higher plasma temperature and shorter density scale length in mid-$Z$ coronal profiles indicate that SRS and CBET will also be reduced. On the other hand, the laser energy saved from a reduced CBET effect may become available to contribute to TPD and SRS growth.

Simulations of single-mode perturbations have demonstrated that mid-$Z$-ablator–ignition designs and plastic designs have similar hydrodynamic stability properties. Multimode simulations indicate that the three targets are robust to both the inner-ice-surface and outer-surface roughnesses well above the NIF specifications. The overall stability of these targets to laser-imprint perturbations exhibits enough margin to achieve ignition and high gains for a uniform drive. Using a mid-$Z$ ablator does not appear to mitigate the RT growth of perturbations seeded by either fabrication defects or laser-drive nonuniformities for ignition-scale target designs. For more-realistic laser irradiation, a polar-direct-drive configuration has been developed for each design within the NIF laser specifications. The relative energy among the beams, the pulse shapes, the beam pointing, and the beam spot shapes were varied to find an optimal configuration for the target drive uniformity, resulting in ignition and high target gains. Therefore, mid-$Z$ ablator targets represent a viable option for direct-drive–ignition designs since they present better overall performances than plastic ablators by decreasing the detrimental effects of LPI on the implosion without a significant degradation of hydrodynamic stability properties.

## ACKNOWLEDGMENT

This work was supported by the U.S. Department of Energy National Nuclear Security Administration under Award Numbers DE-NA0001944 and DE-FC02-04ER54789, the University of Rochester, and the New York State Energy Research and Development Authority. The support of DOE does not constitute an endorsement by DOE of the views expressed in this article.

## REFERENCES


1. J. D. Lindl, *Inertial Confinement Fusion: The Quest for Ignition and Energy Gain Using Indirect Drive* (Springer-Verlag, New York, 1998).
2. S. Atzeni and J. Meyer-ter-Vehn, *The Physics of Inertial Fusion: Beam Plasma Interaction, Hydrodynamics, Hot Dense Matter*, International Series of Monographs on Physics (Clarendon Press, Oxford, 2004).
3. G. H. Miller, E. I. Moses, and C. R. Wuest, Opt. Eng. **43**, 2841 (2004).
4. M. V. Goldman, Ann. Phys. **38**, 117 (1966).
5. T. R. Boehly, D. L. Brown, R. S. Craxton, R. L. Keck, J. P. Knauer, J. H. Kelly, T. J. Kessler, S. A. Kumpan, S. J. Loucks, S. A. Letzring, F. J. Marshall, R. L. McCrory, S. F. B. Morse, W. Seka, J. M. Soures, and C. P. Verdon, Opt. Commun. **133**, 495 (1997).
6. R. L. McCrory, D. D. Meyerhofer, R. Betti, R. S. Craxton, J. A. Delettrez, D. H. Edgell, V. Yu. Glebov, V. N. Goncharov, D. R. Harding, D. W. Jacobs-Perkins, J. P. Knauer, F. J. Marshall, P. W. McKenty, P. B. Radha, S. P. Regan, T. C. Sangster, W. Seka, R. W. Short, S. Skupsky, V. A. Smalyuk, J. M. Soures, C. Stoeckl, B. Yaakobi, D. Shvarts, J. A. Frenje, C. K. Li, R. D. Petrasso, and F. H. Séguin, Phys. Plasmas **15**, 055503 (2008).
7. V. A. Smalyuk, D. Shvarts, R. Betti, J. A. Delettrez, D. H. Edgell, V. Yu. Glebov, V. N. Goncharov, R. L. McCrory, D. D. Meyerhofer, P. B. Radha, S. P. Regan, T. C. Sangster, W. Seka, S. Skupsky, C. Stoeckl, B. Yaakobi, J. A. Frenje, C. K. Li, R. D. Petrasso, and F. H. Séguin, Phys. Rev. Lett. **100**, 185005 (2008).
8. T. C. Sangster, V. N. Goncharov, P. B. Radha, V. A. Smalyuk, R. Betti, R. S. Craxton, J. A. Delettrez, D. H. Edgell, V. Yu. Glebov, D. R. Harding, D. Jacobs-Perkins, J. P. Knauer, F. J. Marshall, R. L. McCrory, P. W. McKenty, D. D. Meyerhofer, S. P. Regan, W. Seka, R. W. Short, S. Skupsky, J. M. Soures, C. Stoeckl, B. Yaakobi, D. Shvarts, J. A. Frenje, C. K. Li, R. D. Petrasso, and F. H. Séguin, Phys. Rev. Lett. **100**, 185006 (2008).
9. Lord Rayleigh, Proc. London Math Soc. **XIV**, 170 (1883).
10. G. Taylor, Proc. R. Soc. London Ser. A **201**, 192 (1950).
11. H. Takabe *et al.*, Phys. Fluids **28**, 3676 (1985).
12. R. Betti, V. N. Goncharov, R. L. McCrory, and C. P. Verdon, Phys. Plasmas **5**, 1446 (1998).
13. S. Fujioka *et al.*, Phys. Plasmas **11**, 2814 (2004).
14. J. Sanz, R. Betti, V. A. Smalyuk, M. Olazabal-Loume, V. Drean, V. Tikhonchuk, X. Ribeyre, and J. Feugeas, Phys. Plasmas **16**, 082704 (2009).
15. A. Simon, R. W. Short, E. A. Williams, and T. Dewandre, Phys. Fluids **26**, 3107 (1983).
16. V. A. Smalyuk, R. Betti, J. A. Delettrez, V. Yu. Glebov, D. D. Meyerhofer, P. B. Radha, S. P. Regan, T. C. Sangster, J. Sanz, W. Seka, C. Stoeckl, B. Yaakobi, J. A. Frenje, C. K. Li, R. D. Petrasso, and F. H. Séguin, Phys. Rev. Lett. **104**, 165002 (2010).
17. S. X. Hu, D. T. Michel, D. H. Edgell, D. H. Froula, R. K. Follett, V. N. Goncharov, J. F. Myatt, S. Skupsky, and B. Yaakobi, Phys. Plasmas **20**, 032704 (2013).
18. D. H. Froula, D. T. Michel, I. V. Igumenshchev, S. X. Hu, B. Yaakobi, J. F. Myatt, D. H. Edgell, R. Follett, V. Yu. Glebov, V. N. Goncharov, T. J. Kessler, A. V. Maximov, P. B. Radha, T. C. Sangster, W. Seka, R. W. Short, A. A. Solodov, C. Sorce, and C. Stoeckl, Plasma Phys. Control. Fusion **54**, 124016 (2012).
19. P. B. Radha, J. P. Knauer, T. C. Sangster, V. N. Goncharov, I. V. Igumenshchev, R. Betti, R. Epstein, D. D. Meyerhofer, and S. Skupsky, Bull. Am. Phys. Soc. **52**, 143 (2007).
20. S. X. Hu, G. Fiksel, V. N. Goncharov, S. Skupsky, D. D. Meyerhofer, and V. A. Smalyuk, Phys. Rev. Lett. **108**, 195003 (2012).
21. G. Fiksel, S. X. Hu, V. N. Goncharov, D. D. Meyerhofer, T. C. Sangster, V. A. Smalyuk, B. Yaakobi, M. J. Bonino, and R. Jungquist, Phys. Plasmas **19**, 062704 (2012).
22. J. P. Knauer, P. B. Radha, V. N. Goncharov, I. V. Igumenshchev, R. Betti, R. Epstein, F. J. Marshall, S. P. Regan, V. A. Smalyuk, D. D. Meyerhofer, and S. Skupsky, Bull. Am. Phys. Soc. **52**, 233 (2007).
23. C. Stoeckl, J. A. Delettrez, J. H. Kelly, T. J. Kessler, B. E. Kruschwitz, S. J. Loucks, R. L. McCrory, D. D. Meyerhofer, D. N. Maywar, S. F. B. Morse, J. Myatt, A. L. Rigatti, L. J. Waxer, J. D. Zuegel, and R. B. Stephens, Fusion Sci. Technol. **49**, 367 (2006).
24. T. J. B. Collins, J. A. Marozas, K. S. Anderson, R. Betti, R. S. Craxton, J. A. Delettrez, V. N. Goncharov, D. R. Harding, F. J. Marshall, R. L. McCrory, D. D. Meyerhofer, P. W. McKenty, P. B. Radha, A. Shvydky, S. Skupsky, and J. D. Zuegel, Phys. Plasmas **19**, 056308 (2012).
25. J. Delettrez, R. Epstein, M. C. Richardson, P. A. Jaanimagi, and B. L. Henke, Phys. Rev. A **36**, 3926 (1987).
26. R. E. Kidder, Nucl. Fusion **14**, 53 (1974).
27. B. Strömgren, Z. Astrophys. **4**, 118 (1932).
28. B. F. Rozsnyai, Phys. Rev. A **5**, 1137 (1972).
29. R. Epstein, T. J. B. Collins, J. A. Delettrez, S. Skupsky, and R. P. J. Town, Bull. Am. Phys. Soc. **43**, 1666 (1998).
30. B. I. Bennett *et al.*, Los Alamos National Laboratory, Los Alamos, NM, Report LA-7130 (1978).
31. W. F. Huebner *et al.*, Los Alamos National Laboratory, Los Alamos, NM, Report LA-6760-M (1977).
32. L. Spitzer, Jr. and R. Härm, Phys. Rev. **89**, 977 (1953).
33. Prism Computational Sciences, Inc., Madison, WI 53711.
34. *LLE Review Quarterly Report* **133**, 1, Laboratory for Laser Energetics, University of Rochester, Rochester, NY, LLE Document No. DOE/NA/28302-1093 (2012).
35. P. Chang, K. Anderson, and R. Betti, Bull. Am. Phys. Soc. **54**, 260 (2009).

36. B. Yaakobi, A. A. Solodov, J. F. Myatt, J. A. Delettrez, C. Stoeckl, and D. H. Froula, Phys. Plasmas **20**, 092706 (2013).

37. D. H. Froula, B. Yaakobi, S. X. Hu, P.-Y. Chang, R. S. Craxton, D. H. Edgell, R. Follett, D. T. Michel, J. F. Myatt, W. Seka, R. W. Short, A. Solodov, and C. Stoeckl, Phys. Rev. Lett. **108**, 165003 (2012).

38. D. T. Michel, A. V. Maximov, R. W. Short, S. X. Hu, J. F. Myatt, W. Seka, A. A. Solodov, B. Yaakobi, and D. H. Froula, Phys. Rev. Lett. **109**, 155007 (2012).

39. B. Yaakobi, P.-Y. Chang, A. A. Solodov, C. Stoeckl, D. H. Edgell, R. S. Craxton, S. X. Hu, J. F. Myatt, F. J. Marshall, W. Seka, and D. H. Froula, Phys. Plasmas **19**, 012704 (2012).

40. J. F. Myatt, J. Zhang, J. A. Delettrez, A. V. Maximov, R. W. Short, W. Seka, D. H. Edgell, D. F. DuBois, D. A. Russell, and H. X. Vu, Phys. Plasmas **19**, 022707 (2012).

41. D. F. DuBois, D. A. Russell, and H. A. Rose, Phys. Rev. Lett. **74**, 3983 (1995).

42. D. A. Russell and D. F. DuBois, Phys. Rev. Lett. **86**, 428 (2001).

43. J. F. Myatt, H. X. Vu, D. F. DuBois, D. A. Russell, J. Zhang, R. W. Short, and A. V. Maximov, Phys. Plasmas **20**, 052705 (2013).

44. W. Theobald, R. Nora, M. Lafon, A. Casner, X. Ribeyre, K. S. Anderson, R. Betti, J. A. Delettrez, J. A. Frenje, V. Yu. Glebov, O. V. Gotchev, M. Hohenberger, S. X. Hu, F. J. Marshall, D. D. Meyerhofer, T. C. Sangster, G. Schurtz, W. Seka, V. A. Smalyuk, C. Stoeckl, and B. Yaakobi, Phys. Plasmas **19**, 102706 (2012).

45. H. A. Baldis, E. M. Campbell, and W. L. Kruer, in *Handbook of Plasma Physics*, edited by M. N. Rosenbluth and R. Z. Sagdeev, Vol. 3: Physics of Laser Plasma, edited by A. Rubenchik and S. Witkowski (North-Holland, Amsterdam, 1991), Chap. 9, p. 377.

46. I. V. Igumenshchev, D. H. Edgell, V. N. Goncharov, J. A. Delettrez, A. V. Maximov, J. F. Myatt, W. Seka, A. Shvydky, S. Skupsky, and C. Stoeckl, Phys. Plasmas **17**, 122708 (2010).

47. I. V. Igumenshchev, D. H. Froula, D. H. Edgell, V. N. Goncharov, T. J. Kessler, F. J. Marshall, R. L. McCrory, P. W. McKenty, D. D. Meyerhofer, D. T. Michel, T. C. Sangster, W. Seka, and S. Skupsky, Phys. Rev. Lett. **110**, 145001 (2013).

48. C. Yañez *et al.*, Phys. Plasmas **18**, 052701 (2011).

49. V. Drean *et al.*, Phys. Plasmas **17**, 122701 (2010).

50. S. Fujioka *et al.*, Phys. Rev. Lett. **92**, 195001 (2004).

51. P. B. Radha, V. N. Goncharov, T. J. B. Collins, J. A. Delettrez, Y. Elbaz, V. Yu. Glebov, R. L. Keck, D. E. Keller, J. P. Knauer, J. A. Marozas, F. J. Marshall, P. W. McKenty, D. D. Meyerhofer, S. P. Regan, T. C. Sangster, D. Shvarts, S. Skupsky, Y. Srebro, R. P. J. Town, and C. Stoeckl, Phys. Plasmas **12**, 032702 (2005).

52. J. D. Hager, T. J. B. Collins, V. A. Smalyuk, J. P. Knauer, D. D. Meyerhofer, and T. C. Sangster, Phys. Plasmas **20**, 072707 (2013).

53. S. Skupsky, R. W. Short, T. Kessler, R. S. Craxton, S. Letzring, and J. M. Soures, J. Appl. Phys. **66**, 3456 (1989).

54. S. Skupsky, J. A. Marozas, R. S. Craxton, R. Betti, T. J. B. Collins, J. A. Delettrez, V. N. Goncharov, P. W. McKenty, P. B. Radha, T. R. Boehly, J. P. Knauer, F. J. Marshall, D. R. Harding, J. D. Kilkenny, D. D. Meyerhofer, T. C. Sangster, and R. L. McCrory, Phys. Plasmas **11**, 2763 (2004).

55. J. A. Marozas, F. J. Marshall, R. S. Craxton, I. V. Igumenshchev, S. Skupsky, M. J. Bonino, T. J. B. Collins, R. Epstein, V. Yu. Glebov, D. Jacobs-Perkins, J. P. Knauer, R. L. McCrory, P. W. McKenty, D. D. Meyerhofer, S. G. Noyes, P. B. Radha, T. C. Sangster, W. Seka, and V. A. Smalyuk, Phys. Plasmas **13**, 056311 (2006).

56. A. M. Cok, R. S. Craxton, and P. W. McKenty, Phys. Plasmas **15**, 082705 (2008).

57. N. S. Krasheninnikova, S. M. Finnegan, and M. J. Schmitt, Phys. Plasmas **19**, 012702 (2012).

58. P. B. Radha, J. A. Marozas, F. J. Marshall, A. Shvydky, T. J. B. Collins, V. N. Goncharov, R. L. McCrory, P. W. McKenty, D. D. Meyerhofer, T. C. Sangster, and S. Skupsky, Phys. Plasmas **19**, 082704 (2012).

59. K. S. Anderson, R. Betti, P. W. McKenty, T. J. B. Collins, M. Hohenberger, W. Theobald, R. S. Craxton, J. A. Delettrez, M. Lafon, J. A. Marozas, R. Nora, S. Skupsky, and A. Shvydky, Phys. Plasmas **20**, 056312 (2013).

60. N. S. Krasheninnikova *et al.*, Phys. Plasmas **21**, 042703 (2014).

61. R. S. Craxton, F. J. Marshall, M. J. Bonino, R. Epstein, P. W. McKenty, S. Skupsky, J. A. Delettrez, I. V. Igumenshchev, D. W. Jacobs-Perkins, J. P. Knauer, J. A. Marozas, P. B. Radha, and W. Seka, Phys. Plasmas **12**, 056304 (2005).

62. R. S. Craxton and D. W. Jacobs-Perkins, Phys. Rev. Lett. **94**, 095002 (2005).

63. P. B. Radha, F. J. Marshall, J. A. Marozas, A. Shvydky, I. Gabalski, T. R. Boehly, T. J. B. Collins, R. S. Craxton, D. H. Edgell, R. Epstein, J. A. Frenje, D. H. Froula, V. N. Goncharov, M. Hohenberger, R. L. McCrory, P. W. McKenty, D. D. Meyerhofer, R. D. Petrasso, T. C. Sangster, and S. Skupsky, Phys. Plasmas **20**, 056306 (2013).

64. M. J. Schmitt, P. A. Bradley, J. A. Cobble, J. R. Fincke, P. Hakel, S. C. Hsu, N. S. Krasheninnikova, G. A. Kyrala, G. R. Magelssen, D. S. Montgomery, T. J. Murphy, K. A. Obrey, R. C. Shah, I. L. Tregillis, J. A. Baumgaertel, F. J. Wysocki, S. H. Batha, R. S. Craxton, P. W. McKenty, P. Fitzsimmons, A. Nikroo, and R. Wallace, Phys. Plasmas **20**, 056310 (2013).

65. G. P. Schurtz, Ph. D. Nicolaï, and M. Busquet, Phys. Plasmas **7**, 4238 (2000).

66. J. A. Delettrez, T. J. B. Collins, P. B. Radha, D. T. Michel, D. Cao, and G. Moses, Bull. Am. Phys. Soc. **58**, 323 (2013).

# Channeling Multikilojoule High-Intensity Laser Beams in an Inhomogeneous Plasma

Propagating a laser beam at relativistic intensities (>$10^{18}$ W/cm$^2$) through a plasma with a large density scale length is dominated by highly nonlinear interactions including ponderomotive expulsion of electrons,[1] channeling,[2–4] and developing hosing and bifurcation instabilities.[3,4] These effects are important for both fundamental aspects of relativistic laser–plasma interaction physics and applications such as fast ignition in inertial confinement fusion.[5] The central idea of the fast-ignition concept is to first compress a DT ice capsule with a nanosecond, megajoule laser to a high areal density and then use an ultrapowerful short-pulse laser to subsequently ignite the fuel. Since laser light at nonrelativistic intensities propagates in the plasma corona up to only the critical density $n_c = \omega_0^2 m_e \varepsilon_0 / e^2$ (where $\omega_0$ is the laser angular frequency, $m_e$ is the electron mass, $\varepsilon_0$ is the permittivity of free space, and $e$ is the elementary charge), the idea is to use one high-intensity pulse to form a channel through the corona and then inject the ignition pulse into the lower-density plasma column as in an optical waveguide[6] to deposit sufficient energy in the core for ignition. In contrast to the cone-in-shell concept,[7] the channeling concept has the advantage that it uses symmetric implosions and can be readily applied to cryogenic targets. Cryogenic cone-in-shell targets are technically challenging and so far have not been demonstrated. Channeling into dense plasmas relies on the laser intensity to provide sufficient ponderomotive pressure against the outflowing plasma and a laser pulse duration that is long enough to sustain the channel formation. When the laser reaches densities >$n_c$, it may continue to push forward through its ponderomotive pressure ("hole boring") and relativistic transparency. The ponderomotive hole-boring velocity[8,9] is found by balancing the light pressure against the pressure arising from the material stagnating against the head of the channel. For an increasing laser intensity, a higher hole-boring velocity is obtained. For a laser system of fixed energy, increased intensity comes at a price of decreased laser pulse duration or smaller spot size, and the balance between laser intensity and duration must be optimized to provide the longest channel. Channeling experiments with short[10] and long[11] laser pulses were performed, and it was demonstrated both in experiments[12] and simulations[4] that channels have a higher transmission for a trailing pulse compared to an unperturbed plasma. These experimental observations were carried out using a variety of diagnostics including interferometry,[12] self-emission,[13] and x-ray grid image refractometry.[14] These diagnostics were limited to plasma densities below $n_c$ [here, $n_c$ always refers to infrared (IR) laser light ($\lambda_{IR}$ = 1.054 $\mu$m)]. The channel region in the vicinity of $n_c$ was unexplored because of the strong refraction of the probe radiation at high plasma densities.

This article describes the observation of laser channeling in millimeter-sized inhomogeneous plasmas by measuring the depth of a channel for laser pulses with peak intensities between ~1 × $10^{19}$ and ~4 × $10^{19}$ W/cm$^2$. The density scale length is comparable to those obtained in high-compression shots with spherical shells on the OMEGA laser. This experiment is relevant to future integrated fast-ignition channeling experiments. To our knowledge, it represents the first measurements of the channel up to $n_c$ in a laser-driven blowoff plasma of this size. The observations reported here were made possible by using a probe with a short wavelength ($\lambda_p$ = 0.263 $\mu$m) and a sufficiently large solid angle of the collection optics (~$f$/4). Measurements of the plasma density in the channel and in the background plasma are presented. The time for the short pulse to reach $n_c$ was measured and compares well to simulation predictions. The experimental results show that for a fixed laser energy, a lower-intensity, longer pulse propagates deeper into a long-scale-length plasma.

The experiments were carried out on the OMEGA EP Laser System.[15] Figure 140.21 shows a schematic of the interaction and probing geometries. Two ultraviolet (UV) ($\lambda_{UV}$ = 0.351 $\mu$m) laser beams smoothed by distributed phase plates (eighth-order super-Gaussian with 800-$\mu$m full width at half maximum)[16] irradiated a 125-$\mu$m-thick planar plastic (CH) target to create and heat a blowoff plasma. The UV irradiation delivered 2 kJ of total energy in a 1-ns square pulse. The channeling laser pulse was an IR beam with an energy ranging from 0.75 kJ to 2.6 kJ. An intensity comparison was performed by using 100-ps and 10-ps pulse widths, respectively. The wavefront of the channeling beam was measured and the focal-spot irradiance map was inferred for each shot.[17] Eighty percent

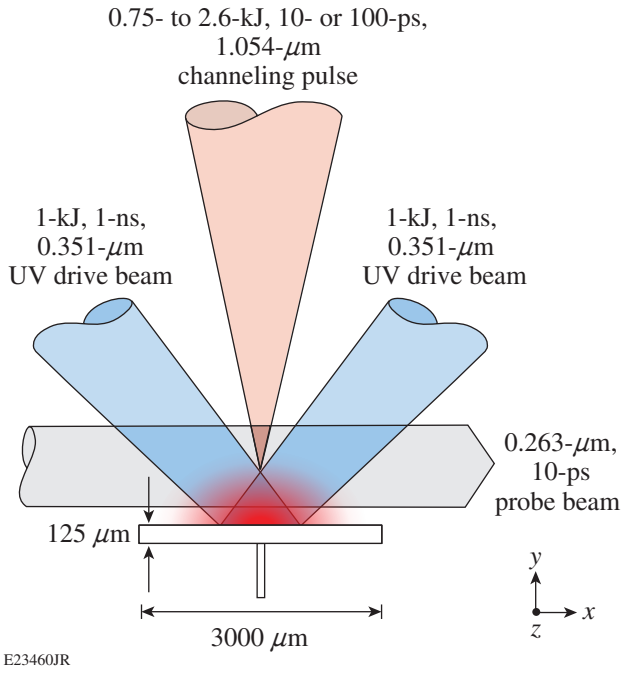


Figure 140.21
Schematic of the experimental setup. A plastic target is illuminated by two UV beams to generate a large expanding plasma plume. Following the UV beams, an IR channeling laser beam is injected into the plume along the density gradient. The interaction is observed by a UV optical probe pulse that is timed to arrive at a specific delay from the start of the channeling pulse.

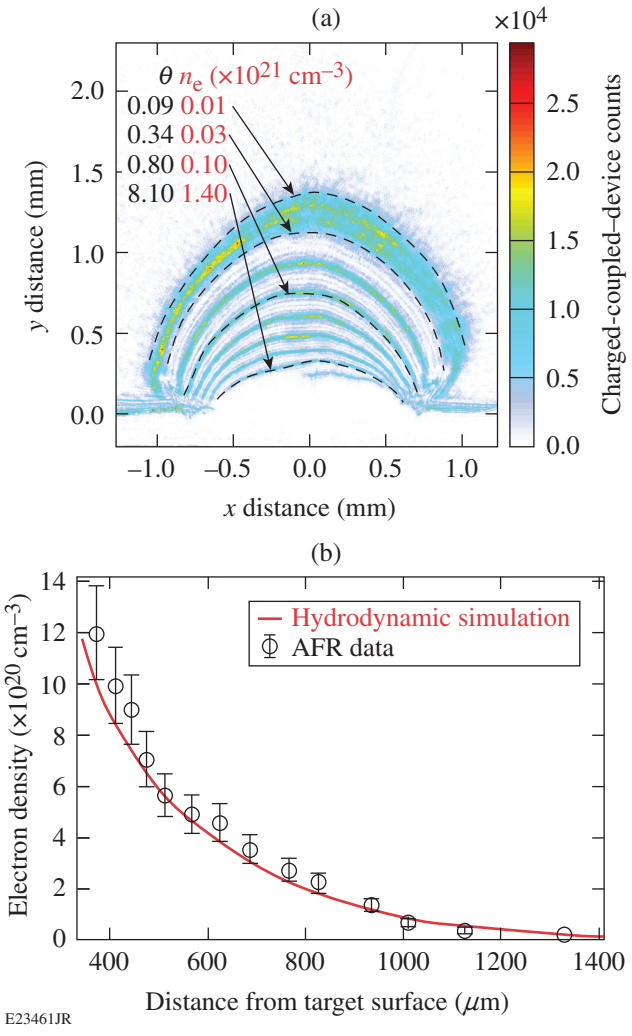


Figure 140.22
(a) Measured optical probe image of the unperturbed long-scale-length plasma (45 ps prior to the arrival of the channeling beam). The original target surface is located at $y = 0$. Contours of the constant refraction angle and associated electron densities are also shown. (b) On-axis lineout of the measured values of the unperturbed electron density (points) versus distance from the target surface. The solid line is a prediction from a 2-D hydrodynamic simulation.

of the laser energy was contained in a 25-$\mu$m spot resulting in vacuum peak intensities of $\sim 1 \times 10^{19}$ and $\sim 4 \times 10^{19}$ W/cm$^2$ for 2.6-kJ, 100-ps and 1-kJ, 10-ps pulses, respectively. The average laser intensities in the focal spot were about an order of magnitude lower. The focal position of the channeling beam was set to 750 $\mu$m from the original target surface, and the corresponding electron plasma density was predicted to be $n_e = 2.5 \times 10^{20}$ cm$^{-3}$, which is close to $n_c/4$. It has been suggested in Ref. 18 that focusing the laser beam to $n_c/4$ might provide the most-favorable condition for relativistically enhanced propagation. The probe beam[19] was a 10-ps, 0.263-$\mu$m laser with 10 mJ of energy. The relative timing between the probe and channeling pulse was measured with an accuracy of better than 20 ps on each shot.

The expanding blowoff plasma was measured by using a new method of optical probing—angular filter refractometry (AFR)[20]—which visualizes gradients in the refractive index $n$ of an object. The refractive index of an unmagnetized, collisionless plasma is given by $n = \sqrt{1 - n_e/n_c}$. Figure 140.22(a) shows an example of such a measurement shortly before the arrival of the channeling beam. The probe light that has passed through the plasma is collected and filtered in the focal plane of the collection optics where the spatial locations of probing rays depend on their refraction angle. A bull's-eye–patterned filter with alternating transparent and opaque rings provides isocontours of the refraction angle in the image plane. Using AFR allows one to measure the angular deviation of probe rays while preserving the fine structures in the image, which is a considerable advantage over other methods. AFR, as a refractive method, is capable of probing large plasma volumes, whereas, e.g., interferometric techniques that rely on fringe-shift measurements are severely limited by the large

phase shifts accumulated along the path. The electron plasma density profile shown in Fig. 140.22(b) was inferred from the measured angular deviation $\theta$ of probing rays, assuming a hemi-spherical plasma with a varying refractive index. The analysis is described in detail in Ref. 20. The unperturbed on-axis plasma profile in Fig. 140.22(b) is in agreement with two-dimensional (2-D) hydrodynamic simulations with the code *DRACO*.[21] The simulated electron temperature is 1.8 keV. The experimentally determined radial density scale length in the observed region varies from 200 to 320 $\mu$m with 250 $\mu$m being the average. The last contour in the collection system ($\theta \approx 8.1°$) corresponds to light that is refracted through a peak density above $n_c$ ($1.4 \times 10^{21}$ cm$^{-3}$).

Figure 140.23 shows measured channels at different probing times for 10-ps and 100-ps laser irradiation. The channel is visualized by the perturbations in the AFR contours. The contours bend as a result of strong density gradients created by the channeling pulse. Figures 140.23(a)–140.23(d) show the results for the 10-ps pulse. At 6 ps the head of the channel reached a position of 450 $\mu$m from the original target surface. The electron density at this location corresponds to 0.6 $n_c$. The channel was observed up to 200 ps after its creation. Later in time, the tip of the channel retreats backward with a velocity of $\sim 3 \times 10^7$ cm/s away from the target surface. There is a clear difference in the channel depth between the 10-ps and 100-ps pulses. The 100-ps pulse [Figs. 140.23(e)–140.23(h)] reach the contour closest to the original target surface, indicating that a density $>1.4 \times 10^{21}$ cm$^{-3}$ has been reached. The 100-ps pulse [as shown in Fig. 140.23(e)] reached, in only 18 ps, about the same depth as the 10-ps pulse. The 100-ps pulse continued to bore through the plasma, reaching overcritical density at 65 ps after the start of the laser beam. The upper contour bands in the lower-density region are smoothly shifted in space, while the contours at higher density inside the channel are highly distorted and obscured. This is likely caused by sharp density modulations at the channel wall that are also observed in particle-in-cell (PIC) simulations.[3,22] Bright fourth-harmonic emission of the channeling beam was measured in the vicinity of the critical surface [Figs. 140.23(e)–140.23(h)] with the 100-ps pulse. Harmonics from the critical-density surface have been observed in experiments with high-intensity laser beams interacting with solid-density plasmas.[23] No harmonic emission was observed with the 10-ps pulse, indicating that it did not reach $n_c$.

Figure 140.24 shows a radial cross section of the measured density profile in the channel. The density is calculated using an Abel inversion of the phase, which is inferred from the angular refraction in the AFR image. The density profile in the channel

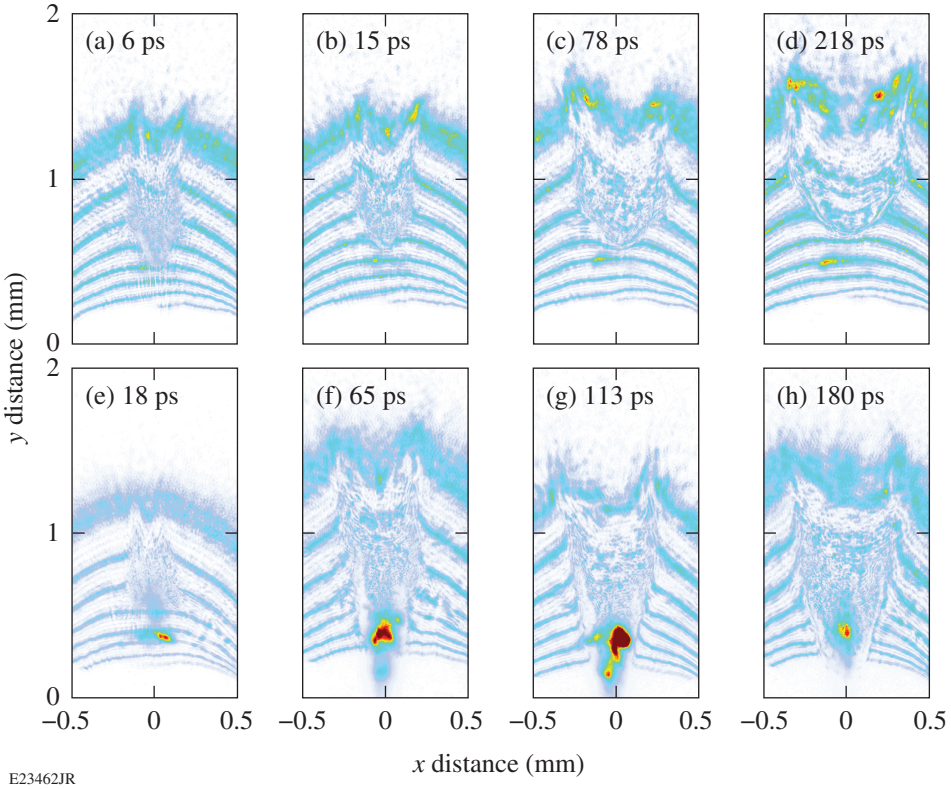


Figure 140.23
Optical probe images for 10-ps and 100-ps channeling laser pulses at various times showing greater penetration depth for the longer pulse. [(a)–(d)] The 10-ps, 125-TW laser pulse never reaches $n_c$ and, therefore, does not produce fourth-harmonic emission. Since the detector integrated over a time much longer than the duration of the probe pulse, the harmonic signal is present even in frames taken before the channel reaches the critical surface in the probe image. Time zero is defined as the start of the short pulse. The background plasma was always the same as the one shown in Fig. 140.22(a). [(e)–(h)] The red spots are caused by fourth-harmonic generation from the 100-ps, 20-TW channeling pulse reaching $n_c$.

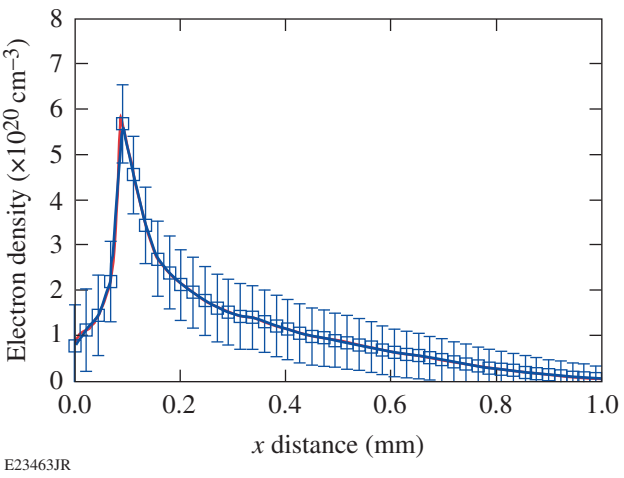


Figure 140.24
Density profile of a channel created by a 100-ps pulse and probed at ~65 ps into the pulse along the $x$ axis at $y$ = 0.8 mm. The density on axis is reduced by 65% with respect to the density of the unperturbed plasma at the same location ($n_e = 2 \times 10^{20}$ cm$^{-3}$). Error bars are calculated from the uncertainty in the measurement of $\theta$.

region takes on a parabolic-like shape bounded on either side by walls with a density higher than the background density. For the specific image shown here, the density in the channel has been reduced from $2 \times 10^{20}$ cm$^{-3}$ to $7 \times 10^{19}$ cm$^{-3}$—a reduction of 65%. The measured density in the channel is about a factor of 2 higher than that predicted by PIC simulations for similar conditions.[3] This image was taken at 65 ps into a 100-ps pulse, so the density may be reduced further. At later times, contours become impossible to identify as the density gradient at the channel wall steepens.

The intensity distribution in the experimental laser focus was not diffraction limited and contained some spatial inhomogeneity,[17] which probably seeded the filamentation instability and self-focusing in the plasma driven by ponderomotive and relativistic effects. Filamentation was predicted by solving the paraxial wave equation with a split-step algorithm, taking into account the ponderomotive and relativistic effects in the refractive index of the plasma and using the measured wavefront map of the channeling beam. The calculated beam inside the plasma was similar in size to the measured channel width. In addition, simultaneous measurements of the strong electrostatic and magnetic fields inside the plasma with proton radiography[24] also concluded the existence of filamentary structures at a location between 0.5 and 1 mm from the initial target surface. Three-dimensional (3-D) hydrodynamic simulations including relativistic corrections and the effect of charge separation have demonstrated that aberrated beams do not channel as effectively as diffraction-limited beams.[25] Filamentation is sensitive to the power in the laser speckles and, therefore, is expected to be more severe for higher-power pulses. When sufficiently driven, this might cause beam spraying and result in the breakup of the beam so that it cannot reach a higher density. The 100-ps channeling beam had ~4× less power than the 10-ps pulse and is expected to be less affected by filamentation, which might be one of the reasons why this beam propagated deeper into the plasma.

Two- and three-dimensional PIC simulations with large (~500-$\mu$m) plasmas studied the propagation and channeling for conditions similar to this experiment.[3,4] The laser power greatly exceeds the power threshold for relativistic self-focusing[26,27] and beam filamentation occurs in the early stage of the simulation. The local intensity increases in the filaments and the resulting transverse ponderomotive force pushes most of the electrons out of the filaments. The resulting space-charge force causes the ions to follow, creating several microchannels that eventually merge together and form a single density channel along the laser-propagation axis. The simulations predict that besides laser hosing, channel bifurcation, and self-correction, the laser front will pile up material at the channel head that will reach densities $n_c$, even though the surrounding plasma is underdense. The simulations predict that after a short initial period (~ps), when the pulse propagates with a speed close to the linear group velocity, it quickly slows down and, after ~5 ps, approaches the ponderomotive hole-boring velocity.[8,9] The plasma density gradient rapidly steepens in front of the pulse and the laser light essentially interacts most of the time with steep overcritical plasma.[3,4]

The channel propagation velocity can be obtained from the experiment. The depth of the channel is found by measuring the distance from the original target surface to the closest point of perturbed contours in the probe image. A channel progression velocity of >3±1 $\mu$m/ps was obtained from the data. The Mach angle gives another measure of the velocity of the supersonic advancing front in the gas. The velocity of the front of the channel is found by measuring the angle of the wake left behind by the channel. The Mach angle relates the front Mach number $M$ to the angle $\theta_m$ by $\sin(\theta_m) = 1/M$. The Mach angle is measured to be ~8° [in Fig. 140.23(f)], which gives a channel head Mach number of $M \sim 7$ and a velocity of 2 $\mu$m/ps, slightly lower than from the depth measurement.

The measured channel progression velocity is in agreement with PIC simulations, showing that it approaches the hole-boring velocity, given by

$$v_h = c\sqrt{Z\left(n_c/n_e\right)\left(m_e/M_i\right)\left(2-\eta_a\right)I_{18}\,\lambda_\mu^2/2.74} \qquad (1)$$

for normal incidence light.[9] Here $c$ is the speed of light, $Z$ is the average charge state of the plasma, $M_i$ is the ion mass, $\eta_a$ is the laser absorption fraction, $I_{18}$ is the laser intensity in units of $10^{18}$ W/cm$^2$, and $\lambda_\mu$ is the laser wavelength in units of $\mu$m. The hole-boring velocity decreases with $\sqrt{1/n_e}$ when the pulse propagates deeper into the plasma, forcing more material to pile up. For an average intensity of $I = 10^{18}$ W/cm$^2$, fully ionized plastic, $\eta_a = 1$, and $n_e/n_c$ between 1 and 2, $v_h$ is estimated with 3.2 $\mu$m/ps and 2.2 $\mu$m/ps, respectively, which is consistent with the measurement.

The 3-D simulations provide scalings for the time $T_c$ that is required for the channel head to reach the position of $n_c$ and the required laser energy $E_c$, which are given by $T_c$ (ps) = $1.5 \times 10^2\, I_{18}^{-0.64}$ and $E_c$(kJ) = $0.85\, I_{18}^{0.32}$ (Ref. 4). The estimated times and energies are between ~35 ps, 1.9 kJ and ~150 ps, 0.85 kJ for $10^{19}$ W/cm$^2$ and $10^{18}$ W/cm$^2$, respectively, in rough agreement with the experimental values. This scaling also demonstrates that the 10-ps pulse is too short and does not have enough energy to reach $n_c$. The time it takes for the pulse to bore through one scale-length distance is 250 $\mu$m/(3 $\mu$m/ps) ~ 80 ps. This indicates that the channeling process is driven primarily by the ponderomotive force as predicted by the 2-D and 3-D PIC simulations.[3,4]

## ACKNOWLEDGMENT

This work was supported by the U.S. Department of Energy National Nuclear Security Administration under Award Number DE-NA0001944, the OFES ACE Fast Ignition grant No. DE-DE-FG02-05ER54839, the DOE Laboratory Basic Science Program, the University of Rochester, and the New York State Energy Research and Development Authority. The support of DOE does not constitute an endorsement by DOE of the views expressed in this article. Part of this work is supported with the Grant-in-Aid for Scientific Research A (No. 22246122) and B (No. 23360412) as well as with the Japan-U.S. Collaboration in Fusion Research and Development under MEXT and NIFS.

## REFERENCES

1. K.-C. Tzeng and W. B. Mori, Phys. Rev. Lett. **81**, 104 (1998).
2. A. Pukhov and J. Meyer-ter-Vehn, Phys. Rev. Lett. **76**, 3975 (1996).
3. G. Li, R. Yan *et al.*, Phys. Rev. Lett. **100**, 125002 (2008).
4. G. Li *et al.*, Phys. Plasmas **18**, 042703 (2011).
5. M. Tabak *et al.*, Phys. Plasmas **1**, 1626 (1994).
6. C. G. Durfee and H. M. Milchberg, Phys. Rev. Lett. **71**, 2409 (1993).
7. R. Kodama *et al.*, Nature **412**, 798 (2001).
8. W. L. Kruer, E. J. Valeo, and K. G. Estabrook, Phys. Rev. Lett. **35**, 1076 (1975).
9. S. C. Wilks *et al.*, Phys. Rev. Lett. **69**, 1383 (1992).
10. K. A. Tanaka *et al.*, Plasma Phys. Control. Fusion **46**, B41 (2004).
11. P. E. Young *et al.*, Phys. Rev. Lett. **75**, 1082 (1995).
12. J. Fuchs *et al.*, Phys. Rev. Lett. **105**, 225001 (2010).
13. M. Borghesi *et al.*, Phys. Rev. Lett. **78**, 879 (1997).
14. K. Takahashi *et al.*, Phys. Rev. Lett. **84**, 2405 (2000).
15. L. J. Waxer, D. N. Maywar, J. H. Kelly, T. J. Kessler, B. E. Kruschwitz, S. J. Loucks, R. L. McCrory, D. D. Meyerhofer, S. F. B. Morse, C. Stoeckl, and J. D. Zuegel, Opt. Photonics News **16**, 30 (2005).
16. T. J. Kessler, Y. Lin, J. J. Armstrong, and B. Velazquez, in *Laser Coherence Control: Technology and Applications*, edited by H. T. Powell and T. J. Kessler (SPIE, Bellingham, WA, 1993), Vol. 1870, pp. 95–104.
17. B. E. Kruschwitz, S. W. Bahk, J. Bromage, M. D. Moore, and D. Irwin, Opt. Express **20**, 20,874 (2012).
18. T. Matsuoka *et al.*, Plasma Phys. Control. Fusion **50**, 105011 (2008).
19. D. H. Froula, R. Boni, M. Bedzyk, R. S. Craxton, F. Ehrne, S. Ivancic, R. Jungquist, M. J. Shoup, W. Theobald, D. Weiner, N. L. Kugland, and M. C. Rushford, Rev. Sci. Instrum. **83**, 10E523 (2012).
20. D. Haberberger, S. Ivancic, S. X. Hu, R. Boni, M. Barczys, R. S. Craxton, and D. H. Froula, Phys. Plasmas **21**, 056304 (2014).
21. P. B. Radha, T. J. B. Collins, J. A. Delettrez, Y. Elbaz, R. Epstein, V. Yu. Glebov, V. N. Goncharov, R. L. Keck, J. P. Knauer, J. A. Marozas, F. J. Marshall, R. L. McCrory, P. W. McKenty, D. D. Meyerhofer, S. P. Regan, T. C. Sangster, W. Seka, D. Shvarts, S. Skupsky, Y. Srebro, and C. Stoeckl, Phys. Plasmas **12**, 056307 (2005).
22. L. Willingale, P. M. Nilson, A. G. R. Thomas, J. Cobble, R. S. Craxton, A. Maksimchuk, P. A. Norreys, T. C. Sangster, R. H. H. Scott, C. Stoeckl, C. Zulick, and K. Krushelnick, Phys. Rev. Lett. **106**, 105002 (2011).
23. J. Zhang *et al.*, Phys. Rev. A **54**, 1597 (1996).
24. Y. Uematsu, S. Ivancic, T. Iwawaki, H. Habara, A. L. Lei, W. Theobald, and K. A. Tanaka, Rev. Sci. Instrum. **85**, 11E612 (2014).
25. D. E. Hinkel *et al.*, Phys. Plasmas **5**, 1887 (1998).
26. C. Max, J. Arons, and A. B. Langdon, Phys. Rev. Lett. **33**, 209 (1974).
27. B. I. Cohen and C. E. Max, Phys. Fluids **22**, 1115 (1979).

# Dependence of Tritium Release on Temperature and Water Vapor from Stainless Steel

## Introduction

Tritium has applications in the pharmaceutical industry as a radioactive tracer, in the radioluminescent industry as a scintillant driver, and in nuclear fusion as a fuel. When metal surfaces are exposed to tritium gas, compounds absorbed on the metal surfaces (such as water and volatile organic species) chemically react with the tritons. Subsequently, the contaminated surfaces desorb tritiated water and volatile organics. Contact with these surfaces can pose a health hazard to workers. Additionally, desorption of tritiated species from the surfaces constitutes a respirable dose.

Understanding the mechanisms associated with hydrogen adsorption on metal surfaces and its subsequent transport into the bulk can reduce the susceptibility of surfaces becoming contaminated and can lead to improved decontamination techniques. More generally, tritium can be used as a sensitive tracer to study surface chemistry and hydrogen transport. Elemental tritium readily converts into tritiated water on metallic surfaces.[1,2] Desorption of water from inner surfaces of process lines containing ultrapure gas streams can compromise the reliability of semiconductor chips. Additionally, reactive gases used to fabricate large-scale integrated chips combine with this water to form acids or submicron-sized particles that degrade interconnects on the chips to reduce their lifespan and reliability.[3–5]

This article compares the effectiveness of heat and moisture to desorb gases from metal surfaces using tritium as a tracer. In the first series of experiments, temperatures up to 600°C were used to measure the desorption spectrum from stainless-steel samples under dry purge conditions. The second series of experiments compared tritium release at a fixed humidity of 8760 ppm in the carrier while varying the metal temperature from 100°C to 130°C. The final set of measurements investigated the impact of varying humidity while holding the sample at a fixed temperature of 100°C.

## Experimental Procedure

These experiments used 316 stainless-steel samples that were 5 cm long × 1.8 cm wide × 0.3 cm thick. The samples were exposed to 690 Torr of DT gas, 40% T/D ratio, for 23 h at room temperature and stored under vacuum at room temperature until retrieved for the desorption studies, after which they were stored under helium. The experiments were conducted 440 days after exposure. The samples were exposed briefly to air during the transfer from storage to the desorption facility.

The desorption facility, described in detail in Ref. 6, comprises a 100-$cm^3$, heated quartz tube that holds the sample, a set of two gas spargers to extract water-soluble gases from the helium purge stream, and an on-line liquid scintillation counter to measure the activity collected in the spargers in real time. The performance of the spargers has been discussed in detail in Ref. 7. Tritium that desorbs from metal surfaces is predominantly found in water-soluble species.[7]

Each sample was heated by convection in a uniform heating zone within the quartz furnace. A thermocouple attached to the sample provided a direct measurement of the sample temperature. The humidity of the helium purge stream was adjusted by blending a purge steam that bubbled through a humidifier with a bypass stream. The humidity was measured on-line and indirectly from the rate of water loss from the humidifier.

The on-line liquid scintillation counter tracked the activity increase in the first sparger, containing 100 ml of liquid scintillation fluid, as the desorption progressed. This signal provided a measure of the tritium inventory contained in the sample. The differential of this signal provided the tritium outgassing rate as a function of time as the desorption proceeded. The overall system response time was of the order of 2 min.

## Results

1. Thermally Driven Outgassing into a Dry Stream

To investigate the effect of temperature on the outgassing rate, each sample was subjected to six sequential bake-outs at progressively higher temperatures in a dry helium purge. Each trial started by holding the sample at room temperature for 1 h to establish a background outgassing rate. The temperature was ramped to the dwell temperature and held at that temperature

for roughly an additional 3 h. The sample attained the dwell temperature within 5 min of starting the temperature ramp. After each run, the sample was allowed to cool to room temperature. The same sample was used for all of the runs in this series. Runs were conducted in order of increasing temperature.

The activity collected in the first sparger for these runs is shown in Fig. 140.25. The background levels observed in the first hour have been arbitrarily set to zero. Activity is observed to increase in the first sparger ~5 min after the initiation of the temperature ramp. A total of 5.5 mCi of tritium was recovered from this sample. This tritium inventory is representative of all the samples exposed to 690 Torr of 40% T/D gas during the campaign. The percentage recovered after each sequential run is listed in the inset of Fig. 140.25. The majority of the tritium was released from the surface when the bake-out temperature was of the order of 300°C. This finding is consistent with previous studies.[6]

The outgassing rates were computed by differentiating the table inset shown in Fig. 140.25. The outgassing rate for each run is plotted in Fig. 140.26. The outgassing rate increases rapidly with increasing temperature, even in the absence of humidity. A 120-fold increase in the outgassing rate is observed when the bake-out temperature increases from 75°C to 300°C.

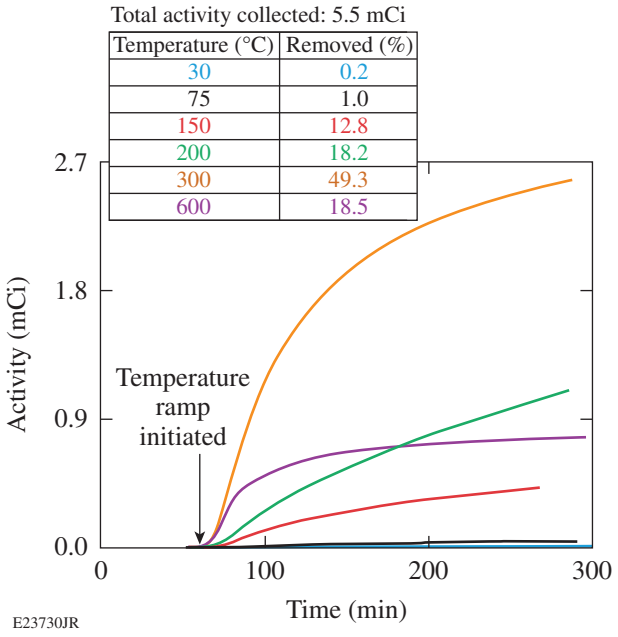


Figure 140.25
The cumulative quantity of tritium released from a stainless-steel sample for sequential bake-outs at progressively higher temperatures in a purge stream containing 4 ppm of water vapor.

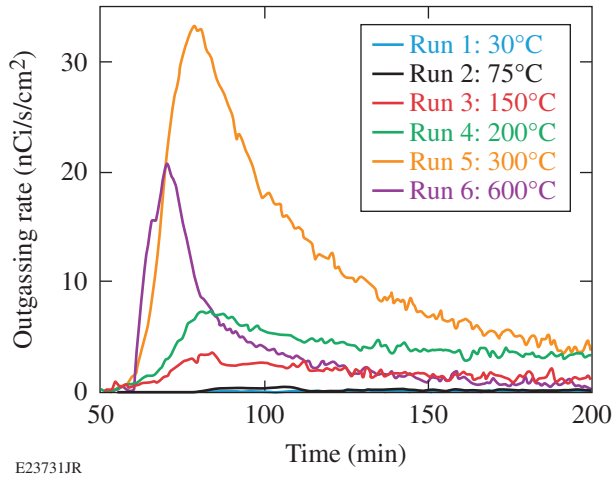


Figure 140.26
The outgassing rates of tritium from a stainless-steel sample for sequential bake-outs at progressively higher temperatures in a 4-ppm purge stream.

The exception to this trend is Run 6, conducted at 600°C. The lower outgassing rate in that case suggests that the tritium inventory within the sample has been depleted.

2. Humidity-Stimulated Outgassing from 30°C Metal

The effect of humidity on the outgassing rate was measured by purging a fresh sample with helium containing two sequentially increasing amounts of moisture—1120 ppm and 6740 ppm of water vapor in the carrier. Each run was initially purged with the helium stream containing 4 ppm of water vapor for 2 h to establish a baseline outgassing rate. The outgassing rate for each of the three runs is provided in Fig. 140.27.

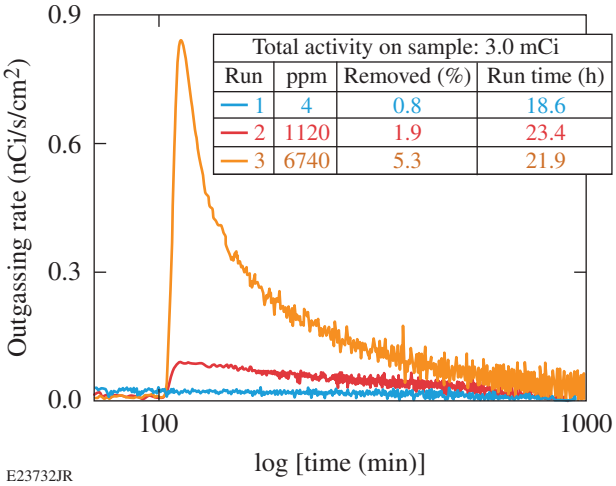


Figure 140.27
The outgassing rates of tritium from a stainless-steel sample at 30°C exposed to increased moisture content in the purge stream.

An inspection of Fig. 140.27 provides two conclusions: (1) the peak outgassing rate increases with increasing humidity and (2) increasing the water content in the purge stream sixfold from 1120 ppm to 6740 ppm increases the peak outgassing rate tenfold from 0.084 to 0.84 nCi/cm$^2$/s. In both humid runs, the outgassing rate approaches the low-humidity outgassing rate, even though the residual tritium inventory on the sample remains high. Only 2% of the tritium is removed from the sample when it is exposed to 1120 ppm of moisture in helium, and an additional 5.3% is removed when the water content is increased to 6740 ppm. Diffusion of tritons from the near surface to the surface of the stainless steel or from the inner oxide layers appears to limit the rate of tritium outgassing at room temperature. It is noteworthy that ~8% of the tritium inventory resides in and can be removed from the near surface with humidity. Finally, humidity-stimulated peak outgassing rates are seen to be at least one order of magnitude lower than thermally driven peak outgassing rates. For example, a peak outgassing rate of 34 nCi/cm$^2$/s was attained at 300°C compared to 0.84 nCi/cm$^2$/s achieved with 6740 ppm of water vapor.

Figure 140.28 further demonstrates that the rate-limiting step in humidity-stimulated outgassing is triton diffusion to the surface. A second stainless-steel sample was decontaminated using a similar purge protocol to that described above. In this case, however, a second high-humidity run (Run 4) was added to the protocol.

Overall, the outgassing behavior of the second stainless-steel sample is very similar to that observed for the first sample. The quantities of tritium removed from the two samples are also similar. However, repeating a second run with high humidity 2 h after the first high-humidity run did not recover the original enhanced outgassing rate. The outgassing rate is only slightly higher than that observed at the end of the first high-humidity run. Tritons were not available at the sample surface for exchange with water vapor, even though ~90% of the tritium inventory remains in the sample.

3. Humidity-Stimulated Outgassing from Warm Metals

The relative contribution of humidity to the outgassing rate from warm metal surfaces was measured by subjecting a fresh sample to four sequential bake-outs at progressively higher temperatures in a wet purge stream. The humidity was fixed at 8760 ppm of water vapor in the carrier. The bake-out temperatures increased from 100°C to 130°C in 10°C steps. The outgassing rates for the four runs, provided in Fig. 140.29, were arbitrarily set to zero at the start of each run for the comparison.

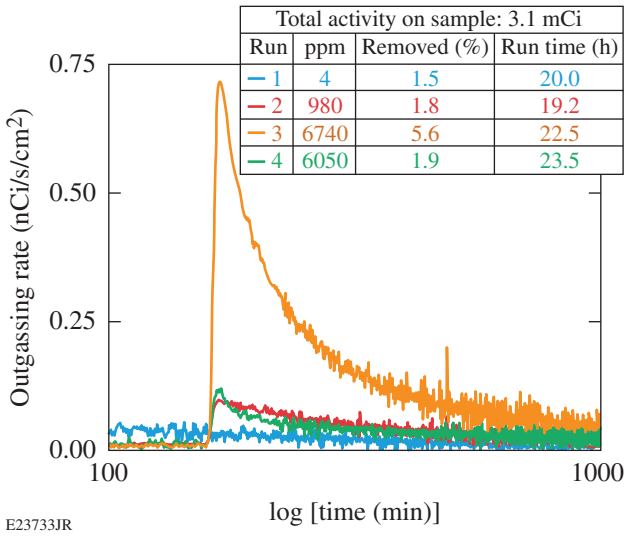


Figure 140.28
The humidity-stimulated outgassing rates of tritium from a second stainless-steel sample at 30°C.

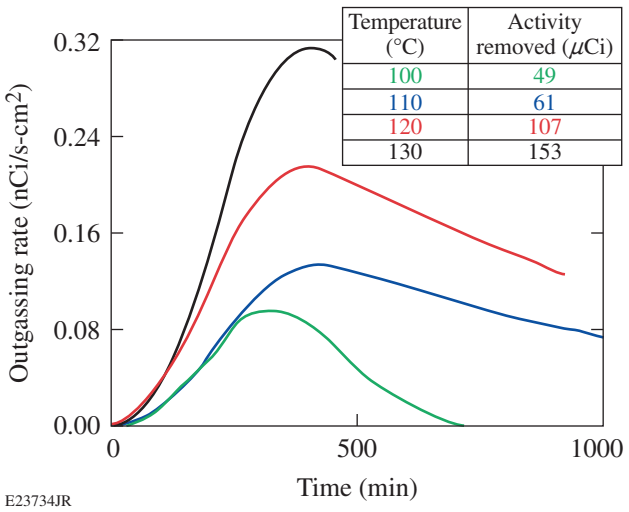


Figure 140.29
Outgassing rates for stainless steel heated from 100°C to 130°C in 10°C steps into a helium purge stream containing 8760 ppm of water vapor.

Three observations can be drawn from Fig. 140.29: (1) the quantity of tritium extracted from the sample increases with metal temperature as expected; (2) the peak outgassing rate increases with temperature; and (3) the rate of change in the outgassing rate also increases with temperature. With the exception of the 100°C run, the outgassing rate appears to decline more rapidly with time after the peak as the sample temperature increases, suggesting that the inventory of tritons that can participate in the desorption process is finite. Increasing the sample temperature appears to involve tritons deeper in the subsurface but this reservoir is depleted more rapidly.

In a second experiment set up to investigate humidity-stimulated desorption from warm stainless steel, the temperature was fixed at 100°C and the humidity changed from 4 ppm to 1000 ppm. The stainless-steel sample was purged with a dry (4 ppm of water vapor) helium stream at room temperature to establish the baseline outgassing rate. After 30 min, the sample temperature was raised to and held at 100°C. Five hours later, the humidity of the purge stream was increased from 10 ppm of water to 1000 ppm. The outgassing curves are provided in Fig. 140.30.

Figure 140.30 shows that outgassing rates for the two cases evolved in a similar manner, first increasing to a peak and then decreasing toward a steady-state outgassing rate after a long time. The profiles are more reminiscent of thermal desorption than humidity-stimulated desorption. Increasing the humidity increased the tritium removal rate. Tritium desorption from stainless steel held at 100°C depends on the water-vapor flux to the surface or on the isotherm for water adsorption on stainless steel.

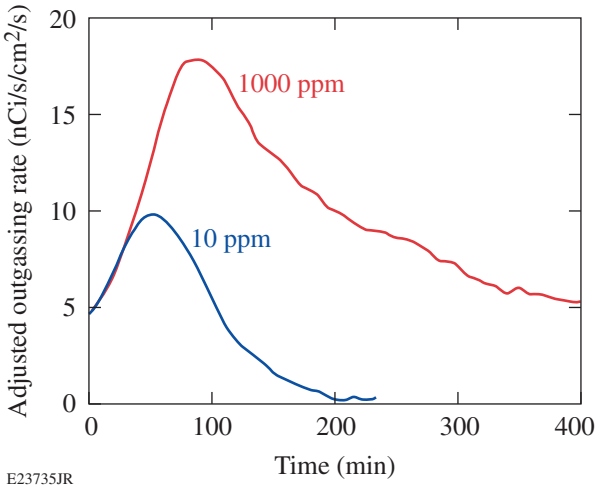


Figure 140.30
The temporal evolution of the outgassing rate variation from stainless steel held at 100°C and exposed to a purge stream containing 10 ppm and then 1000 ppm of water vapor.

## 4. Discussion

The tritium-concentration profile's dependence on distance was calculated using the Crank–Nicolson equation.[8] This approach relies on flux balances across a grid spanning the metal depth and uses a finite-difference solution to the diffusion equation. The calculation determines where the tritium is located during the loading phase and how that profile evolves during the storage of the stainless-steel samples. Three major assumptions were used in this calculation:

(a) The concentration of tritium at the surface was constant during loading.

(b) No tritium was lost during the storage period.

(c) The oxide and metal bulk concentrations at the oxide–metal interface were related by the ratio of their respective solubilities:

$$C_{\text{oxide}} = \frac{S_{\text{oxide}}}{S_{\text{bulk}}} * C_{\text{bulk}} . \quad (1)$$

While the metal bulk solubility is a known value, the oxide solubility was determined by varying its value until the calculated total activity in the sample agreed with the measured value. The difference between calculation and experiment was minimized with the Minuit routine contained in the ROOT data analysis package from CERN. The resulting oxide solubility is 6000±200 times greater than the metal bulk solubility.

To calculate the amount of tritium that participates in each experiment, the penetration depth must be known. As tritium diffuses from the bulk to the surface, the tritium concentration profile in the metal will develop into an error function. The concentration at the oxide–metal interface will be low compared to the concentration deep in the bulk. The distance ($z$) that a triton can diffuse from the bulk into the oxide layer at a given temperature depends on time ($t$) according to Eq. (2):

$$z = \sqrt{4 * D(T) * t} , \quad (2)$$

where $D$ is the diffusivity of the triton in stainless steel at temperature $T$. The tritium diffusivity in stainless steel[9,10] at 130°C is $9.9 \times 10^{-10}$ cm$^2$/s. Tritons in the bulk metal located 109 $\mu$m beyond the oxide–metal interface cannot contribute to the desorption flux over the course of a 500-min experiment. The diffusivity decreases to $5.4 \times 10^{-12}$ cm$^2$/s at 30°C and the tritons penetration depth drops to 8 $\mu$m.

Integrating the tritium concentration profile over the penetration depth yields the calculated amount of tritium that can contribute during an experiment. Using a depth of 8 $\mu$m, which corresponds to the data in Fig. 140.27, the calculated activity that can contribute is 281 $\mu$Ci. This value compares with 243 $\mu$Ci of tritium collected during the three runs shown in Fig. 140.27.

## 5. Conclusions

Baking out stainless steel at or above 300°C is an effective method of reducing the tritium inventory in stainless steel. Humidity-stimulated peak outgassing rates are seen to be at least one order of magnitude lower than thermally driven peak outgassing rates.

The quantity of tritium removed increases with humidity. A sixfold increase in moisture content in the purge stream generates at least a tenfold improvement in the peak outgassing rate.

Calculations show more activity is present than is actually removed during each experiment, suggesting that the bulk diffusivity limits tritium removal.

## ACKNOWLEDGMENT

This material is based upon work supported by the Department of Energy National Nuclear Security Administration under Award Number DE-NA0001944, the University of Rochester, and the New York State Energy Research and Development Authority. The support of DOE does not constitute an endorsement by DOE of the views expressed in this article.

## REFERENCES

1. A. B. Antoniazzi, W. T. Shmayda, and R. A. Surette, Fusion Technol. **21**, 867 (1992).
2. A. B. Antoniazzi and W. T. Shmayda, Fusion Technol. **26**, 673 (1994).
3. T. Ohmi *et al.*, J. Electrochem. Soc. **139**, 2654 (1992).
4. T. Ohmi *et al.*, Rev. Sci. Instrum. **64**, 2683 (1993).
5. Y. Shirai *et al.*, in *Proceedings of the Microcontamination 94 Conference and Exposition* (Canon Communications, Santa Monica, CA, 1994), pp. 272–281.
6. M. J. Quinlan, W. T. Shmayda, S. Lim, S. Salnikov, Z. Chambers, E. Pollock, and W. U. Schröder, Fusion Sci. Technol. **54**, 519 (2008).
7. W. T. Shmayda, A. B. Antoniazzi, and R. A. Surette, Ontario Hydro Research Division, Toronto, Canada, Report 92-51-K (1992).
8. J. Crank, *The Mathematics of Diffusion* (Oxford University Press, Oxford, 1979), p. 189.
9. M. R. Louthan Jr. and R. G. Derrick, Corros. Sci. **15**, 565 (1975).
10. J. H. Austin and T. S. Elleman, J. Nucl. Mater. **43**, 119 (1972).

# The Sixth Omega Laser Facility Users Group Workshop

## Introduction

A capacity gathering of over 100 researchers from 25 universities and laboratories met at the Laboratory for Laser Energetics (LLE) for the Sixth Omega Laser Facility Users Group (OLUG) workshop. The purpose of the 2.5-day workshop was to facilitate communications and exchanges among individual OMEGA users, and between users and the LLE management; to present ongoing and proposed research; to encourage research opportunities and collaborations that could be undertaken at the Omega Laser Facility and in a complementary fashion at other facilities [such as the National Ignition Facility (NIF) or the Laboratoire pour l'Utilisation des Lasers Intenses (LULI)]; to provide an opportunity for students, postdoctoral fellows, and young researchers to present their research in an informal setting; and to provide feedback from the users to LLE management about ways to improve and keep the facility and future experimental campaigns at the cutting edge. The interactions were wide-ranging and lively, as illustrated in the accompanying photographs.

The OLUG consists of over 400 members from 44 universities and many research centers and national laboratories. Names and affiliations can be found at **http://www.lle.rochester.edu/media/about/documents/OLUGMEMBERS.pdf**. OLUG is by far the largest users group in the world in the field of high-energy-density (HED) physics and also one of the most active.

The first two mornings of the workshop comprised six science and facility presentations. The facility talks proved especially useful for those unfamiliar with the art and complexities of performing experiments at the Omega Laser Facility. Since the facility is constantly evolving and improving, even experienced users significantly benefited from these updates. The overview science talks, given by leading world authorities, described the breadth and excitement of HED science either being currently undertaken at the Omega Laser Facility or well within the reach of the facility with improvements or upgrades.

A total of 63 students and postdoctoral fellows, 53 of whom were supported by travel grants from the National Nuclear Security Administration (NNSA), participated in the workshop. The content of their presentations encompassed the spectrum from target fabrication to simulating aspects of supernovae; the presentations generated spirited discussions, probing questions,

U1738JR

Figure 140.31
A capacity gathering of over 100 researchers, from universities and laboratories around the world, participated in this year's workshop. The Users Group itself has over 400 members who come from 44 universities and 25 laboratories, making it by far the largest users group in the world in high-energy-density physics. The next annual OMEGA Users Workshop will occur on 22–24 April 2015.

and friendly suggestions. In total there were 93 posters, including eight that focused on the Omega Laser Facility.

An important function of the workshop was to develop a set of **Findings and Recommendations** (p. 247) to help set and define future priorities for the Omega Laser Facility. They were grouped into three broad areas: OMEGA EP, 60-beam OMEGA, and general facility improvements and the accessibility and transparency of OMEGA operational information. LLE management uses these recommendations as a guide for making decisions about Omega Laser Facility operations, priorities, and future changes. In addition, the status of these OLUG **Findings and Recommendations** was updated and reviewed at a satellite evening meeting during the fall American Physical Society's Division of Plasma Physics Conference (New Orleans, 27 October 2014). They will also form the grist for the forthcoming workshop.

One highlight of the workshop, as in past workshops, was the panel of students and postdocs who discussed their experiences at the Omega Laser Facility along with their thoughts and recommendations on facility improvements. Engaging discussions sparked by this forum resulted in the student/postdoctoral recommendations for the facility.

A new and very well attended event was the Wednesday evening session, sponsored by the students and postdocs. The event featured the University of Chicago's Petros Tzeferacos, who gave a tutorial on the radiation–hydrodynamics code *FLASH* that is used widely in the HED community.

For the second time, three posters were presented by LLE's Summer High-School Research Program students. Participants found their work impressive!

Finally, one of the important decisions made at the workshop was the selection of 22–24 April 2015 as the date of the next workshop. Planning for this event has already begun.

Several of the **Findings and Recommendations** of past workshops were either completed or are well underway. Some of the most-recent accomplishments include an enhanced tritium fill capability; an update of the OMEGA Users Guide; establishing a support group from whom the users can get technical help and assistance contact (Chuck Source and team); development of low-energy neutron spectroscopy; initiation of high-resolution x-ray imaging; the Wednesday evening Student/Postdoc Tutorial session; full implementation of the super gas Cherenkov detector (GCD-3) gamma-ray spectrometer; implementation of compact 14.1-MeV neutron spectrometers; and initiation of the Phase I differential nuclear burn diagnostic for $D_2$, $D^3He$, and $T^3He$.

The photographs on the following pages provide a representative sampling of the workshop's talks, interactions, and ambience.

U1739JR

Figure 140.32
A total of 63 students and postdoctoral fellows attended and nearly all made poster presentations. An NNSA grant provided travel assistance for 53 of these attendees. The workshop emphasizes the participation and involvement of young researchers.

U1740JR

Figure 140.33
The Wednesday morning registration brought in researchers from around the world; MIT students welcome and registered the arrivals.

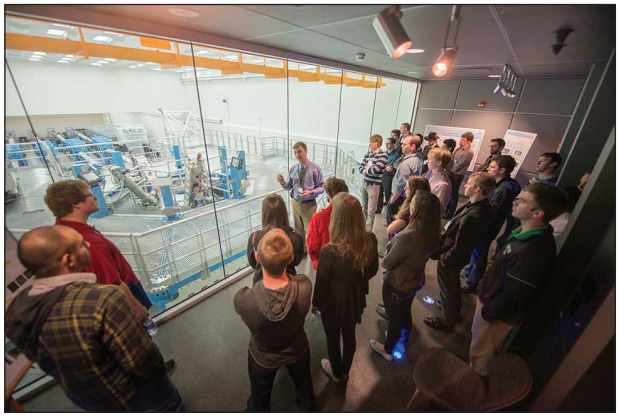

U1742JR

Figure 140.35
Tours of the OMEGA and OMEGA EP Laser Systems help researchers understand the complexity of the facilities and get a first-hand taste of the knowledge required to implement a successful campaign.

U1741JR

Figure 140.34
A total of 93 posters were presented in three different poster sessions, engendering lively discussions and often new insights. Students and postdocs, many of whom traveled to the workshop through the support of the NNSA travel grant, presented 63 of the posters.

U1743JR

Figure 140.36
The student and postdoc sessions/town meetings are wonderful forums for young researchers to talk about their current research, as well as to delve into issues that particularly concern them in the course of implementing an OMEGA campaign.


U1744JR

Figure 140.37
The spirited Findings and Recommendation sessions are central to the mission of the workshop for formulating and discussing ways, both technologically and through greater information transparency, to improve the facility and keep it at the forefront of high-energy-density research.

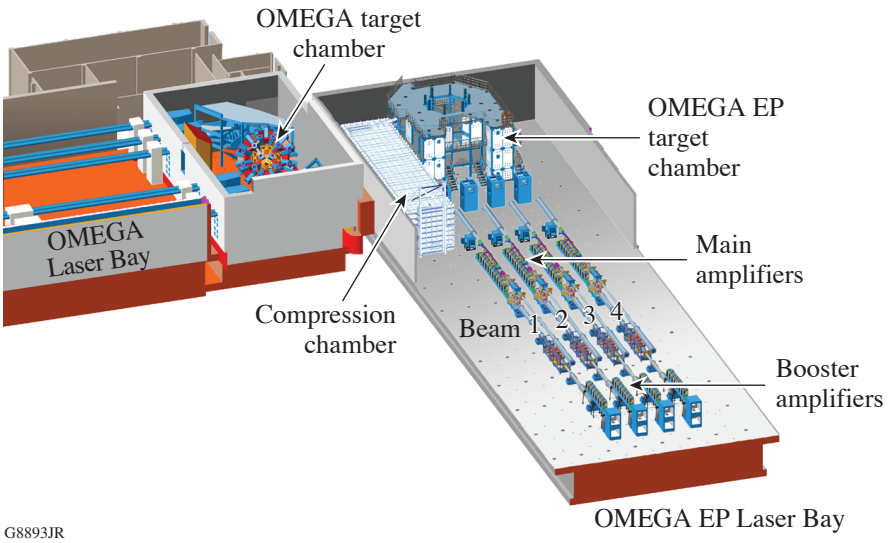


Figure 140.38
One of the important and challenging Findings and Recommendations, first discussed by General Atomic's Mingsheng Wei, is the redirection of OMEGA EP Beam 4 so that it opposes Beam 3.

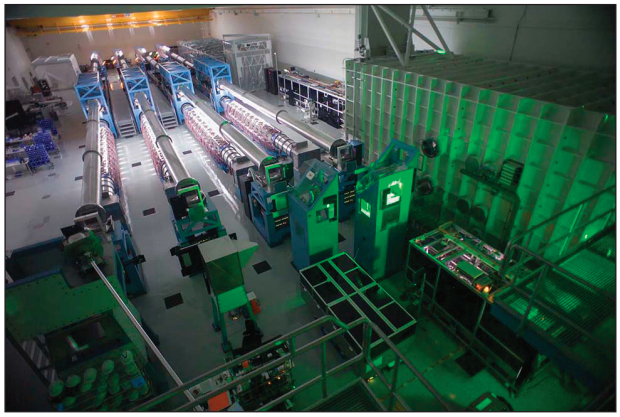


Figure 140.39
Beam 4 is the left-most beam in the OMEGA EP Bay, as seen from the target chamber.

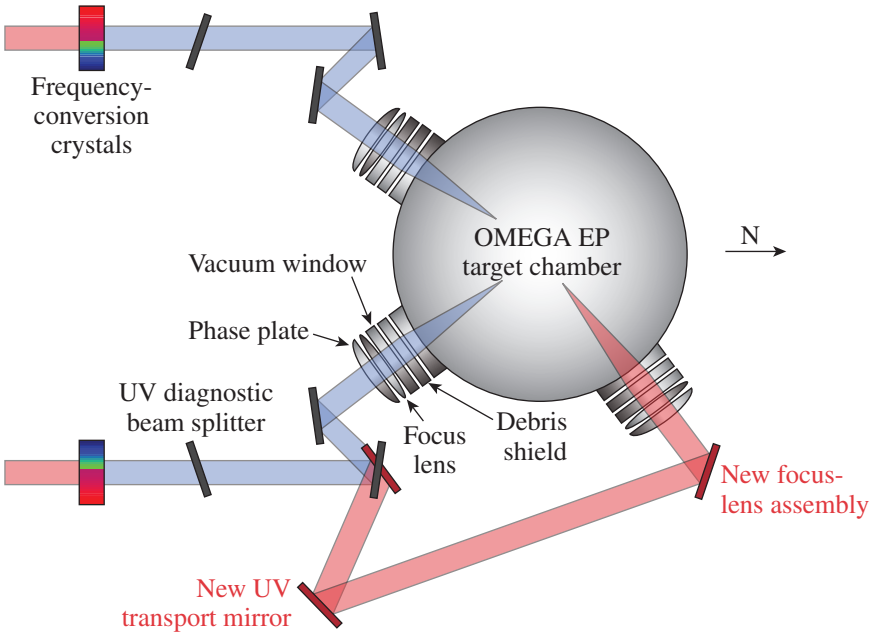


Figure 140.40
The cost and time to implement the "opposing beam" Findings and Recommendations is about $1.5 million and would take about 18 months to implement. Importantly, it would have a very minimum impact on facility use. The enabling high-energy-density laboratory physics science would be transformative; examples of this were presented by Mingsheng Wei, Patrick Harrtigan, Raymond Jeanloz, Chikang Li, Gianlucca Grigori, Michel Koenig, and Channing Huntington among others. The opposing-beam concept and white paper were presented to the Fusion Energy Sciences Advisory Committee on 4 June 2014.

**Principal Findings and Recommendations of 2014 Workshop**

*OMEGA EP:*

1. Thomson scattering on OMEGA EP with 4$\omega$ probe laser
2. Continuation of work for OMEGA EP to full specifications
3. Investigation of ~100-ns pulses on OMEGA EP
4. Opposing beams on OMEGA
5. Pulse-shaping capability of 1 ps to 10 ps on OMEGA EP
6. 4$\omega$ interferometry on OMEGA EP
7. Four phase plates similar to the IDI-300 for smoother, higher-intensity spots on OMEGA EP
8. Scoping of beam splitter on OMEGA EP for short-pulse mode
9. Developing guidance for OMEGA EP debris shield use

*OMEGA Centric and Overarching Considerations:*

1. A 61st beam for Thomson scattering OMEGA
2. Independent operations of the three legs of OMEGA
3. Improvements of streaked optical pyrometer/active shock breakout on OMEGA
4. *In-situ* gas-fill capability on OMEGA and OMEGA EP
5. Large phase plates for OMEGA (2 mm or larger, nominally ten in number)
6. Installation of hardware to enable the absolute timing of OMEGA neutron time-of-flight detectors
7. New and updated National Laser Users' Facility Guide
8. Theory/simulations and diagnostics to explore multifluid/kinetic effects
9. Reduction of $D_2$ contamination in $^3$He to of the order of $1 \times 10^{-6}$

## ACKNOWLEDGMENT

OLUG gratefully acknowledges the financial assistance of NNSA for travel support of students and postdocs to OLUG Workshop 2014; to the Fusion Science Center, to OFES, to MIT, and especially to LLE and Dr. Robert L. McCrory, Laboratory Director, for sustained support of myriad aspects of the Workshop and activities, including implementation of many of the User Findings and Recommendations. Thank you!

U1746JR

Figure 140.41
The Workshop banquet at the Meliora offers a wonderful time for old and new friends to mingle in a congenial ambiance.

# LLE's Summer High School Research Program

During the summer of 2014, 16 students from Rochester-area high schools participated in the Laboratory for Laser Energetics' Summer High School Research Program. The goal of this program is to excite a group of high school students about careers in the areas of science and technology by exposing them to research in a state-of-the-art environment. Too often, students are exposed to "research" only through classroom laboratories, which have prescribed procedures and predictable results. In LLE's summer program, the students experience many of the trials, tribulations, and rewards of scientific research. By participating in research in a real environment, the students often become more excited about careers in science and technology. In addition, LLE gains from the contributions of the many highly talented students who are attracted to the program.

The students spent most of their time working on their individual research projects with members of LLE's technical staff. The projects were related to current research activities at LLE and covered a broad range of areas of interest including laser physics, computational modeling of implosion physics, radiation physics, experimental diagnostic development, cryogenic targets, theoretical and experimental chemistry, tritium capture, electronics, image display, and 3-D virtual modeling (see Table 140.II).

The students attended weekly seminars on technical topics associated with LLE's research. Topics this year included laser physics, fusion, holography, nonlinear optics, atomic force microscopy, electronic paper, and attosecond science. The students also received safety training, learned how to give scientific presentations, and were introduced to LLE's resources, especially the computational facilities.

The program culminated on 27 August with the "High School Student Summer Research Symposium," at which the students presented the results of their research to an audience including parents, teachers, and LLE staff. The students' written reports will be made available on the LLE Website and bound into a permanent record of their work that can be cited in scientific publications.

Three hundred and twenty-eight high school students have now participated in the program since it began in 1989. This year's students were selected from nearly 70 applicants.

At the symposium LLE presented its 18th annual William D. Ryan Inspirational Teacher Award to Dr. Jeffrey Lawlis, Chair of the Science Department at Allendale Columbia High School. This award is presented to a teacher who motivated one of the participants in LLE's Summer High School Research Program to study science, mathematics, or technology and includes a $1000 cash prize. Teachers are nominated by alumni of the summer program. Dr. Lawlis was nominated by Alex Frenett, a participant in the 2013 program. Describing his physics class, Alex wrote, "Dr. Lawlis began the year challenging the students, not spoon-feeding them information. He not only taught them to derive the necessary equations (instead of having us memorize them), but also used his background in science to make the class entertaining, as he constructed many of the lab setups himself." He proceeded to say, "Dr. Lawlis' dedication to students is rare to find. Throughout the year, you could find his students in his classroom, working one-on-one with him for help…His class, his help, and his distinctive puns somehow inspired intelligent thinking." He concluded, "This combination of intellect, support, and talent exemplifies how this man has devoted himself to his school, his community, and, most of all, his students in a way that only the best teachers ever do." Dr. Lawlis also received strong support from Mr. Michael Gee, principal of Allendale Columbia High School, who described him as "a knowledgeable person who has raised the bar of the Science Department."

Table II: High School Student and Projects—Summer 2014.

| Name | High School | Supervisor | Project Title |
|---|---|---|---|
| Ryan Dens | Allendale Columbia | D. W. Jacobs-Perkins | Display of Scientific Image Sources with Mobile Devices |
| Pranav Devarakonda | Brighton | R. Epstein | The Use of Rosseland- and Planck-Averaged Opacities in Multigroup Radiation Diffusion |
| William Franceschi | Victor | B. E. Kruschwitz and A. Kalb | Optimization of Wavefront Control Using a High-Resolution Wavefront Sensor |
| Emma Garcia | Penfield | R. S. Craxton | Optimization of Uniformity for Current Polar-Drive Implosion Experiments on the National Ignition Facility |
| Jack Gumina | Harley | K. L. Marshall | Next-Generation Polymers for High-Power UV Optics |
| Krishna Patel | Webster Schroeder | W. T. Shmayda | Capturing Hydrogen on a Chilled Molecular Sieve |
| Sophia Rogalskyj | Mercy | W. T. Shmayda | Isotopic Exchange on a Platinum-Coated Molecular Sieve |
| Liam Smith | Webster Schroeder | R. W. Kidder | Evaluation of a Collaborative Networking Environment for Experimental Configurations |
| Jeremy Weed | Victor | D. Hassett, R. Peck, and D. Axman | Creating an Open Source LLE-Based Ethernet to LonTalk Adapter |
| Felix Weilacher | Penfield | P. B. Radha | Optimizing Beam Profiles for Polar-Drive Implosions on the National Ignition Facility |
| Kyle Xiao | Webster Schroeder | K. L. Marshall | Computational Modeling of Azobenzenes for Optically Addressable Liquid Crystal Alignment |
| Nathan Xu | Pittsford Sutherland | S. X. Hu | Effects of Alpha-Particle Stopping-Power Models on Inertial Confinement Fusion Implosions |
| Christopher Ye | Webster Schroeder | J. A. Delettrez | Limits on the Level of Fast-Electron Preheat in Direct-Drive Ignition Designs |
| Robin Zhang | Webster Schroeder | C. Kingsley | Statistical Investigation of Cryogenic Target Defects |
| Roger Zhang | Webster Schroeder | R. S. Craxton | Polar-Driven X-Ray Backlighter Targets for the National Ignition Facility |
| Junhong (Sam) Zhou | Victor | C. Stoeckl | Analyzing the Sensitivity of a Hard X-Ray Detector Using Monte Carlo Methods |

# FY14 Laser Facility Report

During FY14, the Omega Laser Facility conducted 1405 target shots on OMEGA and 699 target shots on OMEGA EP for a total of 2104 target shots (see Tables 140.III and 140.IV). OMEGA averaged 11.1 target shots per operating day with Availability and Experimental Effectiveness averages for FY14 of 95.8% and 93.3%, respectively.

OMEGA EP was operated extensively in FY14 for a variety of internal and external users. A total of 638 target shots were taken into the OMEGA EP target chamber and 61 joint target shots were taken into the OMEGA target chamber. OMEGA EP averaged 7.6 target shots per operating day with Availability and Experimental Effectiveness averages for FY14 of 95.7% and 92.8%, respectively.

**Highlights of Achievements in FY14**

1. IR Transmission Diagnostic

Hardware was installed to collect final optics transmission data for the short-pulse beams on OMEGA EP. These optics will be characterized after each campaign to understand the resultant degradation of the surfaces from target debris and increase accuracy of on-target energy measurements. The diagnostic will also be used to collect data for debris-shield policy modifications.

Table 140.III: OMEGA Laser System target shot summary for FY14.

| Laboratory | Planned Number of Target Shots | Actual Number of Target Shots | ICF | Shots in Support of ICF | Non-ICF |
|---|---|---|---|---|---|
| CEA | 61 | 67 | 0 | 0 | 67 |
| DTRA | 22 | 26 | 0 | 0 | 26 |
| LANL | 187 | 206 | 33 | 0 | 173 |
| LBS | 154 | 165 | 0 | 0 | 165 |
| LLE | 495 | 484 | 0 | 455 | 29 |
| LLNL | 253 | 270 | 70 | 0 | 200 |
| NLUF | 165 | 178 | 0 | 0 | 178 |
| Maintenance | 0 | 9 | 0 | 9 | 0 |
| Total | 1337 | 1405 | 103 | 464 | 838 |

Table 140.IV: OMEGA EP Laser System target shot summary for FY14.

| Laboratory | Planned Number of Target Shots | Actual Number of Target Shots | ICF | Shots in Support of ICF | Non-ICF |
|---|---|---|---|---|---|
| LANL | 12 | 15 | 7 | 0 | 8 |
| LBS | 90 | 133 | 0 | 0 | 133 |
| LLE | 168 | 242 | 0 | 128 | 114 |
| LLNL | 60 | 70 | 39 | 0 | 31 |
| NLUF | 84 | 88 | 0 | 0 | 88 |
| SNL | 12 | 13 | 13 | 0 | 0 |
| Maintenance | 0 | 138 | 0 | 138 | 0 |
| Total | 426 | 699 | 59 | 266 | 374 |

2. OMEGA Digital Imaging System

The aging laser alignment video system for OMEGA is being replaced with modern digital equipment. The core infrastructure has been installed and many of the cameras have been replaced as part of project work this year. As with the system in OMEGA EP, integration of GigE-based camera diagnostics can be supported in shorter time frames.

3. Short- and Long-Pulse Late-Cycle Wavefront Control

The late-cycle control software has been implemented to optimize focal-spot performance. It coordinates the wavefront control and device motion control during the amplifier charge sequence on OMEGA EP. This capability significantly reduces the amount of time between final wavefront correction and each shot. Results include reduced wavefront error and consistent on-target short-pulse spot sizes of less than 20-$\mu$m radius.

4. OMEGA EP ASBO Laser Installation and ASBO/VISAR Diagnostic Tune Up

The OMEGA EP active shock breakout (ASBO) and velocity interferometer system for any reflector (VISAR) diagnostic have been significantly refurbished to ensure optimum measurements. An additional source laser for OMEGA EP was commissioned to reduce dependence on the OMEGA source, mitigate campaign conflicts, and provide a spare resource for OMEGA. With this system operational, both laser systems are able to support campaigns that require ASBO diagnostic measurements on the same day.

5. OMEGA Arbitrary Waveform Generator on the SSD Driver

The OMEGA smoothing by spectral dispersion (SSD) driver pulse-shaping system has been converted from aperture-coupled stripline technology to modern digital arbitrary waveform generator technology. Accuracy and repeatability of pulse-shape generation have been dramatically improved. The facility has also extended available pulse-shaping features by adding a fourth-picket capability. The changing hardware required a redesign of all pulse shapes. The facility used this opportunity to update the pulse nomenclature to improve clarity and correlate the pulse shape name more closely to the design features.

6. 4$\omega$ Probe Polarimetry Diagnostic

The 4$\omega$ probe polarimetry diagnostic was activated over the past year and is being used to measure the polarization rotation of the probe beam after transmission through plasma formed at the target chamber center (TCC). The primary purpose is to diagnose magnetic fields generated at TCC that induce Faraday rotation of the 4$\omega$ probe-beam polarization as it passes through a plasma or dielectric medium. The angular filter refractometry diagnostic is simultaneously used to measure the plasma density profile complementing the plasma characterization and enabling one to calculate the magnetic fields.

7. Co-Propagation Activation

The OMEGA EP beam combiner optic coating has been re-engineered to withstand the fluences present in the beam path. With this advancement, LLE has activated a mode where the short-pulse signal from the upper and lower compressors is co-propagated to the target along the same beam path. The co-propagation option is available for either the backlighter beam path (on OMEGA EP) or the OMEGA target chamber beam path. In addition to simultaneous co-propagation, the ability to alternate shots using a single laser source through the same beam path to target is now available to users to achieve a higher shot rate.

8. 3$\omega$ Beam Timing Prototype System

The use of a target-sized scattering sphere enables one to directly measure UV light at the target chamber center. A procedure has been developed to launch a 5-Hz-repetition-rate infrared pencil beam into one of the beamlines such that sufficient energy is present at the frequency-conversion crystals to make several nanojoules of UV light. The signal scattered from the target is captured and characterized relative to a reference beamline, allowing the path-length adjustment to be characterized for co-timing of all 60 beams. The initial data have shown that less-than-10-ps peak-to-peak timing can be achieved with this system.

9. Experimental Operations

Ten qualifications have been completed in FY14 to improve the capabilities of OMEGA and OMEGA EP, including the MIT split nose for the proton temporal diagnostics, the LLNL B-dot probes, and the LANL gas Cherenkov detector #3. As in previous years, many of the new instruments and capabilities were developed by, or in collaboration with, other laboratories.

Several infrastructure projects were completed this year to support target diagnostics: the final two ten-inch manipulators (TIM's) have been retrofitted with modern mechanical and electrical control systems; the magneto-inertial fusion energy delivery system (MIFEDS) has been qualified in two additional TIM locations; and a pressurized gas-handling system has been implemented to support the gas Cherenkov and gamma reaction history diagnostics for LANL.

The National Ignition Facility (NIF) x-ray spectrometer (NXS) has been qualified for use on OMEGA, calibrated on a two-day shot campaign, and then transferred to the NIF. Image plates for NXS were subsequently cross calibrated to those actively used on the NIF.

# National Laser Users' Facility and External Users' Programs

Under the facility governance plan implemented in FY08 to formalize the scheduling of the Omega Laser Facility as a National Nuclear Security Administration (NNSA) User Facility, Omega Facility shots are allocated by campaign. The majority of the FY14 target shots were allocated to the Inertial Confinement Fusion (ICF) Campaign conducted by integrated teams from the national laboratories and LLE and the High-Energy-Density (HED) Campaigns conducted by teams led by scientists from the national laboratories.

The Fundamental Science Campaigns accounted for 26.9% of the shots taken in FY14. Nearly half of these were dedicated to university fundamental science under the National Laser Users' Facility (NLUF) Program, and the remaining shots were allotted to the Laboratory Basic Science (LBS) Program, comprising peer-reviewed fundamental science experiments conducted by the national laboratories and by LLE, including the Fusion Science Center (FSC).

The Omega Laser Facility is also used for several campaigns by teams from the Commissariat à l'Énergie atomique et aux energies (CEA) of France and the Atomic Weapons Establishment (AWE) of the United Kingdom. These programs are conducted at the facility on the basis of special agreements put in place by DOE/NNSA and participating institutions.

The facility users during this year included 11 collaborative teams participating in the NLUF Program; 16 teams led by Lawrence Livermore National Laboratory (LLNL) and LLE scientists participating in the LBS Program; many collaborative teams from the national laboratories conducting ICF experiments; investigators from LLNL and Los Alamos National Laboratory (LANL) conducting experiments for high-energy-density–physics programs; and scientists and engineers from CEA.

In this section, we briefly review all the external user activity on OMEGA during FY14.

**FY14 NLUF Program**

FY14 was the second of a two-year period of performance for the NLUF projects approved for the FY13–FY14 funding and OMEGA shots. Eleven NLUF projects (see Table 140.V) were allotted Omega Laser Facility shot time and conducted a total of 265 target shots at the facility. This NLUF work is summarized in the following section.

In response to a DOE-issued solicitation in late FY14 for FY15–FY16 experiments, 23 proposals were received. The proposals were to be reviewed by a technical evaluation panel in October 2014 so that DOE may decide which proposals can be accepted and receive shots at the Omega Facility.

***Study of Fast-Electron Transport into Imploded High-Density Plasmas Using Cu-Doped CD Shell Targets***

Principal Investigators: F. N. Beg (University of California, San Diego) and M. S. Wei (General Atomics)

Co-investigators: R. B. Stephens (General Atomics); C. McGuffey, B. Qiao, and H. Sawada (University of California, San Diego); A. A. Solodov, W. Theobald, C. Stoeckl, J. A. Delettrez, R. Betti, F. J. Marshall, and C. Mileham (LLE); M. H. Key, P. K. Patel, and H. S. McLean (LLNL); T. Yabuuchi, T. Iwawaki, and H. Habara (ILE); and J. J. Santos and D. Batani (University of Bordeaux, France)

Lead Graduate Student: L. C. Jarrott (University of California, San Diego)

Understanding the generation of fast electrons inside the cone and its subsequent transport into hot dense plasmas is crucial to the success of the cone-guided fast-ignition (FI) scheme of inertial confinement fusion. In our prior work, we developed a new platform that measured, for the first time, the spatial map of fast-electron transport in the vicinity of the core of an imploded shell in joint OMEGA and OMEGA EP experiments. In this University of California San Diego (UCSD)-led NLUF project, we use the same platform to investigate several methods of improving coupling efficiency into an imploded CH/CD

Table 140.V: NLUF proposals approved for shots at the Omega Laser Facility for FY13–FY14.

| Principal Investigator | Institution | Project Title |
|---|---|---|
| F. N. Beg | University of California, San Diego | Systematic Study of Fast-Electron Energy Deposition in Imploded Plasmas with Enhanced OMEGA EP Laser Contrast and Intensity |
| R. P. Drake | University of Michigan | Experimental Astrophysics on the OMEGA Laser |
| T. Duffy | Princeton University | Dynamic Compression of Earth and Planetary Materials Using OMEGA |
| W. Fox | University of New Hampshire | Dynamics and Instabilities of Magnetic Reconnection Current Sheets in High-Energy-Density Plasmas |
| P. Hartigan | Rice University | Astrophysical Dynamics in the Laboratory: Mach Stems and Magnetized Shocks |
| R. Jeanloz | University of California, Berkeley | Journey to the Center of Jupiter, Recreating Jupiter's Core on OMEGA |
| H. Ji | Princeton University | Study of Particle Acceleration and Fine-Scale Structures of Collisionless Magnetic Reconnection Driven by High-Energy Petawatt Lasers |
| R. D. Petrasso | Massachusetts Institute of Technology | Studies of Laboratory Astrophysics, Inertial Confinement Fusion, and High-Energy-Density Physics with Nuclear Diagnostics |
| B. Qiao | University of California, San Diego | Dynamics of High-Energy Proton Beam Focusing and Transition into Solid Targets of Different Materials |
| A. Spitkovsky | Princeton University | Generation of Collisionless Shocks in Laser-Produced Plasmas |
| R. B. Stephens | General Atomics | Investigation of the Dependence of Fast-Electron Generation and Transport on Laser Pulse Length and Plasma Materials |

shell attached to a re-entrant gold cone target. The shell has an outer diameter of 870 $\mu$m, consisting of a 15-$\mu$m-thick outer CH ablator and a 23-$\mu$m-thick inner CD layer. *A Cu dopant (at ~1% atomic number density of CD) is added to the CD layer of the shell, which makes it possible to characterize fast-electron transport via its induced Cu K-shell fluorescence radiation.*

Fifty-four OMEGA beams (with a total energy of ~18 kJ) were used to compress the shell. The 10-ps OMEGA EP Beamline 2 was tightly focused at the inner cone tip with various time delays relative to the OMEGA driver chosen to be before and after breakout on the inner cone tip. In this experiment, air was evacuated from the shells and the driver pulse shape was modified because radiation–hydrodynamic simulations predicted increased density at the instant of cone-tip breakout.

The breakout timing was measured by the active shock breakout (ASBO) diagnostics for this new configuration. A zinc Von Hamos (ZVH) x-ray spectrometer tuned to measure the Cu K shell and ionic line emission provided spatially integrated Cu $K_\alpha$ yield measurements. As seen in Fig. 140.42, *the total Cu $K_\alpha$ yield increased significantly (up to a factor of 3.5) in the joint shots compared to the OMEGA-only implosion shots.* Fast-electron energy coupling to the compressed core was found to increase with the OMEGA EP beam energy. Neutron yield from D–D fusion, measured by a liquid crystal neutron time-of-flight detector, was also found to increase with OMEGA EP energy by a factor of up to 2.9, compared to those from only the implosion.

While the ZVH provided the total yield of Cu $K_\alpha$, a monochromatic spherical crystal imager (SCI) (centered at 8048 eV with a 6-eV bandwidth) gave unprecedented spatial information about where the fast electrons deposit their energy. Figures 140.43(a)–140.43(c) show data from joint shots at three delays. *They clearly show that fast electrons penetrated through the cone (wall and tip) into the compressed shell, producing strong Cu $K_\alpha$ emission from the region of the imploded high-density plasmas.* The brightness, characteristic shape, and size change as a function of delay. The spatially resolved SCI data indicate that nearly all of the enhancement in Cu $K_\alpha$ yield is a result of emission from within 150 $\mu$m of the cone tip's position.

A comprehensive hierarchy of simulation tools was used to model the entire process from the implosion (2-D radiation–hydrodynamics code *DRACO*), cone pre-plasma (2-D radiation–hydrodynamics code *HYDRA*), electron generation, and finally, electron-beam transport particle-in-cell (PIC) code *LSP*. Diagnostic capabilities were implemented into the final transport steps

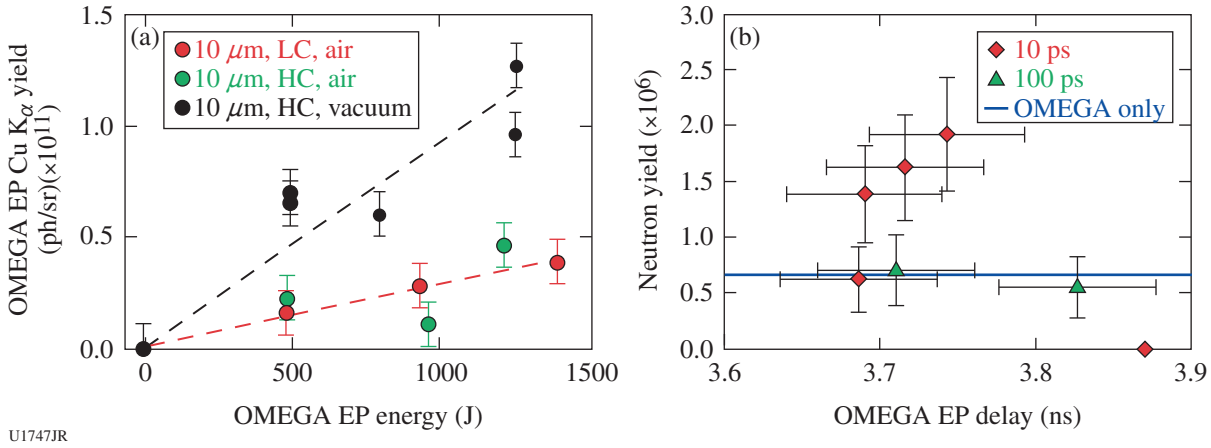


Figure 140.42
(a) Cu $K_\alpha$ yield from the zinc Von Hamos (ZVH) spectrometer showed enhancement with OMEGA EP in all three configurations investigated. The cone tip's diameter was either 10 or 40 $\mu$m, the OMEGA EP contrast was high (HC) or low (LC, prior to upgrade), and the shells had residual air or were evacuated with corresponding reduced driver picket. (b) D–D neutron yield was enhanced with the high-contrast, high-intensity (10-ps) OMEGA EP in joint shots prior to tip breakout.

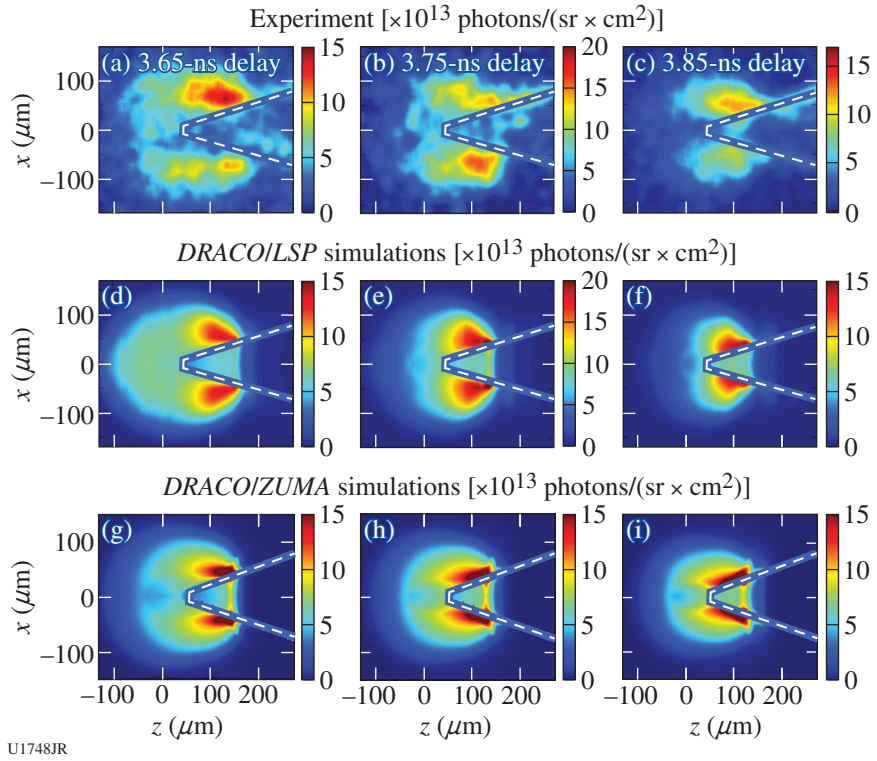


Figure 140.43
[(a)–(c)] Cu $K_\alpha$ images showing the emission from the vicinity of the cone tip at various delays with the OMEGA EP beam energy at ~500 J. The dotted line is added to visualize the cone position. [(d)–(f)] Simulated data using a series of codes reproduce the emission around and in front of the cone tip at the same delays. [(g)–(i)] Simulated data with the hybrid particle-in-cell (PIC) code *ZUMA* allowed for comparison to data over a wide range of source position, divergence, and energy.

to emulate the generation of Cu $K_\alpha$ photons, taking into account temperature effects on emission and crystal response caused by the shifting and broadening of the Cu $K_\alpha$ spectral line at plasma temperatures increasing above the order of 150 eV (using the code *PrismSPECT3D*), opacity, and 2-D projection for direct comparison to the experimental images. Figures 140.43(d)–140.43(f) show simulated data at the same three delays, reproducing several of the features as functions of time, including decrease in size, closeness to the walls, and decreased signal in the forward direction because of heating. Transport studies were also carried out with the hybrid PIC code *ZUMA* for rapid comparison over a wide range of electron source parameters. These simulations were also able to reproduce the characteristics of the SCI data, as shown in Figs. 140.43(g)–140.43(i), and further identified the parameters that were most important in determining the energy-deposition spatial profile and total coupling.

In summary, the FY14 UCSD-led NLUF fast-electron transport experiment used the cone-in-Cu-doped-shell platform developed previously to investigate two methods for improving the coupling from OMEGA EP to an imploded core: mitigation of pre-plasma in the cone by increasing the cone tip's diameter and optimization of the implosion. The changes led to Cu $K_\alpha$ yield enhancement by as much as a factor of 3.5. The increased yield from the core region along with the enhanced neutron yield gives two independent figures of merit showing increased energy coupling to the high-density core. This platform identified the crucial parameters to the coupling of energy to the core, and the data validated modeling codes and tests of new target designs so that coupling to the core can be improved—a critical step forward in the evaluation of fast-ignition laser fusion.

### *Laboratory Astrophysics Investigation into the Structure of Accretion Shocks*

Principal Investigator/Project Director and Technical Point of Contact: Professor R. P. Drake

Co-Principal Investigator: C. C. Kuranz (University of Michigan)

Co-investigators: S. Ross (LLNL); C. K. Li and A. Zylstra (MIT); S. Klein and M. Trantham (University of Michigan); and D. H. Froula, G. Fiksel, and P.-Y. Chang (LLE)

This work involves the design and implementation of laboratory astrophysics experiments on OMEGA to study accretion shocks at the surface of young stars. In the current model of accretion, material from the accretion disk surrounding the young star funnels to the stellar surface along magnetic-field lines (see Fig. 140.44). By understanding the structure of these accretion shocks, we hope to give astronomers the tools to better calculate accretion rates and, thereby, develop better models for the evolution of young stars—much like the Sun some five billion years ago.

Since the material is supersonic, it creates a shock and a region of heated plasma when it hits the stellar surface. By studying the spectra of young stars, astronomers can tell that a small fraction (on average 1%) is covered by very hot plasma (roughly 3 MK) and a slightly larger fraction (on average 5%) is covered by less hot plasma (roughly 2 MK). But what do these fractions tell us about the accretion process? Are the 3-MK hot spots and the 2-MK hot spots caused by independent accretion streams with different densities or are the 2-MK hot spots just heated regions surrounding the 3-MK hot spots? Figure 140.45 illustrates the dilemma. By understanding the structure of accretion shocks, we hope to determine which of these scenarios is more likely and, thereby, enable astronomers to make more-accurate studies of accretion rates.

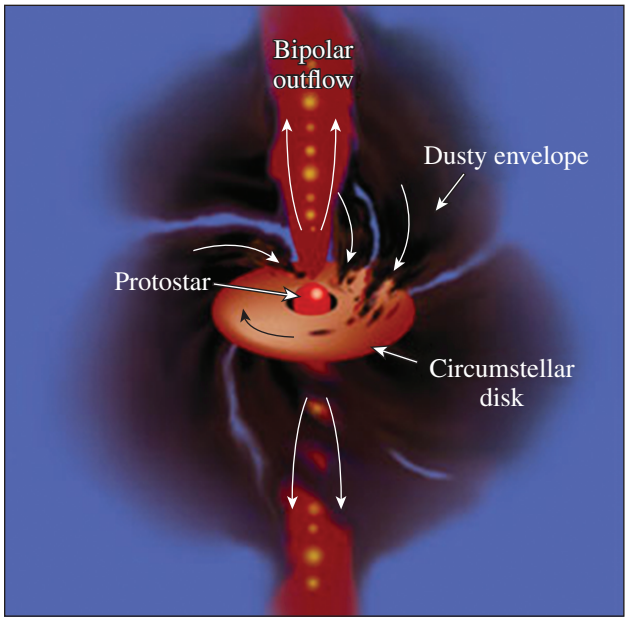


U1750JR

Figure 140.44
A diagram of an accreting protostar system. The protostar is surrounded by an active accretion disk and the star-disk system generates bipolar outflows. There is a gap between the inner edge of the disk and the surface of the star; material bridges this gap by flowing along magnetic-field lines. Credit: Thomas Greene, American Scientist, July–August (2001).

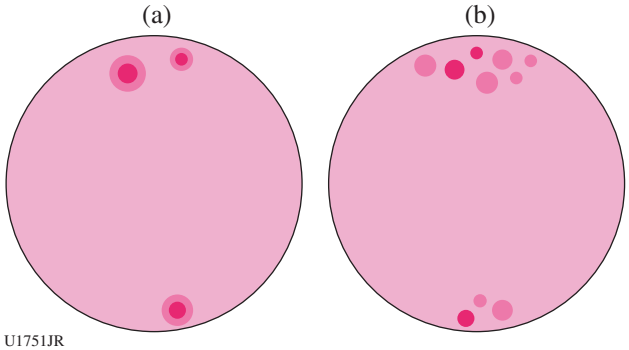


U1751JR

Figure 140.45
(a) Is the 2-MK plasma (shown in medium pink) associated with the 3-MK plasma (shown in dark pink) or (b) are the 2-MK and 3-MK hot spots independent? Understanding which of these scenarios applies has implications when trying to calculate an accretion rate.

Our experiment involves creating a plasma flow by rear-irradiating a thin acrylic cone with seven OMEGA full-power beams (see Fig. 140.46). This plasma (the "accreting flow") travels roughly 3 mm and impacts a solid block (the "stellar surface"). We impose a magnetic field parallel to the plasma flow with a magneto-inertial fusion electrical discharge system (MIFEDS)

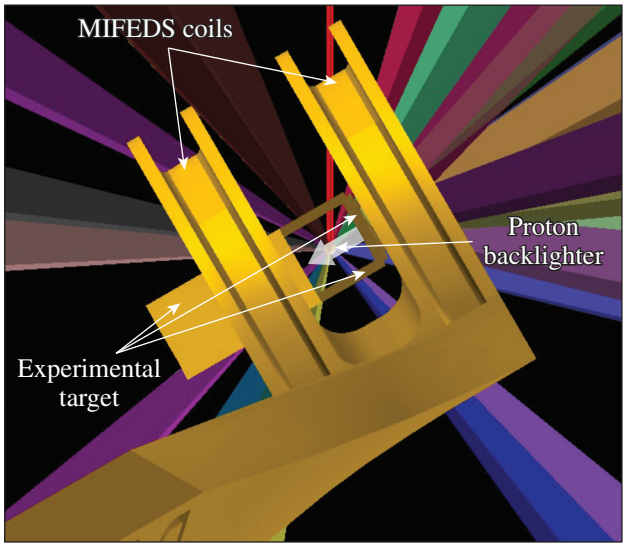


U1752JR

Figure 140.46
The experimental target has three pieces: a magneto-inertial fusion electrical discharge system (MIFEDS) structure, which imposes a magnetic field on the experiment; an experimental target, which is aligned inside the MIFEDS structure; and a proton backlighting capsule. For reference, the experimental target is 3 mm × 3 mm × 8 mm.

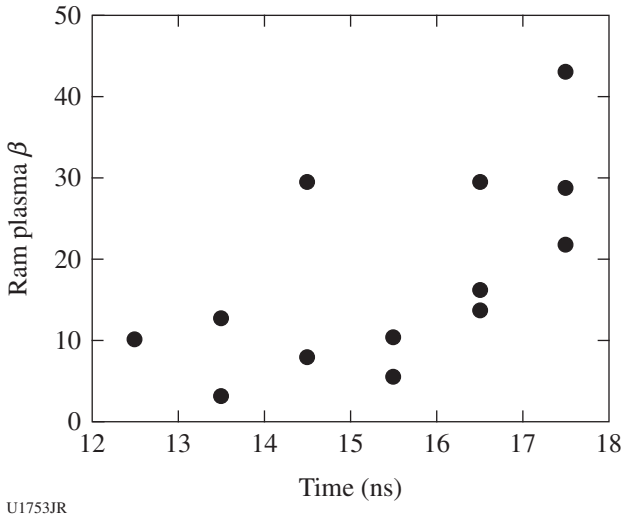


U1753JR

Figure 140.47
The plasma $\beta$ (ratio of ram pressure to magnetic pressure) for jets made by the method employed for Fig. 140.46. These data are from OMEGA shots in April 2012.

device and image the experiment with proton radiography to capture the magnetic distortion caused by the impact.

Previous experience with plasma jets generated in this fashion demonstrates that we have plasma $\beta \approx 5$ to 50, where $\beta$ is the ratio of ram pressure to magnetic pressure. This is similar (to an order of magnitude) to the plasma $\beta$ present on young stars with low magnetic fields. Figure 140.47 shows plasma $\beta$ versus time for a magnetic field of 7 T and plasma parameters from Thomson-scattering data from five shots in April 2012.

### *Structure of Molybdenum and Iron Oxide Under Dynamic Compression on OMEGA*

Principal Investigator: T. Duffy (Princeton)
Co-investigators: R. Smith and F. Coppari (LLNL); J. Wang and J. Wicks (Princeton); and T. R. Boehley (LLE)

During FY14, we carried out a series of experiments as part of our long-term effort to constrain the structure and properties of key materials of interest in geophysics and high-pressure science. This year we focused on molybdenum (Mo), a high-pressure standard material, and iron oxide, a key constituent of the deep mantle and core of terrestrial planets. The OMEGA laser was used to ramp or shock compress these materials to as high as 1 TPa of pressure, and the powder x-ray diffraction image plate (PXRDIP) diagnostic was used to record x-ray diffraction patterns. Active shock breakout (ASBO) was used to measure free surface and interface velocities from which pressure in the sample could be determined.

Molybdenum is an important body-centered-cubic (bcc) transition metal that has been extensively studied at high pressure but significant unanswered questions and discrepancies remain. The nature of the stable phase along the Hugoniot above 210 GPa is uncertain. There is also a large discrepancy between static and shock-wave experiments and theoretical calculations regarding the pressure at which Mo melts on the Hugoniot and the slope of the melting curve with pressure. In our experiments, Mo was shock compressed between 250 and 450 GPa. Between 250 to 380 GPa, we observed a diffraction peak consistent with the strong (110) reflection of bcc molybdenum. Other possible phases, such as the hexagonal-close-packed and face-centered-cubic structures, are not consistent with the observed diffraction pattern. Our results agree well with the most-recent sound velocity measurements and theoretical calculations for Mo and enable us to rule out a phase transition at 210 GPa. At 390 GPa, the diffraction pattern changes, with the strong, textured (110) peak replaced by a weak, untextured broad feature. This is consistent with partial melting of Mo beginning near 390 GPa. Our melting results are in agreement with theoretical calculations and demonstrate that the melting temperature of Mo increases strongly with pressure. This work shows that direct structural determinations by x-ray diffraction on dynamically compressed materials on OMEGA can provide key insights into material behavior along the Hugoniot.

Iron oxide (FeO) is an important material for modeling Earth and planetary interiors. Understanding its properties and measuring its equation of states at multi-megabar pressures are crucial to building reliable geophysical models. FeO shows a complex polymorphism below 200 GPa, and experimental data on its structure and density exist only up to 300 GPa. In our experimental campaigns on OMEGA, we ramp-compressed FeO from 350 to 750 GPa and measured the high-pressure polymorph in a totally unexplored pressure regime. The *d* spacings reported in Fig. 140.48 as a function of pressure show that the stable structure in this pressure regime is the B2 phase, which has never been measured experimentally to such a high pressure. These data will allow us to experimentally determine the stress–density relation for B2–FeO and its equation of state and will provide an experimental benchmark to theoretical simulations.

### *Dynamics of Magnetic-Reconnection Current Sheet in High-Energy-Density Plasmas*

Principal Investigator: W. Fox and A. Bhattacharjee (Princeton, Plasma Physics Laboratory)

Co-investigators: G. Fiksel, P. M. Nilson, S. X. Hu, and D. Haberberger (LLE)

We have developed and conducted experiments on OMEGA EP to study the phenomenon of magnetic reconnection. Magnetic reconnection occurs when regions of opposite directed magnetic fields in a plasma can interact and relax to a lower-energy state; it is an essential plasma physics process in many systems that governs the storage and explosive release of magnetic energy in systems such as the earth's magnetosphere, the solar corona, and magnetic-fusion devices. The energy liberated in this way can produce heat flows and enable the acceleration of a large number of particles to high energies.

These experiments on OMEGA EP used an externally applied magnetic field of the order of 12 T as the seed field for reconnection. With an externally applied field, the fields undergoing reconnection are under experimental control, so it is possible to conduct experiments with variable fields and topologies. In our first experiment, we conducted the "zero-field" case, in which the plumes can interpenetrate and drive the Weibel instability,[1] which is also very interesting as a mechanism to produce unmagnetized shocks in astrophysical blast waves.

We have now also successfully *magnetized* and collided the counterpropagating plasmas and observed reconnection of the fields as the plumes collided.[2] Figures 140.49(a)–140.49(d) shows a sequence of proton radiography images of the collision and interaction of the magnetized plasmas. The results are qualitatively different than the unmagnetized case and show the formation of a pair of magnetized "ribbons" propagating toward one another. These ribbons are regions of a deficit of protons to the film and indicate regions of strong magnetic field—magnetized plasma—which has steered the

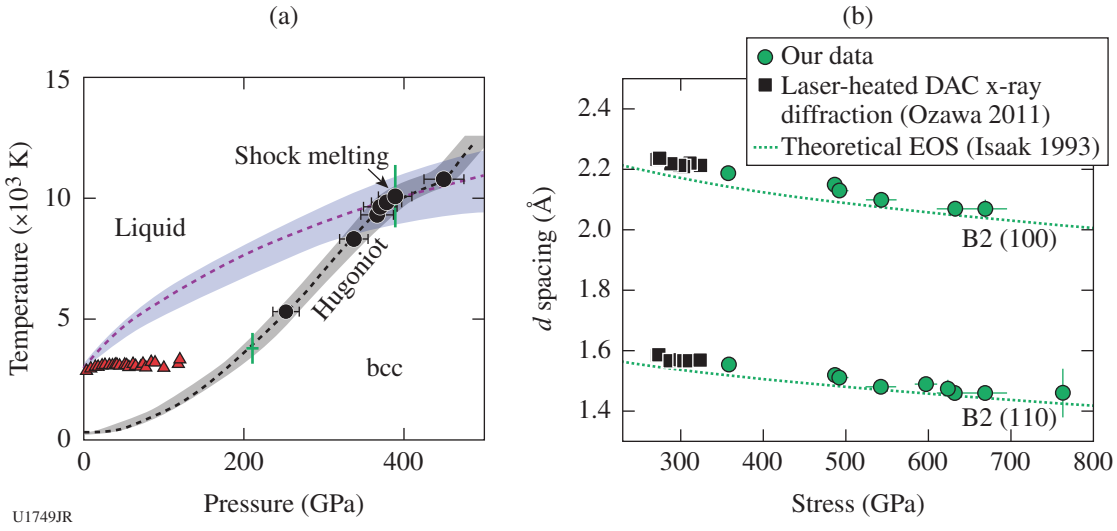


Figure 140.48

(a) Phase diagram of molybdenum (Mo). Black circles represent our experimentally measured shock pressures. The black and purple dashed lines show the calculated Hugoniot temperatures and melting curve for Mo. Our results are consistent with theoretical calculations that melting begins on the Hugoniot near 390 GPa and require a steeper melting curve than suggested from diamond anvil cell (DAC) data (red triangles). (b) Experimentally determined *d* spacings for FeO as a function of pressure as obtained in our ramp-compression experiments. Green circles represent our data, which are compared with static compression experiments (black squares) and theoretical simulations (green dotted lines). Our data show that the B2 phase of FeO is stable at least up to 750 GPa.

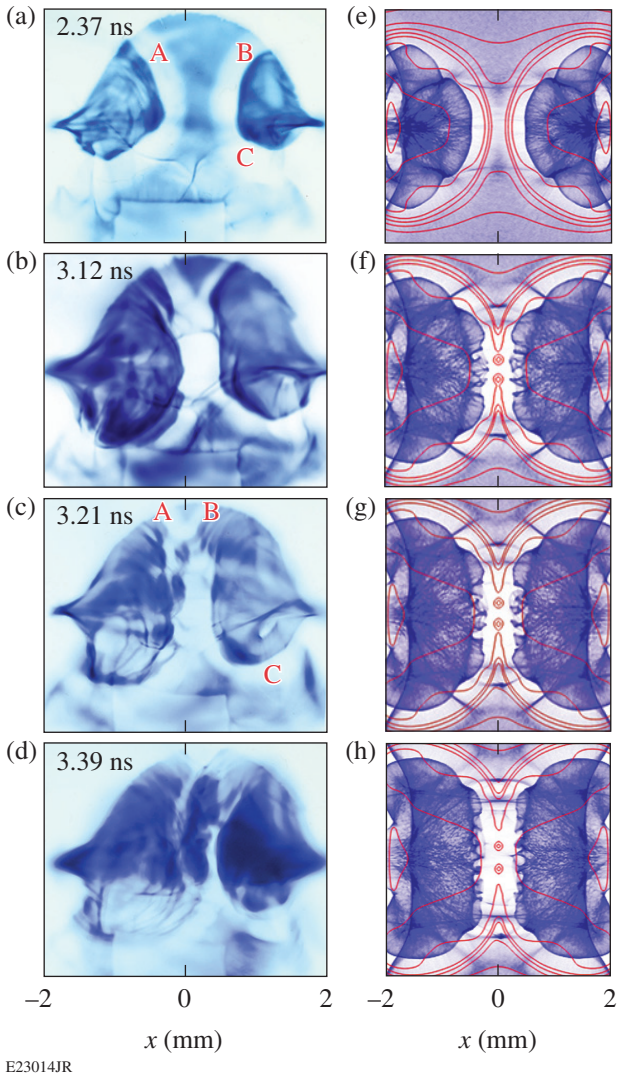


Figure 140.49
Proton radiography data and associated particle-in-cell simulations post-processed with a virtual proton radiography diagnostic for comparison. The white areas [(e)–(h)] indicate regions of strong magnetic fields (~30 T). As the two plumes expand and collide, the magnetic fields are brought together and reconnect. (From Ref. 1.)

diagnostic proton beam off-film. The successful formation of these pairs of ribbons is non-trivial: it was found that it was essential to add a third, "background" plasma source, triggered before the blowoff forms the two primary targets, to fill the experimental volume with a diffuse low-density plasma. In Fig. 140.49 a sequence of images from both the experiments and associated particle-in-cell simulations show the ribbons propagating toward one another and colliding at the midplane, generating bubble-like structures as the regions of oppositely magnetized plasmas interact and drive the reconnection of the magnetic fields.

Finally, in our most-recent results, we added the angular filter refractometry (AFR) diagnostic based on the new fourth-harmonic optical probe beam on OMEGA EP. This diagnostic measures density structures; in particular, transition bands occur in the image at specific values of the plasma density gradients (see Fig. 140.50 for an example). We are presently working to unfold these measurements to provide the plasma density in the reconnection region. Additionally, we observe very narrow AFR features that indicate steep density jumps at the edges of the plumes, coincident with where the magnetic fields are compressing, likely indicating formation of a shock. Similar features in the magnetic fields and density gradients are observed in our particle-in-cell simulations; we are investigating the specific mechanisms for shock formation.

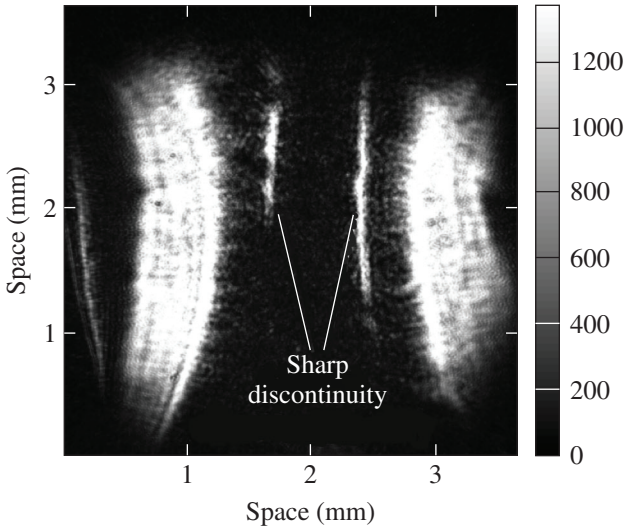


Figure 140.50
Angular filter refractomety image of two colliding magnetized plumes. The transition bands correspond to specific values of the plasma density gradient. A sharp density jump is formed at the edge of the plumes and coincident with the magnetic-field ribbons.

### *Astrophysical Dynamics in the Laboratory: Mach Stems and Magnetized Shock Waves*

Principal Investigator: P. Hartigan (Rice University)
Co-investigators: J. Foster and P. Rosen (AWE); C. Kuranz (University of Michigan); G. Fiksel (LLE); A. Frank (University of Rochester); B. Blue (General Atomics); A. Liao (Rice University); and P. Graham (AWE)

Supersonic flows are associated with a wide variety of astrophysical phenomena, including stellar winds, jets from young stars and black holes, and interacting binary systems; they are pervasive throughout both the interstellar and intergalactic

media. All of these types of objects have magnetic fields of sufficient strength to affect how the systems evolve dynamically. In the past year we have been using the MIFEDS system on OMEGA to explore different experimental designs with the goal of creating a platform that we can use to study strongly magnetized, high-Mach-number shock waves in a controlled laboratory environment.

While highly magnetized plasmas are the norm in most astrophysical contexts, the densities in the laboratory are much larger, so that when magnetic fields are compressed by strong shock fronts, the fields tend to diffuse out of the compressed material, which limits the effects that fields have on the flow dynamics. This problem can be particularly acute when magnetic fields are applied externally, for example, through the application of Helmholtz coils. One way to eliminate the problem of magnetic diffusion is simply to drive a supersonic flow into a wire that carries a strong current. With this type of setup, the current in the wire continues to generate the field, which can then be compressed by the supersonic flow.

Numerical simulations of this configuration are shown in Fig. 140.51. Using the MIFEDS coils on OMEGA, we are able to achieve a magnetic-field strength of ~20 T at the surface of the wire. The importance of this field dynamically is determined by the parameter $\sigma$, which is the ratio of the ram pressure $\rho v^2$ to the magnetic pressure $B^2/8\pi$. The simulations [Fig. 140.51(a)] show that the magnetic case should create a well-known morphology of a bow shock, where incident material is decelerated, and a magnetopause that defines the boundary of the compressed magnetic field around the wire. A plot [Fig. 140.51(b)] of the equilibrium position of the bow shock and magnetopause reveals that even when $\sigma$ is as large as ~50, the position of the bow shock in the magnetized case should be displaced by a measureable offset (~30 $\mu$m) compared with the nonmagnetic case.

Our first laser shots using this configuration were completed in mid-October 2014. In Fig. 140.52 we show the magnetic images (green) superposed upon the nonmagnetic ones (red). A clear offset exists between the bow shock in the two cases, in the sense that the magnetic field from the wire maintains the bow shock at a larger distance from the wire surface. We have also obtained streaked optical pyrometer data for each shot and will be analyzing these to better quantify how the velocities varied in the experiment. This work shows great promise for producing a platform with which we will be able to study supersonic magnetic phenomena.

### *Journey to the Center of Jupiter, Recreating Jupiter's Core on OMEGA*

Principal Investigator: R. Jeanloz (University of California, Berkeley)

Co-investigators: M. Millot (LLNL); and P. Loubeyre and S. Brygoo (CEA)

Our experimental documentation of $He/H_2$ phase separation, the insulator–metal transition in the vicinity of the predicted plasma phase transition (PPT), and the transport of dense hydrogen is significantly different from predictions by

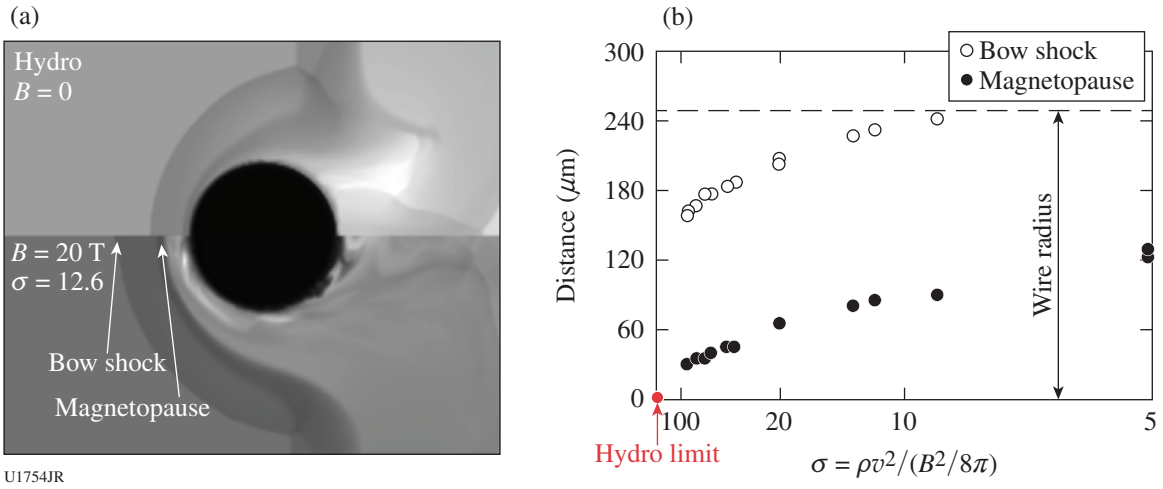


Figure 140.51

Numerical simulations of a supersonic flow moving past a current-carrying wire. (a) The flow is incident from the left and produces a bow shock and a magnetopause in the magnetic case (bottom half) as compared with the nonmagnetic case (top half). (b) Predicted offset of the bow shock (open circles) and magnetopause (solid circles) relative to the wire plotted as a function of the ratio $\sigma$ of the ram pressure and magnetic pressure at the wire surface. Even a relatively small field produces a measureable magnetosphere.[3]

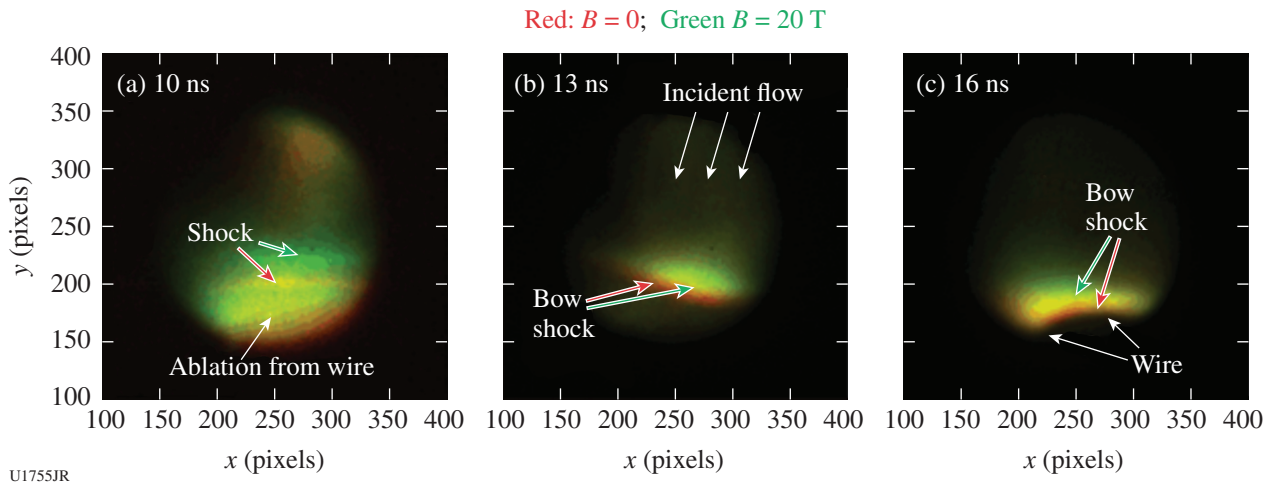


Figure 140.52
Optical images of the bow shock that forms around a wire. Left to right shows a time sequence of images as the flow moves from the top of the frame past the wire at the bottom. At early times there is significant ablation from the wire in response to irradiation from the laser drive. The color offset between the red and green shocks clearly demonstrates the effect of the magnetic field.

first-principles calculations. It also reveals the rich quantum nature of hydrogen up to tenfold compression and provides thermodynamic constraints on the hydrogen phase diagram that is otherwise based mainly on theory.

A few years ago, we launched a new capability to explore $H_2$, He, and $H_2/He$ mixtures at the Omega Laser Facility. The first step of our work was used to benchmark new techniques; produce new data to test structure and evolution models for Saturn and Jupiter; and extend the Hugoniot of hydrogen, deuterium, and helium as determined by several groups on different platforms: gas gun, *Z*, and lasers. Using diamond-anvil high-pressure cells (at room temperature) to tune the initial density of hydrogen to that of a cryogenic liquid, we established these techniques by comparing to previous data and validated our sample metrology, Hugoniot, reflectivity, and temperature measurements. The second step has been to significantly extend the Hugoniot, temperature, and transport measurements off the principal Hugoniot by changing the precompression of the sample.

We have now collected shock data with precompressed samples at initial pressures in the range 0.15 GPa to 9 GPa, (0.7 to 4× the cryogenic fluid density), giving access to a broad new range of warm-dense-matter conditions for hydrogen and helium systems (Fig. 140.53). This led to several significant discoveries: (a) the maximum compression of the Hugoniot depends strongly on initial density, which provides a stringent test of existing equation-of-state models, and allows for the determination of several derivatives such as the specific heat, Grüneisen coefficient, adiabatic exponent, thermal coefficient of expansion, etc.;[4] (b) the reflectivity of hydrogen changes abruptly in the vicinity of the predicted plasma phase transition, with this transition from electrically insulating to conducting states appearing related to the recently observed maximum in the melting curve; and (c) the electrical conductivity of hydrogen deduced from reflectivity data differs from values predicted with current models at the highest densities examined.

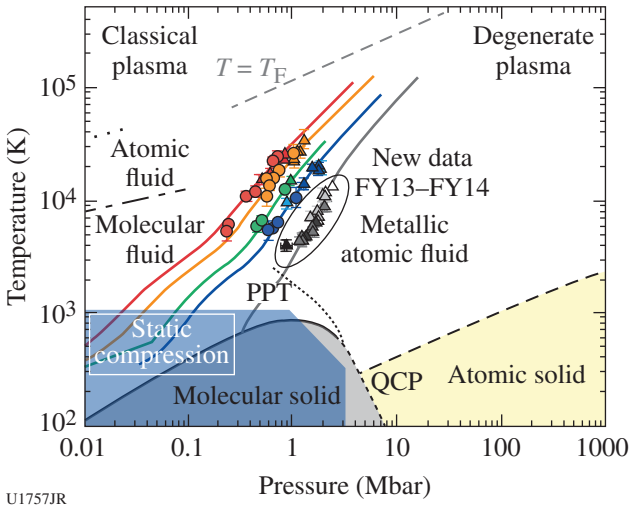


Figure 140.53
Pressure–temperature phase diagram of hydrogen with new data (gray and black symbols) at 6-GPa precompression together with lower precompression data (symbols) and predictions from density functional molecular dynamics (DFT-MD) numerical simulations. New data at 9-GPa precompression are being analyzed (not shown). PPT: plasma phase transition; QCP: quantum critical point.

### *Magnetic-Reconnection Experiments in Laser-Driven, High-Energy-Density Plasmas*

Principal Investigator: H. Ji (Princeton)

In FY14, the team led by Princeton University carried out experiments on magnetically driven reconnection in laser-driven high-energy-density (HED) plasmas using a novel magnetic-field–generation technique. A schematic of the experimental setup on OMEGA EP is shown in Fig. 140.54. The main interaction target is comprised of two parallel copper plates, connected with two copper wires. Two OMEGA EP 2.5-kJ, 1-ns laser pulses pass through the laser entrance holes on the front plate and are focused on the back foil, generating a beam of superthermal hot electrons. The hot electrons stream onto the front plate and build up an electrical potential between the plates. This, in turn, drives large currents in both wires and creates magnetic reconnection because anti-parallel magnetic-field lines exist in the middle plane. Ultrafast proton radiography was utilized to probe the reconnection process at various times with high spatial and temporal resolutions. To characterize the magnetic-field generation around the wire, targets with double plates connected with a single wire were also used.

The experiments successfully demonstrate a large external field source on OMEGA EP and provide a solid platform toward realizing magnetic reconnection in magnetically driven HED systems. Figure 140.55 shows the experimental results. Figure 140.55(a) is an example proton image for the single-wire case, taken at $t = t_0 + 3.101$ ns for 20-MeV protons, where $t_0$ is the arrival time of the long-pulse drive beams at the copper foil surface. The image is high quality, showing the location of the copper plate and the wire. In particular, a light bubble is formed when incident protons are deflected by the azimuthal magnetic field around the wire. The results show ~500-T magnetic fields at a distance of 40 $\mu$m from the wire surface. Energetically, the generated magnetic energy by the coil is of the order of 1% of the total energy of two incidental lasers. Figure 140.55(b) shows an example proton image for the two-wire case, taken at $t = t_0 + 4.088$ ns for 20-MeV protons. Besides the features of copper plate and copper wire, two light bubbles and a jet-like feature in the center are observed. Detailed analysis on the cause of the jet is underway.

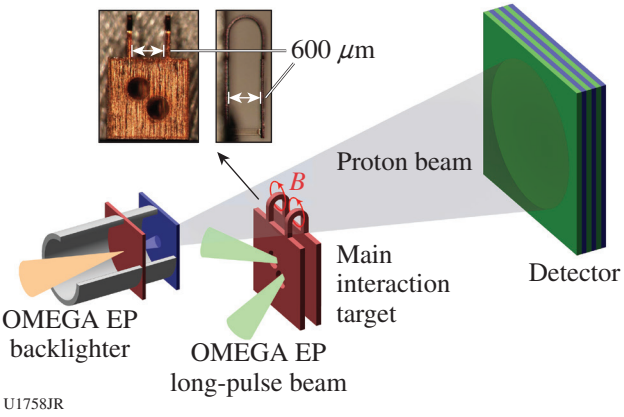


Figure 140.54
Experimental setup for the recent reconnection experiments on OMEGA EP based on a novel field-generation technique. The main target is comprised of two copper plates connected with two wires. Target parameters are well characterized before the experiment. Two OMEGA EP long-pulse beams pass through the holes on the first plate to reach the second plate, where hot electrons are released to charge up the first plate and form electric currents through the coils. Energetic protons generated by the OMEGA EP short-pulse beam are used to probe the reconnection process.

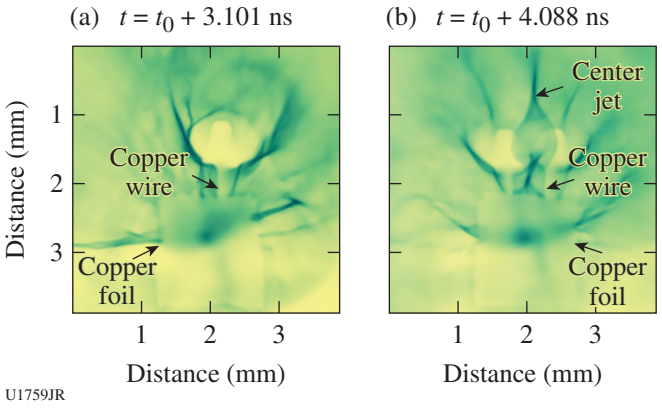


Figure 140.55
(a) A proton radiograph of a single-wire case where the light bubble is caused by magnetic fields around the wire deflecting incident protons. (b) A proton image for the two-wire case.

### *Studies of High-Energy-Density Plasmas, Inertial Confinement Fusion Implosions, and Nuclear Science for Astrophysics*

Principal Investigators: R. D. Petrasso and C. K. Li (MIT)
Co-investigators: F. H. Séguin, J. A. Frenje, and M. Gatu Johnson (MIT); T. C. Sangster, V. Yu. Glebov, D. D. Meyerhofer, and R. Betti (LLE); and O. L. Landen (LLNL)

MIT work in FY14 included a wide range of experiments applying proton radiography, charged-particle spectrometry, and neutron-spectrometry methods developed by MIT and collaborators to the study of high-energy-density physics (HEDP) and inertial confinement fusion (ICF) plasmas. In FY14 eight papers,[5–12] one MIT Ph.D. thesis,[13] one MIT M.Sc. thesis,[14]

and one MIT senior thesis[15] about NLUF-related research were published; there were also many invited and contributed talks presented at conferences. Two additional papers have been submitted for publication.[16,17] The students also won numerous awards, including the 2014 *Marshall N. Rosenbluth Outstanding Doctoral Thesis Award*, given to Dr. M. Manuel for NLUF work.[18–20] This award has never before been given for HEDP research. In addition, recent Ph.D. M. Rosenberg has accepted a position at LLE.

Among recent publications are two Physical Review Letters[5,6] by MIT students who presented analyses of OMEGA data, shedding new light on the important topic of kinetic/multi-ion effects in plasmas. Most ICF simulations are carried out with single average-ion, radiation–hydrodynamic codes, but we now know that deviations from hydrodynamic conditions are prevalent during the early stages of implosions when strongly shocked, low-density plasmas are affected by kinetic physics related to long ion mean free paths. Reference 5 discusses a series of NLUF experiments on OMEGA that provide clear evidence of a transition from hydrodynamic-like to strongly kinetic behavior in shock-driven ICF implosions as the initial equimolar D$^3$He gas density was decreased (illustrated in Fig. 140.56). References 6 and 7 discuss OMEGA experiments that lead to the first kinetic mix mechanisms in shock-driven ICF implosions; an important aspect of these data is illustrated in Fig. 140.57. These results are very important for testing non-benchmarked ion diffusion models and codes that have recently been developed for high-energy-density (HED) plasmas.

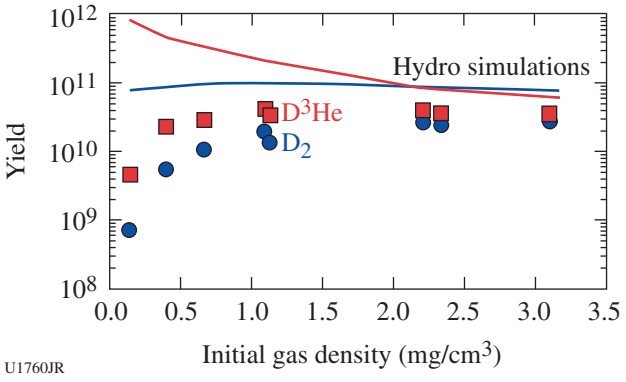


Figure 140.56
Comparison of measured (markers) and 2-D hydrocode-simulated (lines) D–D (blue) and D–$^3$He (red) yields as a function of initial D$^3$He gas density in shock-driven implosions on OMEGA. As the initial gas density decreases, plasma conditions become increasingly "kinetic" and the measured yields strongly deviate from hydrodynamic predictions. Ion kinetic effects—the escape of ions out of the hot-plasma region and the reduction in fusion reactivity caused by the depletion of high-energy-tail ions—are responsible for this trend. (This figure is from Ref. 5.)

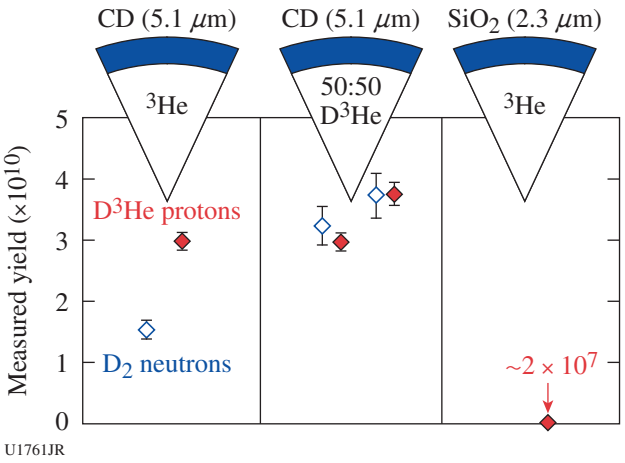


Figure 140.57
Measured D–$^3$He yields (solid red) from 30-kJ OMEGA implosions of CD shells filled with $^3$He gas are similar to D–$^3$He yields from implosions of CD shells filled with 50:50 D$^3$He gas. Implosions of glass shells filled with $^3$He gas produce yields that are three orders of magnitude lower, ruling out D$_2$ contamination of the gas as an explanation for this result. The observed D–$^3$He yields require the amount of shell deuterium mixed into the $^3$He gas to be ~10% of the $^3$He gas density. Ion diffusion is one mechanism that can generate such levels of mix in shock-driven implosions. (This figure is from Ref. 6.)

Another publication in Physical Review Letters[10] describes how monoenergetic proton radiography[21] was used on OMEGA (as illustrated in Fig. 140.58) for the first observations of the structures, dynamics, and self-generated fields of pairs of laser-generated, high-Mach-number plasma jets that collide at various angles. Proton radiography has great sensitivity to fields, unlike x ray or other optical diagnostics.[22] The observed self-generated magnetic fields, largely azimuthal around the colliding jets and generated by the well-known $\nabla T_e \times \nabla n_e$ Biermann battery effect near the periphery of the laser spots, were demonstrated to be "frozen in" the plasma and advected along the jet streamlines of the electron flow. For comparison to the proton radiographs, Fig. 140.58 shows electron flow streamlines predicted by an analytic model[23] and a plasma simulation using the 2-D hydrodynamic code *DRACO*[24] for the 180° collision case. The radiographs of collisions of noncollinear jets are relevant, for example, to the asymmetric structures and dynamics of the collisions in jet-driven, differentially rotating quasi-planar disk associated with accretion disks and outflows in astrophysics.

Results of other recent NLUF work will soon be submitted for publication. Topics will include implementation of a new

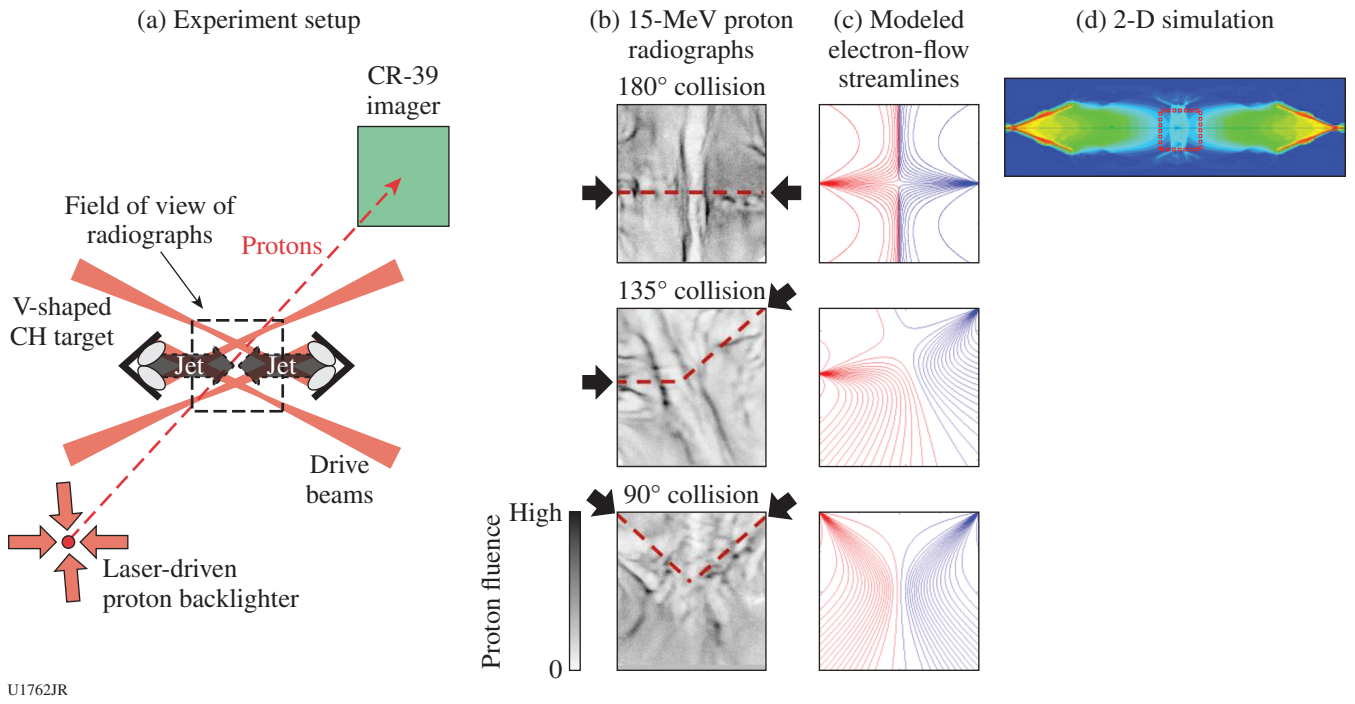


Figure 140.58
(a) A proton radiography setup on OMEGA and (b) recorded images of plasma jets colliding at various angles. (c) The images are compared to an analytic model of electron-flow streamlines and (d) to a 2-D *DRACO* simulation of the head-on collision case. The backlighter ($D^3He$-gas–filled, thin-glass-shell capsule imploded by 30 OMEGA laser beams and producing 3- and 14.7-MeV protons) was positioned 1 cm from the jet collision region. Each jet was formed by the collision of two plasma bubbles generated by laser beams incident on a V-shaped target (a). The angle between the two jets, determined by the positions of the two V-shaped targets, was either 180° (head-on), 135°, or 90°, as seen in the radiographs (b). The relative timing between backlighter and V-shaped–target drive was adjusted to sample the jets' propagation and collision at 4.7 ns from the onset of the drive on the V-shaped targets. (These results are from Ref. 12.)

multiple particle temporal diagnostic (multi-PTD) for probing kinetic and multi-ion-fluid effects; charged-particle stopping in weakly to moderately coupled plasmas; ion–electron equilibration in plasmas; hohlraum physics; nuclear reactions relevant to stellar and big-bang nucleosynthesis, and new work on magnetic reconnection.

***Dynamics of High-Energy Proton-Beam Focusing and Transition into Solid Targets of Different Materials***

Principal Investigator: B. Qiao (University of California, San Diego)

Co-investigators: C. McGuffey, J. Kim, and F. N. Beg (University of California, San Diego); M. S. Wei, P. Fitzsimmons, M. Evans, and R. B. Stephens (General Atomics); J. Fuchs and S. N. Chen (LULI, France); P. M. Nilson, D. Canning, and D. Mastrosimone (LLE); and M. E. Foord and H. S. McLean (LLNL)

The Proton Dynamics NLUF project, led by the University of California, San Diego, studied proton generation in the regime of a kilojoule, multipicosecond (multi-ps) laser driver. High-current applications, such as proton fast ignition, may prefer this regime, but the focusing and transport of such high-current beams in materials have not been explored. A curved chemical vapor deposition (CVD) diamond target was shot with an OMEGA EP backlighter (BL) (1250 J in 10 ps) to focus protons into a Cu foil. Al (13-$\mu$m) or Ag (7-$\mu$m) transport layers were deposited on the front side of the Cu foil to investigate the material's dependence on transport of the intense proton beam.

The Cu $K_\alpha$ (8.048-keV) emission was imaged with the spherical crystal imager (SCI), as shown in Figs. 140.59(d)–140.59(f) for three target types [Figs. 140.59(a)–140.59(c)]. For the case of freestanding, separated foils, the Cu $K_\alpha$ signal was weak and diffuse over the entire Cu foil. This confirmed that the inherently diverging electron beam from the interaction contributed minimally to the Cu $K_\alpha$ signal at this standoff distance. For the case in which the gap was filled by a wedged structure [Fig. 140.59(b)], however, the signal was increased on the wedge center plane [Fig. 140.59(e)]. The emission is

greatest in the center, not at the edges of the wedge connection vertices, and no signal enhancement is observed in the region directly in contact with the wedge walls. This suggests that the signal is caused by *focused*, free-streaming particles within the vacuum gap rather than particles transporting through the wedge. For the case with a cone filling the gap [Figs. 140.59(c) and 140.59(f)], the effect was even clearer, with an 8× higher peak signal than the freestanding case. Cu $K_\alpha$ yields are plotted in Fig. 140.59(g). These data indicate beam focusing in one dimension by the wedge and in two dimensions by the cone. This focusing effect has been studied in detail by our group using a subpicosecond laser[25] and particle-in-cell simulations,[26] *while this result demonstrates that structures are still effective for focusing in the kilojoule, multipicosecond regime*.

Two-dimensional particle-in-cell simulations are underway to further study the accelerating and focusing dynamics relevant to the OMEGA EP experiment. Two cases are being run: the freestanding target case and a conical enclosure case. In the freestanding case, protons are initially focused because of the curvature of the target; however, a significant fraction of them diverge away. In the case with the cone, a strong focusing field is observed to persist along the cone's inner surface [Fig. 140.59(h)] with a strength comparable to the focusing field from the curved target, which confines the protons and increases their density. These simulations will continue to run for at least 30 ps as the protons continue to move. A diagnostic plane at the end of the cone collects individual particle information, including energy, which will be used to calculate the predicted Cu $K_\alpha$ yield from both electrons and protons for comparison to the experiment.

The proton and ion spectra were also measured continuously for energies down to 0.4 MeV, using a Thomson parabola spectrometer (TPIE) in-line with the axis of the curved target. In Fig. 140.60, the source spectrum from the curved foil is shown in black. This spectrum is in agreement with previous measurements using radiochromic film (RCF).[27] The cone cases (red)

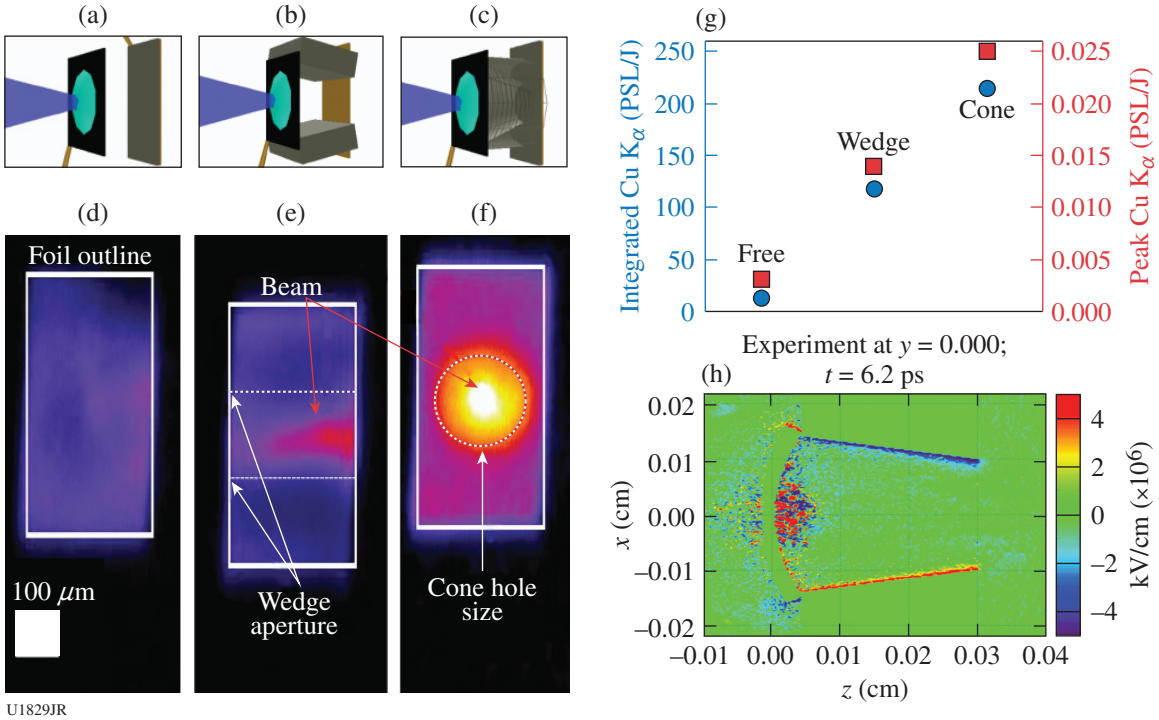


Figure 140.59
[(a)–(c)] Three target types used in the OMEGA EP experiment show heating by a focused beam as indicated by [(d)–(f)] the emission profiles of 8.048-keV Cu $K_\alpha$. (g) Comparison of the signals shows that the total Cu $K_\alpha$ yield increased for the targets with structure, indicating a highly diverge source from the free case. The cone focused the beam, resulting in a 100-$\mu$m FWHM emission region. (h) Large-scale plasma suite (*LSP*) code simulation plot of the transverse electric field $E_x$ at time $t$ = 6.2 ps for a cone target.

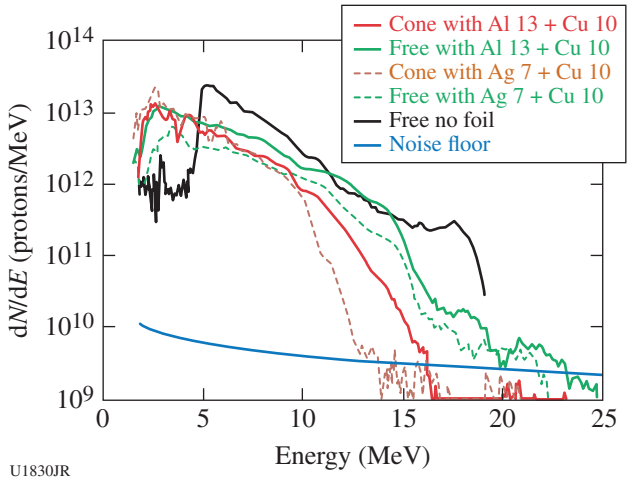


Figure 140.60
The absolute proton spectra measured with a Thomson parabola without the metals (black) and transmitted through two metals for both target types.

showed spectra similar to the free cases (green) except above 10 MeV. This is in agreement with our understanding of electron escape from the target: electrons that escape the target into the cone create an accelerating sheath that is quickly dampened, reducing the highest energy gained but not reducing the charge.

The peak beam current is estimated to be $4 \times 10^9$ A/cm$^2$, 300 $\mu$m behind the curved target, based on the recorded spectrum, assumed beam duration of 10 ps, and SCI emission region of 100-$\mu$m full width at half maximum. This density is sufficient to heat the metal foils locally to a warm dense matter, which models predict can cause self-modified beam transport. Our particle-in-cell codes predict that the stopping range can be measurably changed as beam densities increase from $10^9$ to $10^{10}$ A/cm$^2$, but thicker transport layers may be necessary.

### *Magnetic Shock*

Principal Investigators: A. Spitkovsky (Princeton) and C. Huntington (LLNL)

The FY14 joint MagShock Campaigns (4 February and 18 August 2014) used the OMEGA laser to drive counter-propagating, colliding plasma flows to study their interaction. Characterization of the plasma conditions in this system on previous experiments provided a ready platform to investigate the electromagnetic-field structure generated during the flow interaction. The MagShock Campaigns studied the flow dynamics as the plasma interacts with a 10-T magnetic field supplied by the magneto-inertial fusion electrical discharge system (MIFEDS). The physics of this OMEGA experiment are analogous to many astrophysical phenomena, including the dynamics of supernova ejecta streaming through a magnetized cosmic background plasma or interacting with magnetized star clusters.

The campaigns focused on proton radiography, interleaving shots where protons were generated via either target-normal sheath acceleration (TNSA) using an OMEGA EP beam or laser compression of a D$^3$He-filled capsule. The quasi-monoenergetic 14.7-MeV protons from the capsules were particularly effective at imaging the field structure, as seen in Fig. 140.61. The long, narrow filaments stretched along the direction of plasma flow are consistent with the Weibel instability. Also persistent in the images are horizontal "plates"—a signature of magnetic Biermann-battery fields advected from the target surface to the imaging field of view. These results are currently under review in a manuscript titled "Observation of Magnetic-Field Generation Via the Weibel Instability in Interpenetrating Plasma Flows."

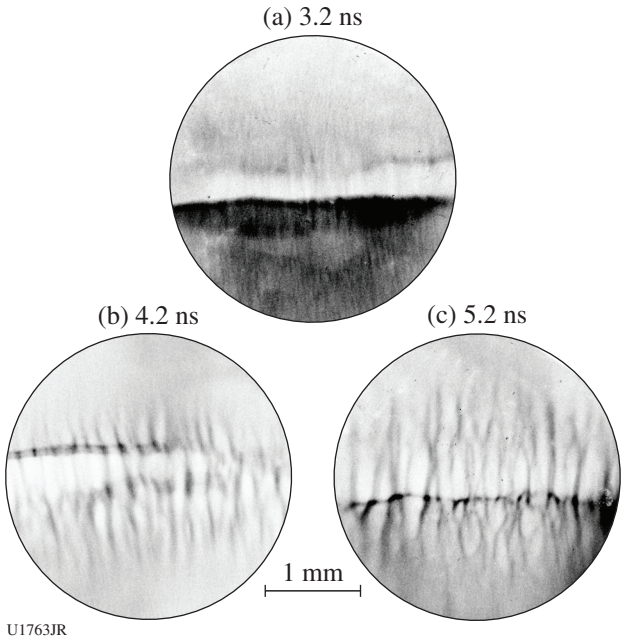


Figure 140.61
A time sequence of proton radiographs, each produced by the etching of a CR39 nuclear track detector to reveal the flux of 14.7-MeV protons. In each case, plasma flows enter from the top and bottom of the frame and interact near the mid-plane of the image. Strong filament growth occurs between 3 and 4 ns, consistent with the Weibel instability. The top–bottom asymmetry in the proton flux at early time will be investigated further in future experiments.

On OMEGA EP (EP-MagShock-14A in November 2013) we succeeded in porting our MIFEDS configuration to OMEGA EP utilizing the OMEGA EP MIFEDS system. This allows for increased experimental efficiency since we can use only one laser system to have both the magnetic fields and proton diagnostics. On OMEGA EP-MagShock-14A we tried a different magnetic configuration using a Helmholz coil. It provided a magnetic field (7 T on axis) along the direction of the flow, unlike our previous work where the field was orthogonal to the flow. While overall the plate-filament structure was not significantly affected by the applied field, plasma did get onto the magnetic-field lines and new features in the proton image were detected. In Fig. 140.62 we show (a) the experimental configuration of this day along with two proton images taken at 4 ns for shots (b) without a $B$ field and (c) with $B$ field parallel to the flow. The Biermann plates are clearly visible, although they are tilted in these experiments likely because additional plasma was ablated off of the MIFEDS stalk by reflected laser light. The differences induced by the $B$ field are highlighted with a blue arrow [Fig. 140.62(c)]. We notice new wispy proton caustics indicating field enhancement on plasma-loaded field lines that undergo sideways expansion. This experiment suggests that we can produce magnetized plasma, if plasma is loaded along the magnetic field, and points to the way forward to generate magnetized shocks in the laboratory.

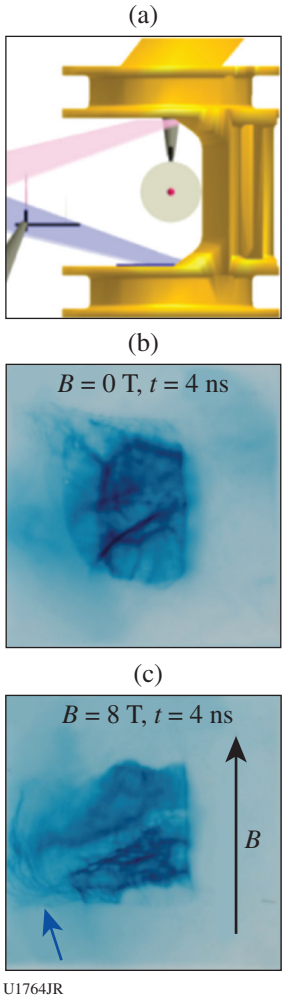


Figure 140.62
Experiments with the external field parallel to the flow direction (EP-MagShock-14A). (a) View of the experimental setup from the direction of proton film; (b) proton image without external field at $t = 4$ ns; and (c) proton image with external field. Note the blowout area indicated by the blue arrow.

### *Study of Relativistic Laser–Plasma Interaction and Fast-Electron Beam Dynamics Using the 10-ps High-Contrast OMEGA EP Laser with a Controlled Pre-Plasma*

Principal Investigators: M. S. Wei and R. B. Stephens (General Atomics)
Co-investigators: C. McGuffey, B. Qiao, and F. N. Beg (University of California, San Diego); A. Link and H. S. McLean (LLNL); W. Theobald, D. Haberberger, and A. Davies (LLE); and Y. Sentoku (University of Nevada, Reno)
Lead graduate student: J. Peebles (University of California, San Diego)

Efficient conversion of high-intensity laser energy to fast electrons and their subsequent transport are fundamental to high-energy-density (HED) science, which has many potential applications such as fast-ignition (FI) laser fusion, warm dense matter by isochoric heating, and a short-pulse, bright x-ray source. The energy coupling is controlled by the laser–plasma interaction (LPI) dynamics, which strongly depends on laser-intensity distribution and the plasma density scale length at the LPI interface as well as the dynamic response of the transport material. In our previous experiments using the high-intensity, high-energy (up to 1.5 kJ) OMEGA EP laser with low-contrast pulses, we observed electron beams dynamically evolved from a single diffuse spot in subpicosecond interaction into multiple angularly separated electron filaments over a 10-ps interaction.[28] Particle-in-cell simulations suggest that high-intensity laser beams undergo filamentation, hole-boring, and hosing instabilities over multiple picoseconds in the preformed plasma created by the intrinsic nanosecond pedestal prepulse, leading to the observed electron filaments.[29] The objectives of this General Atomics NLUF project is to further investigate the LPI dynamics and fast-electron transport dependence on pre-plasma, pulse duration, and target material using the high-contrast OMEGA EP laser. In our FY13 NLUF experiments we showed that the high-contrast OMEGA EP laser produces a more-confined electron beam, leading to an improved energy coupling to the target.[30]

In the FY14 NLUF experiment, we focused on the investigation of the pre-plasma effect on relativistic LPI and the resultant fast-electron beam dynamics by systematically varying pre-plasma scale length using a separate UV beam prior to the high-intensity OMEGA EP pulse. For this study, we used the identical multilayered planar foil targets composed of an Al substrate with a Cu x-ray tracer layer buried ~125 $\mu$m below the front surface and a large, 2-mm × 2-mm, 1-mm-thick conductive carbon layer at the back to minimize refluxing, similar to that used in previous experiments. A low-energy UV beam (20 J, 1-ns pulse duration) was focused onto the target's front surface with a large focal spot using a 750-$\mu$m distributed phase plate to produce pre-plasma. The 10-ps, high-energy (up to 1250 J), high-intensity ($3 \times 10^{19}$ W/cm$^2$) OMEGA EP pulse was normally incident onto the target with several timing delays, i.e., 0.2, 0.5, 0.7, and 1.0 ns, with respect to the beginning of the UV beam. For comparison, shots were also taken without the UV beam–produced pre-plasma. A 2-D radiation–hydrodynamics simulation using the *HYDRA* code suggested that the scale length of the preformed plasmas was about 14, 40, 80, and 110 $\mu$m, respectively, for the corresponding OMEGA EP beam-delay times mentioned above. The intrinsic prepulse (1 mJ, 3-ns duration)–produced pre-plasma had a scale length of ~4 $\mu$m. Fast electrons were characterized by measuring their induced Cu $K_\alpha$ fluorescence spot with a spherical crystal imager (SCI) and the total $K_\alpha$ yield by a calibrated x-ray spectrometer using a curved highly oriented pyrolytic graphite (HOPG) crystal (ZVH). A fast-electron–induced, high-energy bremsstrahlung spectrum was monitored by two fixed-port bremsstrahlung MeV x-ray spectrometers (BMXS's). A magnetic spectrometer was also fielded along the axis of the OMEGA EP beam to monitor the escaped fast-electron energy spectrum. In addition, an angular filter refractometer (AFR) with a short-pulse (10-ps), 4$\omega$ optical probe was used to characterize a pre-plasma electron density profile. A proton probe was also utilized to map electromagnetic fields and structures in relativistic LPI's.

As shown in Fig. 140.63(a), the fast-electron temperature inferred from the measured bremsstrahlung radiation spectrum decreases with increasing pre-plasma scale length. It drops from ~3 MeV with the intrinsic prepulse produced pre-plasma (scale length of $L$ = 4 $\mu$m) to ~1.2 MeV with the UV beam–produced large pre-plasma ($L$ = 110 $\mu$m). Compared with the intrinsic prepulse case, the measured 2-D SCI Cu $K_\alpha$ images indicate that the fast-electron beam significantly spreads out when relativistic LPI occurrs in a large-scale-length pre-

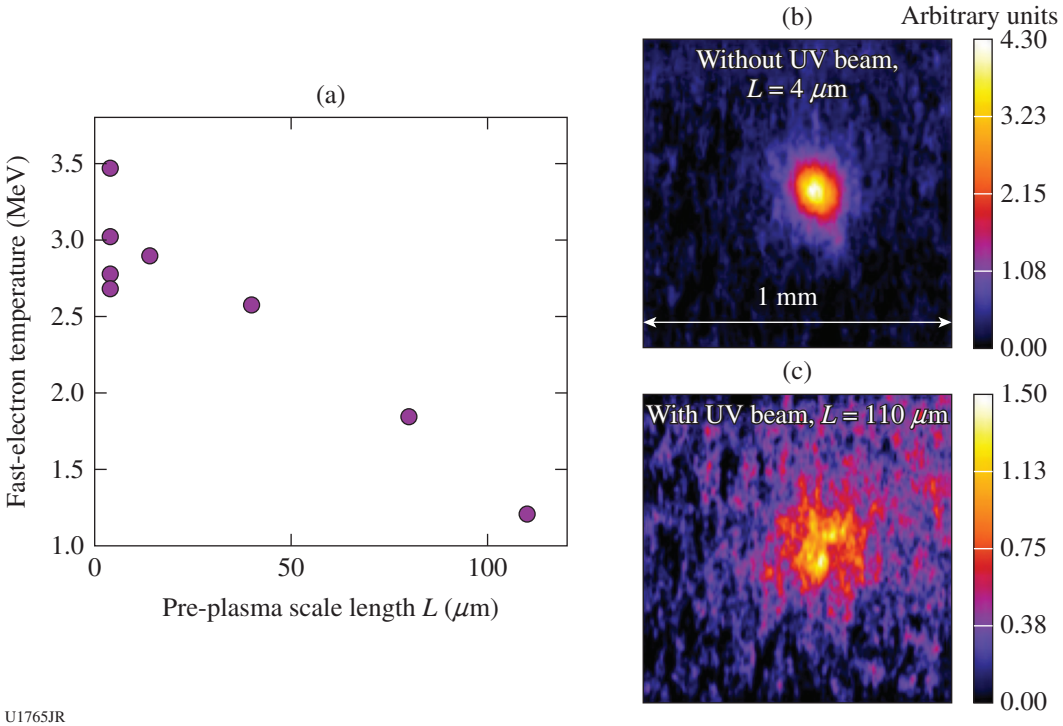


Figure 140.63
(a) The inferred hot-electron temperature from the measured bremsstrahlung x-ray spectrum as a function of the preformed plasma density scale length. (b) The measured 2-D Cu $K_\alpha$ spot from the 10-ps relativistic interaction without the UV beam and (c) with the UV beam-produced pre-plasma.

plasma. The measured $R_{50}$ spot size is nearly doubled for the $L$ = 110-$\mu$m pre-plasma case [Fig. 140.63(c)] compared to the intrinsic pre-plasma case [Fig. 140.63(b)], i.e., 266 $\mu$m versus 136 $\mu$m, where $R_{50}$ is the radius of the spot that contains 50% of the total $K_\alpha$ yield. We also note that there was 2.3× less energy within the center spot with a radius of 125 $\mu$m for the $L$ = 110-$\mu$m case compared to the intrinsic pre-plasma case.

High-resolution proton probing images of electromagnetic fields that result from relativistic LPI have revealed strong nonlinear phenomena when interactions occurred in large preformed plasmas. Figure 140.64 shows the observed field structures during the high-intensity OMEGA EP laser interaction with an $L$ = 40-$\mu$m-scale-length pre-plasma. Multiple channels and bubbles can be clearly seen. Such phenomena were not observed with the intrinsic pre-plasma case. Instead, a planar sheath (not shown here) was seen expanding backward with a high velocity (30% of the speed of light) from the target's front surface.

In summary, the FY14 General Atomics–led NLUF experiment has been successfully performed to further investigate the effect of preformed plasma in a controlled way with added diagnostics. Strong nonlinear interaction phenomena such as channel and bubbles were directly observed during relativistic LPI in large preformed plasmas. This led to a significant spread of the fast-electron beam and the reduced fast-electron temperature observed on the solid targets. Detail data and PIC modeling is underway.

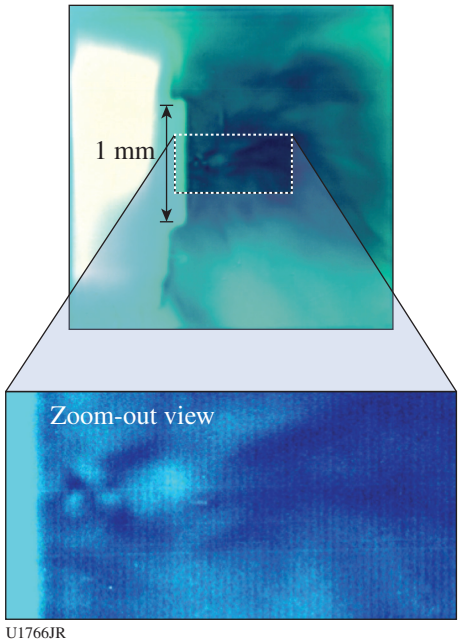


Figure 140.64
Proton probing images (false color) of electromagnetic-field structures during nonlinear relativistic laser–plasma interaction with a UV beam-produced large pre-plasma ($L$ = 40 $\mu$m). Channels and bubbles are clearly visible.

**FY14 Laboratory Basic Science (LBS) Program**

In FY14, LLE issued a solicitation for LBS proposals to be conducted in FY15. A total of 25 proposals were submitted. An independent review committee reviewed and ranked the proposals; on the basis of these scores, 14 proposals were allocated 20 shot days at the Omega Laser Facility in FY15. Table 140.VI lists the approved FY15 LBS proposals.

Seventeen approved LBS projects were allotted Omega Facility shot time and conducted a total of 269 target shots at the facility in FY14 (see Table 140.VII). This work is summarized in this section.

***Search for Nuclear Excitation by Electron Capture in Osmium and Thulium***

Principal Investigator: L. Bernstein (LLNL)
Shot Principal Investigator: R. F. Heeter (LLNL)
Co-investigators: D. Bleuel, J. Emig, and S. Ross (LLNL); M. Comet, V. Meot, F. Phillippe, and C. Reverdin (CEA)

Nuclear excitation by electron capture (NEEC) is an exotic process that has never been observed in the laboratory, but in stellar plasmas it is thought to populate low-lying nuclear excited states and may modify neutron capture and other astrophysical rates. In laser-driven plasmas created on ~1-ns time scales, NEEC may be observed through gamma decays re-emitted on ~5-ns time scales, after the plasma has cooled and x-ray emission is negligible. Earlier experiments searched for 8.41-keV NEEC in $^{169}$Tm hohlraums (made from rolled thulium foil), using erbium as a null comparison, and found an ambiguous signature.

The FY14 experiments revisited these measurements and also searched for 9.76-keV NEEC decay emission in isotopically pure $^{187}$Os-lined Ti hohlraums, with $^{192}$Os as a null comparison. Ti was chosen because it could be electroplated with $^{187}$Os, while not providing any x-ray contamination in the NEEC spectral band. The hohlraums were 0.6 mm in diameter and were driven at 10 kJ in 1 ns using 20 beams of the 60-beam OMEGA.

In the experiments, optical Thomson-scattering data obtained 300 $\mu$m outside the cavity laser entrance hole showed electron temperatures of ~4.3 keV and densities ~$4 \times 10^{20}$/cm$^3$. A suite of time-integrated and time-resolved x-ray spectra were obtained

Table 140.VI: LBS proposals approved for shots in FY15.

| Principal Investigator | Affiliation | Title | OMEGA shot days allocated | OMEGA EP shot days allocated | Joint shot days** |
|---|---|---|---|---|---|
| R. Smith | LLNL | X-Ray Diffraction Study to Map Out Pressure–Temperature Phase Space in a Key Planetary Mineral: MgO | 2 | 0 | 0 |
| G. Fiksel | LLE | Detailed Study of Magnetic Fields During Magnetic Reconnection in High-Energy-Density Plasma | 0 | 1 | 0 |
| R. Betti | LLE | Ultra-Strong Spherical Shock for High-Energy-Density Physics Studies | 2 | 0 | 0 |
| D. E. Fratanduono | LLNL | Exploring Earth's Lower Mantle | 1 | 0 | 0 |
| M. Beckwith | LLNL | EXAFS Study of Iron Melting Temperature at Earth's Core Conditions | 2 | 0 | 0 |
| H.-S. Park | LLNL | Weibel Instabilities and Astrophysical Collisionless Shocks from Laser-Produced Plasmas | 2 | 0 | 0 |
| W. Theobald | LLE | Integrated Channeling for Fast Ignition | 1 | 1 | 1 |
| H. Chen | LLNL | Demonstration of a Relativistic Electron–Positron Pair Plasma | 0 | 2 | 0 |
| J. R. Davies | LLE | Laser-Driven Adiabatic Compression of Magnetized Plasma | 1 | 0 | 0 |
| C. Stoeckl | LLE | Spectroscopy of Neutrons Generated Through Nuclear Reactions with Light Ions in Short-Pulse Laser Interaction Experiments | 0 | 1 | 0 |
| A. Pak | LLNL | Phase Separation of Hydrocarbons at High Pressure | 0 | 1 | 0 |
| C. Wehrenberg | LLNL | Flow Stress and Deformation Mechanisms for Plasticity in Shock-Compressed Vanadium | 0 | 1 | 0 |
| C. J. Forrest | LLE | Studies of the Deuteron Break-up Reaction at 14 MeV Using High-Energy-Density Plasmas (HEDP's) | 1 | 0 | 0 |
| D. Martinez | LLNL | Eagle Pillar Formation on OMEGA EP | 0 | 1 | 0 |

with CEA's X-Ray CEA Crystal Spectrometer (XCCS) and LLNL's MSPEC and HENWAY spectrometers; the XCCS view is illustrated in Fig. 140.65. These measurements failed to show NEEC emission in either $^{169}$Tm or $^{187}$Os within the sensitivities of these instruments but are able to set an upper bound on the highly uncertain NEEC rates. Improved measurements with larger quantities of $^{187}$Os and more-sensitive spectrometers could further constrain NEEC rates.

***Viscosity Measurements on Liquid Silica***

Principal Investigator: P. M. Celliers (LLNL)
Co-investigators: M. A. Barrios and A. E. Gleason (LLNL)

This campaign was the third in a series to demonstrate a method for determining the viscosity of a high-pressure fluid created by propagating a strong shock front through an initially transparent sample. This measurement technique is based on observing the evolution of a spectrum of perturbations imposed on a multimegabar shock front passing through the sample material. The viscosity of the liquid state just behind the shock front is expected to influence the decay rate of the perturbations as the shock front propagates; detailed measurements of the perturbation state can be compared with calculations in order to assess the viscosity. The sample under study is liquid silica ($SiO_2$), produced by propagating the shock through samples of either alpha quartz or fused silica. The viscosity of high-pressure liquid silica has obvious geophysical relevance, and measurements in the megabar domain are not possible with conventional methods. Two earlier campaigns in 2010 and 2012 examined the shock response

Table 140.VII: Approved FY14 LBS proposals.

| Principal Investigator | Affiliation | Project Title |
|---|---|---|
| A. Bernstein | LLNL | Nuclear Excitation by Electron Capture in a Reduced-Scale Hohlraum |
| P. M. Celliers | LLNL | Measurement of the Viscosity of Shock-Compressed Fluids of Water and Silica |
| H. Chen | LLNL | Exploring Pair Plasmas and Their Applications Using the OMEGA EP and OMEGA Lasers |
| G. Fiksel | LLE | Magnetized ICF Implosions on OMEGA |
| R. F. Heeter | LLNL | Gattling-Gun Long-Duration Radiation Sources on OMEGA EP for Sustained-Drive Hydrodynamics and Low-Density Atomic Physics Applications on OMEGA EP and the NIF |
| S. Ivancic | LLE | Channeling Through Long-Scale-Length Plasmas |
| M. Lafon | LLE | Gigabar Shocks for Shock-Ignition and High-Energy-Density-Physics Studies |
| T. Ma | LLNL | Creation and Measurements of Novel High-Pressure Electride States of Matter |
| D. Martinez | LLNL | Imprint-Driven Richtmyer–Meshkov Instability in Thick Planar Targets |
| D. McNabb | LLNL | Thermonuclear Reactions in Stellar Plasmas |
| S. Nagel | LLNL | Measuring Charged-Particle Stopping Powers Using Short-Pulse Lasers |
| P. M. Nilson | LLE | Radiation Hydrodynamics of Double-Ablation Fronts |
| H.-S. Park | LLNL | Astrophysical Collisionless Shocks and Magnetic Fields in Laser-Produced Plasmas |
| P. K. Patel | LLNL | Fast-Electron Focusing Using Ellipsoidal-Tip Cone Targets for Fast Ignition |
| J. R. Rygg | LLNL | Structure and Equation of State of Solid and Superionic Warm Dense Matter |
| R. Smith | LLNL | Understanding Strength Effects in Diamond Ablators Used for Ramp Compression |
| C. Stoeckl | LLE | Spectroscopy of Neutrons Generated Through Nuclear Reactions with Light Ions in Short-Pulse Laser Interaction Experiments |

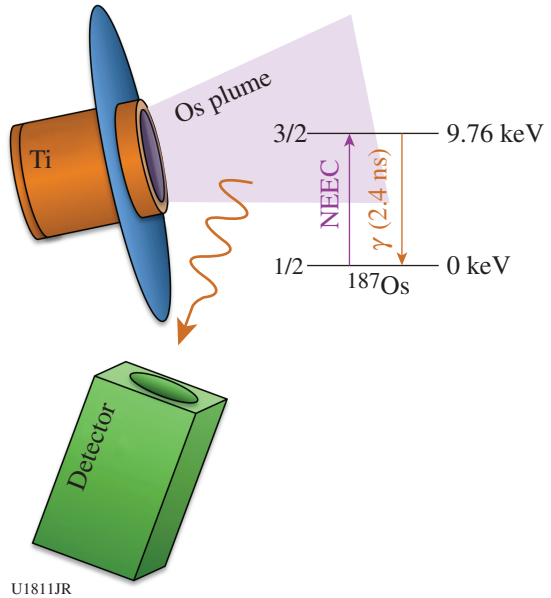


Figure 140.65
Experimental configuration showing the Os-lined Ti hohlraum with an over-the-shoulder view of CEA's x-ray CEA crystal spectrometer (XCCS), together with the level diagram for nuclear excitation by electron capture (NEEC) and subsequent gamma decay in $^{187}$Os.

to perturbation spectra that were generated by both random and coherent patterns imposed on the sample surface at the interface with the ablator. These initial experiments demonstrated the feasibility of using the OMEGA high-resolution velocimeter (OHRV) to produce quantitative measurements of the multimode velocity perturbations directly from the surface of the reflecting rippled shock front.

In the 2014 experiments, the shocks were driven using a hohlraum coupled to a 50-$\mu$m CH (PMMA) ablator followed by the sample. Although measurements on water samples as well as silica were envisaged for this campaign, that option assumed successful fabrication of novel water cell targets, which turned out to be more difficult than expected and precluded collecting a dataset on water in this campaign. Nevertheless, excellent data were obtained for silica.

In the experiments, as the shock passed through this interface, the perturbations were transferred to the shock front, where they were detected and measured quantitatively by the OHRV. Figure 140.66 shows an example velocity spectrum for an ~200-GPa shock driven into fused silica. The

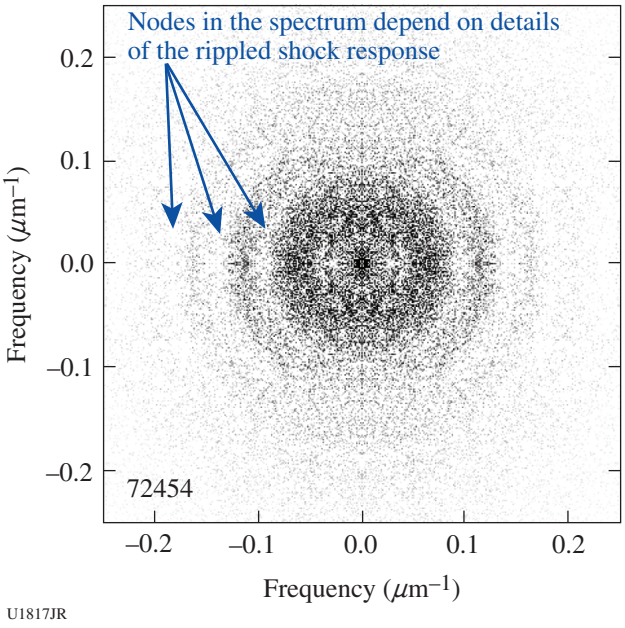


Figure 140.66
Two-dimensional velocity spectral density of a rippled shock front generated at a roughened interface between a PMMA ablator and a fused-silica sample recorded 800 ps after passage of the shock through the interface (shot 72454). The gray scale is proportional to the mode velocity amplitude. Nodal regions are where the mode velocity is near zero at the time of the probing, corresponding to those modes that are undergoing a velocity reversal at the probing time.

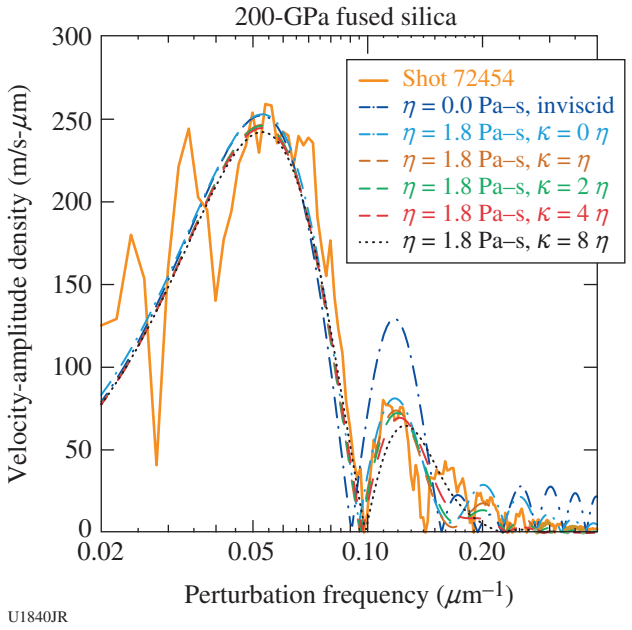


Figure 140.67
Background-subtracted and azimuthally averaged mode amplitude as a function of mode spatial frequency. The first node is near 0.09 $\mu$m$^{-1}$, the second near 0.14 $\mu$m$^{-1}$, and so on. Also shown are theoretical mode amplitudes expected for the inviscid response and several viscous cases, where the bulk viscosity $\kappa$ is taken to be different multiples of the shear viscosity $\eta$. The data suggest the viscosity is ~1.8 Pa-s (18 poise).

spectrum shows the presence of nodal zones—modes whose instantaneous oscillation velocity was near zero at the time of the OHRV probe. These nodal patterns are expected from the multimode solution of the rippled shock evolution. Details of the amplitudes and positions of the nodes depend on the viscosity. Model calculations employing an analytical expression derived by Miller and Ahrens[31] are used to estimate the mode amplitude as a function of spatial frequency, shown in Fig. 140.67. Here, we see that the observed spectrum is consistent with viscosities ~1.8 Pa-s (20 poise).

### *Exploring Pair Plasmas and Their Applications*

Principal Investigator: H. Chen (LLNL)

In FY14, an LLNL/LLE team continued the project "Exploring Pair Plasmas and Their Applications" with two LBS shot days on OMEGA EP. The experiments used the short-pulse beams to produce jets of electron–positron antimatter pairs. The experiments focused on measuring the pair yield and its dependence on the target material. The experiments successfully probed the basic physics processes involved in pair generation, and the data reveal discrepancies between experiments and theory. A total of 31 shots were performed.

The OMEGA EP short-pulse beams (~1 kJ in 10 ps) irradiated 1-mm-thick targets of Sn, Ta, Au, Pb, and U. Unexpectedly high positron yields were recorded from the Ta, Pb, and U targets (see preliminary results in Fig. 140.68), in disagreement with the expected ~$Z^4$ scaling from the Bethe–Heitler process. The reasons for the discrepancy, once understood, should significantly impact future pair-production experiments. Previous experiments almost exclusively used gold targets. The prior experiments showed that quasi-monoenergetic relativistic positron jets are formed during high-intensity irradiation of thick gold targets[32,33] and that these jets can be strongly collimated[34] using the magneto-inertial fusion electrical discharge system (MIFEDS).[35] The external field produces a 40-fold increase in the peak positron and electron signal.[34] The FY14 results suggest that the pair density could be increased up to an order of magnitude with U instead of Au targets. This would enable the laboratory study of relativistic pair plasmas that are important to understanding some of the most exotic and energetic systems in the universe.[36]

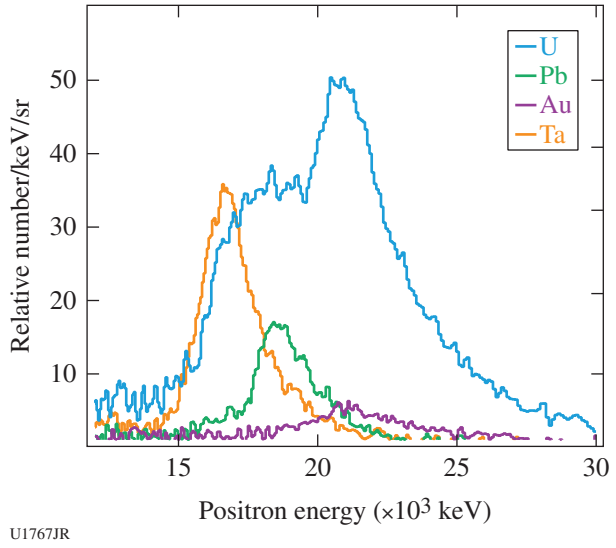


Figure 140.68
The *Z*-dependent positron-yield measurement on OMEGA EP in FY14.

***Fusion Enhancement in Spherically Imploded Magnetized Targets MagICF_14A***

Principal Investigator: G. Fiksel (LLE)

The purpose of the MagICF Campaign on 16 July 2014 was to demonstrate a neutron-yield enhancement in magnetized spherical ICF implosions. A magnetic field of up to 15 T was embedded in a spherical target, which was a spherical plastic (CH) shell with a thickness of 22.3±0.4 $\mu$m, filled with 10 atm of $D_2$ gas. The field was created using a single magnetic coil on the equatorial plane of the target, energized by MIFEDS. The coil was tilted along the P5–P8 axis to accommodate different diagnostics, and the spherical target was compressed using 40 OMEGA beams in a polar-direct-drive configuration along the same axis, delivering ~16.9 kJ of energy on target (see Fig. 140.69 for the experimental setup).

The results were compared to the result published in 2011 (Ref. 37) when an 8-T field was embedded in the target, leading to a 30±5% neutron-yield enhancement while the simulation predicted a 22% increase. Ten successful shots were conducted on the shot day, including four shots without a magnetic field as the baseline, four shots with $B$ = 15 T, and two shots with $B$ = 12 T. One of the shots with a 12-T field had very different target specifications (23.4 $\mu$m in shell thickness) and was not included in the analysis. For the shots with a 15-T seed magnetic field, the average neutron-average ion temperature and the average neutron yield increased by 9±2% and 30±7%, respectively. These results agree with the results of 2011 and with the simulation-predicted neutron yield increase of 35.6% (see Fig. 140.70).

Furthermore, the x-ray framing camera shows a brighter self-emission from the central hot region in magnetized targets, which indeed indicates a higher temperature in magnetized implosions.

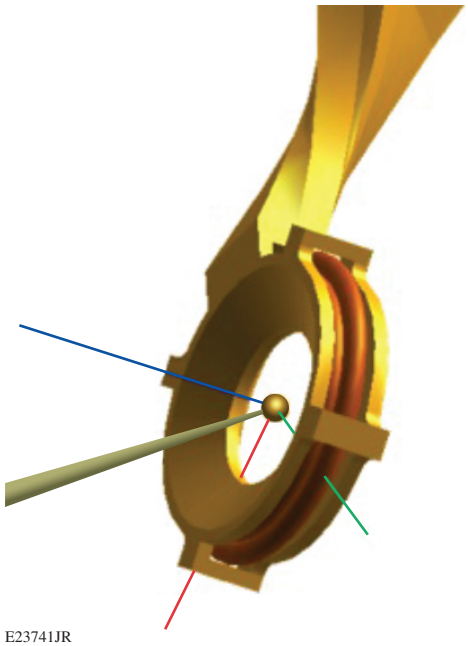


Figure 140.69
Experimental setup showing the coil and the target.

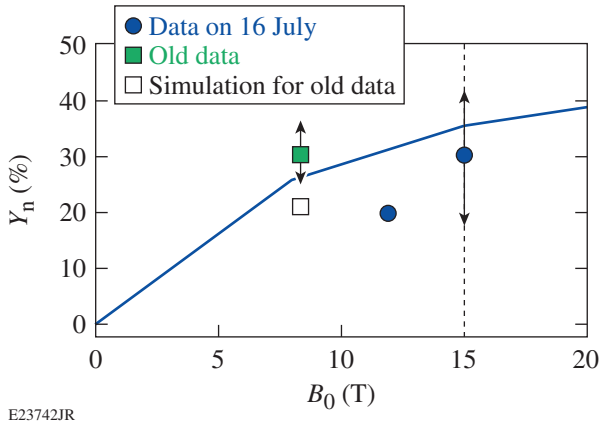


Figure 140.70
Comparison of recent and previous experimental results and simulations.

***Initial Applications of the Sustained-Drive "Gatling-Gun" X-Ray Source***

Principal Investigator: R. F. Heeter (LLNL)
Shot Principal Investigator: D. Martinez (LLNL)
Co-investigators: J. Kane (LLNL); R. C. Mancini (University of Nevada, Reno); and B. Villette and A. Casner (CEA)

This FY14 OMEGA EP campaign continued the successful development of "Gatling-gun" multihohlraum-array x-ray sources began in FY13, in which a radiation temperature of 90 eV was produced for 30 ns. This capability is important for multiple physics experiments, including investigations of (a) x-ray photoionization equilibrium at relatively low plasma densities of ~$10^{18}$ ions/cm$^3$ and (b) the hydrodynamics of pillar formation from directional radiation relevant to the Eagle nebula.

The FY14 campaign used a copper three-hohlraum array [shown in Fig. 140.71(a)] to drive a Ti photoionization sample and a hydrodynamics sample, simultaneously, demonstrating the capabilities of the Gatling-gun hohlraum. The three hohlraums were heated in succession using three UV beams, each with 10-ns square pulses and 3.8 kJ of energy. The hohlraum temperature was measured with CEA's Mini-DMX, which again recorded 80 to 100 eV over 30 ns.

(a)

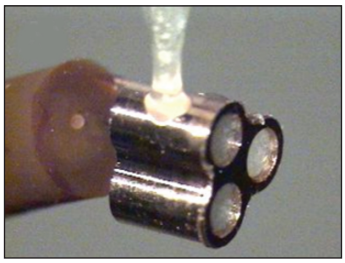

(b)

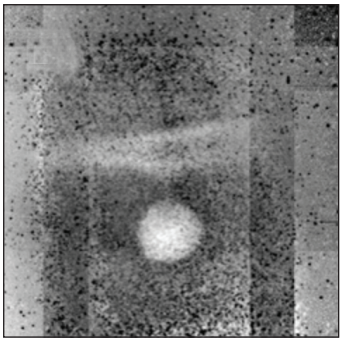

U1810JR

Figure 140.71
(a) Target image showing the Gatling-gun triple hohlraum and attached resorcinol formaldehyde (R/F) foam with an embedded solid-density CH ball. (b) Radiograph reconstructed from a 16-pinhole array gated at $t = 35$ ns.

The photoionization sample consisted of a 0.6-mm × 0.6-mm × 0.5-$\mu$m Ti foil sandwiched between two 1-$\mu$m-thick tamper layers of 1-mm × 1-mm CH. The emission spectrum, recorded using the variable-spaced grating (VSG) diffraction-grating spectrometer, showed strong Cu emission from the hohlraum and a weak signal in the expected range of the Ti L-shell emission lines. Interpretation of the spectrum is ongoing.

The hydrodynamics sample consisted of 50 mg/cm$^3$ of resorcinol formaldehyde (R/F) foam with an embedded, solid-density CH ball of 350-$\mu$m diameter. The hydrodynamics of the sample was studied using a Ti area backlighter driven by a 1-ns, 1.25-kJ UV beam with a 500-$\mu$m focal spot. The backlit image was imaged onto a single-frame x-ray framing camera with a 4 × 4, 20-$\mu$m pinhole array, providing a detailed composite radiograph from the multiple images. Figure 140.71 shows the recorded images, in which the shock front has propagated into the R/F foam past the CH ball.

Both aspects of the experiments successfully demonstrated the application of the Gatling gun, resulting in additional shots for further specific applications.

***Laser Channeling Through Large-Scale-Length Plasmas***

Principal Investigators: S. Ivancic and W. Theobald (LLE)
Co-investigators: C. Stoeckl and C. Ren (LLE); and H. Habara and K. A. Tanaka (Osaka University, Japan)

Propagating a laser beam at relativistic intensities (>$10^{18}$ W/cm$^2$) through a plasma with a large density scale length is dominated by highly nonlinear interactions. These effects are important for both fundamental aspects of relativistic laser–plasma interaction physics and applications such as fast ignition in inertial confinement fusion.[38] The purpose of this LBS experiment was to study the physics of channel formation with high-intensity IR laser pulses of a longer, 100-ps pulse duration and compare the results to previous results from a shot day with 10-ps pulses. The experiments showed that 100-ps infrared pulses with a peak intensity of $1 \times 10^{19}$ W/cm$^2$ produced channel-to-plasma densities beyond critical, while 10-ps pulses with the same energy but higher intensity did not propagate as far.[39] The experiments were carried out on the OMEGA EP Laser System using two UV laser beams to create, on planar plastic targets, large-density-scale-length plasmas with a scale length of 250 $\mu$m at the critical density ($n_c$) of the IR laser. The channel-

ing laser pulse was an IR beam with energy of up to 2.6 kJ. The vacuum peak intensities were $1 \times 10^{19}$ W/cm$^2$ for 2.6-kJ, 100-ps pulses compared to $4 \times 10^{19}$ W/cm$^2$ for 1-kJ, 10-ps pulses. The average laser intensities are about an order of magnitude lower. The focal position of the channeling beam was set to 750 $\mu$m from the original target surface, and the corresponding electron plasma density at that location was predicted to be $n_e = 2.5 \times 10^{20}$ cm$^{-3}$. The plasma was diagnosed using an optical diagnostic employing a 10-ps, 263-nm probe laser[40] to measure simultaneously the background plasma density and to image the channel. The phase gradients are discriminated by a technique using an angular spectral filter [angular filter refractometry (AFR)] that is placed in a Fourier plane behind the collection optics of the probe beam.[41]

Figure 140.23 from **Channeling Multikilojoule High-Intensity Laser Beams in an Inhomogenous Plasma** (p. 235) shows measured channels at different probing times for 10-ps and 100-ps laser irradiation. The channel is visualized by the perturbations in the AFR contours. The contours bend as a result of strong density gradients created by the channeling pulse. The top row shows the results for the 10-ps pulse. The head of the channel reached at 6 ps to a position 450 $\mu$m from the original target surface, corresponding to 0.6 $n_c$. The last contour in the collection system corresponds to light that is refracted through a peak density above $n_c$ ($1.4 \times 10^{21}$ cm$^{-3}$). The channel was observed up to 200 ps after its creation. Later in time, the tip of the channel retreats backward with a velocity of $\sim 3 \times 10^7$ cm/s away from the target surface. There is a clear difference in the channel depth between the 10-ps and 100-ps pulses. The 100-ps pulse [Figs. 140.23(e)–140.23(h)] reaches to the contour closest to the original target surface, indicating that a density $>1.4 \times 10^{21}$ cm$^{-3}$ has been reached. The 100-ps pulse shown in Fig. 140.23(e) reached in only 18 ps to about the same depth as the 10-ps pulse. The 100-ps pulse continues to bore through the plasma, reaching overcritical density at 65 ps after the start of the laser beam. The upper-contour bands in the lower-density region are smoothly shifted in space, while the contours at higher density inside the channel are highly distorted and obscured. Bright fourth-harmonic emission of the channeling beam was measured in the vicinity of the critical surface [Figs. 140.23(e)–140.23(h)] with the 100-ps pulse. Harmonics from the critical-density surface have been observed in experiments with high-intensity laser beams interacting with solid-density plasmas.[42] No self-generated harmonic emission was observed with the 10-ps pulse, confirming that it did not reach as high a density as the 100-ps pulse.

***Spherical Strong-Shock Experiments Using Medium-Z Ablators on OMEGA***

Principal Investigators: M. Lafon and W. Theobald (LLE)
Co-investigators: R. Nora, R. Betti, J. R. Davies, K. S. Anderson, M. Hohenberger, and C. Stoeckl (LLE); A. Casner (CEA); and X. Ribeyre (University of Bordeaux, France)

The shock-ignition concept[43] is an alternative to the conventional hot-spot approach of inertial confinement fusion that involves generating of an intense shock at the end of the assembly pulse. The ignitor shock is generated by a power spike at the end of the laser pulse. The shock strength increases as a result of convergence and reaches 3 to 5 Gbar as the shock travels through the imploding shell. A key milestone for shock ignition to be a credible path to ignition is to demonstrate the generation of a seed shock pressure of at least 0.3 Gbar at laser intensities of $5 \times 10^{15}$ to $1 \times 10^{16}$ W/cm$^2$. The spherical strong-shock platform was developed to study the seed pressures at shock-ignition–relevant laser intensities on OMEGA. The experiments are very promising and have demonstrated seed pressures exceeding 0.3 Gbar (Ref. 44). At such intensities, laser–plasma instabilities play an important role in the coupling of laser energy to the target. The goal of this LBS day was to study the effect of different $Z$ ablator materials on shock generation and laser–plasma instabilities producing hot electrons.

The 60 UV beams from the OMEGA laser are focused to high intensity (overlapping beam intensity of $\sim 6 \times 10^{15}$ W/cm$^2$) on the surface of spherical solid targets to launch a shock wave that converges in the center. The targets with an outer diameter of 430 $\mu$m consist of an inner plastic (CH) core that is doped with titanium with an atomic concentration of 5% and an outer ablator layer of a different material. Four different ablator materials were used: 20 $\mu$m Be, 34 $\mu$m CH, 28 $\mu$m C, and 20 $\mu$m $SiO_2$. The shock wave converges in the center of the solid target and heats a small volume (radius <10 $\mu$m) to temperatures of several hundred eV. The heated plasma is ionized and emits a short burst of x-ray radiation that is detected with an x-ray framing camera. The hot electrons are characterized from the measured hard x-ray bremsstrahlung emission. Figure 140.72(b) shows the measured x-ray flash time for different ablator materials with smoothing by spectral dispersion (SSD) (squares) and without SSD (circles). An earlier flash time was measured with a plastic ablator, indicating that a stronger shock was produced in the laser–target interaction. The data show that turning SSD off shortened the flash time by ~50 ps for most

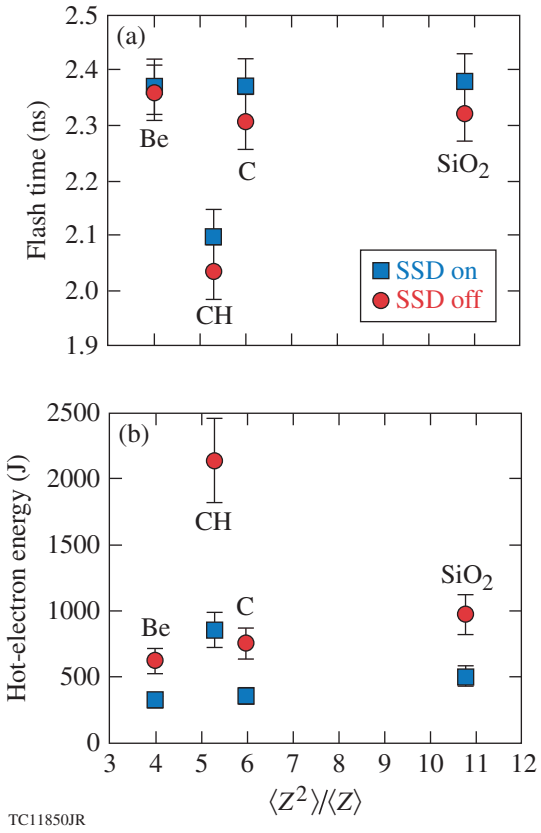


Figure 140.72
(a) Measured x-ray flash time from the convergent shock wave from the target center for different ablator materials with smoothing by spectral dispersion (SSD) (squares) and without SSD (circles) . An earlier flash time was measured with a plastic ablator, indicating that stronger shocks were produced. There is also an indication that turning SSD off increased the shock strength. (b) Measured hot-electron energy deposited in the target for different ablator materials. More hot electrons are generated with a plastic ablator and SSD turned off.

of the different ablators. This indicates that stronger shocks were produced when SSD was turned off. Figure 140.72(b) shows the measured hot-electron energy for the different ablator materials. For each of the materials, about a factor of 2 more hot electrons were produced without SSD. The plastic ablator produced, by far, the most hot electrons and more than 2 kJ of hot-electron energy without SSD, which corresponds to a conversion efficiency of ~9% of the total laser energy. This is more than a factor of 2 more than what is produced in $SiO_2$ and almost a factor of 3 more than in carbon, which is very close in effective atomic number to plastic. Simulations are underway to study the effect of the ablator material to understand why plastic produced a stronger shock and more hot electrons.

### *Creation and Measurement of Novel High-Pressure Electride States of Matter*

Principal Investigator: T. Ma (LLNL)
Co-investigators: A. Pak, B. Bachmann, S. LePape, and T. Doeppner (LLNL)

Density functional theory (DFT) simulations predict a new material phase in highly compressed matter, where valence electrons, instead of becoming delocalized, actually bunch up in interstitial pockets. This creates an electron lattice co-existing within the ion lattice. This experiment used x-ray Thomson scattering to search for the existence of this electride phase by probing the lattice spacing that corresponds to the electrides.

Magnesium foils, 100 $\mu$m thick, were shock compressed to 5 to 8 Mbar (Fig. 140.73) using a single-sided ramp drive utilizing nine OMEGA beams with up to a total of 800 J of energy. The shocked samples were probed using Zn $He_\alpha$ x rays (8.9 keV) at a time corresponding to peak pressure. By varying the scattering angle between the shots, the static structure factor was directly probed, where the scattering profile would show pronounced peaks at low-$k$ values because of the additional reflections and interferences of the electride lattice. Excellent scattering data were acquired at the various phases of Mg reached under varying shock conditions; however, preliminary data analysis does not seem to show scattering variations that would immediately indicate the existence of electrides. Further data analysis is required.

### *Ablative Richtmyer–Meshkov Experiments*

Principal Investigator: D. Martinez (LLNL)

The ablative Richtmyer–Meshkov (RM) instability driven from laser imprinting in the presence of a phase inversion was explored on the 60-beam OMEGA Laser System. Figure 140.74 shows the experimental configuration. Planar 30- and 50-$\mu$m-thick CH targets were directly driven with three UV beams using a 3-ns square pulse shape, a total energy of ~0.7 kJ, and a laser intensity of ~$5 \times 10^{13}$ W/cm$^2$. Initial target modulations were imposed by laser imprinting, using a beam with a special 2-D phase plate with a modulation wavelength of ~30 $\mu$m and timing advanced by ~200 ps relative to the other drive beams, which had regular OMEGA distributed phase plates (DPP's). The growth of

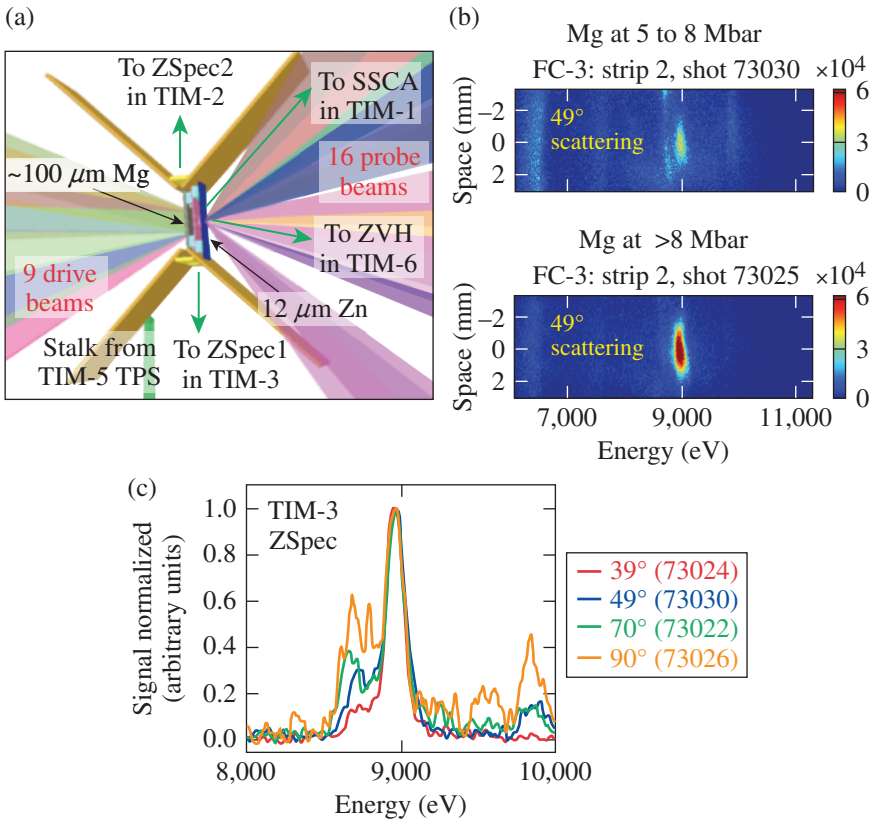


U1807JR

Figure 140.73
(a) Experimental configuration. (b) Raw scattering data taken at 49° for Mg compressed to between 5 to 8 Mbar [face-centered cubic (fcc) phase] and >8 Mbar [simple hexagonal (sh) phase]. (c) Comparison of scattering profiles for four shots taken at various scattering angles for Mg shock compressed to fcc (5 to 8 Mbar) phase. TIM: ten-inch manipulator; SSCA: x-ray streak camera; TPS: target positioning system.

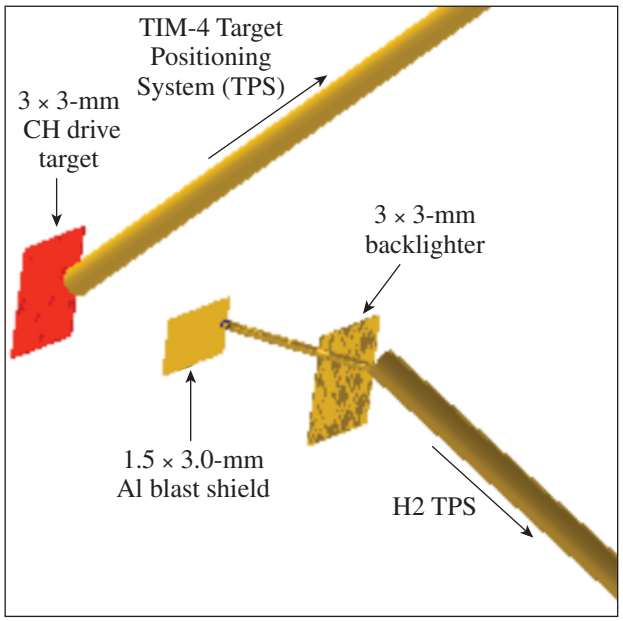


U1803JR

Figure 140.74
Experimental configuration for FY14 ablative Richtmyer–Meshkov experiments.

target modulations was measured with gated x-ray radiography using samarium (~1.8-keV) and tantalum (~2.2-keV) backlighters, 10-$\mu$m spatial resolution, and 80-ps temporal resolution. The backlighters were driven with a 2-ns square pulse shape at ~3 × $10^{14}$ W/cm$^2$ using seven additional UV beams. Figure 140.75(a) shows a typical radiograph of the RM instability for a shot using laser imprinting. For comparison, foils with preimposed modulations were also used to observe the differences between the RM instability from preimposed modulations and the data shown in Fig. 140.75(b). Although the modulations were not purely orthogonal, the power spectrum shows that the modulations are sufficiently separated [Fig. 140.75(c)]. Figure 140.76 shows that the imprinted and preimposed modulations follow the same growth trajectory, suggesting that imprint, in the observed case, had little to no influence on the RM instability after the initial seed. Simulations using the *CHIC* code from CEA and the *DRACO* code from LLE disagree with the trajectory of the modulations; one possible explanation is that the codes overpredict the ablation velocity. Investigation into the disagreement is ongoing.

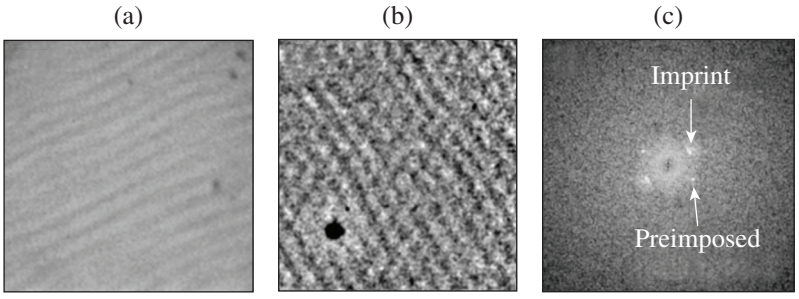


Figure 140.75
Data showing (a) imprint modulations in 30-$\mu$m-thick foil at 0.8 ns; (b) imprint and preimposed growth at 0.8 ns in a 50-$\mu$m-thick CH target; and (c) the Fourier power spectrum of (b).

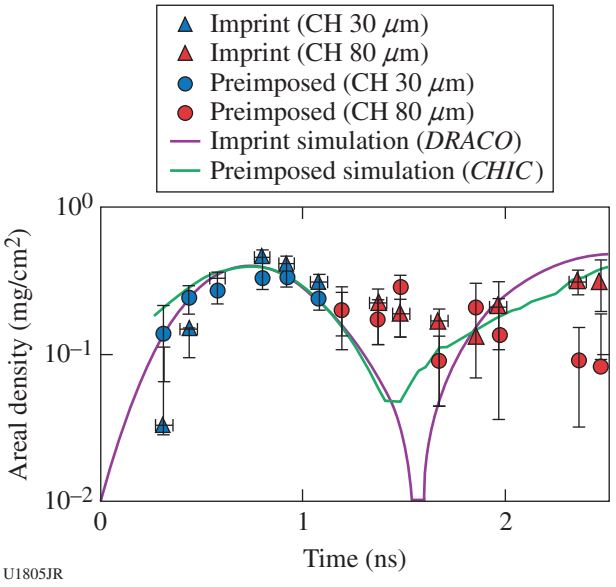


Figure 140.76
Richtmyer–Meshkov growth for 30-$\mu$m- and 80-$\mu$m-thick CH foils for imprinted (triangles) and preimposed (circles) modulations. Shock breakout is expected at 0.9 ns for 30-$\mu$m-thick foils and 2.4 ns for 80-$\mu$m-thick foils.

### *Thermonuclear Reactions in Stellar Plasmas*

Principal Investigator: D. McNabb (LLNL)
Shot Principal Investigator: M. Gatu Johnson (MIT)

Two distinct Laboratory Basic Science (LBS) "Stellar Rates" Campaigns were fielded in FY14, in conjunction with a related NLUF effort and with extensive collaboration between LLNL, MIT, LLE, and LANL. The main goals of the first campaign were to study stratification (between T and $^3$He) and nuclear product spectra in T$^3$He implosions (with trace D in the fuel). Understanding the impact of stratification on implosion yields is a key step toward using the implosion platforms developed in inertial confinement fusion (ICF) research to measure cross sections relevant to stellar and big-bang nucleosynthesis. T$^3$He(D) is an ideal fuel mixture to study stratification because of the many measurable nuclear yields produced from these implosions (T$^3$He-p, T$^3$He-d, D$^3$He-p, DT-n, TT-n). Trace quantities of D are not expected to significantly impact stratification between the T and $^3$He majority ions. Although detailed data analysis and post-shot simulations are in progress, Fig. 140.77 shows preliminary measured D$^3$He/DT yield ratios (points with error bars) for these shots as a function of partial $^3$He pressure in the fuel. Three different fill mixtures were shot to test a theoretical prediction that stratification effects will cancel out in T$^3$He fuel at 90:10 T:$^3$He (Ref. 45). Also shown in the figure is the pre-shot simulation of the D$^3$He/DT ratio, from hydro-simulations (ARES) that do not consider possible stratification effects. Stratification between T and $^3$He would show up as a deviation from the predicted ratio. Pending post-shot simulations, the preliminary indication is that stratification effects are small in these experiments.

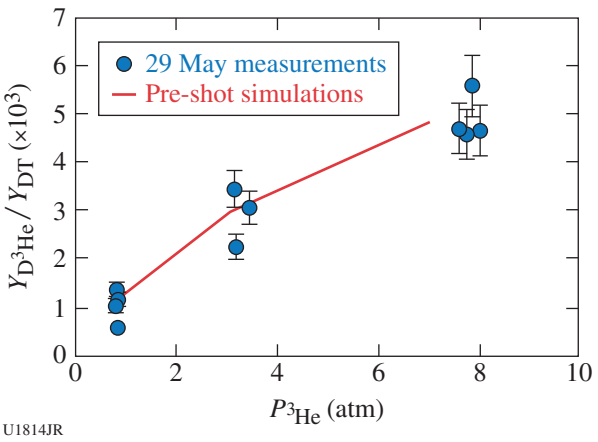


Figure 140.77
Preliminary measured D$^3$He-to-DT yield ratios as a function of partial $^3$He fill pressure in the capsule (points with error bars). Also shown is the ratio predicted in pre-shot simulations (red line) assuming no stratification of the T and $^3$He.

In the second experiment, the γ rays from the p + D fusion reaction were measured for the first time in an ICF plasma, at a center of mass (Gamow peak) energy of ~16 keV. This reaction is relevant to astrophysics. In particular, during big-bang nucleosynthesis, it produces $^3$He (at particle energies ≳100 keV), and in protostars and brown dwarfs, it is the primary source of nuclear energy (at particle energies <1 keV). The low energy of this γ (5.5 MeV) necessitated the use of the new gas Cherenkov detector (GCD)-3 detector by LANL. Excellent data were acquired for the p + D reaction, highlighted in Fig. 140.78. These shots also measured the DD-γ for the first time in ICF, which is the primary source of background for the p + D measurement.

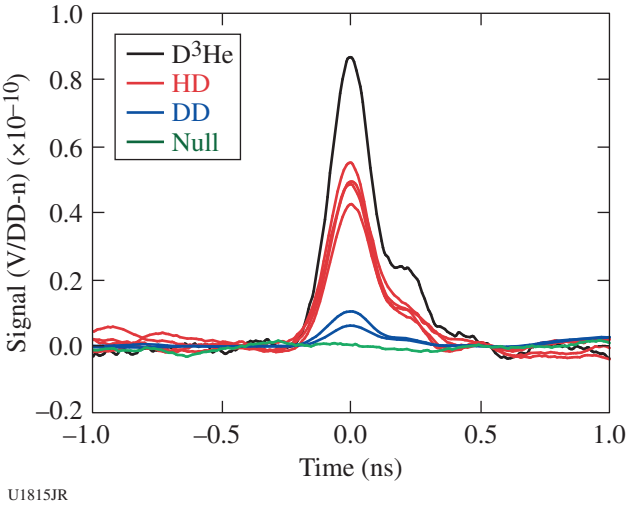


Figure 140.78
Cherenkov detector signals for the p + D experiments, showing four shot types: D$^3$He (detector calibration, black), HD (primary signal, red), DD (background, blue), and null (background, green). Excellent p + D fusion data were acquired for the first time.

### *Measurements of Charged-Particle Stopping Power on OMEGA EP*

Principal Investigator: S. Nagel (LLNL)
Co-investigator: A. Zylstra (MIT)

Calculations of charged-particle energy loss in ICF-relevant plasma conditions still depend on untested theories. To address the need to validate these theories, a platform is being developed on OMEGA EP to measure charged-particle energy loss. Strongly coupled or fully degenerate conditions are difficult to obtain, but warm-dense-matter (WDM) plasmas that have temperatures of several tens of eV and approximately solid densities ($10^{22}$ to $10^{23}$) are well within the moderately coupled and degenerate regimes.

The experimental schematic is shown in Fig. 140.79. A short-pulse beam is used to generate energetic protons via the target-normal sheath acceleration (TNSA) mechanism to probe a warm foam target. The foam target is heated by x rays using a halfraum driven by three long-pulse UV beams. Compared to previous campaigns on OMEGA EP, this method showed an improvement of the proton-beam smoothness, better pointing of the proton beam through the material, and reduced cross-talk between the heating and proton probing. This, therefore, significantly advanced the platform, and new measurements are planned.

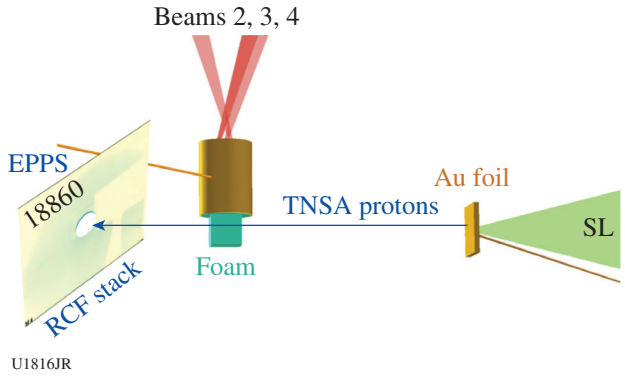


Figure 140.79
Experimental schematic. One OMEGA EP short-pulse laser beam is used to create the probing protons, whose proton-beam profile and spectra were characterized by a new combination of both radiochromic film and the electron–proton–positron spectrometer (EPPS). The other three beams are used to heat the foam target. RCF: radiochromic film; SL: sidelighter.

### *Radiation Hydrodynamics of Double Ablation Fronts*

Principal Investigator: P. M. Nilson (LLE)
Co-investigators: M. Lafon and R. Betti (LLE)

Laser-driven ablator dynamics in moderate-*Z* materials provide a basic test for radiation–hydrodynamic model predictions in a regime where electron and radiation transport are dynamically significant. This series of experiments studied directly driven ablator dynamics in brominated plastic (CHBr) targets where double ablation fronts are known to form. Ablation is driven at the first front by an electron heat flux and at the second front by a radiative heat flux. The system is optically thin in the outer ablation front and close to the corona. The system is optically thick at the inner ablation front and in the plateau region. Here, radiation and matter are almost in equilibrium and the radiative energy flux is described by a thermal heat wave. Combining streaked x-ray radiography with self-emission imaging allows one to track these regions as a function of time for comparison with model predictions.

The experiments were carried out on the OMEGA EP Laser System. CHBr (6 at. %) targets were driven with a 2.5-ns square pulse at focused intensities of $10^{14}$ W/cm$^2$. Target trajectories and density profiles were measured using time-resolved x-ray radiography based on a laser-driven Ti x-ray source and a one-dimensional slit imager coupled to an x-ray streak camera. With appropriate filtration, emission from the hot coronal plasma was simultaneously imaged. An example radiograph for a 20-$\mu$m-thick target with superposed x-ray self-emission imaging is shown in Fig. 140.80. The data show x-ray transmission and coronal emission consistent with a density plateau where the double ablation front forms. Tracking the location of the ablation fronts and measuring the hydrodynamic efficiency of the driven target provide a novel and direct test for equation-of-state and opacity model predictions. Detailed analysis of these data is underway.

***Astrophysical Collisionless Shock Experiments with Lasers (ACSEL) on OMEGA EP***

Principal Investigator: H.-S. Park (LLNL)
Shot Principal Investigator: C. Huntington (LLNL)

The ACSEL collaboration is studying high-velocity plasma flow interactions and the role of self-generated or amplified magnetic fields in such systems. Study of these phenomena is essential to understanding a range of astrophysical systems, including gamma-ray bursts, supernova remnants, and young stellar objects. The FY14 experiments using OMEGA EP expanded on the collisionless shock platform common to ACSEL (LBS) and MagShock (NLUF), with the former concentrating exclusively on plasmas without externally applied magnetic fields. Irradiating a pair of opposing planar targets with 2.2 kJ (OMEGA EP), counter-propagating flows are created, each with bulk velocity near 1000 km/s. The flows interact near the midplane between the targets, where the interpenetrating plasma is susceptible to a range of instabilities, including the two-stream and Weibel instabilities.

The FY14 campaigns studied the effect of varying the target material, including the effect of collisional flow from higher-$Z$ target materials. Figure 140.81 compares data obtained for $CH_2$ (the same as most of the previous studies), Al, and Cu targets. The central magnetic-field advection feature[46,47] is very different among these target types. The data show that the two horizontal features, thought to be associated with piled-up magnetic fields from the Biermann battery at the laser spot, move apart over time, which is different from collisionless flow experiments where the two features stay at the same place. This is likely caused by pressure buildup in the interaction region, which pushes the features apart. Both *FLASH* and *OSIRIS* simulations show qualitative agreement with the experimental data. On the other hand, the actual size of the interaction region remains narrow, and the fact that the two plates are still horizontal indicates that the turbulence is probably not very developed. This implies that turbulence in the collisional flow plays an important role in the formation of the magnetic field. Further experiments are planned in FY15.

***Fast Ignition Using Elliptical-Tip Cone-in-Shell Targets***

Principal Investigators: P. K. Patel and F. Pérez (LLNL)
Co-investigators: H. Sawada (University of Nevada, Reno); W. Theobald and A. A. Solodov (LLE); L. C. Jarrott and F. N. Beg (University of California, San Diego); M. S. Wei (General Atomics); and A. Link, Y. Ping, and H. S. McLean (LLNL)

The fast-ignition (FI) approach to inertial confinement fusion has the potential to achieve higher energy gain compared to central hot-spot–ignition schemes. Fast ignition uses a separate short-pulse ignition laser to locally heat the fuel core near the time of peak compression. This ignition laser is focused inside the tip of a

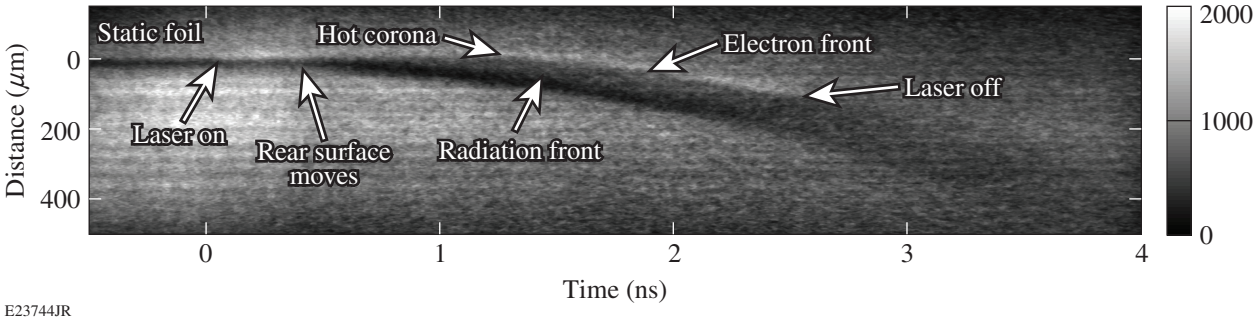


Figure 140.80
Streaked x-ray radiograph of double ablation front formation in a 20-$\mu$m-thick CHBr (6 at. %) target driven with a 2.5-ns square pulse at focused intensities of $10^{14}$ W/cm$^2$. The ablation front driven by radiative energy flux propagates into the target ahead of the electron-driven ablation front.

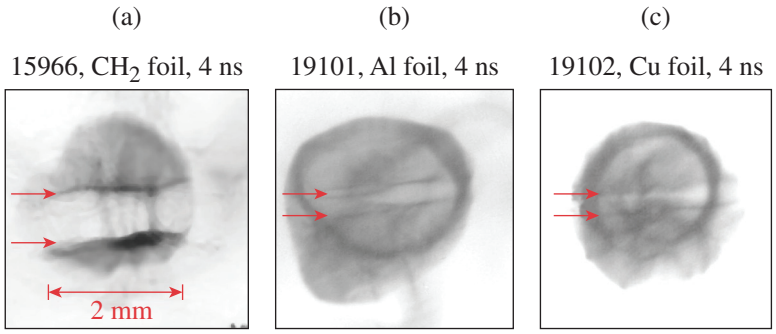


Figure 140.81
Comparison of magnetic fields from interpenetrating high-velocity flows. The higher-$Z$ targets create colliding flows that affect the magnetic-field advection generated by the Biermann battery from the target surface. This indicates that turbulence in the collisional flows plays an important role in the formation of the magnetic field.

re-entrant gold cone and accelerates a large number of high-energy electrons. The efficiency of heating the fuel to thermonuclear conditions can be greatly increased if the electrons accelerated from the laser-interaction region can be guided to the dense fuel.

This year's experiments investigated electron-beam guiding using resistivity discontinuities through structured material interfaces. The OMEGA EP picosecond laser was focused on a slab of plastic containing short aluminum wires of various shapes. Laser-generated electrons tend to stay localized inside the wire because of magnetic fields generated along the resistivity discontinuity. As illustrated in Fig. 140.82, a copper slab was attached at the back of the CH/Al foil to detect the location of the electrons exiting the foil. Wires of three formats were used: traversing the whole slab ("long"), traversing only a short portion of the slab ("short"), or in the shape of an ellipsoid. The latter have been predicted to provide better focusing characteristics, in the manner of elliptical mirrors in optics. The electrons passing through the Cu foil induce Cu-$K_\alpha$ x-ray emission, which was imaged using the spherical crystal imager (as shown in Fig. 140.83). The presence of the wires clearly produced structure in the electron beam, showing that some guiding is occurring. In this experiment, however, the ellipsoids were not proven to be more efficient than straight wires. A simulation effort is benchmarking the current models to these results and extending the models to ignition-scale situations. It is expected that the guiding effects will be enhanced in full-scale scenarios.

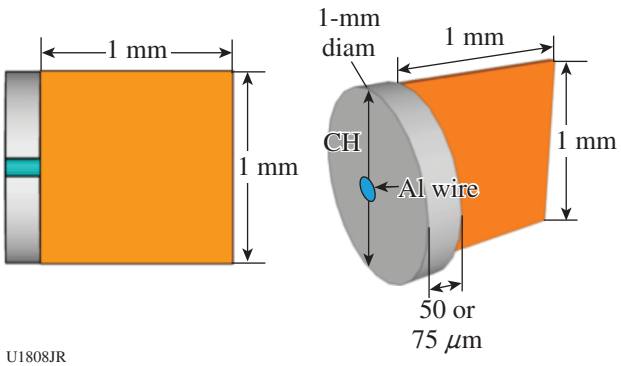


Figure 140.82
Schematic of the targets.

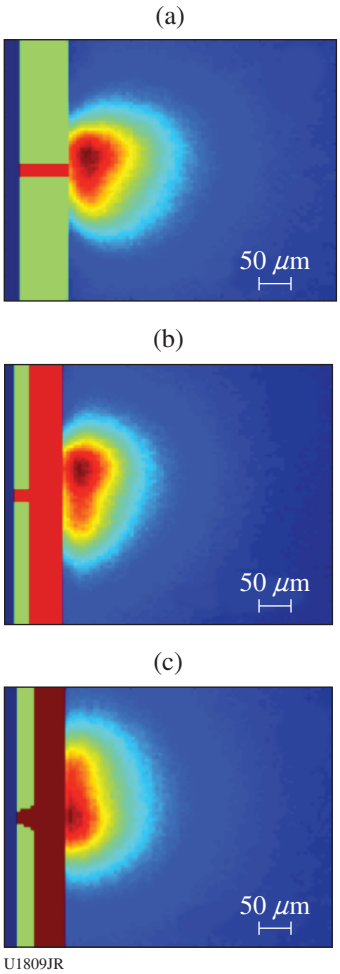


Figure 140.83
Cu-$K_\alpha$ images, reflecting the shape of the electron beam through the Cu foil. The green blocks correspond to plastic and the red blocks correspond to Al. The (a) long wire; (b) short wire; and (c) ellipsoid structure.

### *Structure and Equation of State of Solid and Superionic Warm Dense Water*

Principal Investigator: J. R. Rygg (LLNL)
Shot Principal Investigators: F. Coppari and M. Millot (LLNL)

The structure and equation of state of solid and superionic warm dense water at the core conditions of Uranus and Neptune were investigated to explore a proposed superionic phase, essentially a solid lattice of oxygen ions surrounded by fluid-like diffusing protons. Its existence in the deep interiors of icy giant planets would have a dramatic impact on their internal structure and evolution.

The experiments on the 60-beam OMEGA Laser System employed new laser dynamic compression techniques, novel liquid-cell targets, and advanced diagnostics, including both optical diagnostics and x-ray diffraction. Multishock compression in these experiments squeezed initially liquid water into solid and superionic ices at pressures of several megabars, while keeping the temperature below 0.5 eV. Data were obtained using streaked optical reflectivity and pyrometry and interferometric Doppler velocimetry (VISAR), as well as x-ray diffraction. Ongoing analysis of the recently obtained x-ray diffraction data will provide unprecedented insight on the equation of state and structure of solid and superionic megabar water ices in the portion of phase space shown in Fig. 140.84.

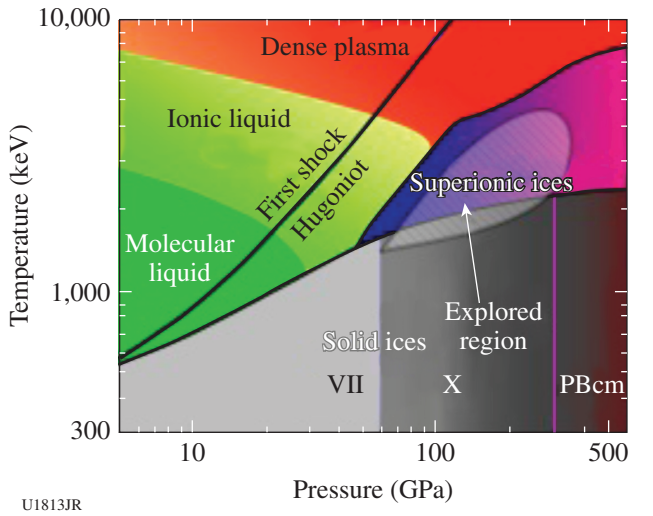


Figure 140.84
Pressure–temperature phase diagram of warm dense water, showing the region explored with multishock compression of liquid water using ultrafast optical diagnostics and x-ray diffraction on the OMEGA Laser System. PBcm: a particular type of crystal structure, characteristic of high-density water ices.

### *Spectroscopy of Neutrons Generated Through Nuclear Reactions with Light Ions in Short-Pulse Laser Interaction Experiments*

Principal Investigators: C. Stoeckl, U. Schroeder, and V. Yu. Glebov (LLE)

The experimental objective of this project is to study nuclear reactions in light ions by measuring the spectrum of neutrons generated in short-pulse laser-interaction experiments and compare it with simulated spectra based on the published cross sections.

Planar targets are irradiated with one short-pulse beam focused at the target's front surface. Charged particles from the back side of the target create neutrons and charged particles through nuclear reactions in a second converter target placed closely behind the primary interaction target. The spectrum of the neutrons generated in the converter target is measured using a three-channel scintillator photomuliplier–based neutron time-of-flight (nTOF) detector system. Charged-particle detectors are used to measure the spectra of the primary particles.

The previous experiments in FY13 with CD primary and CD secondary targets resulted in neutron spectra showing a clear DD fusion neutron peak. For these experiments a pre-plasma was created on the front side of the primary target using a 100-J, 100-ps UV laser pulse, which was fired 0.5 ns before the main IR short pulse. This pre-plasma significantly reduced the number and energy of charged particles on the front surface of the primary target and significantly improved the signal-to-background ratio.

Two shot days were allocated for these experiments in FY14. On the first day LiD secondary targets were used with the reduced background primary CD target developed in FY13. Unfortunately no DT neutrons were recorded from the tritium generated in Li breakup reactions. Preliminary analysis of the data indicates that the cross sections for the Li breakup reactions are too small to generate enough tritium, given the flux and spectrum of the primary ions and the geometry of the experimental setup.

On the second day a neutron pickup reaction in Be [$Be^9$(d,t) $Be^8$] was chosen to produce the tritium, which then generated the DT fusion neutrons. The theoretical cross sections of this reaction reach ~150 mb above 1-MeV deuteron energy. The experimental values reported in the literature are varying significantly between ~20 mb and 200 mb. For these experiments, a Be foil of ~50- to 100-$\mu$m thickness was attached in front of the 2-mm-thick CD secondary target.

Figure 140.85 shows the nTOF spectra from the BeCD secondary target compared to the results from a CD secondary target.

With the BeCD secondary target, the neutrons are recorded much earlier compared to the CD secondary, indicating a higher energy. The short signal seen before –50 ns in the nTOF spectrum is caused by the x rays from the laser interacting with the primary target and can be used as a timing reference. Using the x-ray timing reference, the energy of the neutrons can be estimated to be ~2.5 MeV for the CD foil, typical for DD fusion neutrons, and ~4.3 MeV for the BeCD target. The ~4.3-MeV neutron emission is consistent with a $Be^9(d,n)B^{10}$ nuclear reaction. Few data have been published about this reaction. Typical cross sections shown in the literature are of the order of ~100 mb. A more-detailed analysis of this data is in progress.

## FY14 LLNL OMEGA Experimental Programs

R. F. Heeter, K. B. Fournier, K. Baker, M. A. Barrios Garcia, L. Bernstein, G. Brown, P. M. Celliers, H. Chen, F. Coppari, D. E. Fratanduono, C. Huntington, A. Lazicki, R. Kraus, T. Ma, D. Martinez, D. McNabb, M. Millot, A. Moore, S. Nagel, H.-S. Park, P. K. Patel, F. Pérez, Y. Ping, B. Pollock, J. S. Ross, J. R. Rygg, R. Smith, G. W. Collins, O. L. Landen, A. Wan, and W. Hsing (LLNL); and M. Gatu Johnson and A. Zylstra (MIT)

In FY14, LLNL's High-Energy-Density (HED) Physics and Indirect-Drive Inertial Confinement Fusion (ICF-ID) Programs conducted several campaigns on the OMEGA and OMEGA EP Laser Systems, as well as campaigns that used the OMEGA and OMEGA EP beams jointly. Overall, these LLNL programs led 324 target shots in FY14, with 246 shots using only OMEGA, 62 shots using only OMEGA EP, and 16 joint shots using OMEGA and OMEGA EP jointly. Approximately 31% of the total number of shots (62 OMEGA shots, 42 OMEGA EP shots) supported the ICF-ID Campaign. The remaining 69% (200 OMEGA shots and 36 OMEGA EP shots, including the 16 joint shots) were dedicated to experiments for the HED Campaign. Highlights of the various HED and ICF campaigns are summarized in the following reports.

## Indirect-Drive Inertial Confinement Fusion Experiments

### *Thomson-Scattering Measurements from Laser-Driven Gold Spheres*

Principal Investigator: J. S. Ross
Co-investigators: R. F. Heeter and M. Rosen (LLNL); and D. H. Froula (LLE)

In the FY14 AuSphere and GasCoSphere Campaigns, we performed experiments using high-*Z*–coated spheres illuminated uniformly in direct-drive geometry to investigate atomic physics models and radiative properties of the laser-spot plasma relevant to inertial confinement fusion (ICF) indirect-drive–ignition hohlraum plasmas. Bare Au and gas-covered Au spheres (shown in Fig. 140.86) were both investigated.

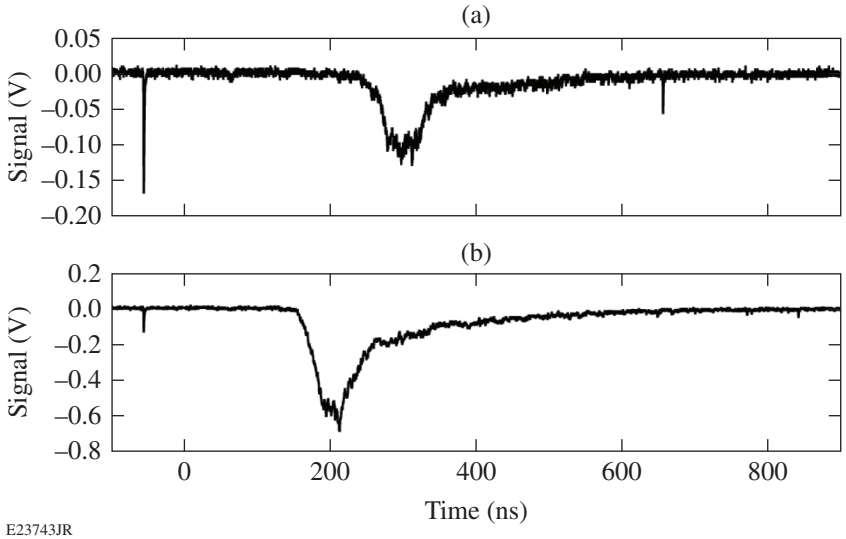


Figure 140.85
Neutron time-of-flight signals from the experiments with (a) CD primary and CD secondary and (b) BeCD secondary targets. The arrival time of the neutrons shifts significantly earlier with the BeCD, indicating a change in the average neutron energy from 2.45 to ~4.3 MeV.

The laser irradiation of $1 \times 10^{14}$ to $10^{15}$ W/cm$^2$ is similar to the intensities found in National Ignition Campaign (NIC) hohlraums. The gas-covered Au sphere experiments use a gas fill of 1 atm of propane or 1 atm of a 70/30 mix of propane and methane to achieve initial electron densities of 7.5% and 6.0% of the critical density, respectively, of the $3\omega$ drive beams. The plasma temperature and density at various radial positions in the blowoff plasma are characterized using optical Thomson scattering. The probe beam was aligned at various radial locations ranging from 100 to 300 $\mu$m from the target surface for Thomson-scattering characterization of the low-density plasma blowoff. The laser beams used either a 1-ns square laser pulse or a two-step laser pulse (1-ns square foot, 1-ns square peak) designed to reduce the shock produced by the gas-bag window.

The electron temperature and density, the plasma-flow velocity, and the average ionization state are measured by fitting the theoretical Thomson-scattering form factor to the observed data. Examples of the Thomson-scattering data from ion-acoustic fluctuations are shown in Fig. 140.86 for both target types. The measured data are then compared to post-shot simulations with different atomic physics and electron-transport models. The different models predict different electron temperatures for the experimental conditions; sample results are shown for the bare Au spheres in Fig. 140.87.

The simulation with the XSN nonlocal model most closely reproduces the temperatures measured during the experiment. The XSN model with a flux-limited transport model using a flux limiter of 0.05, previously used to simulate high-$Z$ hohlraums, predicts an electron temperature significantly higher than measured. A detailed analysis of the gas-covered sphere data is currently underway, and a comparison of Thomson-

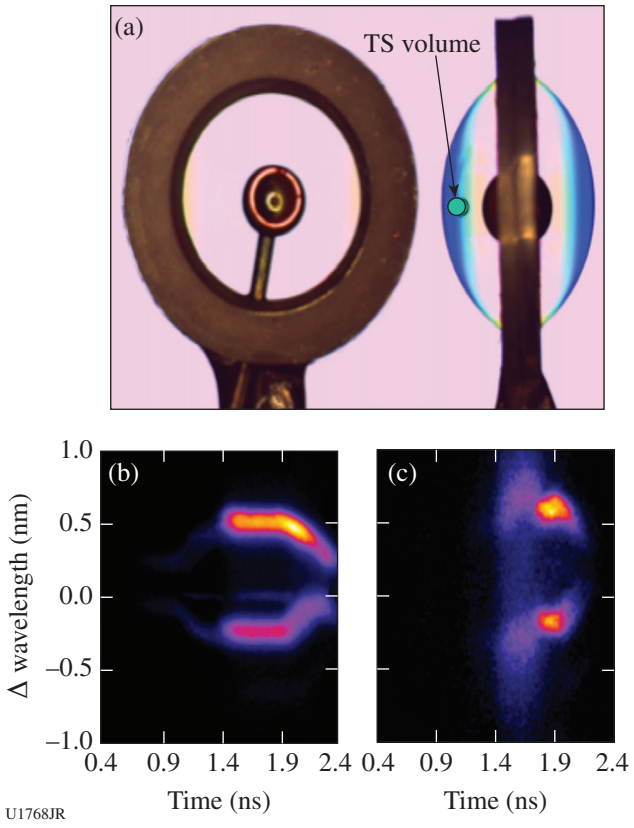


Figure 140.86
(a) A 1-mm-diam Au sphere centered in a 2.6-mm-diam gas bag. The gas bag is filled with 1 atm of propane or a mix of methane and propane to achieve different initial electron densities. The location of the Thomson-scattering (TS) volume is shown. (b) TS spectrum as a function of time for Au sphere. (c) TS spectrum as a function of time for gas-covered Au spheres.

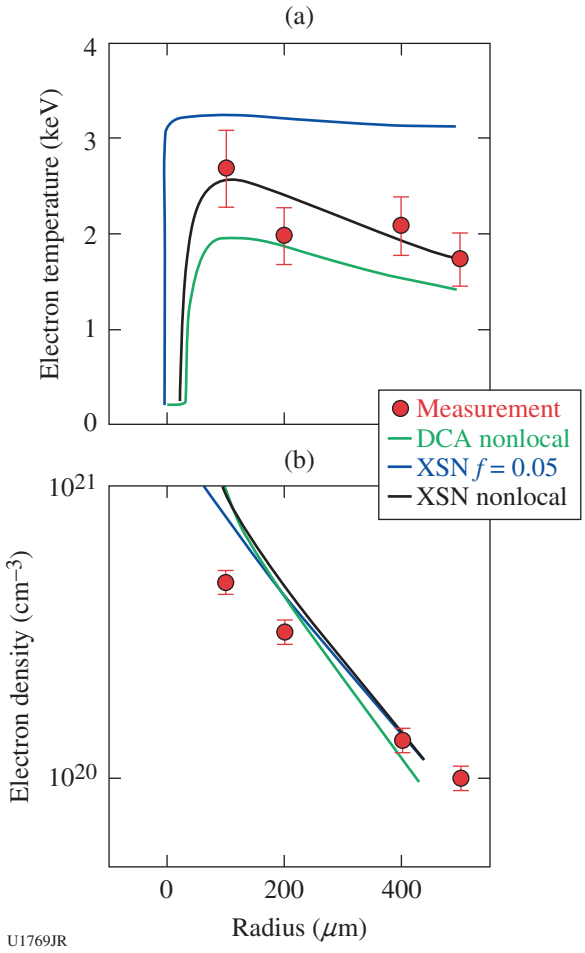


Figure 140.87
For bare Au spheres, the (a) measured electron temperature and (b) electron density are compared to post-shot simulations using the detailed-configuration accounting (DCA) nonlocal model (green line), the XSN flux-limited model with a flux limiter of 0.05 (blue line), and a nonlocal heat-transport model (black line) for an intensity of $5 \times 10^{14}$ W/cm$^2$.

scattering data, Dante absolute x-ray flux measurements, and x-ray spectroscopy to simulations will be used to further validate the atomic physics models employed in these simulations.

### *Cryogenic Cell Measurements of the Viscosity of Rippled Shocks*

Principal Investigator: P. M. Celliers

The Shock Viscosity Campaigns began as an effort to probe the decay of rippled shocks in National Ignition Facility (NIF) ablator materials as a means of assessing whether the rippled shock response was inviscid or showed evidence of more-complicated viscous behavior. As part of this effort, attempts were initiated to field a planar cryogenic platform compatible with the viewing axis of the 2-D VISAR (velocity interferometer system for any reflector) using the OMEGA high-resolution velocimeter (OHRV). The planar cryogenic platform addresses an important surrogacy issue associated with the CapSeed Campaigns. In all prior campaigns using room-temperature targets, a layer of transparent polymethyl methacrylate (PMMA) was used as the surrogate for the fuel layer. The shock-impedance difference between PMMA and ICF ablators is much less than for DT ice or liquid $D_2$, so any issues associated with the deep release of the ablator into the fuel are not captured accurately in the room-temperature PMMA-based platform. For this reason, the cryogenic platform is expected to produce more-definitive data sets for the level of ablator nonuniformities transmitted into the fuel. The initial cryogenic shots of the Shock Viscosity Campaigns (Figs. 140.88 and 140.89) were aimed at establishing a baseline data set for the response of various ablators releasing into liquid deuterium. A single baseline dataset on glow-discharge polymer (GDP) was collected during the initial campaign, with other targets leaking because the GDP samples stress-fractured at cryogenic temperatures. Based on this experience, improvements were made to the target design and a second campaign produced several more datasets on high-density carbon (HDC) and Be ablator samples. The stress-fracturing issue with GDP remains to be solved.

### *Velocity Fluctuations in Doubly Shocked Glow-Discharge–Polymer Ablators*

Principal Investigator: P. M. Celliers

The CapSeed Campaign in FY14 continued our study of GDP, the plastic polymer material used in NIF ablators. The primary goal was to study the response of GDP at the second shock level, by observing the shock-front nonuniformities shortly after a second shock (launched behind the initial shock) had overtaken the first. Several shots were devoted to tuning the two-shock drive by adjusting the timing delay between two groups of drive beams. The tuning study was completed and two preliminary data sets were recorded (Figs. 140.90 and 140.91). These initial results did not reveal a level of nonuniformity significantly different from the nonuniformity levels that

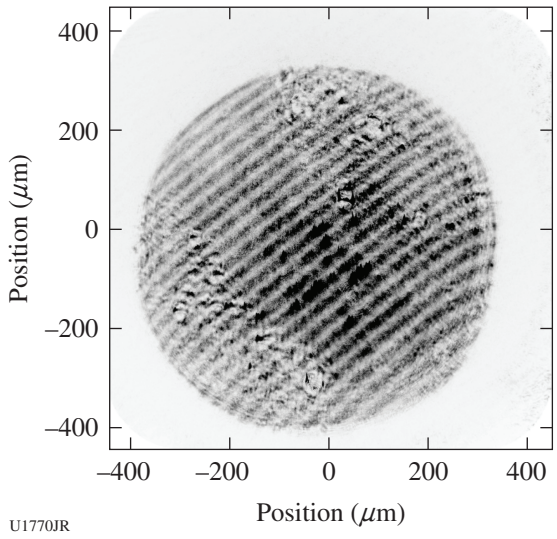


Figure 140.88
Interferogram from the first cryogenic test of a glow-discharge polymer (GDP) ablator releasing into liquid deuterium.

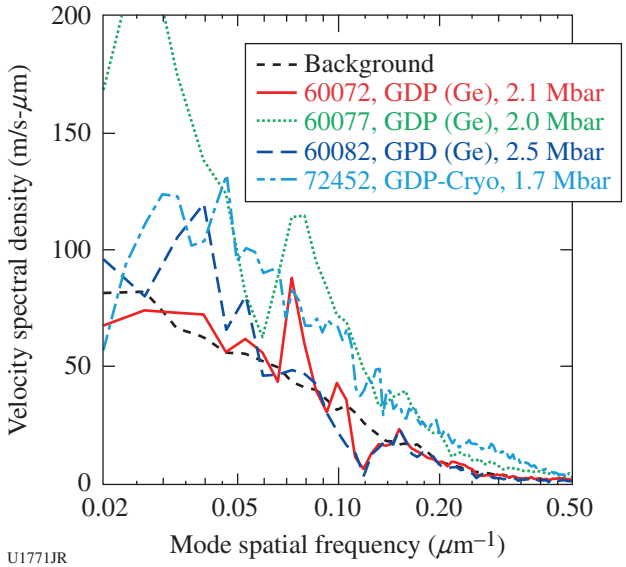


Figure 140.89
Velocity-fluctuation spectra measured for GDP on the first cryogenic test of GDP using the OMEGA high-resolution velocimeter (OHRV) diagnostic, in comparison with data from warm platform tests with PMMA as a surrogate for the fuel. Velocity-fluctuation spectra are very similar for the two platforms.

have been recorded at the first shock level in the GDP material. The current series has laid the foundation for further data collection of GDP using the two-shock drive in a future campaign.

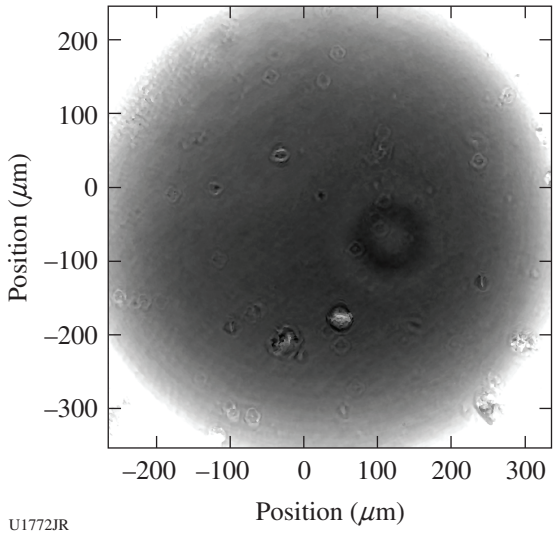


Figure 140.90
Gray-scale representation of the shock-front velocity in a GDP sample double-shocked to ~7 Mbar. The large ripple disturbance originates from a localized defect on the ablation surface; the smaller localized disturbances originate from dust particles trapped at the GDP–PMMA interface during target assembly.

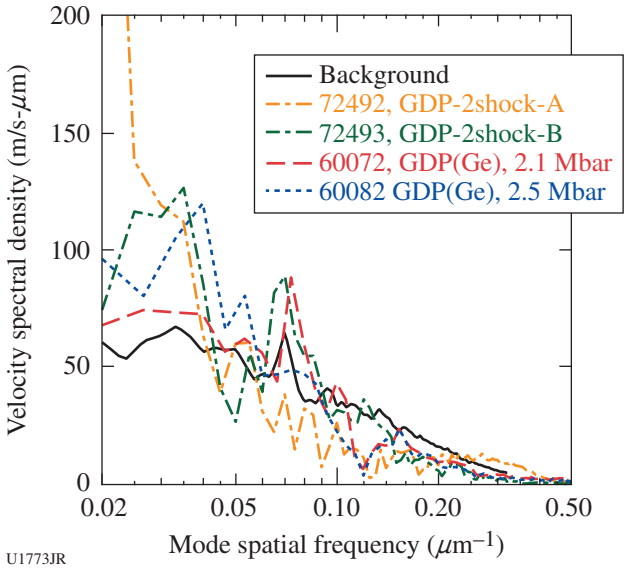


Figure 140.91
Velocity fluctuation spectra measured for GDP on two double-shock GDP experiments compared with earlier single-shock tests. Spectra have had the background subtracted. The background level is shown for comparison.

### *Shock-Release Isentrope Measurements of ICF-Relevant Materials*

Principal Investigator: D. E. Fratanduono

To address concerns regarding uncertainties in the release isentropes of inertial confinement fusion (ICF) ablator materials into low-density gas, experiments were performed to measure the release of glow-discharge polymer (GDP) and CH into methane gas at gas densities comparable to an ICF capsule, to examine the momentum transfer in this low-density kinetic regime. The experiment measured the shock velocity in the GDP prior to shock breakout and the shock transit time through a known methane gas density (0.25 to 1.0 atm). We then utilized a momentum transfer technique to extract $P$–$U_p$ data (the release isentrope). These experiments suffered unexpectedly from nonreproducible effects, which made it difficult to distill conclusions. On average, the shock velocity in the methane gas was anomalously low, suggesting that the equation-of-state model may be overpredicting the release state. Since the results were not consistently reproducible, future experiments will be required to examine this region of phase space in detail.

### *Platform Development for Measuring Charged-Particle Stopping in Warm Dense Plasmas*

Principal Investigator: A. Zylstra (LLNL/MIT Collaboration)

The TransportEP-14A Campaign conducted shots to continue developing a stopping-power measurement platform using the short-pulse lasers on OMEGA EP. In this experiment, the sidelighter beam was used for proton isochoric heating of a warm-dense-matter sample, while the backlighter beam drove a planar foil, generating protons via target-normal sheath acceleration (TNSA) to probe the sample. For the backlighter-driven proton source, the uniformity of the proton beam was studied using source-only shots with a lower-energy drive (40J/1 ps) and smooth wafer targets of chemical vapor deposition (CVD) and Si, compared to standard Au. The proton beam images are shown in Figs. 140.92(a)–140.92(c). While the uniformity has improved over previous higher-intensity shots, modulations in the proton beam remain. The proton isochoric heating configuration sends a TNSA proton beam through a CH slab (200 × 200 × 50 μm), which is heated by proton energy deposition and characterized by x-ray backlighting. The backlighter was a uranium area backlighter, with data taken from 0.5 ns before the slab was heated until 1.5 ns after, as shown in Fig. 140.92(d). Preliminary data analysis suggests nonthermal expansion potentially driven by electromagnetic fields.

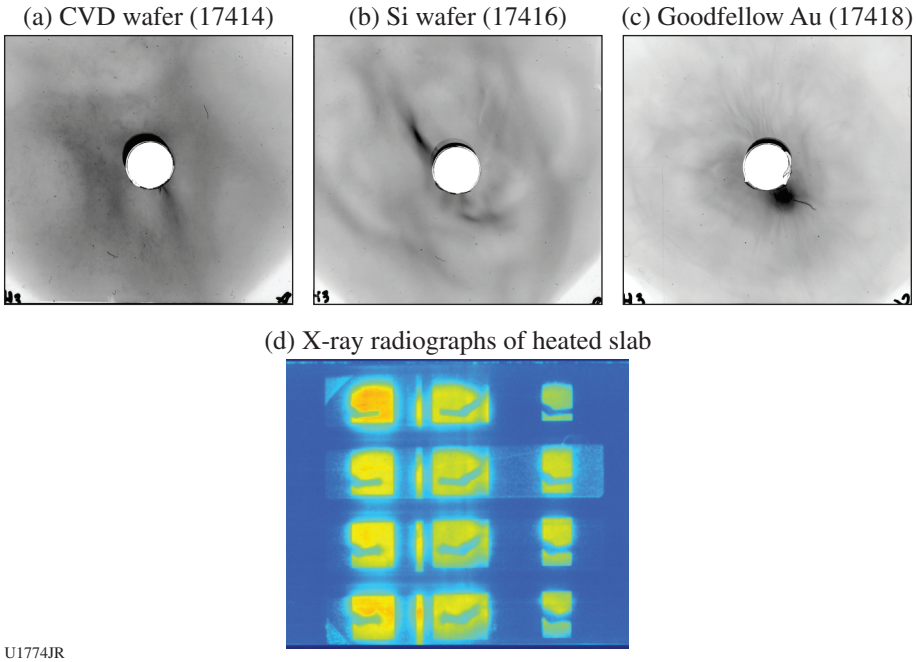


Figure 140.92
[(a)–(c)] Proton source spatial distribution images for various foil targets and (d) x-ray radiography of proton-isochoric–heated slabs.

***Measurements of the Opacity of Silicon in ICF Ablator Conditions***

Principal Investigator: R. F. Heeter
Co-investigators: G. V. Brown, C. Mauche, and B. Wilson

Continuing earlier ablator-opacity measurements, improved experiments were performed to measure the transmission opacity of hot silicon at $T \approx 70$ eV, $\rho \approx 0.2$ g/cm$^3$ on OMEGA EP. At these temperatures and densities from 0.2 to 20 g/cm$^3$, the Atwood number in Si-doped capsules has a strong sensitivity to the Si opacity. The FY14 experiment used a Be-tamped Si foil sample heated by 250-J, 250-ps impulses from two of the long-pulse beams. The sample plasma was characterized with dual-axis, simultaneous backlighting, both face-on and edge-on, using the two short-pulse beams in 10-ps mode. The backlighters were timed 200 ps after the peak of the heating impulse, as verified with the ultrafast x-ray streak camera. The edge-on radiograph measures density via the sample expansion from a known initial thickness (2.1 $\mu$m); the face-on measurement delivers Si ionization balance and transmission opacity data via absorption spectroscopy across the x-ray band from 1600 eV to 3000 eV. To probe the sample at higher density than previously, the edge-on radiography was improved by using a smaller backlighter and samples with improved planarity. The new technique delivered ~10-$\mu$m resolution, verified by radiographing a cold 10-$\mu$m Cu wire and also by discriminating the continuum absorption of the heated Si from the weaker absorption of the underlying Be substrate. A target density of 0.2 g/cm$^3$ was achieved by probing the Si plasma 200 ps after the peak of the heating pulse, when the silicon had expanded to 20 $\mu$m. As illustrated in Fig. 140.93, the Si measurements show absorption features from at least five of the L-shell charge states of Si, plus time-integrated self-emission from earlier in the heating pulse. This high-quality dataset will be analyzed and compared with the opacity models used for the NIF capsules.

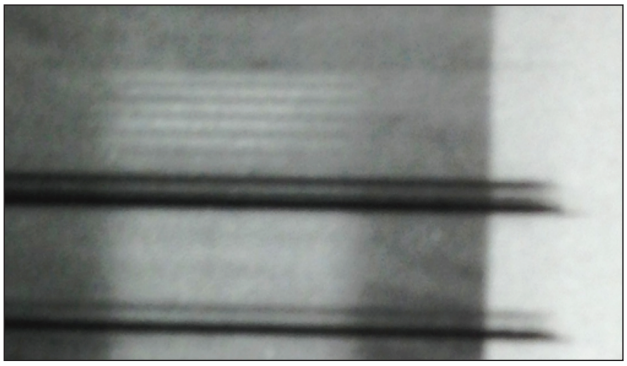


Figure 140.93
Space-resolved absorption spectrum obtained on OMEGA EP using face-on broadband spectroscopy from a Zn bremsstrahlung continuum backlighter. Photon energy increases from top to bottom; emission is dark and absorption is light. Multiple time-resolved absorption and time-integrated emission features of hot silicon are detected with an excellent signal-to-noise ratio.

***Hohlraum Magnetization Using Laser-Driven Currents***
Principal Investigator: B. Pollock
Co-investigators: J. Moody, J. S. Ross, and D. Turnbull

In FY14 the HohlFaradayRot Campaigns on OMEGA EP and the B-FieldHohl Campaign on OMEGA launched an investigation of the feasibility of self-magnetizing hohlraum targets for ICF applications. The first campaign in this new experimental effort employed a target consisting of a half-loop formed by folding a thin gold sheet around a 500-$\mu$m-diam fused Si rod. Figure 140.94 illustrates how the OMEGA EP long-pulse beams shine through the holes in one of two parallel plates on the open side of the loop, producing a plasma at the surface of the second plate. Hot electrons formed by this process collect around the holes in the first plate, essentially charging up a parallel plate capacitor. The half-loop connects the plates, allowing the current to flow and produce a magnetic field on the loop axis. The OMEGA EP 4$\omega$ probe capability was employed to directly measure the magnetic field inside the loop via Faraday rotation along the hohlraum axis. Fields of up to 4.6 T were measured at the time of the probe beam. A new B-dot probe was also developed for this campaign and acquired a signal on all shots. Combining the B-dot probe data with a second set of Faraday rotation measurements from a second piece of fused Si outside of the loop, the produced peak field is inferred to be ~40 T. In the second HohlFaradayRot shot day, the short-pulse backlighter beam was used to drive a proton source for proton-deflectometry measurements of the fringing magnetic fields around the target. This campaign allowed for additional parameter scans and extended the previous dataset.

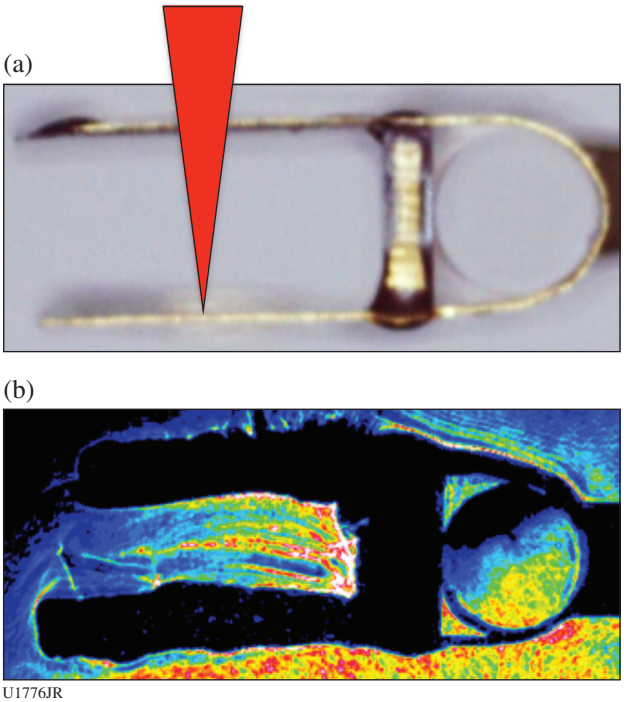

U1776JR

Figure 140.94
(a) Geometry for hohlraum self-magnetization on OMEGA EP with the beam path shown schematically in red; (b) sample of 4$\omega$ probe data used to infer Faraday rotation.

The B-FieldHohl Campaign transitioned the experiment to OMEGA, taking advantage of the 60 beams available and increasing the target diameter from a 0.5-mm half-loop to a 2.0-mm, nearly complete loop. Similar to the OMEGA EP experiment, the magnetic field was driven by using 14 beams to illuminate parallel plates. Another eight beams were directed into the loop to heat the quasi-hohlraum, and the fringing magnetic field outside of the target was diagnosed with proton deflectometry from a $D^3He$ capsule source. The analysis of this recent experiment is ongoing and will be used to guide the FY15 continuation of this effort.

**High-Energy-Density Experiments**
1. Material Equation of State Using Diffraction Techniques

***Kinetics of Melting in Iron***
Principal Investigator: R. Kraus
Co-investigators: F. Coppari, D. E. Fratanduono, A. Lazicki, D. Swift, J. H. Eggert, and G. W. Collins

The iron melting curve at multimegabar pressures is critical to understanding the earth's thermal state and also how its magnetosphere formed and evolves. Dynamic experiments can probe the melting transition at pressures near the inner-core boundary of the earth (~330 GPa). Nguyen and Holmes previously studied the melting transition with a gas gun,[48] using sound velocity measurements, but concerns about the results were raised because of the possible kinetics of melting.

This issue was addressed using *in-situ* x-ray diffraction at the Omega Laser Facility to directly probe the onset and completion of melting along the principal Hugoniot. Polycrystalline diffraction from the high-pressure hexagonal close-packed (hcp) phase of iron was monitored. As the iron was shocked to higher-pressure states along the melt curve, we observed an intensity decrease for the solid diffraction lines together with an increase in the diffuse scattering signal. Attributing this to liquid scattering (Fig. 140.95), we have shown that both incipient and complete melting occurred at the same stress states on the laser time scale (ns) as the gas gun's time scale (100's of ns), so the kinetics of melting are negligible for

these time scales and longer. The data also show that iron stays in the hcp phase along the melt curve until nearly 270 GPa, clarifying an issue that has been debated theoretically.

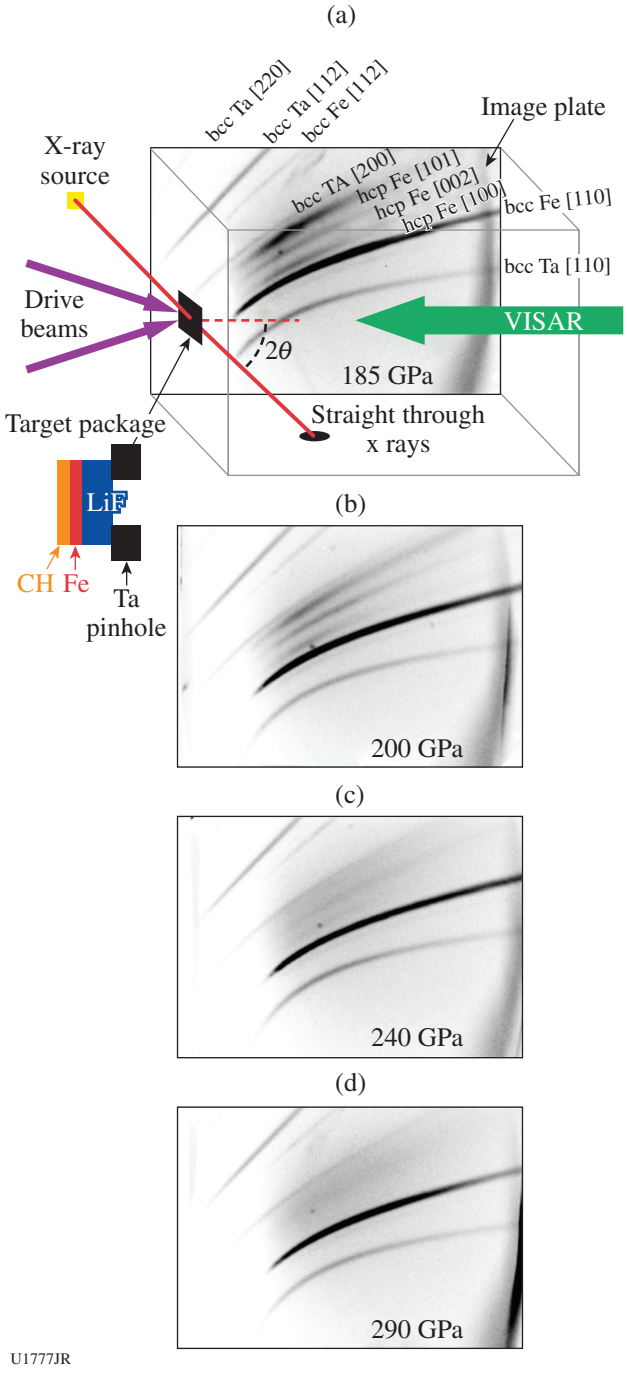


Figure 140.95
(a) Geometry for *in-situ* x-ray diffraction at the Omega Laser Facility. Also shown are image-plate data for shock-induced melting of iron, with a decrease of intensity in the solid diffraction signal and an increase in the diffuse background as melting occurs at higher shock pressures.

### *Kinetics of Melting in Tin*

Principal Investigator: R. Kraus
Co-investigators: F. Coppari, D. E. Fratanduono, A. Lazicki, D. Swift, J. H. Eggert, and G. W. Collins

In this campaign, we used the PXRDIP diagnostic to obtain *in-situ* x-ray diffraction at the Omega Laser Facility. Tin has a complicated high-pressure phase diagram, and the melting curve of tin has come under recent debate. Prior measurements of the melting temperature up to 1 Mbar show a dramatic increase in the slope of the melting curve as the solid phase transitions from a body-centered-orthorhombic (bco) to body-centered-cubic (bcc) structure.[49] Phase transitions in tin are also thought to be sluggish in comparison with other metals.[50] Our campaign's goal was to directly probe the onset and completion of melting along the principal Hugoniot of tin and compare the data with different time-scale experiments to learn about the kinetics of melting. For shock pressures below 50 GPa, the data show strong textured diffraction from the high-pressure phase of tin, whereas above 60 GPa, the data show a strong diffuse scattering signal from liquid tin (Fig. 140.96). These data bracket the melting transition along the principal Hugoniot, in agreement with significantly longer time-scale gas-gun experiments.

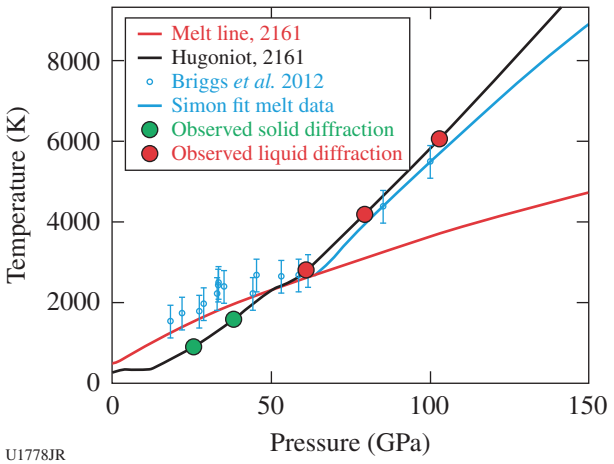


Figure 140.96
Pressure–temperature phase diagram for tin, showing the melting curve data from Ref. 49. Plotted along the Hugoniot of the 2161 *SESAME* equation of state are the pressure states where solid diffraction (green) and liquid diffraction (red) are observed.

***Shock-Resolidification Kinetics of Tin and Iron***

Principal Investigator: R. Kraus
Co-investigators: F. Coppari, D. E. Fratanduono, A. Lazicki, D. Swift, J. H. Eggert, and G. W. Collins

The Diffraction-EP Campaign extended earlier OMEGA experiments on melting kinetics of iron and tin by using OMEGA EP to probe the time scale for resolidification of both materials. Having previously shown that tin and iron can be shock melted on the time scale of a laser-shock experiment, and that melting occurred at the same pressures as in gas-gun experiments (to within the error bars of our measurements), these OMEGA EP experiments sought to quasi-isentropically compress tin and iron from shock-melted states back across the melt curve into the solid phase.

In the tin experiments, we generated an initial shock that was consistently at ~65 GPa (into the liquid phase) and then generated a second shock that brought the tin to a peak pressure of ~160 GPa. The first shock set the initial thermodynamic state of the tin in the liquid phase, and the second shock quasi-isentropically compressed the tin into the solid stability field. After some tuning, we accurately timed the second shock and the backlighter. Figure 140.97 shows the observed strong polycrystalline diffraction peak from resolidified tin. These results are the first unambiguous observation of pressure-driven solidification in a metal. They show great promise that (1) we can probe the kinetics of solidification using laser-shock platforms and (2) *in-situ* x-ray diffraction provides an important tool in diagnosing the resolidification process.

In the iron experiments, we successfully observed strong diffraction from high-pressure hexagonal close-packed (hcp) iron, diffuse liquid scattering, and a very preliminary signature of resolidification. However, the initial thermal state in the liquid could not be accurately confirmed because of the issue with this initial experiment.

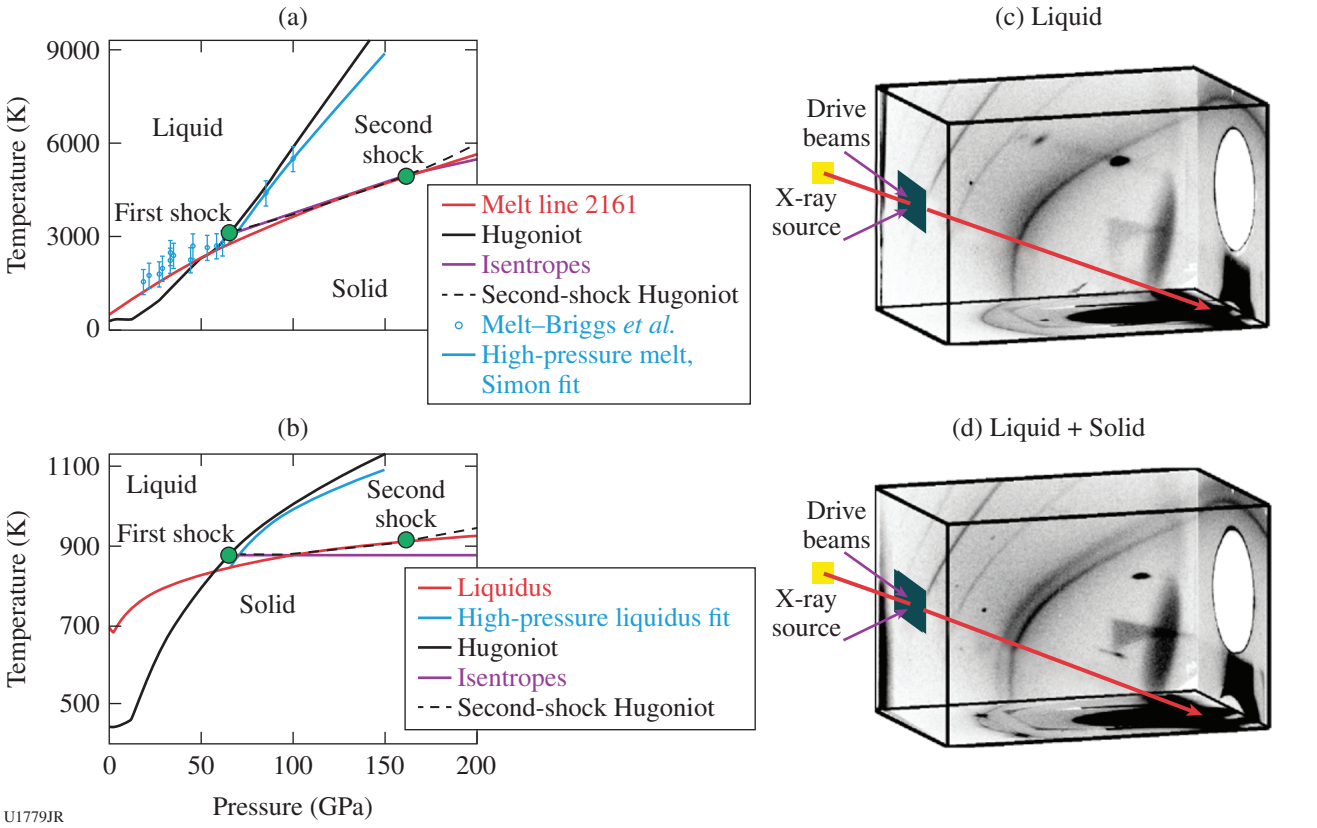


Figure 140.97

(a) Pressure–temperature phase diagram for tin from the *SESAME* 2161 equation of state. Static melting curve measurements (blue points) are from Ref. 49. (b) Pressure–temperature phase diagram for tin from *SESAME* 2161. [(c),(d)] Image plates from a double-shock experiment on Sn (first shock to 65 GPa, second shock to 160 GPa). The second shock in (c) is timed so that the x rays principally interact with unshocked and single-shocked material. The second shock in (d) is timed so that a larger volume of material reaches a second shock state of 160 GPa. Note the strong polycrystalline diffraction line observed in (d) does not exist in (c).

### *Improving the OMEGA High-Pressure Tantalum Diffraction Platform*

Principal Investigator: F. Coppari
Co-investigators: J. H. Eggert, R. Smith, D. E. Fratanduono, A. Lazicki, and J. R. Rygg

This campaign improved the tantalum diffraction platform using the PXRDIP diagnostic on OMEGA by resolving issues related to the high background signal observed in high-pressure shots; it also sought an understanding of the texture evolution when the sample material is ramp compressed to high-pressure states. We tested mitigation schemes that decreased the background signal and improved the platform overall. In particular, a tungsten wire, placed in a specific location of the diagnostic, provided a geometric trace of the background source. Although most of the background is caused by the ablation-generated plasma, some background also comes from the fluorescence of the image plates when hit by the direct x-ray beam. To mitigate this source of background, a fluorescence shield was implemented using a Ta skewed cylinder placed around the region where the direct x rays hit the image plate (Fig. 140.98). This mitigation scheme has also been adopted in the diffraction platform on the NIF with the target diffraction *in-situ* (TARDIS) diagnostic.

The second goal of the campaign was to start looking at the texture formation and evolution in ramp-compressed materials and, in particular, Ta. The shots compared diffraction from Ta samples with three different initial textures: commercial foils, coatings, and pressed powder. Preliminary characterization of the initial texture by laboratory x-ray diffraction and pole-figure analysis indicated that foils and coatings are characterized by a strong fiber texture, while the pressed-powder samples are randomly oriented, so that the corresponding diffraction signal is an untextured diffraction ring. The data show that when laser-driven ramp compression is used to achieve high-pressure states in these three materials, the initial texture is preserved at high pressure and also across a phase transition. The initially untextured powder remained untextured, while samples with initial fiber texture showed a highly textured diffraction signal that persisted even above a solid–solid phase transition. This suggests that some sort of memory mechanism may take place that certainly deserves further investigation in future campaigns.

### *Development of Higher-Energy Backlighters for X-Ray Diffraction*

Principal Investigator: R. Smith

The goal of these shots was to develop and optimize Zr $He_\alpha$ (16.3-keV) and Ge $He_\alpha$ (10.3-keV) x-ray sources for future x-ray diffraction experiments on OMEGA, OMEGA EP, and the NIF. The standard x-ray source for diffraction on OMEGA, using the PXRDIP diagnostic, is the Cu $He_\alpha$ quasi-monochromatic line emission at 8.3 keV. In those experiments[51] the main noise contributor at a high sample pressure is from thermal x rays generated in the sample drive plasma. To increase the signal-to-noise ratio of x-ray diffraction experiments, higher-energy sources that are spectrally decoupled from the drive plasma emission spectrum are necessary for more-effective noise filtering.

The targets for these experiments consisted of a freestanding, 2 × 2-mm, 10-$\mu$m-thick Zr foil or a 6-$\mu$m Ge layer coated on both sides of a 200-$\mu$m pyrolytic graphite substrate. The spectrally resolved emission for a range of laser irradiance conditions was recorded with the XRS Rowland spectrometer and the NRL dual crystal spectrometer (DCS), which covers the x-ray bands from 10.4 to 45 keV and 20 to 120 keV. To optimize the output from Zr $He_\alpha$, up to 20 OMEGA beams were employed in a double-sided illumination geometry. Prepulse and main-pulse laser irradiance conditions on the Zr foil were systematically varied, and the resulting $He_\alpha$ production was measured. The laser power as a function of

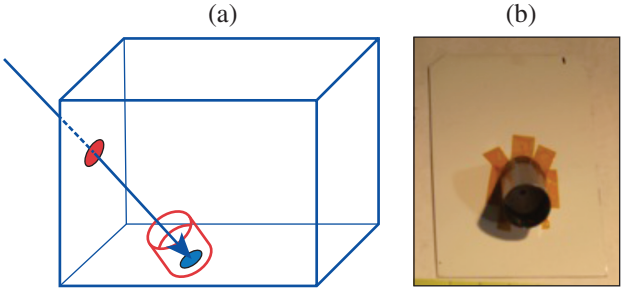


Figure 140.98
Fluorescence shield used on OMEGA to block x rays generated by the fluorescence of the bottom image plate hit by the direct x-ray beam. (a) Drawing of the position of the shield within the PXRDIP diagnostic; (b) a photograph of the shield on the image plate.

time was varied shot-to-shot as illustrated in Fig. 140.99. The resultant PSL (photospectral luminescence) counts on the XRS spectrometer image plates from the $He_\alpha$ line per kJ of main-pulse laser energy are shown in Fig. 140.100 as a function of the main-pulse energy and intensity. The peak 16.3-keV $He_\alpha$ production occurs at an intensity of $\sim 8 \times 10^{15}$ W/cm$^2$. A similar experimental approach and analysis for Ge suggest that the $He_\alpha$ optimization occurs at a laser intensity of $1 \times 10^{15}$ W/cm$^2$.

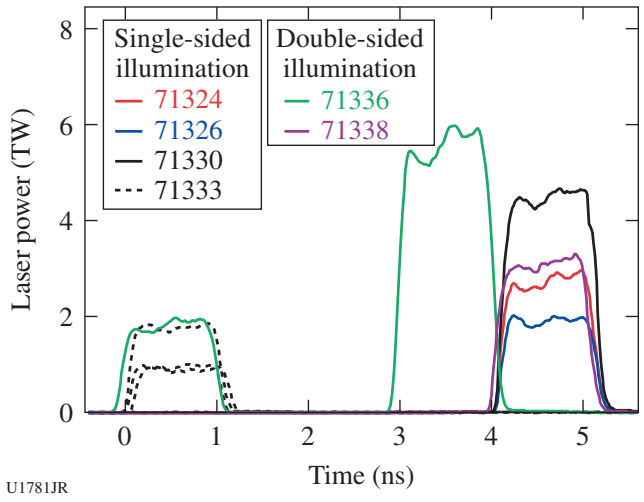


Figure 140.99
Laser power versus time for the ZrHe$_\alpha$ backlighter development campaign.

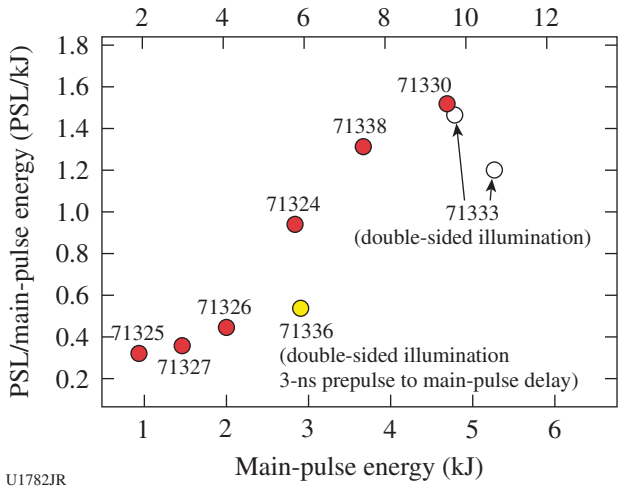


Figure 140.100
PSL (photospectral luminescence) counts on the XRS spectrometer image plates from the 16.3-keV Zr $He_\alpha$ line per kJ of main-pulse laser energy are shown as a function of the main-pulse energy and intensity.

2. Material Equation of State Using Other Techniques

***Measurements of the Lithium Hydride Equation of State***
Principal Investigator: A. Jenei
Co-investigators: J. Hawreliak, R. London, D. E. Fratanduono, and G. W. Collins

The LiH equation-of-state (EOS) measurements started in FY13 were completed in FY14, providing data to constrain the shock Hugoniot EOS of LiH between 0 to 10 Mbar. Two different techniques were employed to determine the shock Hugoniot. The first method used velocimetry data from the VISAR (velocity interferometer system for any reflector) diagnostic to infer the velocities of reflecting shocks in a target with layers of single-crystal quartz and single-crystal LiH and pyrometry data from the streaked optical pyrometer (SOP) diagnostic to determine temperatures. Quartz was used as the EOS reference standard to determine the velocities and temperatures in LiH. Figure 140.101(a) shows an example of the raw data from this configuration, which succeeded in measuring the Hugoniot up to nearly 12 Mbar.

In the second approach, a framing camera radiographed the shock front and pusher/sample interface positions as a function of time in a shock-compressed sample backlit using a chlorine-doped plastic (2.8-keV) area backlighter. The motion of these fronts can provide absolute data on the shock and particle velocities. Although the pulse length was insufficient to generate a steady shock long enough to make an accurate EOS measurement, this experiment demonstrated successful imaging of the interfaces, as shown in Fig. 140.101(b). The information gathered about contrast and resolution provided valuable feedback for future experiment designs.

***Equation-of-State Measurements on Single-Crystal Diamond***
Principal Investigator: D. E. Fratanduono

NIF diffraction EOS experiments utilize single-crystal diamond in the target design to ramp compress the sample to high pressure and minimize the diffraction signal from the diamond. These experiments require an accurate stress–density response of single-crystal diamond. Previous OMEGA[52] and NIF experiments[53] measured the stress–density response of CVD (polycrystalline) diamond, but there has been concern that the stress–density response of single-crystal diamond (⟨100⟩ and ⟨110⟩) could be different from the CVD measurements. To address this, experiments were performed on OMEGA to measure the response of single-crystal diamond in the ⟨100⟩ and

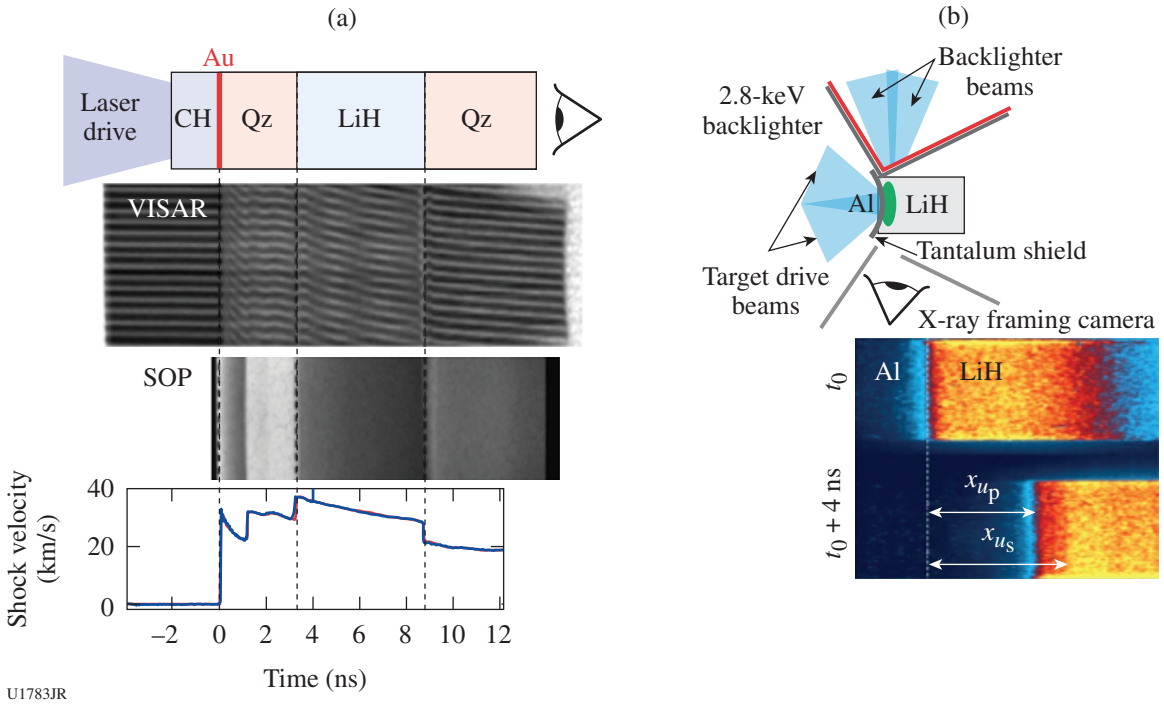


Figure 140.101
(a) LiH equation-of-state (EOS) measurements using a shock Hugoniot configuration and sample data using quartz as a reference standard. (b) Radiographic configuration and sample data for absolute EOS measurements.

⟨110⟩ orientations, with a key result shown in Fig. 140.102. The stress–density response of single-crystal diamond is in excellent agreement with the stress–density response of CVD (polycrystalline) diamond, but results indicate that the "pullback" features observed in NIF experiments are significantly reduced in the ⟨110⟩ orientation when compared to ⟨100⟩. Radiation–hydrodynamics simulations have demonstrated a better predictive capability for the ⟨110⟩ orientation versus ⟨100⟩, but the EOS at high pressure must be improved. Future "A versus B comparison" experiments of the EOS of diamond ⟨110⟩ versus ⟨100⟩ will greatly assist in our development of a diamond strength model and will further probe the stress–density response up to 10 Mbar.

***Extended X-Ray Absorption Fine-Structure Measurements of Ramp-Compressed Ta up to 200 GPa***
Principal Investigator: Y. Ping
Co-investigators: F. Coppari, J. H. Eggert, and G. W. Collins (LLNL); and B. Yaakobi (LLE)

Based on successful improvements of the extended x-ray absorption fine-structure (EXAFS) platform in FY13,[54] high-quality EXAFS data of compressed Ta up to 200 GPa were

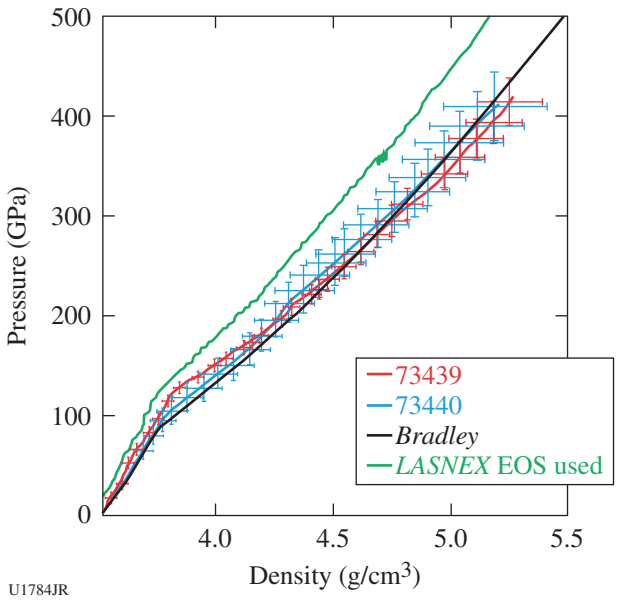


Figure 140.102
Newly measured pressure–density EOS data for single-crystalline diamond (red and blue curves), compared with prior data on polycrystalline diamond (black curve) and a reference EOS model (green curve).

obtained in FY14. The spectra at three pressures are shown in Fig. 140.103. The data at ambient conditions and at 65 GPa are consistent with Ta in the body-centered-cubic (bcc) phase, whereas the data at 200 GPa cannot be fit with the bcc phase, indicating that Ta undergoes a phase transition above 1 Mbar. Subsequent shots reached 350 GPa; however, the quality of this EXAFS data was not as good as previous data. Two reasons have been identified: First, the target alignment fiducial was not as accurate as before, reducing the number of observable channels from 5 to 2, significantly degrading the signal-to-noise ratio. Second, the backlighter brightness was ~40% less than on prior shots for reasons under investigation but not yet understood. Both findings provide important guidance for upcoming FY15 shots.

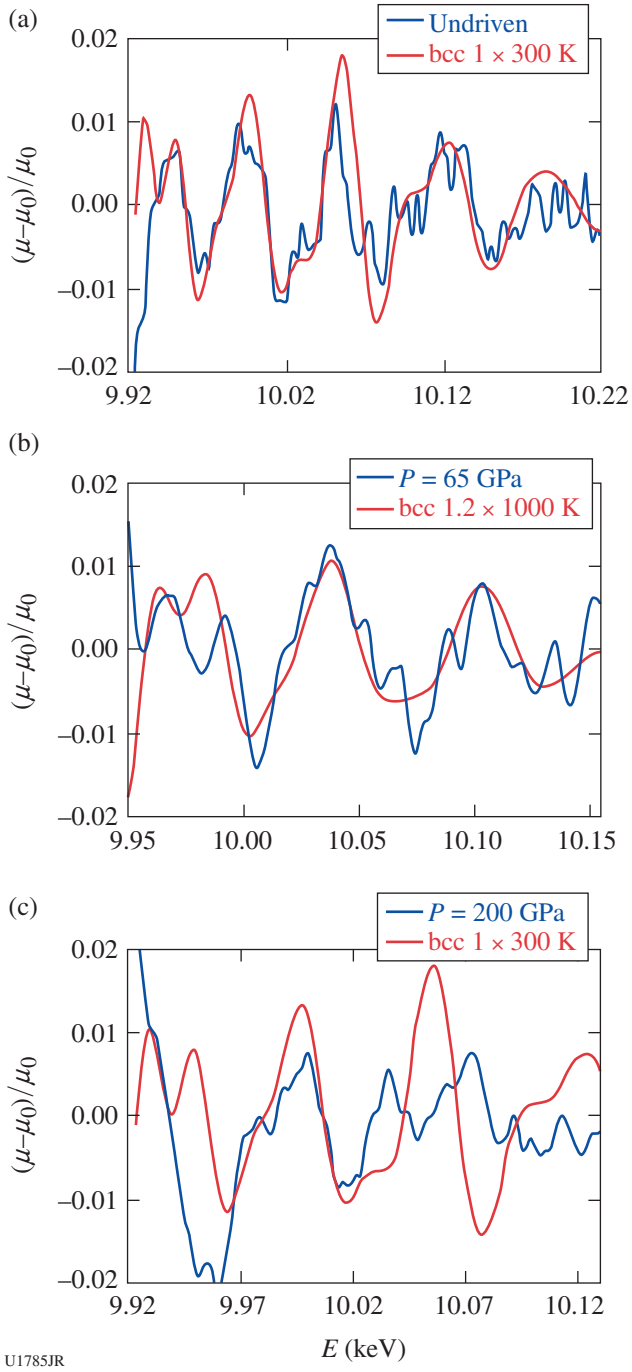


Figure 140.103
EXAFS data of Ta at (a) ambient conditions, (b) 65 GPa, and (c) 200 GPa. The measurements are shown in blue and the calculated EXAFS spectra for the bcc phase are shown for comparison in red. The 200-GPa data demonstrate that Ta is no longer in the bcc phase at such high pressures.

## 3. Hydrodynamics

### *Mix-Width Measurements of Accelerated Copper Foam on OMEGA*

Principal Investigator: K. Baker

This campaign evaluated two experimental configurations to determine the mix width of accelerated copper foams and measured the effect of the internal structure of the copper foams on the measured mix width to compare the experimental results with simulations. All the targets were cylindrical shock tubes with a reduced-density copper (Cu) foam, 1 g/cm$^3$, pusher-accelerated into a low-density carbonized resorcinol formaldehyde (CRF) foam at 50 mg/cm$^3$. The Cu foams, which could contain voids as large as 5 to 10 $\mu$m, were characterized via x-ray–computed tomography at either the Advance Photon Source or with an X-Radia MicroXCT. An example is displayed in Fig. 140.104.

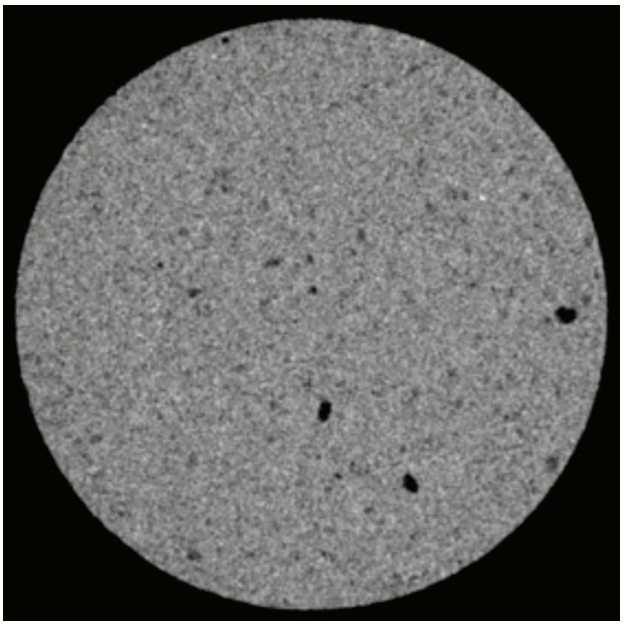


Figure 140.104
Reconstructed density profile of a copper foam. The voxel size of the reconstructed density is a cube, ~7 $\mu$m per side.

In the first configuration, the copper foam was reduced to an 800-$\mu$m-diam cylinder for the 120 $\mu$m closest to the Cu/CRF interface (to reduce edge effects in the images) and radiographed using the OMEGA EP backlighter. The removed Cu foam was replaced with CH. The second experimental configuration used a nickel $He_\alpha$ backlighter at 7.66 keV and a modified target design to accommodate the lower energy and minimize edge effects. Figure 140.105 shows a radiograph of the accelerated copper foam obtained using the OMEGA EP backlighter in the first configuration; Fig. 140.106 shows a lineout through the radiograph. The mix width for this foam was determined to be 135 $\mu$m.

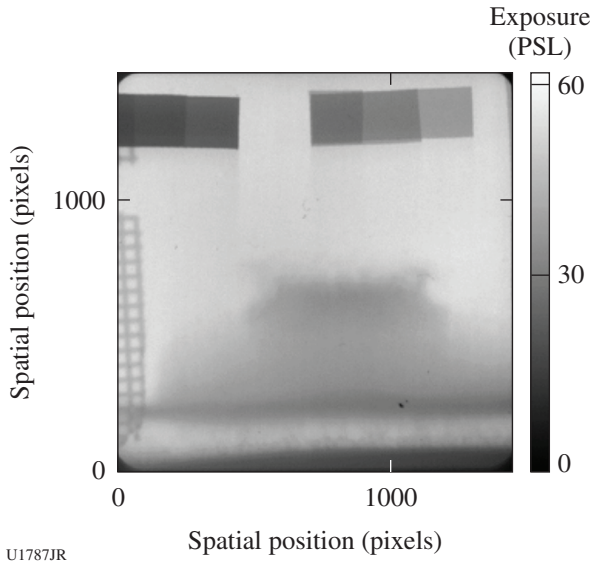


Figure 140.105
Radiograph of an accelerated copper foam 25 ns after the start of the hohlraum drive.

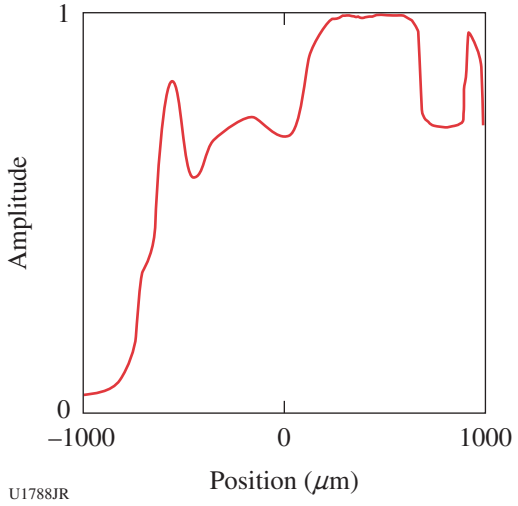


Figure 140.106
Vertical lineout through the accelerated copper foam shown in Fig. 140.105. The mix width comes from the 10% to 90% region between 0 and 250 $\mu$m of the graph.

### *Shock Transit Time Measurements on Novel CH Foams*

Principal Investigator: K. Baker

Shock breakout times from x-ray–driven samples of newly formulated $CH_{1.6}$ foams were measured on this campaign for comparison with traditional carbonized resorcinol formaldehyde (CRF) foams. The foams were positioned as packages on the end of a gold halfraum. To account for differences in the drive between experiments, the hohlraum drive history was measured via breakout from an aluminum witness plate, as well as via shock speeds in $\alpha$ quartz using the velocity interferometer system for any reflector (VISAR). As illustrated in Fig. 140.107, all shots returned good VISAR data, showing the breakout times of the foam into and out of the VISAR window and the breakout of the shock from the $CH_{1.6}$ or CRF foams. The corresponding VISAR unfold of the drive is inset in the lower right-hand corner of the figure. Comparison of experimental breakout times with simulations showed very good agreement with the CRF foams and good agreement with the $CH_{1.6}$ foams.

Additionally, three Ross pair channels were implemented in Dante to look at the gold M-band emission from the laser-driven hohlraum: Saran, silver, and Mo. Four Ross pair channels were also implemented in a time-integrated x-ray pinhole camera to look at the M-band wall emission: Si, Zr, Mo, Saran, and

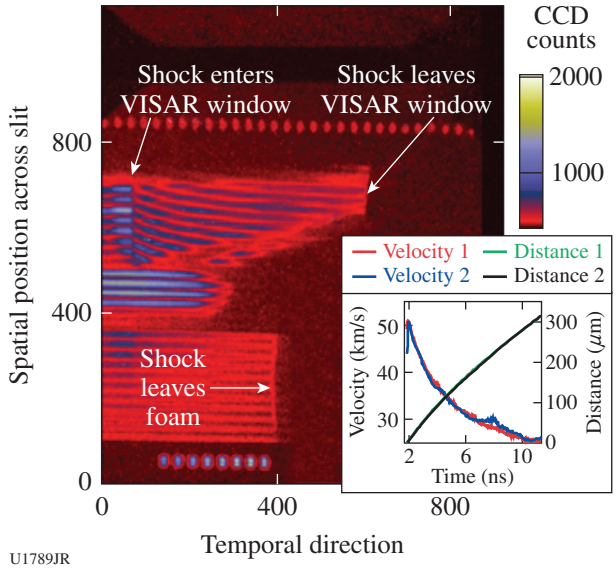


Figure 140.107
Drive and sample shock-speed measurements for $CH_{1.6}$ foams. CCD: charge-coupled device.

Kapton. These also look promising for determining the time-integrated M-band spatial and spectral distribution on the wall.

***Copper Foam Shock Breakout Measurements on OMEGA***
Principal Investigator: A. Moore

High-$Z$ metal foams made via a copper ceramic casting process and with ~1/10th solid density (~1 g/cm$^3$) have been developed at LLNL and are being produced routinely at the Atomic Weapons Establishment (AWE). This campaign investigated the relative shock propagation in foams having 1.0-$\mu$m characteristic pore sizes to qualify the equation of state (EOS) for use in future experiments. Propagation of a single shock through a material sample is an established technique to quantitatively validate the EOS model for that material via the simple dependence of the shock velocity on the pressure and, therefore, the internal energy of the material, but it had not been applied previously to these novel foams. The platform to measure the shock transit time in Cu foams was unchanged from prior campaigns of this type, using a 1.6-mm-diam, 1.0-mm-long hohlraum driven by 5.5 kJ of 351-nm laser energy using 15 beams of the OMEGA Laser System. To improve the measured accuracy of the x-ray drive from the hohlraum, however, an Al witness sample was added so that the target package on the halfraums included a foam sample with a polystyrene ablator along a 60-$\mu$m aluminum sample backed by 300 $\mu$m of quartz. When the shock breaks out into the quartz, it can be measured directly using the active shock breakout (ASBO) or VISAR diagnostic, and the pressure history at the hohlraum ablator interface can be inferred.[55]

In the experiments the drive pulse shape was varied to extend the density and temperature regimes probed. A 1.0-ns square pulse shape was used on experiments with the $C_8H_8$ ablator and a 2.7-ns ramp-shaped laser pulse on experiments without this ablator. The copper foam samples were 0.7 mm in diameter and nominally 0.35 mm in thickness, with a nominal density of 1.0 g/cm$^3$. On these experiments the hohlraums reached a peak effective radiation temperature of 208±5 eV.

Data from the streaked optical pyrometer (SOP) were obtained on five shots, an example of which is shown in Fig. 140.108(c).

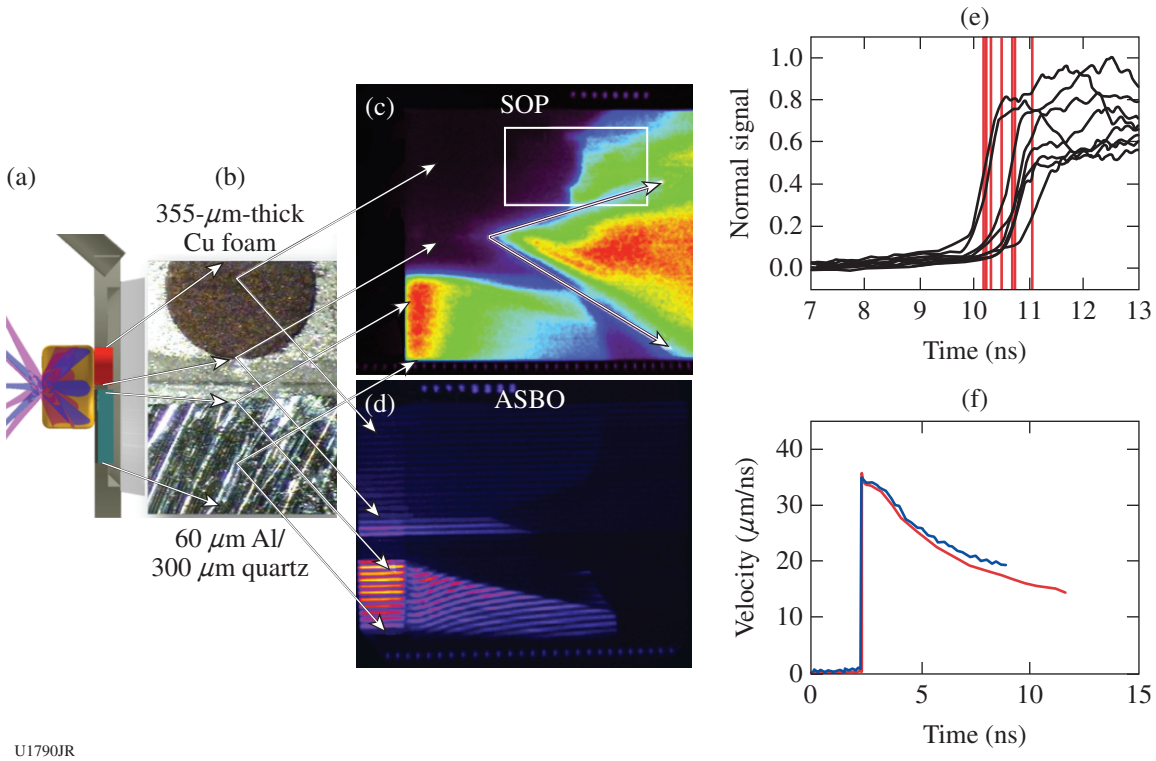


Figure 140.108
Streaked optical pyrometer (SOP) and active shock breakout (ASBO) data from shot 71664 for a hohlraum with no CH ablator driven by a SS2704vA01 shaped pulse. (a) VisRad diagram of the target. (b) Images of the Cu foam (355 $\mu$m thick at a density of 1.084 g/cm$^3$) and Al/quartz surface viewed by the ASBO and SOP. (c) Raw SOP image data with arrows highlighting edge effects caused by the expanding joint between the Cu foam and Al/quartz samples. (d) Raw ASBO image data showing shock breakout times. (e) Normalized optical emission caused by the shock breakout showing that the shock in the Cu foam arrived at 10.48±0.33 ns. (f) Shock velocity in the quartz peaked at 34 km/s, within 3 km/s of pre-shot predictions.

These data indicate that some spatial structure exists in the shock traveling through the Cu foam, but the average shock breakout time was still determined to within ±3%. The ASBO was used on three shots to measure the decaying shock velocity as a function of time in the quartz, returning data very close to pre-shot predictions.

### *High-Energy Point-Projection Backlighter Experiments on OMEGA*

Principal Investigator: K. Baker

The goal of this campaign was to evaluate high-energy backlighters for use on the NIF. The backlighter energies needed on the NIF range from 35 to 45 keV. Previous conversion efficiency (CE) measurements with short-pulse lasers at $1\omega$ indicated a CE of $7 \times 10^{-5}$ for tin through $4 \times 10^{-5}$ for samarium. These efficiencies are close to meeting NIF-required fluences using the Advanced Radiographic Capability short-pulse laser being deployed on the NIF but would require that the NIF detector be placed much closer to the target than previously. However, the previous experiments had been conducted with wire backlighters, and other laser–target geometries are possible to improve x-ray fluence yields. In this campaign, the OMEGA $3\omega$ lasers were used to drive a point-projection backlighter with a Ta pinhole to reduce the source size. Tin and samarium targets were fielded, with and without a prepulse, using either thick solid or exploding-foil plasmas. Figure 140.109 illustrates the target geometry. The transmission crystal spectrometer (TCS) measured the tin and samarium spectra. Figure 140.110 shows the TCS spectra from these shots, together with a prior $1\omega$ short-pulse silver wire backlighter spectrum.

The highest conversion efficiency was seen for thick foils without a prepulse. The prepulsed plasmas may have refracted the drive laser beams, leading to a reduction of yield. Resolution tests using a sharp, opaque gold edge had blurry features for all the targets, indicating a large source size. This could be improved with a significantly thicker or more-advanced pinhole substrate.

### *Radiographic Techniques for Drive Symmetry*

Principal Investigator: D. Martinez

Hohlraum experiments were performed on the OMEGA Laser System to develop and exploit radiographic techniques to study the symmetry of foam balls illuminated with hohlraum x rays. Using a joint OMEGA EP configuration, 10-$\mu$m-thick Ag wire backlighters mounted on 300 × 300-$\mu$m-sq, 10-$\mu$m-thick polyimide foils were irradiated with the ~1-kJ short-pulse OMEGA EP beam in a configuration similar to that expected on the NIF Advanced Radiographic Capability short-pulse laser, with a pulse duration of ~50 ps at a laser intensity of ~$2 \times 10^{17}$ W/cm$^2$. Point-projection x-ray radiographs of the targets with a magnification of ~40 were measured on image plates using the HERIE diagnostic positioned ~50 cm from target chamber center. The high-energy bremsstrahlung spec-

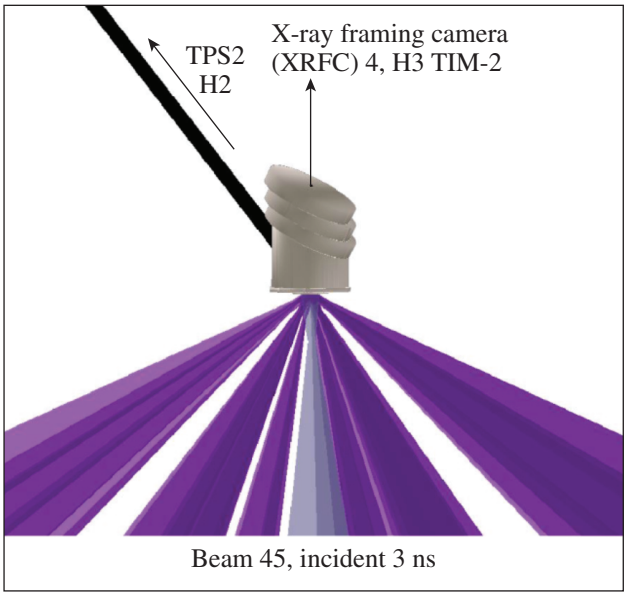


Figure 140.109
Target geometry used to evaluate the efficacy of high-energy point-projection backlighters. The pinhole substrate was 200-$\mu$m-thick Ta, sandwiched between 100-$\mu$m disks of CH to limit the number of hot electrons reaching the pinhole substrate.

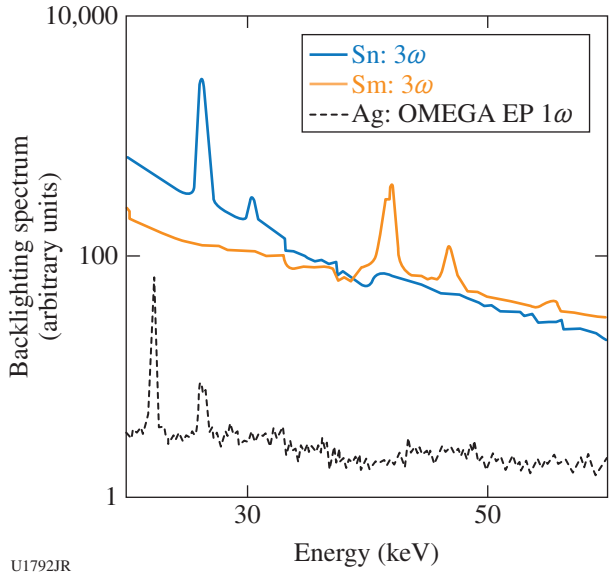


Figure 140.110
Backlighter spectra measured with the transmission crystal spectrometer (TCS).

trum was used to diagnose the target. Figure 140.111 shows data from resolution test objects illustrating the radiographic signal and contrast, which were consistent with previous Ag $\mu$-wire experiments using OMEGA EP and demonstrated 17-$\mu$m resolution. Transmission of the backlighter through a Cu step wedge was measured and used to infer the hot-electron temperature by modeling the backlighter with a simple single-temperature bremsstrahlung spectrum. These experiments produced high-quality radiographs and established a baseline for future complex hydrodynamics experiments on the NIF.

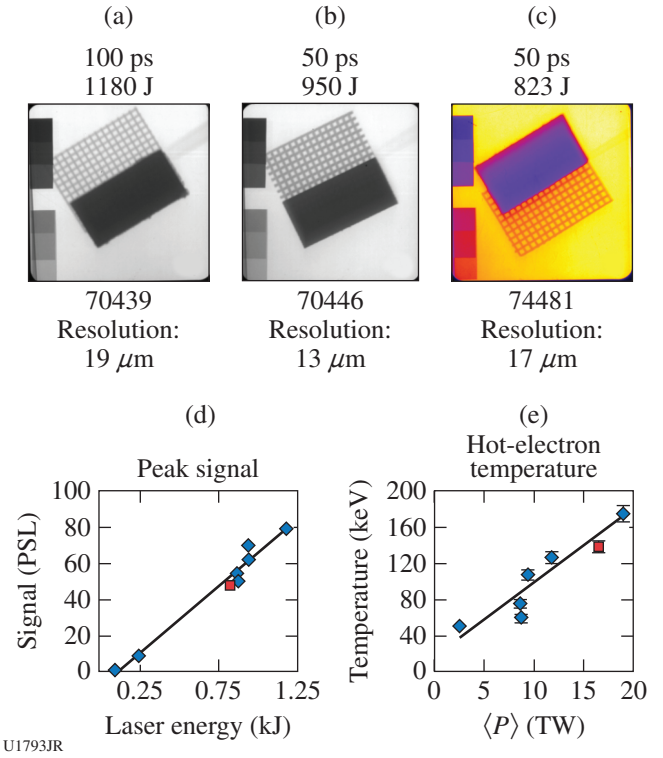


Figure 140.111
[(a),(b)] Silver $\mu$-wire backlighter from past Toto experiments compared with (c) current performance. [(d),(e)] Trends in the peak signal and approximated hot-electron temperature show that results are consistent with previous Ag $\mu$-wire experiments using the same filtering and diagnostic.

### *Proton Heating of Copper Foams on OMEGA EP*

Principal Investigator: A. Moore

High-$Z$ metal foams made by a copper ceramic casting process at ~10% of solid density (~1 g/cm$^3$) provide a novel target material for use in high-energy-density–physics experiments on the NIF, Orion, and OMEGA. For experimental results to be constraining to radiation–hydrodynamics simulation codes, however, the materials must be well characterized, with a good understanding of the material opacity and EOS. These proton-heating experiments developed a platform to access the EOS of the Cu foam via isochoric heating of the material with protons and investigated the feasibility of scaling the approach to the NIF using the upcoming Advanced Radographic Capability short-pulse laser.

Proton heating offers a novel way to measure the low-temperature EOS since the energy is absorbed near-isochorically by the Cu foam, especially when compared to heating with x rays or via direct laser irradiation.[56] If the density profile of the expanding plasma is measured, the isentrope can be extracted directly. These experiments studied density measurements of proton-heated disks of Al and Cu foam and Cu wires. The proton source consisted of a 10-$\mu$m-thick, 500-$\mu$m-diam Au foil irradiated by a high-intensity (~$1 \times 10^{18}$ W/cm$^2$), 1053-nm, 10-ps laser pulse from the OMEGA EP laser. This generated a proton beam through target-normal sheath acceleration (TNSA).[57] The Cu foam and other samples were placed 2 mm from the proton source along the normal to the Au disk. To radiograph the sample expansion, a Ni foil backlighter was positioned 5 mm from the sample perpendicular to the foam disk normal. Beamlines 1, 3, and 4 delivered 1-ns, 351-nm laser pulses to this Ni foil with a 10-ns delay after the short-pulse beam, generating He$_\alpha$ x rays (7.9 keV) to radiograph the expanding Cu foam.

The proton spectrum was measured using a radiochromic film (RCF) stack 25 mm past the Au disk source. Figure 140.112 shows the proton "auto-radiograph" measured using the RCF stack when the Cu-foam disk was present and heated by the

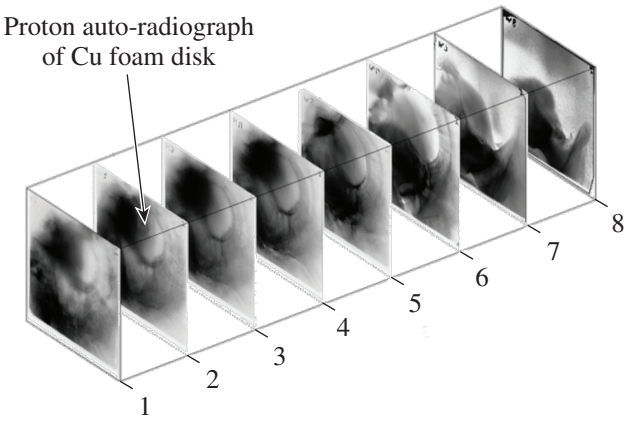


Figure 140.112
"Proton auto-radiograph" of the proton-heated Cu foam measured by a radiochromic film pack in the near-target arm diagnostic.

protons. Figure 140.113 shows the success of the area-backlit radiography in obtaining images of the unheated and heated Cu foams. Work is ongoing to establish the relative contribution of x-ray and proton heating at the front surface of the Cu foam.

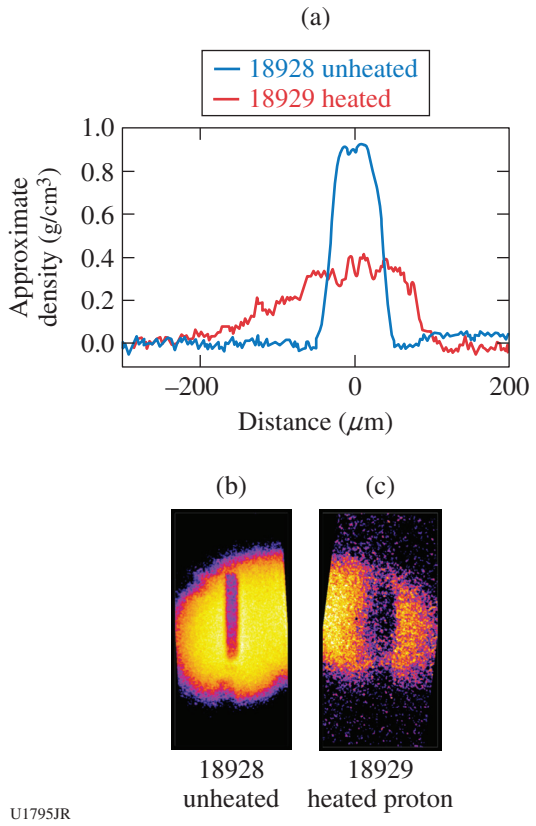


Figure 140.113
Radiograph of unheated (shot 18928) and proton-heated (shot 18929) Cu foam after 10 ns of free expansion. The density profile of the heated foam is obtained assuming no significant changes to the opacity of the Cu foam when heated and calibrating the backlighter x-ray spectrum using the predicted transmission of the 0.9-g/cm$^3$ unheated foam.

## 4. Radiation Transport and Opacity

### *X-Ray Spectroscopy of Fully Characterized Non-LTE Gold Plasmas*

Principal Investigator: G. Brown

Co-investigators: J. A. Emig, M. E. Foord, R. F. Heeter, D. Liedahl, C. A. Mauche, J. S. Ross, M. B. Schneider, and K. Widmann (LLNL); and D. H. Froula and J. Katz (LLE)

Experiments on the NIF have shown a need for a more-precise understanding of the radiative properties of non-LTE gold to improve x-ray drive simulations of laser-driven hohlraums used in inertial confinement fusion and other areas of high-energy-density physics. Expanding on prior work,[58] the AuNLTE-14A Campaign fielded laser-heated beryllium-tamped gold/iron/vanadium foils, with the following primary objectives: (1) high-resolution measurements of time-resolved gold M-band spectra from 2 to 5.5 keV, simultaneously with (2) measurements of the plasma electron temperature ($T_e$) via K-shell emission from helium-like V and Fe ions, (3) independent measurements of $T_e$ using Thomson scattering in a transmission geometry, and (4) measurements of the sample density by time-resolved spectral imaging of its expansion normalized to the initial thickness.

This campaign acquired data for three different target types: (a) "thicker" and (b) "thinner" mixtures of Au, Fe, and V, and (c) a mixture of Fe and V without Au. Simultaneous K-shell spectra from He-like $Fe^{24+}$ and $V^{21+}$ and M-band Au, together with expansion images, were acquired for all three target types (Fig. 140.114). After some adjustments, ion-acoustic–wave (IAW) "transmission" Thomson-scattering data were successfully obtained, for the first time, from plasmas at electron densities >$10^{21}$/cm$^3$. Some of the IAW data were obtained simultaneously with the other measurements, with measured $T_e$ in the ~1-keV range. Although detailed data analysis is ongoing, this suite of measurements is potentially the most-comprehensive non-LTE data set recorded to date. If confirmed in the final analysis, this will yield improved validation benchmarks for non-LTE models.

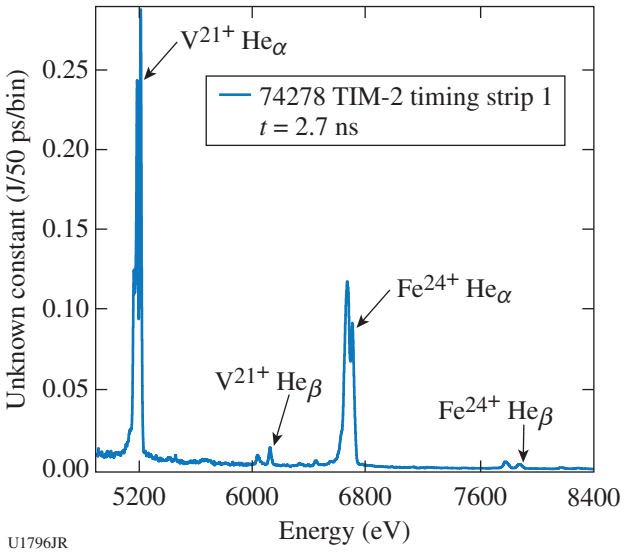


Figure 140.114
Spectrum measured by the MSpec spectrometer of the x-ray emission from K-shell transitions in highly charged vanadium and iron.

5. Material Dynamics and Strength

***Classical Rayleigh–Taylor Growth***
Principal Investigator: C. Huntington

Within the material strength effort aimed at assessing the strength of various metals at high pressure and a high strain rate, the goal of the Classical Rayleigh–Taylor Campaign is to measure Rayleigh–Taylor (RT) growth of samples that behave "classically," i.e., can be fully modeled using a fluid description. Without the stabilization of strength, classical RT growth is characterized by a growth rate $\gamma = \sqrt{kgA_n}$, where $k$ is the wavelength of the unstable mode, $g$ is the acceleration, and the Atwood number $A_n$ quantifies the magnitude of the density jump at the interface. The sample in the experiment is accelerated by the stagnation of a releasing shocked plastic "reservoir," which is directly driven by ~1 kJ of laser energy. The growth of preimposed ripples is recorded using transmission x-ray radiography of a vanadium $He_\alpha$ source, where the opacity of the sample is calibrated to the ripple amplitude. The FY14 campaigns collected data for ripples with 30-$\mu$m, 60-$\mu$m, and 120-$\mu$m wavelengths. An example of 60-$\mu$m data is shown in Fig. 140.115. The area backlighter generates an image with varying brightness across the image; the brightest region is analyzed, and a background curve that captures the shape of the x-ray illumination is subtracted. The pre-shot metrology and measured $\rho R$ of the driven sample together yield the growth factor, which is compared to models of RT growth.

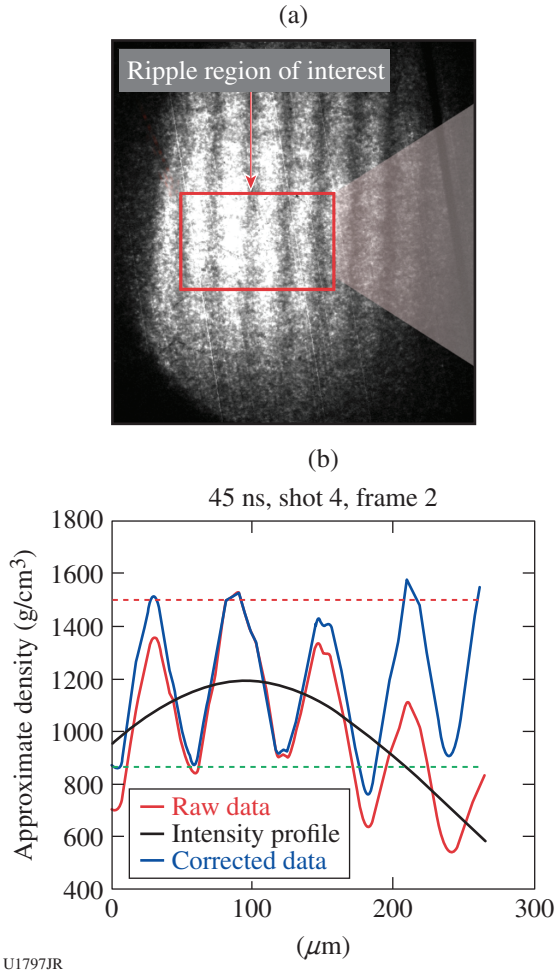


Figure 140.115
(a) A region of interest (shown in red) is selected from a piece of data. (b) The integrated profile of these ripples is shown in red, and the "corrected" trace is shown in blue, after being adjusted by the black curve.

6. X-Ray Source Development and Application

***Calibration of the NIF X-Ray Spectrometer***
Principal Investigator: S. P. Regan (LLE)
Co-investigators: F. Pérez, M. A. Barrios Garcia, K. B. Fournier, G. E. Kemp, J. Pino, J. Emig, and S. Ayers (LLNL); M. Bedzyk, M. J. Shoup III, A. Agliata, B. Yaakobi, and F. J. Marshall (LLE); and J. Jaquez, M. Farrell, and A. Nikroo (GA)

The NIF x-ray spectrometer (NXS) is an elliptically bent crystal spectrometer that provides both time-resolved and time-integrated spectral measurements. The NXS covers a spectral range from 2 to 18 keV in ten discrete spectral windows, each corresponding to a particular crystal configuration. Two FY14 OMEGA campaigns provided data for a photometric calibration for all 30 NXS crystals (each configuration has three interchangeable crystals), by uniformly irradiating millimeter-scale spherical targets coated with various cocktails of mid-$Z$ elements. The targets were designed to generate either L-shell or K-shell emission within the energy range of the NXS' spectral windows. Five different targets were designed for these calibration shots: four coated with CrNiZn, ZnZr, SiAgMo, or: TiCrAg coatings, and one uncoated CH target used to measure continuum emission. Target emission was recorded by five different spectrometers for each shot: three NXS and two XRS spectrometers. The XRS spectrometer crystals were absolutely calibrated off-line and provide an absolute x-ray yield from which the photometric calibration of the NXS crystals will be derived. All data were recorded onto Fuji spatial resolution (SR)-type image plates, which are also being calibrated off-line to provide an end-to-end absolute calibration for the NXS spectrometer.

In preparation for the OMEGA calibration shots, hydrodynamic simulations using *HYDRA* and *ARES* were performed

to predict the emission from the metal-coated targets. Figure 140.116 compares these simulation results with the absolute x-ray yields measured by the XRS spectrometer for all four metal-coated targets. Here, target types A, B, C, and D correspond to SiMoAg, TiCrAg, CrNiZn, and ZnZr coatings, respectively. The predicted line emission agrees qualitatively with the XRS results. Details on the simulations and comparison with the XRS data have been published.[59] A more-rigorous comparison between model and measured data will be performed once the absolute NXS calibration is finalized. Figure 140.117 shows sample data measured for one of the NXS spectrometers. This shot used a CrNiZn-coated target; measured data on the

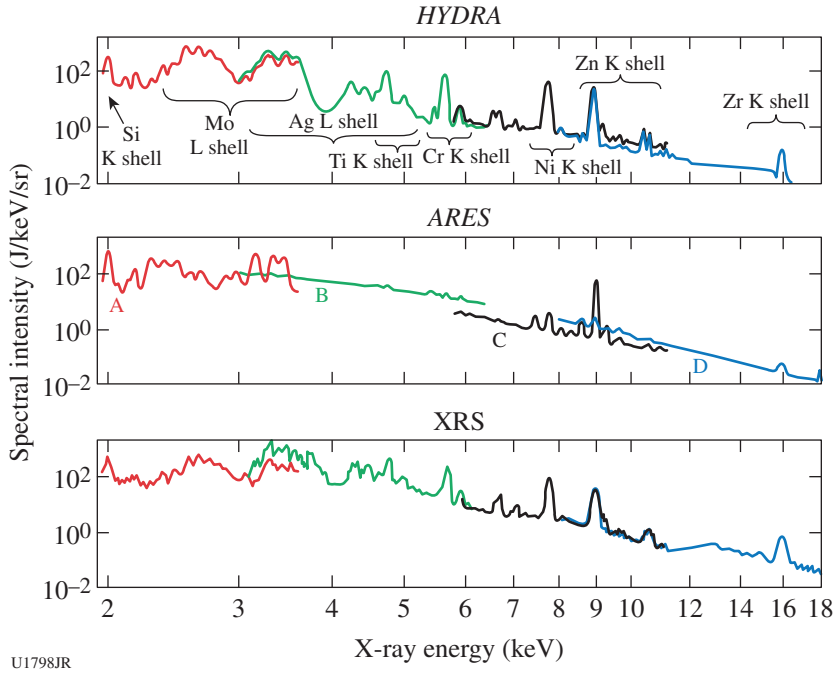


Figure 140.116
Simulated spectra using *HYDRA* and *ARES* hydrodynamics codes are compared to measured XRS data for metal-coated targets A (SiMoAg), B (TiCrAg), C (CrNiZn), and D (ZnZr). Good qualitative agreement between data and simulations is observed.

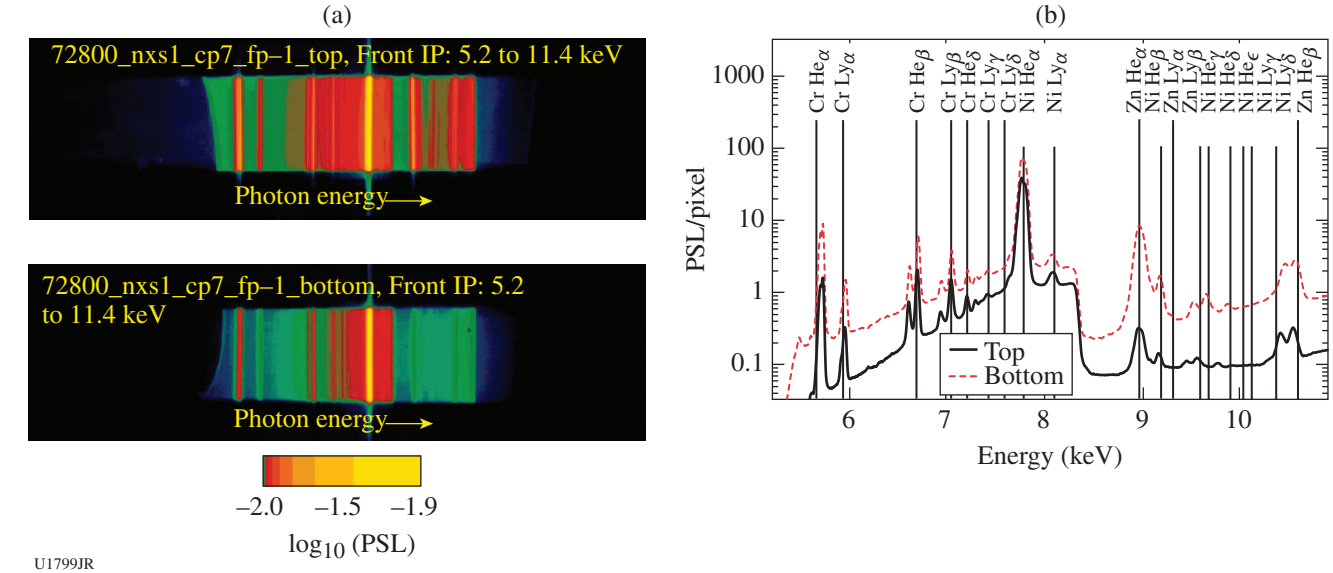


Figure 140.117
Measured data on the NIF x-ray spectrometer (NXS) for one of ten configurations. (a) Measured spectra recoded onto an spatial resolution (SR) image plate, with (b) corresponding data lineouts.

top and bottom image plate are shown in Fig. 140.117(a), with corresponding lineouts in Fig. 140.117(b). Several K-shell emission lines from Cr, Ni, and Zn were observed and identified.

### *X-ray Source Fluence Measured as a Function of Viewing Angle*

Principal Investigator: M. Barrios Garcia
Co-investigators: M. J. May, K. B. Fournier, F. Pérez, and J. D. Colving (LLNL); F. Girard and B. Villette (CEA); S. Seiler and J. Davis (DTRA); and J. Fisher and C. D. Newlander (Fifth Gait Technologies)

The NSView Campaign was designed to understand target fluence as a function of viewing angle for x-ray source applications, to better understand the fluence delivered to material samples and other test objects using these or similar targets as x-ray sources. In this campaign, stainless-steel–lined cavities were symmetrically driven with ~20 kJ of $3\omega$ light delivered in 1 ns. To provide distinct view angles for the diagnostics fielded, three different laser–target orientations were used throughout the day. The target x-ray emission was recorded with a suite of x-ray diagnostics, enabling one to characterize both the temporal evolution and spectral content of the source.

Figure 140.118 shows the measured spectra recorded using the Dante and DMX spectrometers, for view angles relative to the target symmetry axis of 0°, 42°, and 79°, and 5°, 46°, and 75°, respectively. These instruments observe a pronounced view angle dependence on the measured flux for x-ray energies below 4 keV, but little to no dependence on a view angle is observed for the Fe K-shell emission at higher energies. The observed x-ray emission from 4 to 9 keV, describing the Fe K shell, is consistent with a volumetric emitter that is therefore optically thin and independent of view angle. The emission from 2 to 4 keV is also consistent with a volumetric emitter, once geometric and optical-depth corrections are considered. These factors cause the x-ray yield to decrease as a function of increasing view angle. For x-ray emission between 0 to 2 keV, corresponding to the Fe L shell, the observed yields peak at angles ~42° to 46° and show the largest variation between view angles. This low-energy x-ray yield is also the dominant contribution to the total x-ray production. A spectral reconstruction model developed to match these observations suggests the x-ray output between 0 to 2 keV is best described as a surface emitter, where the emission originates from the cavity's inner walls and laser entrance hole. Figure 140.119 compares this

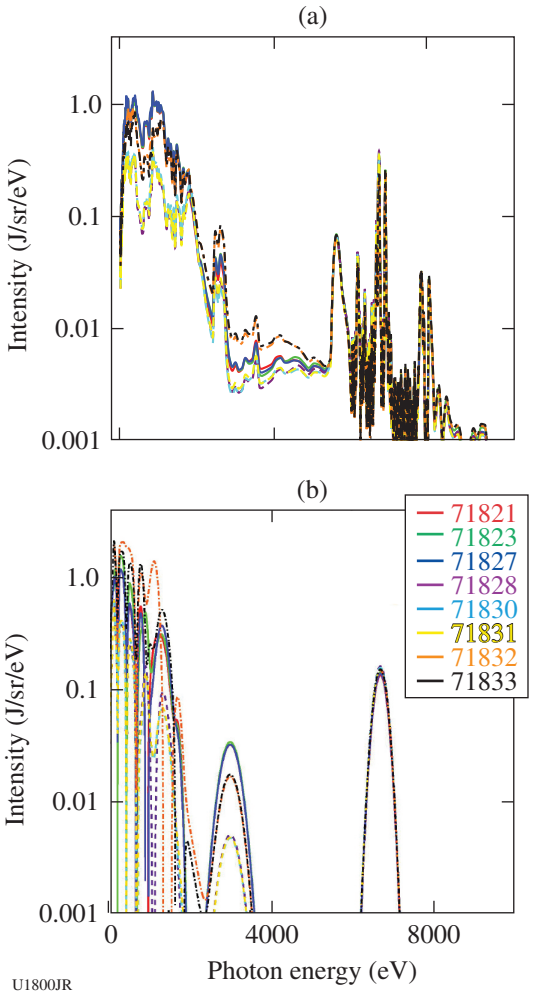


Figure 140.118
Measured (a) DMX and (b) Dante time-integrated spectra.

model with the data. Future work will measure x-ray emission for intermediate angles to better constrain the model and investigate other types of targets.

### *Optimizing X-ray Emission from Nanostructured Copper-Doped Foams*

Principal Investigator: F. Pérez (LLNL)
Co-investigators: J. D. Colvin, K. B. Fournier, M. J. May, S. O. Kucheyev, and S. Charnvanichborikarn (LLNL); and T. E. Felter (Sandia)

In FY13 the X-Ray Source Development team, funded by the Defense Threat Reduction Agency, began a study of the x-ray emission from laser-irradiated Cu-doped foams. The goal is to generate bright, nanosecond-class x-ray pulses

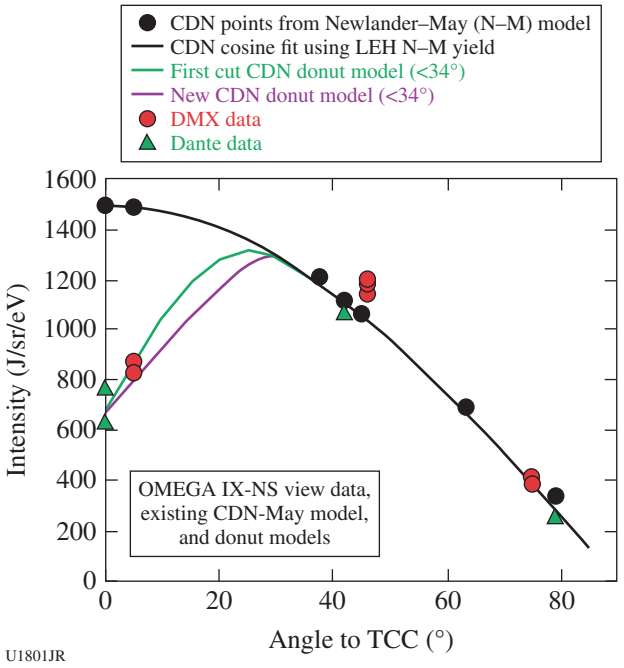


Figure 140.119
Dante and DMX total x-ray yield as a function of view angle, compared to the developed model.

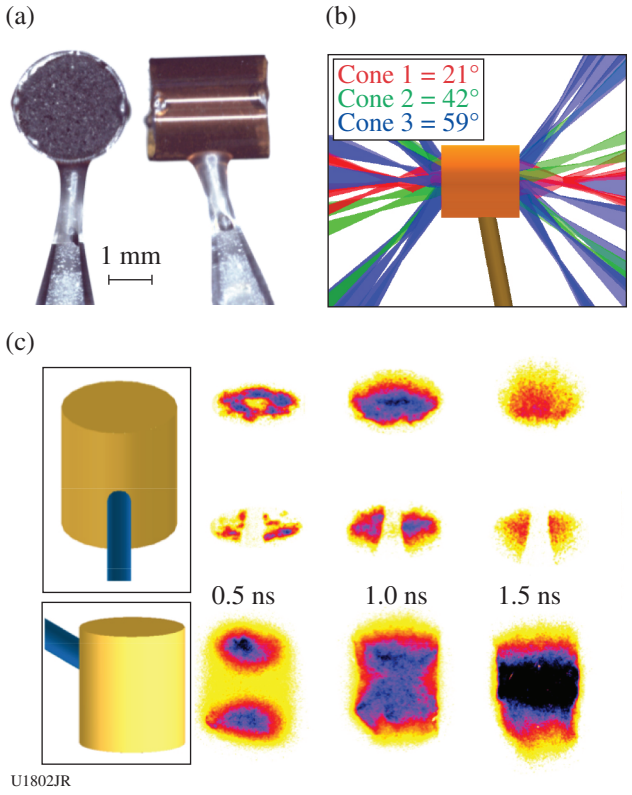


Figure 140.120
(a) Foam sample held in a plastic tube; (b) laser irradiation pattern of the OMEGA laser; (c) x-ray emission images at different times relative to the beginning of the irradiation. The top and bottom rows correspond to foams of 50- and 8-mg/cm$^3$ density, respectively.

with ~9-keV photon energies. A novel fabrication technique successfully produced Cu-doped carbon foams with densities below 50 mg/cm$^3$ for FY13 shots. In 2014 this effort continued, developing another novel foam-fabrication method and yielding, for the first time, doped foam densities below 10 mg/cm$^3$.

These C/Cu foams [Fig. 140.120(a)] were irradiated by 40 beams of the OMEGA laser to generate x rays [Fig. 140.120(b)]. Various foams, with densities ranging from 5 to 50 mg/cm$^3$, were shot on two campaigns. Measurements of the x-ray yield show that the optimal density is close to 10 mg/cm$^3$, where the conversion efficiency from laser energy into Cu K-shell x-ray energy reaches 0.8%. The dynamics of the laser–foam interaction were also investigated using framing and streak cameras, revealing that the low-density foams are heated over a much larger volume [Fig. 140.120(c)]. X-ray spectra also provided information on the plasma temperature. These measurements are currently being used as a simulation benchmark, with the wide range of densities providing tight constraints.

In FY14 this research also led to pure-Cu foams under 20 mg/cm$^3$, which will be fielded in FY15 experiments. This type of material has never been fabricated before and is expected to achieve even higher x-ray yield.

ACKNOWLEDGMENT

This work was performed under the auspices of the U.S. Department of Energy by Lawrence Livermore National Laboratory under Contract DE-AC52-07NA27344.

## FY14 LANL Experimental Campaigns

In FY14, LANL scientists conducted 218 target shots at the Omega Laser Facility including 206 shots on OMEGA and 12 on OMEGA EP. The ICF program accounted for 40 of these shots and the HED program accounted for 174.

### *Shear*

The Los Alamos National Laboratory (LANL) Shear Campaign is examining instability growth and its transition to turbulence relevant to mix in ICF capsules. An experimental platform was developed with antisymmetric flows about a shear

interface to examine the Kelvin–Helmholtz (KH) instability growth. The platform consists of a directly driven shock-tube target with an internal physics package consisting of two hemi-cylindrical foams separated by a layer of tracer material (Fig. 140.121). Gold plugs are situated on opposing ends of the foams to limit shock propagation from the direct drive to only one end of the foam; this sets up a pair of pressure-balanced counter-propagating shocks about the tracer layer. Measurements of the tracer layer (shear interface) mixing dynamics are used to benchmark the LANL Besnard−Harlow−Rauenzhan (BHR) turbulence model.[60] The mixing dynamics are characterized by measuring the mix width of the layer as well as examining multidimensional structure growth along the layer surface.

The FY14 Shear Campaign focused on examining the model's initial condition parameter space by varying the characteristics of the target's tracer layer. In November 2013 the Shear Campaign completed a set of experiments varying the tracer material and thickness, using 12-$\mu$m and 20-$\mu$m Ti tracer foils as opposed to the 20-$\mu$m Al tracer foils used in previous years. In May 2014 the Shear Campaign completed a two-day platform test of streaked imaging for measuring the mixing width of the tracer layer, demonstrating that streaked imaging could be a viable alternative to radiography. The May 2014 experiments were also a successful test for using a controlled increase in the tracer layer's surface roughness as another avenue for changing the mixing/instability initial conditions (see Fig. 140.122). Experiments with enhanced

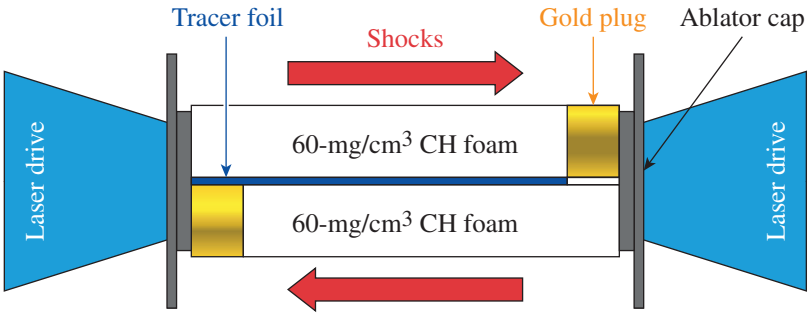


Figure 140.121
Schematic of counter-propagating shear experiment.

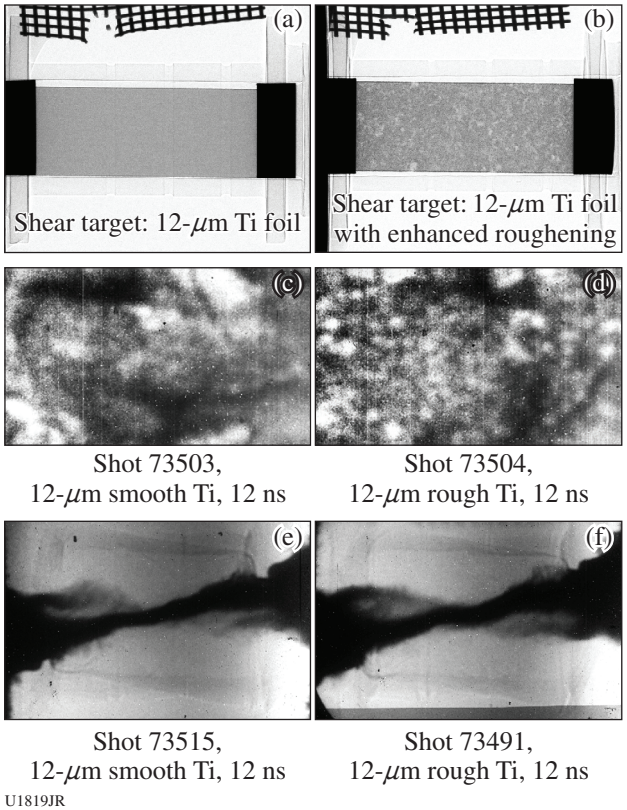


Figure 140.122
X-ray radiographs of edge-on and plan-view shear experiment for smooth and enhanced surface roughness foils.

roughened foils have shown a qualitative difference in early-time tracer-layer surface structures compared to previous experiments. Preliminary analysis also suggests that greater surface roughness can be used to alter the growth rate of the tracer layer.

### *CoaxDiff*

The Coaxial Diffusion Experimental Campaign on the OMEGA laser is a radiation transport experiment specifically designed to challenge the implementation of implicit Monte Carlo (IMC) radiation transport techniques in radiation–hydrodynamics simulations. A gold half-hohlraum is driven with 20 OMEGA laser beams to generate x rays that interact with a low-density $SiO_2$ foam. The x-ray drive from the hohlraum is modified using filtration and apertures to move the physics of the radiation transport through the foam into a regime that requires the use of IMC radiation transport.

In FY14, the coaxial diffusion platform demonstrated the ability to radiograph the hydrodynamic response to the Marshak wave (heat front) when it transitioned from super- to subsonic. This gives a measure of the total energy deposited into the foam as well as information on the anisotropy of the radiation source. Experiments were also performed that demonstrated a new technique to introduce a localized Ti dopant into the foam for absorption spectroscopy measurements (Fig. 140.123) without impacting the overall radiation transport of the experiment. This was achieved by fabricating a Ti-doped $SiO_2$ foam and inserting it into our standard $SiO_2$ foam.

### *WDFeos*

In FY14 we built on recent results of equation-of-state (EOS) measurements of shocked silica ($SiO_2$) aerogel foam at the Omega Laser Facility, which used the velocity interferometer system for any reflector (VISAR) diagnostic to obtain shock-velocity measurement in the foam and a streaked optical pyrometer (SOP) to measure temperature in the shock front. Foams are important low-density pressure standards used in many high-energy-density experiments, including the novel technique of shock and release, and are also used in radiation transport and hydrodynamic instability experiments. Because of their many applications, foams are heavily studied materials and have a well-known Hugoniot curve. This work complements the velocity and pressure measurements with additional independent temperature data providing the full EOS information within the warm-dense-matter regime for the temperature interval of 1 to 15 eV and shock velocities between 10 and 40 km/s, corresponding to shock pressures of

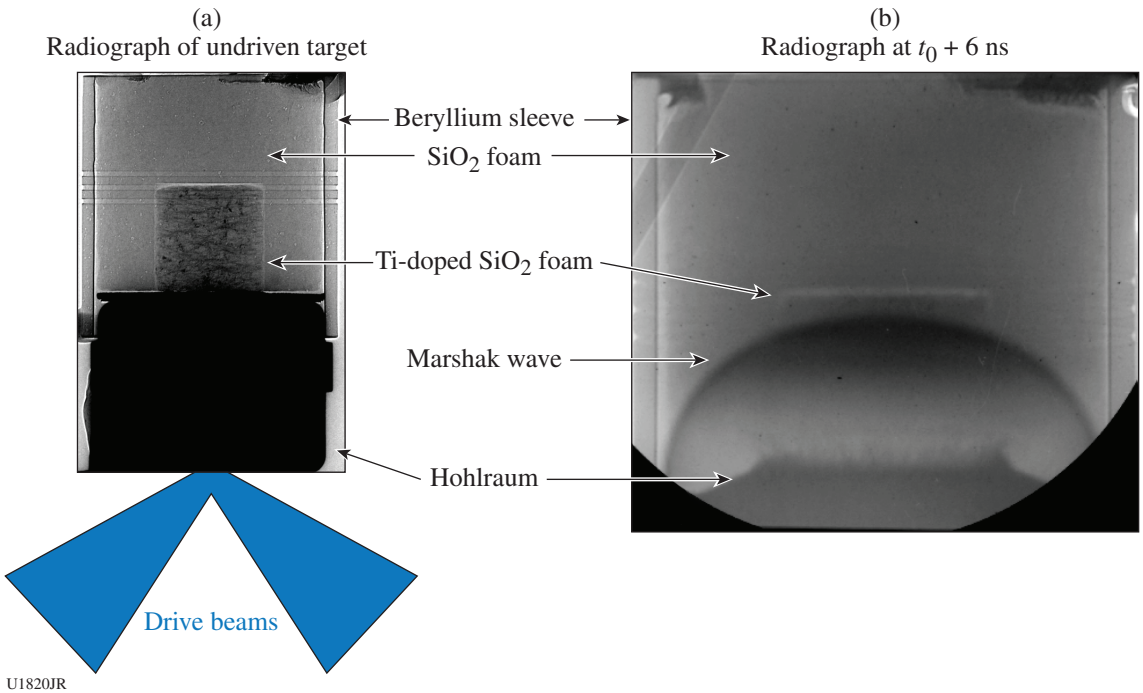


Figure 140.123
(a) A static radiograph of an undriven target using a nested Ti-doped foam for absorption spectroscopy. (b) An x-ray radiograph of the driven target 6 ns after the 1-ns-long hohlraum drive shows a well-developed Marshak wave without discontinuities at the $SiO_2$/Ti-doped $SiO_2$ foam interface. This indicates that the titanium dopant has been introduced in a way that is noninvasive to the overall radiation transport of the problem.

0.3 to 2 Mbar. The experimental results were compared with hydrodynamic simulations and EOS models. We found that the measured temperature was systematically lower than suggested by theoretical calculations. Simulations provide a possible explanation that the emission measured by optical pyrometry comes from a radiative precursor rather than from the shock front, which could have important implications for such measurements. Our previous findings were summarized in Ref. 61.

Consequently, in the latest experiments we used imaging x-ray scattering to directly measure the temperature in the shocked aerogel without relying on self-emission that appears to come from the precursor plasma, not from the bulk of the plasma within the shock wave. In FY14 we focused on CH foams at 0.15 g/cm$^3$, which are not transparent like silica aerogel. The target designs are shown in Fig. 140.124. VISAR and SOP diagnostics are used to obtain shock velocity from breakout timing in a stepped foam sample. A shock wave is driven by laser ablation in the planar-layered targets using 14 OMEGA beams (1-ns square pulse) stacked to give 2-ns drive at high intensity (450 J/beam) and low intensity (300 J/beam). An additional ten OMEGA beams were used to create a Ni $He_\alpha$ x-ray line at 7.8 keV by irradiating a Ni foil at ~2 to 3 × 10$^{15}$ W/cm$^2$, which was used to probe the conditions with x-ray scattering. The scattered signals were measured by the imaging x-ray Thomson spectrometer (IXTS). We obtained excellent VISAR and SOP data, which provided us with consistent shock-velocity measurements (see Fig. 140.125). We also obtained our first x-ray scattering data from the low-density CH foams. The scattering spectra were clear and the signal-to-noise ratio was excellent; however, we found that the quartz pusher was mixing into the field of view of the IXTS diagnostic, causing contamination of the scattering signal (see Fig. 140.126). Based on radiation–hydrodynamics simulations, we have redesigned the scattering targets to use a thicker Al pusher that should minimize this contamination and provide us with scattering data that simplifies the analysis.

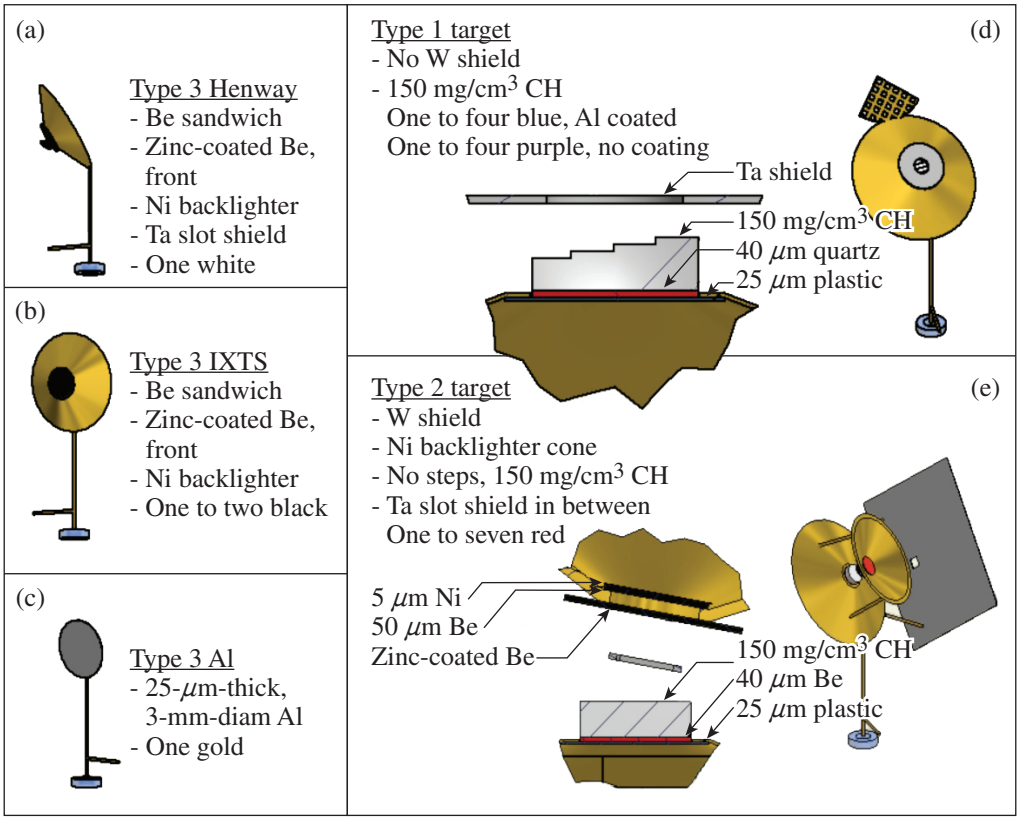


Figure 140.124
Schematic images of the targets. Each target consisted of a 25-μm-thick plastic ablator, a 40-μm quartz pusher, and 0.15 g/cm$^3$ of CH foam (in the VISAR/SOP targets there were four 40-μm-thick steps on the back of the foam).

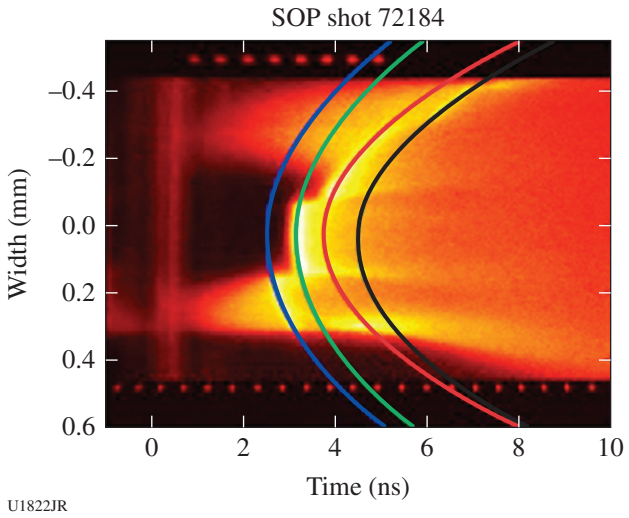


Figure 140.125
Example of the shock breakout measurement across four steps on the back of the foam target using the SOP diagnostic. Parabolic profiles are fit to each step to estimate the timing between the breakout for each step to measure the shock velocity.

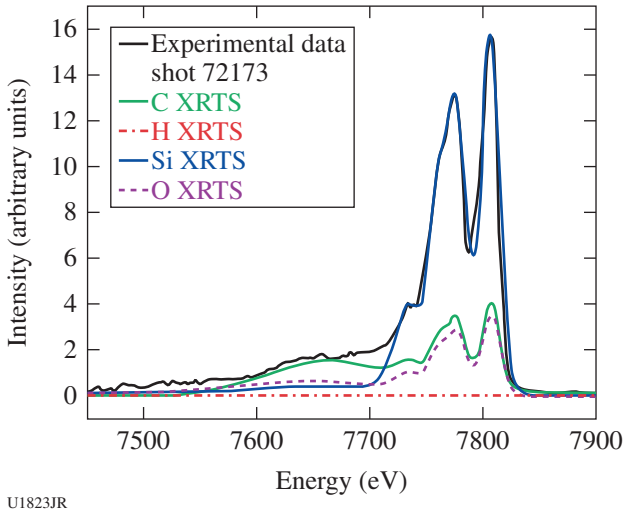


Figure 140.126
Example of x-ray scattering data from shocked CH foam. These datasets suffer from significant contamination scattering from the quartz pusher, which will be mitigated by using a thicker Al pusher for FY15 experiments.

### *ObliShockEP*

The ObliqueShockEP-14A experiment was a test of a new platform designed to investigate the coupling between low-mode and high-mode asymmetries at a shocked interface on the OMEGA EP laser. Single-mode, machined sinusoidal modulations were used as the high-mode asymmetry, and an angled interface with respect to the shock front made up the low-mode asymmetry. Data were taken using the OMEGA EP spherical crystal imager (SCI), a spherical crystal designed for Cu $K_\alpha$ x rays (~8 keV), to radiograph the perturbed interface side-on.

This experiment successfully demonstrated the platform as a viable tool to investigate the nature of oblique shock interactions with high-mode features (Fig. 140.127). The SCI resolu-

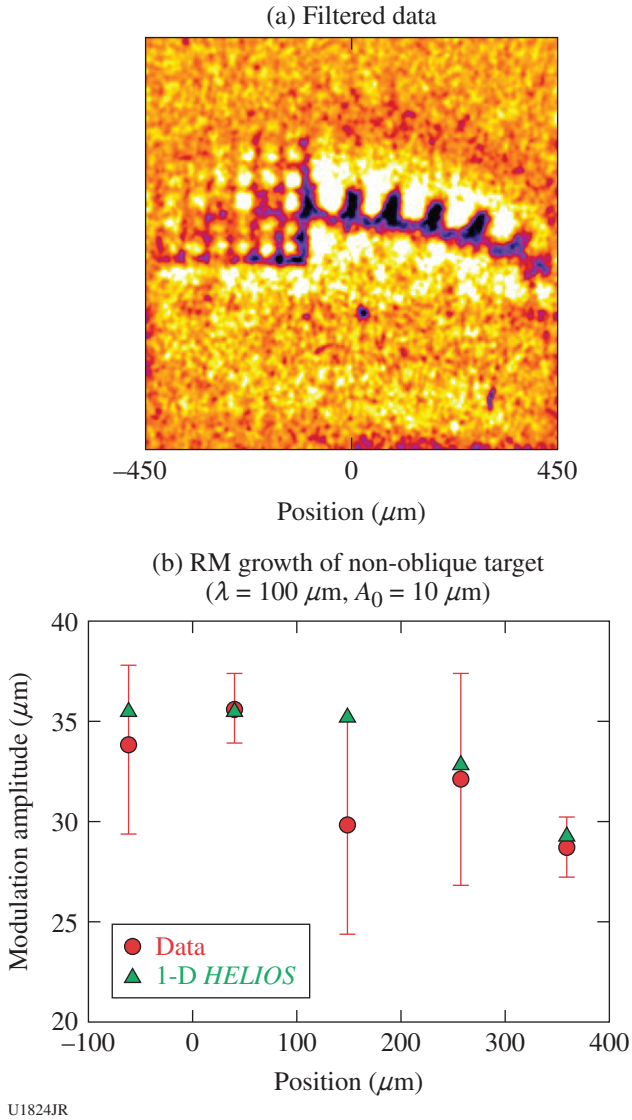


Figure 140.127
(a) Filtered data taken from a nonoblique target shows large single-mode modulations that have two amplitudes of 30 to 35 $\mu$m from an initial amplitude of 10 $\mu$m. (b) The data are overplotted with an analytic model for the classical Richtmyer–Meshkov instability using the 1-D hydrodynamics code *HELIOS* for the hydrodynamic parameters.

tion was ~10 $\mu$m, and the fluence from the backlighter was sufficient to use a low-sensitivity image plate (BAS-SR). Publication-quality data were obtained on all physics shots with the only exception being the placement of the fiducial grid overlapping with the shocked interface on some of the late-time data points.

### *MagLPI*

The goals of the MagLPI experiments in FY14 were to use a large external magnetic field to insulate conduction losses of the underdense plasma within a low-$Z$, gas-filled hohlraum and increase the plasma temperature to improve laser–plasma coupling in gas-filled hohlraum targets. Magnetic insulation is expected to occur when the electron gyroradius in the field is much smaller than the electron–ion collisional mean free path such that the gyroradius sets the step size for thermal transport. A successful demonstration of magnetic insulation may improve laser–plasma coupling in NIF ignition hohlraums.

In the OMEGA experiments, a gas-filled hohlraum was heated with 39 beams in a 1-ns pulse, and an additional 4$\omega$ probe beam measured the plasma temperatures using Thomson scattering. The 4$\omega$ probe beam propagated along the hohlraum axis. The hohlraum was 2.4 mm long and 1.6 mm in diameter with 1.2-mm-diam laser entrance holes, with 500-nm-thick polyimide windows covering the holes. A 0.4-mm-diam diagnostic hole centered in the hohlraum side was used to measure the Thomson-scattered light. The hohlraum wall was 5-$\mu$m-thick Au supported externally by 25-$\mu$m-thick epoxy. The hohlraum was filled with 1 atm of a mixture of $CH_4$ and $C_5H_{12}$ gases to produce a fully ionized average electron density of $4 \times 10^{21}$ e/cm$^3$, and the pressure was monitored for each target up to shot time. An external $B$ field was applied along the hohlraum axis using a Helmholtz coil driven by MIFEDS, and $B$ fields up to 8 T were generated. A schematic of the experiment (without heater beams for simplicity) is shown in Fig. 140.128.

The time-dependent plasma temperature was measured using 4$\omega$ Thomson scattering, and the scattering profiles were fit with ±100-eV accuracy. An increase of up to 50% in electron plasma temperature was measured with an applied field $B$ = 7.5 T. Figure 140.129 shows the measured time-dependent temperatures for an experiment with (red circles) and without (blue triangles) an external $B$ field. Figure 140.130 shows the measured electron temperature early and late in time as a function of applied $B$ field.

### *DPeos*

Accurate measurements and determination of the equation of state (EOS) of light elements at high pressure, solid densities, and moderate temperatures (1 to 100 eV), often referred to as the warm-dense-matter (WDM) regime, are essential to understanding the structure of many astrophysical objects, including giant gaseous planets, and play an important role in the development of inertial confinement fusion (ICF). At WDM conditions, quantum degeneracy and strong interparticle coupling effects become significant and theoretical models of WDM face many challenges. Unfortunately, it is difficult to

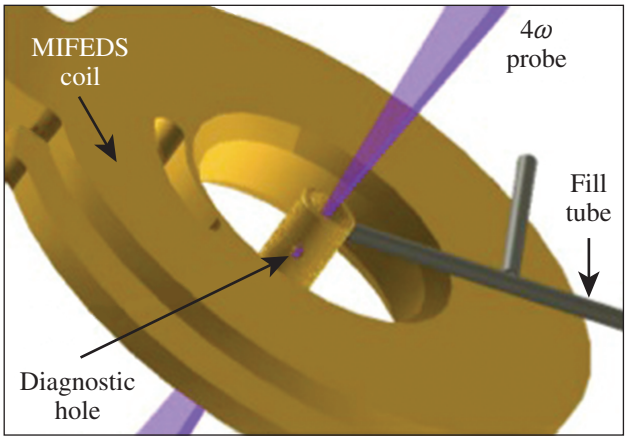


Figure 140.128
Schematic of the experiment as viewed from the Thomson-scattering diagnostic. For simplicity, the heater beams are not shown.

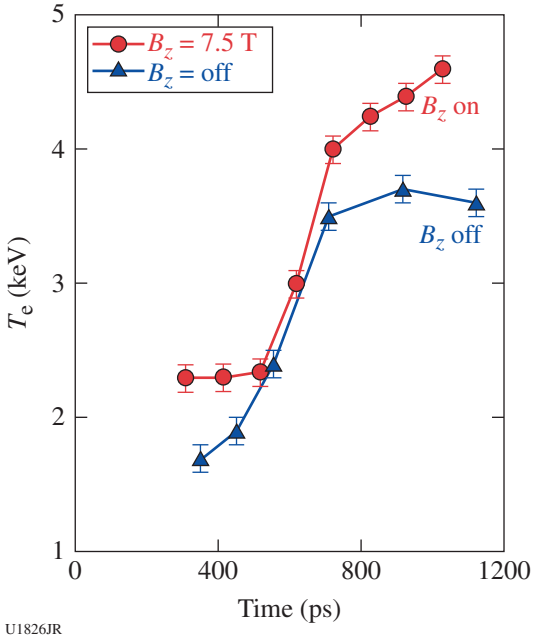


Figure 140.129
Plot of measured temperature versus time for an experiment with (red circles) and without (blue triangles) an external $B$ field.

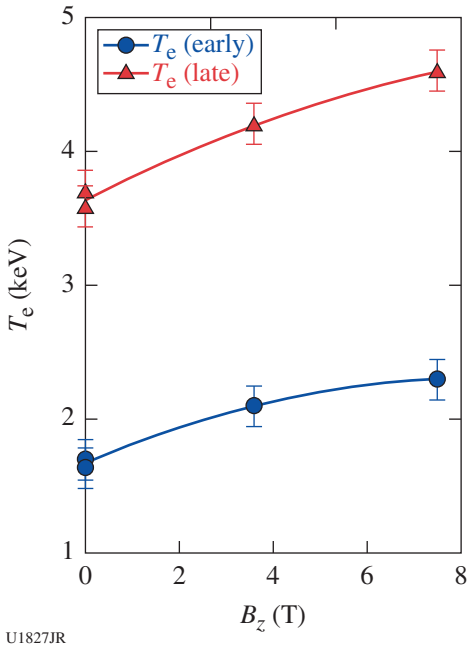


Figure 140.130
Plot of measured temperature versus applied *B* field for early time (blue) and late time (red).

obtain complete EOS information through experiments at these conditions. The goal of our project is to produce uniform dense plasma conditions in an experimental target and to measure three thermodynamic variables to determine the full EOS.

Our approach to obtaining WDM EOS data utilizes a standard shock and release technique, with two important innovations. First, the OMEGA laser was used to drive very strong (10-Mbar) initial shocks into a thin carbon or diamond foil, creating release states previously not accessed by other shock and release EOS experiments. When this shock moves through the foil and follows into a low-density, low shock impedance material (0.2-g/cm$^3$ silica aerogel foam), the shocked carbon sample undergoes a very deep release. This results in generating WDM conditions in the carbon, roughly solid density, and temperatures ~10 eV. These temperatures are far above melt or any phase transitions and are very different from the principal Hugoniot conditions typically produced in shock experiments and used to constrain EOS models like *SESAME*. Our technique, thereby, creates a useful platform for testing EOS models in this important parameter regime where no complete experimental data have been available to date (Fig. 140.131). The second key innovation is the use of x-ray Thomson scattering (XRTS) to determine the temperature of the released WDM carbon in conjunction with additional independent measurements of density and pressure using radiography and velocity interferometry (VISAR)/streaked optical pyrometry (SOP), providing us with a full EOS measurement. We succeeded, for the first time, in obtaining data on all these measurements for material at dense plasma conditions. Previous data with a Ni He$_\alpha$ backlighter as an x-ray-scattering probe driven by beams of 10-ns duration have been recently published (see Ref. 62).

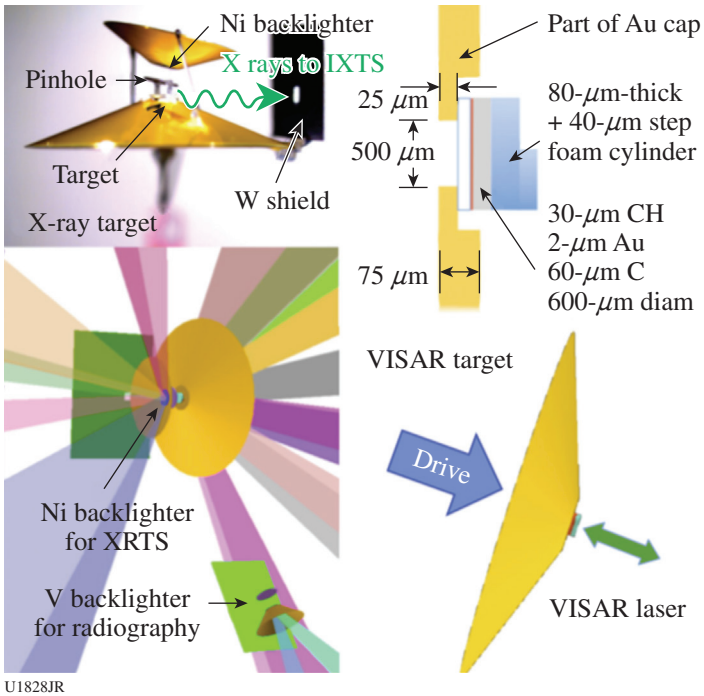


Figure 140.131
Schematic of the x-ray scattering and VISAR targets. The driven target sits inside the larger cone inside a small gold cap and consists of a plastic (CH) ablator, a graphite or diamond sample, and a silica ($SiO_2$) aerogel disk. The second smaller gold cones contain Ni and V backlighted foils for XRTS and radiography measurements, respectively, coated on top of a Be filter on the inner side of the cone. Laser beams then illuminate the driven target and the ablator from the inside of each Au cone. The XRTS target also includes Ta pinholes on top of each backlighter to collimate the x rays. The VISAR target is identical but has no backlighter cones or pinholes and includes a 40-$\mu$m step on the back side of the aerogel disk.

The experiments were performed on carbon at different conditions using graphite and diamond targets driven by either a low laser drive at a total intensity of $5 \times 10^{14}$ W/cm$^2$ and a duration of 4 ns or a 2-ns (high) drive of $1.5 \times 10^{15}$ W/cm$^2$. The targets consisted of planar layers of a plastic ablator, Au radiation shield, the carbon sample (diamond or graphite), and a thick layer of silica aerogel foam, which acted as a low-density release material. The strong shock first travels through the carbon layer and later releases into the foam, while a release wave travels back through the carbon layer, creating the desired WDM conditions. The radiographic measurement using the 5.2-keV-V-He$_\alpha$ line was used to obtain a direct mass-density measurement through transmission. The temperature measurement was obtained from noncollective x-ray Thomson scattering using the IXTS diagnostic. Previously we used ten OMEGA beams to create Ni He$_\alpha$ x rays at 7.8 keV, but in 2014 we began developing a new platform for utilizing a Cu K$_\alpha$ x-ray source to be driven by the OMEGA EP beam conveyed into the OMEGA target chamber. We experienced issues with a strong electromagnetic pulse (EMP) that impaired the charge-coupled–device (CCD) camera in the IXTS diagnostic. We are currently redesigning the diagnostic to use image plates for our FY15 joint OMEGA EP shots. We managed, however, to get some additional scattering data using the old configuration with a Ni backlighter. In 2014 we obtained valuable VISAR, SOP, and radiography data as well (Figs. 140.132–140.134). We also measured an excellent flat-field spectrum that characterized the crystal nonuniformity in the IXTS diagnostic and provided an intensity correction for measured x-ray spectra. The release pressure was obtained from a VISAR/SOP measurement of the velocity in the aerogel using the EOS relationship from *SESAME* Table 7387, which was confirmed by direct measurements by Knudson and Lemke.[63]

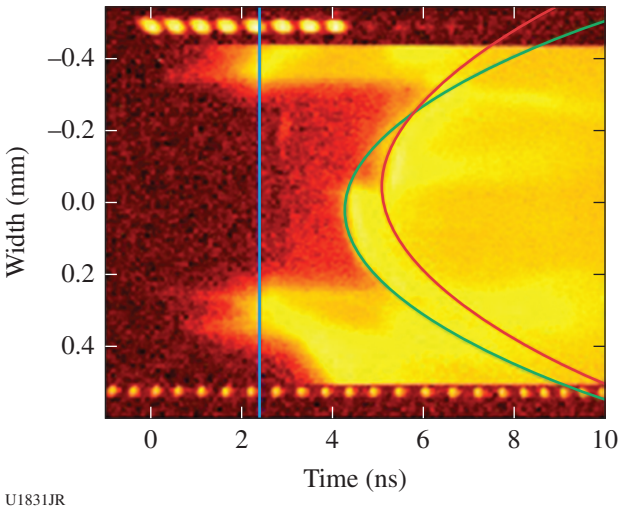


Figure 140.132
An example of shock breakout measurement using the SOP diagnostic. The shock breakout is used to measure shock velocity in the foam, which provides the release pressure in carbon.

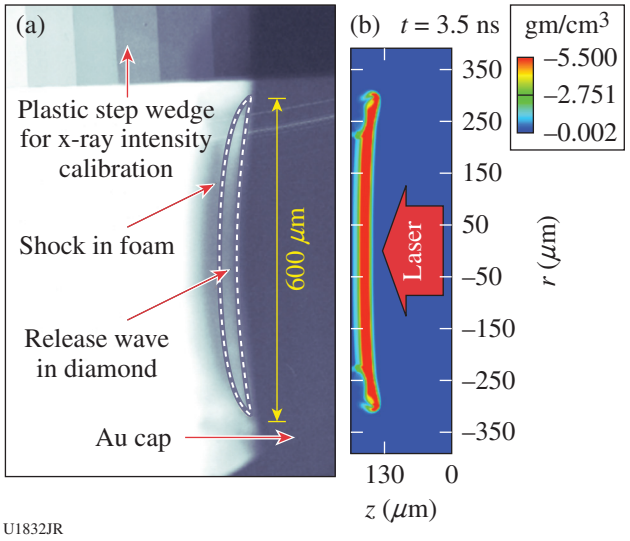


Figure 140.133
An example radiography image of released diamond showing transmitted intensity (a) compared to a mass density plot from 2-D *FLASH* simulation. (b) The 2-D simulations confirm that the transverse effects in warm-dense-matter (WDM) conditions within the release wave are negligible.

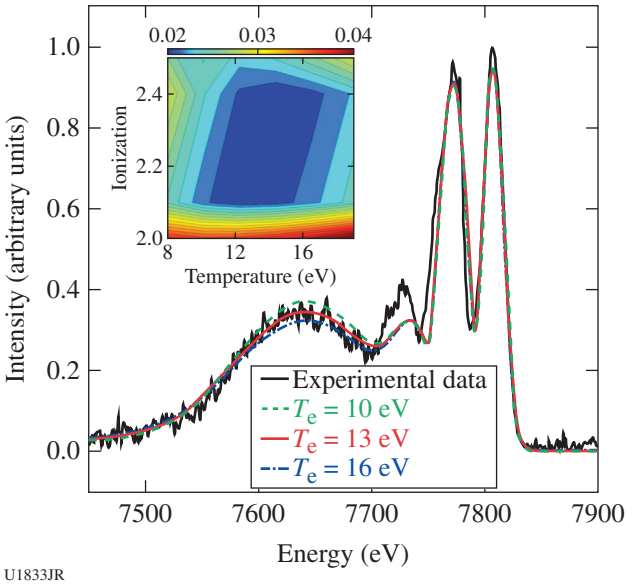


Figure 140.134
X-ray scattering data from shock-released diamond at high drive using the Ni He$_\alpha$ x-ray source. The best-fit conditions were $T_e = 13 \pm 2$ eV, $n_e = 2.6 \pm 0.2$ $10^{23}$ cm$^{-3}$, and $Z = 2.0$ to 2.5. The error bars were determined by a $\chi^2$ fit (inserted image).

### *CDTMixCap*

One of the challenges for developers of radiation–hydrodynamics codes is the proper calculation of burn in turbulent mixing fluids. In 2011, LANL embarked on a three-year program of study to validate turbulent models implemented in LANL's Eulerian Applications Project code suite under the conditions of a reacting plasma. On 3 April 2014 at the Omega Laser Facility, a LANL team successfully executed a day of direct-drive implosions of 865-$\mu$m-diam plastic shells filled with pure tritium. As shown in Fig. 140.135, the plastic shells were manufactured with 1-$\mu$m-thick ($dR_t$) deuterated plastic layers, positioned on the inner surface of the capsule, as well as 1 and 2 $\mu$m from the inner surface ($dR_b$). In these implosions, deuterium–tritium fusion reactions provide a diagnostic for burn and mix.

Nuclear data collected from the implosions included fusion yields from D−D, D−T, and D−T reactions, TT ion temperatures, and gamma and neutron bang times. These data are being used to validate cutting-edge burn physics models being implemented in LANL's Eulerian Applications Project (EAP) code suite. Figure 140.136 shows an example neutron spectrum collected from the data set. The spectrum shows clear evidence of T–T fusions from the hot gas core, D−T fusions from the atomically mixed gas-shell region, and D−D fusions from plastic chunks in the gas-shell mix volume—an experimental first! Simulations of these data and validation of the turbulent mix models in the EAP code suite are currently still ongoing.

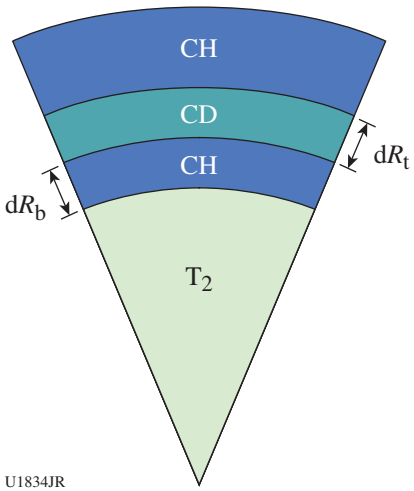


Figure 140.135
Pie diagram of capsules used to validate LANL's Besnard−Harlow−Rauenzhan (BHR) mix model implemented in the Eulerian Applications Project code suite.

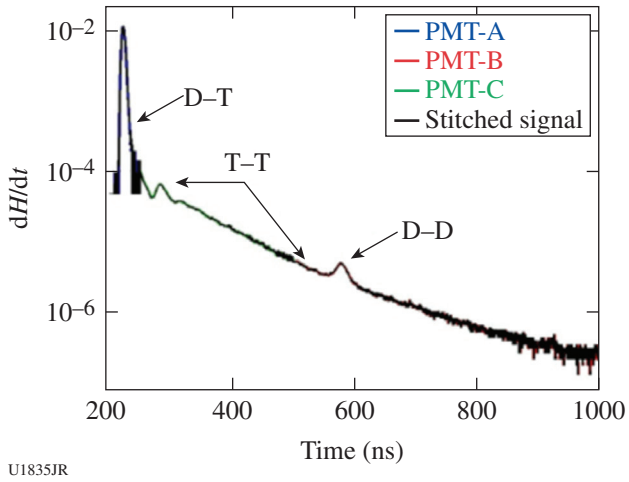


Figure 140.136
Neutron spectrum from a CDT Mixcap shot with 1 $\mu$m of CD on the inside of the shell. Clear evidence of D−T, T–T, and D−D fusion reactions is present in the spectra.

### *Gas Cherenkov Detector 3 (GCD-3)*

In collaboration with LLE, LANL scientists and engineers have designed, constructed, and implemented a new gas Cherenkov detector (GCD-3) on OMEGA, opening a new window to inertial confinement fusion (ICF) gamma-ray spectroscopy. GCD-3 (Figs. 140.137 and 140.138) was funded by the National Nuclear Security Administration ICF Program (LANL C-10). GCD's operate by converting MeV gammas to UV/visible Cherenkov photons for easy detection. They provide a variable energy thresholding based on the pressure and temperature of the Cherenkov conversion gas. Previously two ten-inch manipulator–based GCD's were fielded on OMEGA, both limited to 100 psia of $CO_2$, providing a >6.3-MeV energy threshold. These GCD's were primarily designed to measure DT fusion gammas at 16.75 MeV to provide a fusion reaction history. An additional GCD-type detector, known as gamma reaction history (GRH), operates outside the OMEGA target chamber, restricting sensitivity, and is limited to operation with <215 psia of $SF_6$, lowering the Cherenkov conversion threshold to 2.9 MeV. In addition to reaction history, the improved lower threshold of GRH makes it possible to measure ablator areal density based on the $^{12}C(n,n')$ gamma at 4.44 MeV. The OMEGA GRH acted as the prototype for the four-gas cell GRH-6m, which has been in operation at the National Ignition Facility (NIF) since 2010. The new GCD-3 fulfills the need for greater sensitivity and lower threshold than afforded by the existing detectors. This was achieved by designing GCD-3 to operate inside the target chamber with high-pressure fluorinated gases. It can be safely pressurized up to 400 psia and uses all metal seals

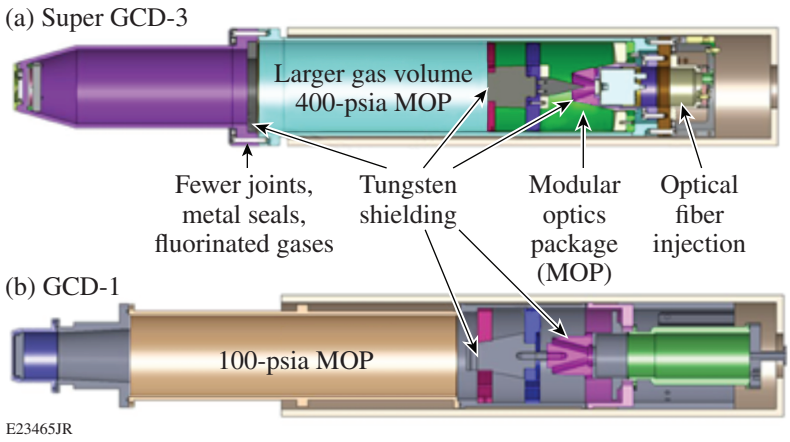


Figure 140.137
CAD model depicting differences between the super gas Cherenkov detector (GCD-3) and GCD-1. Each gas cell is ~1 m long.

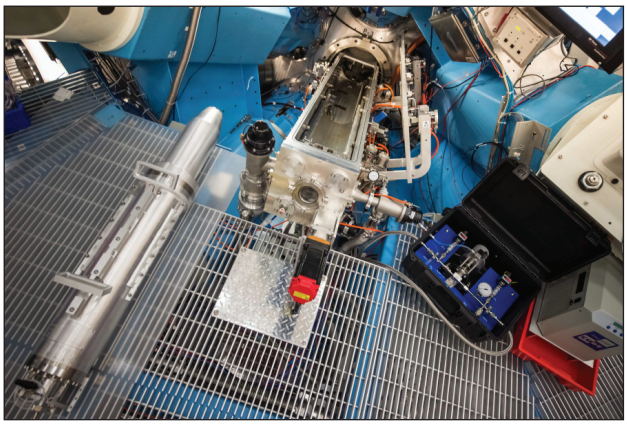


Figure 140.138
GCD-3 pressure vessel prior to insertion in an OMEGA ten-inch manipulator (TIM). GCD-3 is capable of being pressurized to 400 psia, providing Cherenkov thresholds as low as 1.8 MeV.

to virtually eliminate leakage into the target chamber. With this instrument, the energy threshold can be as low as 1.8 MeV, opening a new portion of the gamma-ray spectrum to investigation. Its first use was in collaboration with MIT to measure the cross section for H–D fusion [H + D $\longrightarrow$ $^3$He + $\gamma$(5.5 MeV)], an important step in big-bang nucleosynthesis, brown dwarfs, protostars, and the solar proton–proton fusion chain. It performed as expected with $CO_2$ at 400 psia, successfully measuring H–D gammas for the first time in an ICF experiment. It was also used at the end of August 2014 to compare gamma emission of samples of $^{12}$C and $^{13}$C under 14-MeV neutron exposure as part of a feasibility study for time-dependent "dark-mix" studies on the NIF.

### *HED-MMI*

While deficiencies in modeling of fuel–shell mixing have been suggested to play a role in the under-predicted performance in ICF, we have primarily relied on integrated measurements to test this understanding. In this work our goal is to more severely constrain this modeling via spectroscopic imaging [multiple-monochromatic imager (MMI)] of a Ti tracer layer. The dopant is incorporated into the plastic shell adjacent to the fuel interface.

As an example of the importance of imaging data, we note the integrated time-resolved spectroscopy in our experiments. These data clearly indicate that the Ti accesses a higher temperature than predicted from 1-D simulation, consistent with fuel–shell mixing. This information does not provide, however, a direct measure of the extent of mixing. The near-bang-time MMI images from 7 August 2014 show two principal features: (1) a broadened emission limb (as predicted) with a much-reduced contrast, and (2) an elliptical outer shape with an axis ratio of 1.3 to 1.4 from one of the two views. Analysis of the limb broadening/contrast is ongoing but we note here that little variation was observed in this aspect across thicknesses ranging from 16 to 21 $\mu$m. This insensitivity suggests that the ablative Rayleigh–Taylor does not vary this observable, so the

first FY15 shot day will explore the dependence on fill pressure (related to deceleration-phase Rayleigh–Taylor instability). For the low-mode asymmetry, this feature is observed to persist across all the targets and show no alignment with the target stalk. The ellipticity is also observed both in an undoped target and from the GMXI imager at a view angle 140° from the MMI. Surprisingly, the fluence distribution on target (hard sphere assumption with area corrections from F. Marshall) suggests the larger low-mode drive imbalance (~±2%) from the perspective showing the more-symmetric contour (see Fig. 140.139). This may suggest inaccuracies in the drive characterization or a breakdown in the interpretation of the 3-D implosion within 2-D frameworks. An indication of an understanding of the drive will be obtained in the FY15 experiments that will correct beam energies for the measured area variations.

## FY14 CEA Experiments at the Omega Laser Facility

During FY14 CEA–led teams conducted 67 target shots on the OMEGA laser for several experiments. A brief summary of some of this work is included in this section.

### *Wall Motion*

The objective of the wall motion experiment performed on 18 June 2014 was to characterize the interaction that occurs between the laser beams and the expanded plasma from the hohlraum walls and, more precisely, in the rugby-shaped cavity. The expansion of the gold plasma wall produced by the external laser cone can indeed modify the propagation of laser beams of an internal cone and then directly affect the implosion of the imploded microsphere.

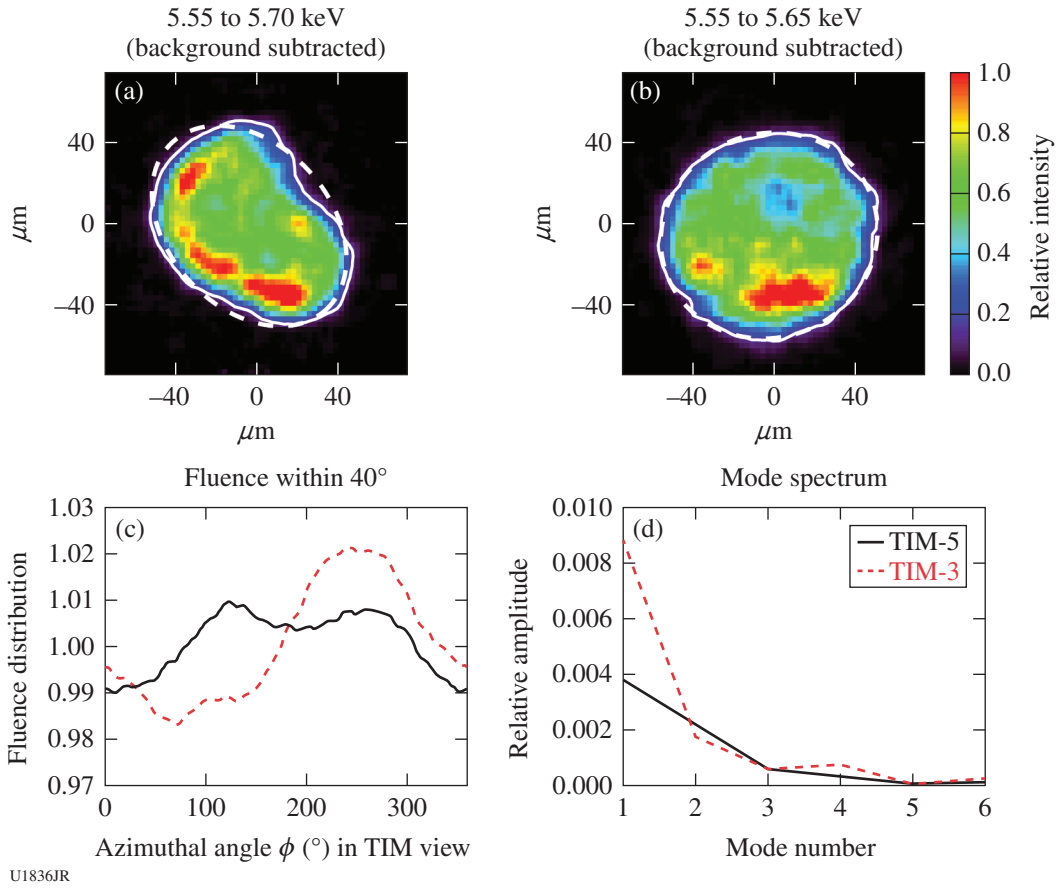


Figure 140.139
HED-MMI images and laser drive characteristics: (a) Narrowband Ti $He_\beta$ image obtained from TIM-5 at ~100 ps prior to nuclear bang time. (b) Image obtained (same shot, same approximate timing) from TIM-3. The gross features of the implosion symmetry are typical of all targets shot for the day. (c) Equatorial fluence distribution with coordinates defined such that the pole ($\theta = 0$) is aligned toward the viewing position. (d) Modal composition of the equatorial fluence distribution.

This experiment on OMEGA was performed with a halfraum (a double-wall design with one wall tilted by 30° relative to the second wall) filled with methane (see Fig. 140.140). At $t_0$, laser beams from the 21° and 59° cones (heating beams) were focused inside the target. The 59° cone was located near the point where the production of the plasma bubbles (in which we are interested) originated. At $t_0 + \delta t$, laser beams from the 42° cone were focused inside the halfraum and propagated through the plasma bubbles, which were more or less expanded, depending on the time delay $\delta t$.

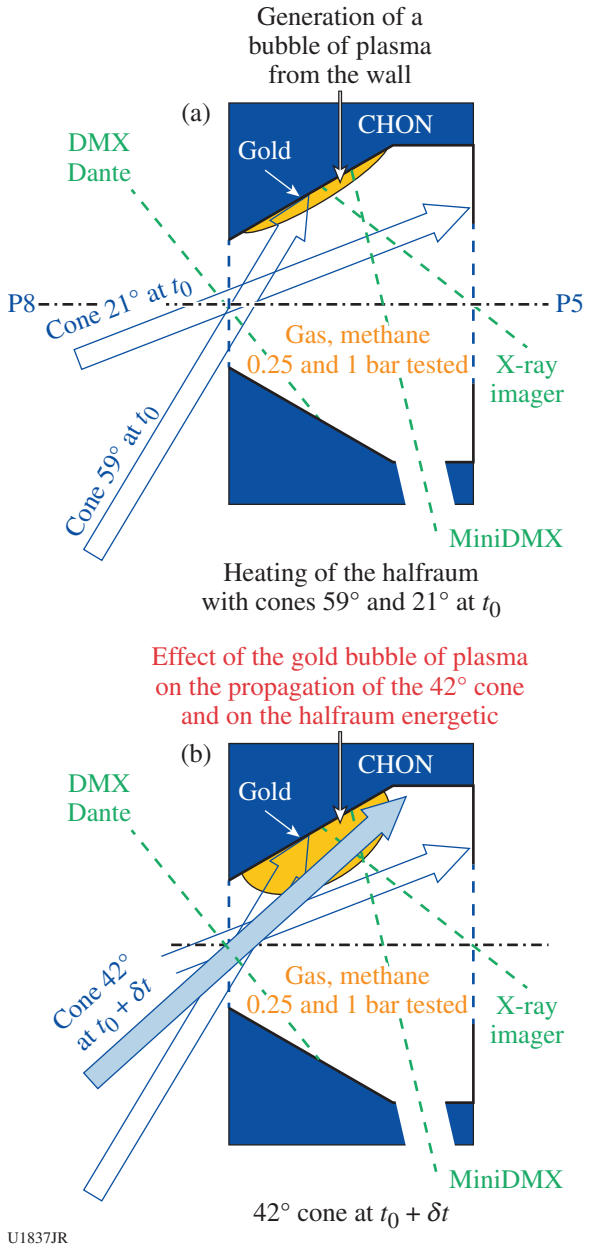


Figure 140.140
Principle of the experiment.

On the opposite side of the laser entrance hole (LEH), a window in the halfraum gives direct access to the plasma bubbles. In configuration "P8" represented in Fig. 140.140, plasma expansion was studied using an x-ray imager positioned in TIM-5. In configuration P5, the target was turned by 180°, and the plasma bubbles were studied using the broadband x-ray spectrometers DMX and Dante.

The x-ray imager in TIM-5 in the P5 configuration gives access to the expansion of the plasma wall produced by the 59°-cone laser beams. Figure 140.141 shows an example of

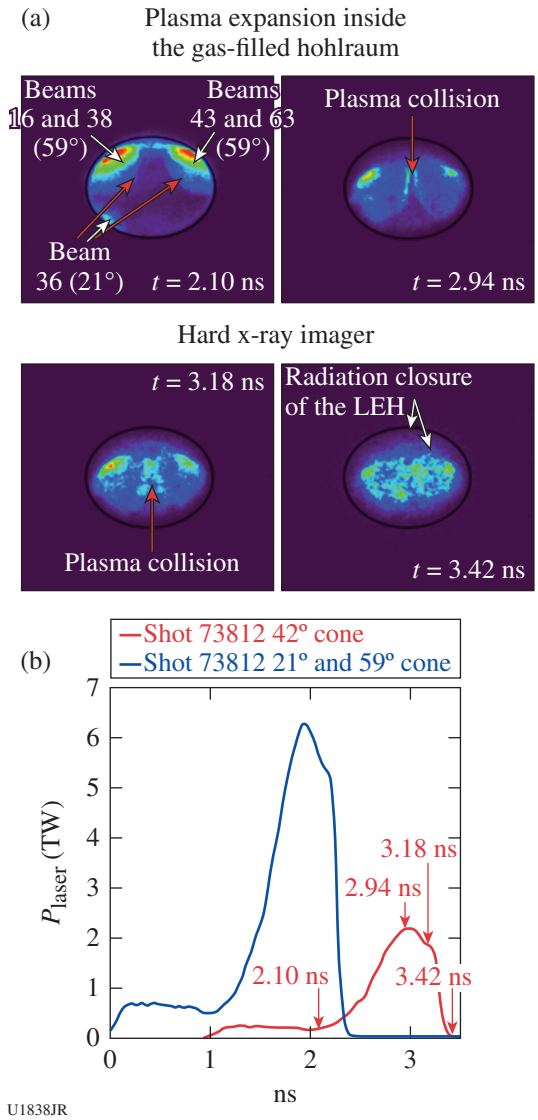


Figure 140.141
Images obtained with the hard x-ray imager in TIM-5 (P5 configuration). LEH: laser entrance hole.

images obtained with $\delta t$ = 1 ns and a gas pressure $P$ = 1 bar, where the collision of two plasmas can be seen.

In the P8 configuration, the hard x-ray imager in TIM-5 can view the laser beams (42° and 59° cones), which impact the halfraum walls. Figure 140.142 shows experimental results obtained with $\delta t$ = 0.5 ns and $P$ = 1 bar. The maximum emission of the heating laser beams (59° cone) can be seen on the first image. Persistence of the signal and features could suggest a 42°-cone laser-beam energy deposition inside the plasma bubble produced by the 59° cone.

***Neutron and X-Ray Imaging on the same axis on OMEGA***

O. Landoas, T. Caillaud, S. Laffite, F. Girard, V. Tassin, and J. L. Bourgade (CEA); F. J. Marshall, V. Yu. Glebov, and T. C. Sangster (LLE)

On 9 July 2014 an experimental campaign labeled Chonomix was conducted at the Omega Laser Facility to study the mix between the target shell and the fuel during implosion. During this shot day, direct-drive implosions of $D_2$, $D_2$-Ar, and DT-filled CH targets were conducted with several laser pulse shapes. The neutron yield ranged from $4 \times 10^9$ to $2 \times 10^{10}$ for D–D implosions and from $10^{11}$ to $3 \times 10^{12}$ for D–T implosions.

Among the many diagnostics activated, the neutron imaging system (NIS) was one of the main diagnostics required to acquire the core image shape. For many years, comparison between neutron and x-ray images was provided by two different diagnostics viewing the target from different target chamber ports and then integrating 3-D effects by different viewing angles. This year, we developed a system to produce neutron and x-ray images simultaneously on the same axis through the same penumbral aperture.

Over the past 15 years, we have developed the Laser Mégajoule Facility (LMJ) NIS diagnostic using a penumbral or annular coded aperture technique.[64–68] With the NIS diagnostic, we are able to use both the small neutron imaging system's (SNIS)[69] and the large neutron imaging system's (LNIS)[70] cameras placed, respectively, at 4 and 13 m from the target.

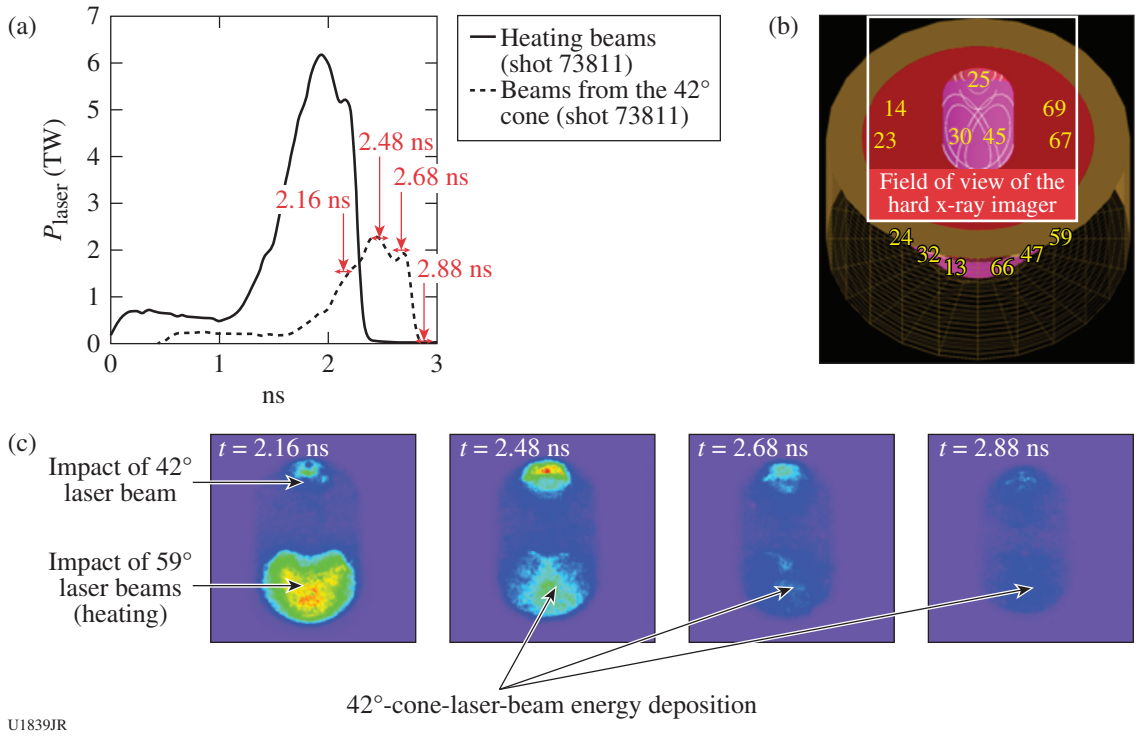


Figure 140.142
(a) Laser pulse for shot 73811 and (b) VISRAD view of the target seen from TIM-5. (c) Images obtained with the hard x-ray imager in TIM-5 (P8 configuration).

To acquire an x-ray image on the same axis as the neutron image, we set a charge-injection–device (CID) camera behind the aperture manipulator (cf., Fig. 140.143).

The CID was placed at 1.4 m from target chamber center (TCC), giving a magnification of slightly higher than 5. Several x-ray filters were set at different places to adjust x-ray transmission. A 50-$\mu$m copper filter was set in front of the CID. A 200-$\mu$m beryllium blast shield and a 100-$\mu$m aluminum filter were set on the front shutter of the aperture manipulator and a 100-$\mu$m-thick aluminum filter on the back shutter. This back shutter can be opened or closed during the shot, allowing us to adjust the x-ray transmission to optimize the signal-to-noise ratio (SNR) on the CID camera. Some preliminary results are presented in Fig. 140.144.

The locations of the CID, SNIS, and LNIS along the line of sight were accurately measured during alignment using a telescope as reference. Previous experiments at CEA were performed to define a referenced pixel on each detector, viewing in the same plane the front and the back of each detector. In this way, we make no hypotheses about the position of the neutron and x-ray sources using the center of the projection of the source through the penumbral aperture.

Preliminary overlaying results of neutron (SNIS) and x-ray (CID) images are presented in Fig. 140.145. The tracking accuracy of SNIS over the CID can be estimated at 15 $\mu$m in the source plan.

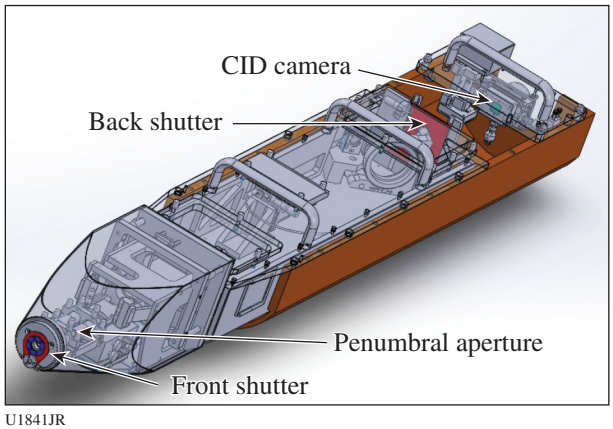


U1841JR

Figure 140.143
Aperture manipulator and CID camera on the TIM-6 line of sight.

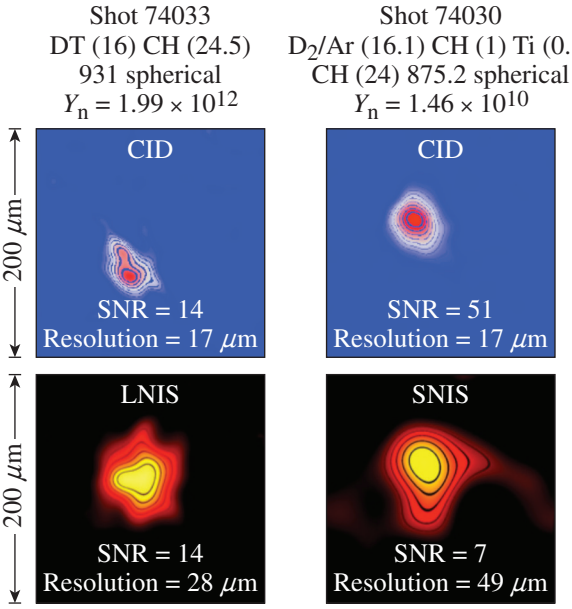


U1842JR

Figure 140.144
X-ray and neutron images.

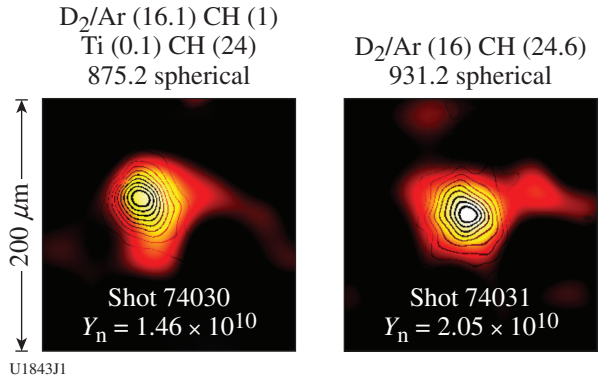


U1843J1

Figure 140.145
Overlaying of neutron and x-ray images for shots 74030 and 74031. X-ray images are represented as image contours at 0.2, 0.3, to 0.9 of maximum.

## REFERENCES

1. W. Fox, G. Fiksel, A. Bhattacharjee, P. Y. Chang, K. Germaschewski, S. X. Hu, and P. M. Nilson, Phys. Rev. Lett. **111**, 225002 (2013).

2. G. Fiksel, W. Fox, A. Bhattacharjee, D. H. Barnak, P.-Y. Chang, K. Germaschewski, S. X. Hu, and P. M. Nilson, Phys. Rev. Lett. **113**, 105003 (2014).

3. A. S. Liao, S. Li, P. Hartigan, P. Graham, G. Fiksel, A. Frank, J. Foster, and C. Kuranz, "Numerical Simulation of an Experimental Analogue of a Planetary Magnetosphere," to be published in High Energy Density Physics.

4. P. Loubeyre, S. Brygoo, J. Eggert, P. M. Celliers, D. K. Spaulding, J. R. Rygg, T. R. Boehly, G. W. Collins, and R. Jeanloz, Phys. Rev. B **86**, 144115 (2012); J. H. Eggert, D. G. Hicks, P. M. Celliers, D. K. Bradley, R. S. McWilliams, R. Jeanloz, J. E. Miller, T. R. Boehly, and G. W. Collins, Nat. Phys. **6**, 40 (2010).

5. M. J. Rosenberg, H. G. Rinderknecht, N. M. Hoffman, P. A. Amendt, S. Atzeni, A. B. Zylstra, C. K. Li, F. H. Séguin, H. Sio, M. Gatu Johnson, J. A. Frenje, R. D. Petrasso, V. Yu. Glebov, C. Stoeckl, W. Seka, F. J. Marshall, J. A. Delettrez, T. C. Sangster, R. Betti, V. N. Goncharov, D. D. Meyerhofer, S. Skupsky, C. Bellei, J. Pino, S. C. Wilks, G. Kagan, K. Molvig, and A. Nikroo, Phys. Rev. Lett. **112**, 185001 (2014).

6. H. G. Rinderknecht, H. Sio, C. K. Li, A. B. Zylstra, M. J. Rosenberg, P. Amendt, J. Delettrez, C. Bellei, J. A. Frenje, M. Gatu Johnson, F. H. Séguin, R. D. Petrasso, R. Betti, V. Yu. Glebov, D. D. Meyerhofer, T. C. Sangster, C. Stoeckl, O. Landen, V. A. Smalyuk, S. Wilks, A. Greenwood, and A. Nikroo, Phys. Rev. Lett. **112**, 135001 (2014).

7. H. G. Rinderknecht, H. Sio, C. K. Li, N. Hoffman, A. B. Zylstra, M. J. Rosenberg, J. A. Frenje, M. Gatu Johnson, F. H. Séguin, R. D. Petrasso, R. Betti, V. Yu. Glebov, D. D. Meyerhofer, T. C. Sangster, W. Seka, C. Stoeckl, G. Kagan, K. Molvig, C. Bellei, P. Amendt, O. Landen, J. R. Rygg, V. A. Smalyuk, S. Wilks, A. Greenwood, and A. Nikroo, Phys. Plasmas **21**, 056311 (2014).

8. A. B. Zylstra, M. Gatu Johnson, J. A. Frenje, F. H. Séguin, H. G. Rinderknecht, M. J. Rosenberg, H. W. Sio, C. K. Li, R. D. Petrasso, M. McCluskey, D. Mastrosimone, V. Yu. Glebov, C. Forrest, C. Stoeckl, and T. C. Sangster, Rev. Sci. Instrum. **85**, 063502 (2014).

9. M. J. Rosenberg, F. H. Séguin, C. J. Waugh, H. G. Rinderknecht, D. Orozco, J. A. Frenje, M. Gatu Johnson, H. Sio, A. B. Zylstra, N. Sinenian, C. K. Li, R. D. Petrasso, V. Yu. Glebov, C. Stoeckl, M. Hohenberger, T. C. Sangster, S. LePape, A. J. Mackinnon, R. M. Bionta, O. L. Landen, R. A. Zacharias, Y. Kim, H. W. Herrmann, and J. D. Kilkenny, Rev. Sci. Instrum. **85**, 043302 (2014).

10. H. G. Rinderknecht, H. Sio, J. A. Frenje, J. Magoon, A. Agliata, M. Shoup, S. Ayers, C. G. Bailey, M. Gatu Johnson, A. B. Zylstra, N. Sinenian, M. J. Rosenberg, C. K. Li, F. H. Séguin, R. D. Petrasso, J. R. Rygg, J. R. Kimbrough, A. Mackinnon, P. Bell, R. Bionta, T. Clancy, R. Zacharias, A. House, T. Döppner, H. S. Park, S. LePape, O. Landen, N. Meezan, H. Robey, V. U. Glebov, M. Hohenberger, C. Stoeckl, T. C. Sangster, C. Li, J. Parat, R. Olson, J. Kline, and J. Kilkenny, Rev. Sci. Instrum. **85**, 11D901 (2014).

11. H. Sio *et al*., Rev. Sci. Instrum, **85**, 11E119 (2014).

12. C. K. Li, D. D. Ryutov, S. X. Hu, M. J. Rosenberg, A. B. Zylstra, F. H. Séguin, J. A. Frenje, D. T. Casey, M. Gatu Johnson, M. J. E. Manuel, H. G. Rinderknecht, R. D. Petrasso, P. A. Amendt, H. S. Park, B. A. Remington, S. C. Wilks, R. Betti, D. H. Froula, J. P. Knauer, D. D. Meyerhofer, R. P. Drake, C. C. Kuranz, R. Young, and M. Koenig, Phys. Rev. Lett. **111**, 235003 (2013).

13. M. Rosenberg, "Studies of Ion Kinetic Effects in Shock-Driven Inertial Confinement Fusion Implosions at OMEGA and the NIF and Magnetic Reconnection Using Laser-Produced Plasmas at OMEGA," Ph.D. thesis, Massachusetts Institute of Technology, 2014.

14. C. J. Waugh, "Improved Methods for Measuring the Absolute DD Neutron Yield and Calibrating Neutron Time-of-Flight Detectors in Inertial Confinement Fusion Experiments," M.Sc. thesis, Massachusetts Institute of Technology, 2014.

15. D. Orozco, "Implementation of Scattering Pinhole Diagnostic for Detection of Fusion Products on CR-39 at High Particle Fluence," B.Sc. thesis, Massachusetts Institute of Technology, 2014.

16. M. J. Rosenberg, C. K. Li, W. Fox, I. Igumenshchev, F. H. Séguin, R. P. J. Town, J. A. Frenje, C. Stoeckl, V. Glebov, and R. D. Petrasso, "A Laboratory Study of Asymmetric Magnetic Reconnection in Strongly-Driven Plasmas," submitted to Nature Communications.

17. H. G. Rinderknecht, M. J. Rosenberg, C. K. Li, N. M. Hoffman, G. Kagan, A. B. Zylstra, H. Sio, J. A. Frenje, M. Gatu Johnson, F. H. Séguin, R. D. Petrasso, P. Amendt, C. Bellei, S. Wilks, J. Delettrez, V. Yu. Glebov, C. Stoeckl, T. C. Sangster, D. D. Meyerhofer, and A. Nikroo, "Ion Thermal Decoupling and Species Separation in Shock-Driven Implosions," submitted to Physical Review Letters.

18. M. J.-E. Manuel, "Rayleigh–Taylor-Induced Electromagnetic Fields in Laser-Produced Plasmas," Ph.D. thesis, Massachusetts Institute of Technology, 2013.

19. M. J.-E. Manuel, C. K. Li, F. H. Séguin, J. Frenje, D. T. Casey, R. D. Petrasso, S. X. Hu, R. Betti, J. D. Hager, D. D. Meyerhofer, and V. A. Smalyuk, Phys. Rev. Lett. **108**, 255006 (2012).

20. M. J.-E. Manuel, C. K. Li, F. H. Séguin, N. Sinenian, J. A. Frenje, D. T. Casey, R. D. Petrasso, J. D. Hager, R. Betti, S. X. Hu, J. Delettrez, and D. D. Meyerhofer, Phys. Plasmas **20**, 056301 (2013).

21. C. K. Li, F. H. Séguin, J. A. Frenje, J. R. Rygg, R. D. Petrasso, R. P. J. Town, P. A. Amendt, S. P. Hatchett, O. L. Landen, A. J. Mackinnon, P. K. Patel, V. A. Smalyuk, T. C. Sangster, and J. P. Knauer, Phys. Rev. Lett. **97**, 135003 (2006).

22. D. R. Farley *et al*., Phys. Rev. Lett. **83**, 1982 (1999).

23. D. D. Ryutov *et al*., Phys. Plasmas **20**, 032703 (2013).

24. P. B. Radha, T. J. B. Collins, J. A. Delettrez, Y. Elbaz, R. Epstein, V. Yu. Glebov, V. N. Goncharov, R. L. Keck, J. P. Knauer, J. A. Marozas, F. J. Marshall, R. L. McCrory, P. W. McKenty, D. D. Meyerhofer, S. P. Regan, T. C. Sangster, W. Seka, D. Shvarts, S. Skupsky, Y. Srebro, and C. Stoeckl, Phys. Plasmas **12**, 056307 (2005).

25. T. Bartal *et al*., Nat. Phys. **8**, 139 (2012).

26. M. E. Foord *et al*., Phys. Plasmas **19**, 056702 (2012); B. Qiao *et al*., Phys. Rev. E **87**, 013108 (2013).

27. L. Gao, P. M. Nilson, W. Theobald, C. Stoeckl, C. Dorrer, T. C. Sangster, D. D. Meyerhofer, L. Willingale, and K. M. Krushelnick, Bull. Am. Phys. Soc. **55**, 377 (2010); and G. Fiksel, Laboratory for Laser Energetics, private communication (2014).

28. M. Wei, R. Mishra, S. Chawla, A. Sorokovikova, F. N. Beg, C. Chen, H. Chen, R. Fedosejevs, J. Jaquez, L. C. Jarrott, G. Kemp, M. Key, J. Kim, A. Link, H. McLean, A. Morace, V. M. Ovchinnikov, P. K. Patel, Y. Ping, B. Qiao, H. Sawada, Y. Sentoku, C. Stoeckl, W. Theobald, and R. B. Stephens, in *Proceedings of the 24th IAEA Fusion Energy Conference* (IAEA, Vienna, 2013), Paper IFE/P6–06.

29. M. Wei, "Fast Electron Generation and Transport in High Intensity Laser Solid Target Interaction Using Fast Ignition Relevant Kilojoule 10-ps OMEGA EP Laser," presented at the 13th International Workshop on the Fast Ignition of Fusion Targets, Oxford, UK, 14–18 September 2014.

30. M. S. Wei, R. Stephens, R. Mishra, A. Sorokovikova, J. Peebles, C. McGuffey, L. Jarrott, F. Beg, Y. Sentoku, H. McLean, P. Patel, and W. Theobald, Bull. Am. Phys. Soc. **58**, 373 (2013).

31. See Eq. (127) in G. H. Miller and T. J. Ahrens, Rev. Mod. Phys. **63**, 919 (1991).

32. H. Chen, S. C. Wilks, J. D. Bonlie, E. P. Liang, J. Myatt, D. F. Price, D. D. Meyerhofer, and P. Beiersdorfer, Phys. Rev. Lett. **102**, 105001 (2009).

33. H. Chen, S. C. Wilks, D. D. Meyerhofer, J. Bonlie, C. D. Chen, S. N. Chen, C. Courtois, L. Elberson, G. Gregori, W. Kruer, O. Landoas, J. Mithen, J. Myatt, C. D. Murphy, P. Nilson, D. Price, M. Schneider, R. Shepherd, C. Stoeckl, M. Tabak, R. Tommasini, and P. Beiersdorfer, Phys. Rev. Lett. **105**, 015003 (2010).

34. H. Chen, G. Fiksel, D. Barnak, P.-Y. Chang, R. F. Heeter, A. Link, and D. D. Meyerhofer, Phys. Plasmas **21**, 040703 (2014).

35. O. V. Gotchev, J. P. Knauer, P. Y. Chang, N. W. Jang, M. J. Shoup III, D. D. Meyerhofer, and R. Betti, Rev. Sci. Instrum. **80**, 043504 (2009).

36. H. Chen, D. D. Meyerhofer, S. C. Wilks, R. Cauble, F. Dollar, K. Falk, G. Gregori, A. Hazi, E. I. Moses, C. D. Murphy, J. Myatt, J. Park, J. Seely, R. Shepherd, A. Spitkovsky, C. Stoeckl, C. I. Szabo, R. Tommasini, C. Zulick, and P. Beirsdorfer, High Energy Density Phys. **7**, 225 (2011).

37. P. Y. Chang, G. Fiksel, M. Hohenberger, J. P. Knauer, R. Betti, F. J. Marshall, D. D. Meyerhofer, F. H. Séguin, and R. D. Petrasso, Phys. Rev. Lett. **107**, 035006 (2011).

38. M. Tabak *et al*., Phys. Plasmas **1**, 1626 (1994).

39. S. Ivancic, D. Haberberger, H. Habara, T. Iwawaki, K. S. Anderson, R. S. Craxton, D. H. Froula, D. D. Meyerhofer, C. Stoeckl, K. Tanaka, and W. Theobald, "Channeling Multikilojoule High-Intensity Laser Beams in an Inhomogeneous Plasma," submitted to Physical Review Letters.

40. D. H. Froula, R. Boni, M. Bedzyk, R. S. Craxton, F. Ehrne, S. Ivancic, R. Jungquist, M. J. Shoup, W. Theobald, D. Weiner, N. L. Kugland, and M. C. Rushford, Rev. Sci. Instrum. **83**, 10E523 (2012).

41. D. Haberberger, S. Ivancic, S. X. Hu, R. Boni, M. Barczys, R. S. Craxton, and D. H. Froula, Phys. Plasmas **21**, 056304 (2014).

42. J. Zhang *et al*., Phys. Rev. A **54**, 1597 (1996).

43. R. Betti, C. D. Zhou, K. S. Anderson, L. J. Perkins, W. Theobald, and A. A. Solodov, Phys. Rev. Lett. **98**, 155001 (2007).

44. R. Nora, W. Theobald, F. J. Marshall, D. T. Michel, W. Seka, B. Yaakobi, M. Lafon, C. Stoeckl, J. A. Delettrez, A. A. Solodov, A. Casner, C. Reverdin, X. Ribeyre, A. Vallet, J. Peebles, F. N. Beg, M. S. Wei, and R. Betti, "Gigabar Spherical Shock Generation on the OMEGA Laser," submitted to Physical Review Letters.

45. G. Kagan and X.-Z. Tang, Phys. Lett. A **378**, 1531 (2014).

46. N. L. Kugland, D. D. Ryutov, P. Y. Chang, R. P. Drake, G. Fiksel, D. H. Froula, S. H. Glenzer, G. Gregori, M. Grosskopf, M. Koenig, Y. Kuramitsu, C. Kuranz, M. C. Levy, E. Liang, J. Meinecke, F. Miniati, T. Morita, A. Pelka, C. Plechaty, R. Presura, A. Ravasio, B. A. Remington, B. Reville, J. S. Ross, Y. Sakawa, A. Spitkovsky, H. Takabe, and H. S. Park, Nat. Phys. **8**, 809 (2012).

47. N. L. Kugland, J. S. Ross, P. Y. Chang, R. P. Drake, G. Fiksel, D. H. Froula, S. H. Glenzer, G. Gregori, M. Grosskopf, C. Huntington, M. Koenig, Y. Kuramitsu, C. Kuranz, M. C. Levy, E. Liang, D. Martinez, J. Meinecke, F. Miniati, T. Morita, A. Pelka, C. Plechaty, R. Presura, A. Ravasio, B. A. Remington, B. Reville, D. D. Ryutov, Y. Sakawa, A. Spitkovsky, H. Takabe, and H. S. Park, Phys. Plasmas **20**, 056313 (2013).

48. J. H. Nguyen and N. C. Holmes, Nature **427**, 339 (2004).

49. R. Briggs *et al*., J. Phys.: Conf. Ser. **377**, 012035 (2012).

50. S.-N. Luo and T. J. Ahrens, Phys. Earth Planet. Inter. **143–144**, 369 (2004).

51. J. R. Rygg, J. H. Eggert, A. E. Lazicki, F. Coppari, J. A. Hawreliak, D. G. Hicks, R. F. Smith, C. M. Sorce, T. M. Uphaus, B. Yaakobi, and G. W. Collins, Rev. Sci. Instrum. **83**, 113904 (2012).

52. D. K. Bradley *et al*., Phys. Rev. Lett. **102**, 075503 (2009).

53. R. F. Smith *et al*., Nature **511**, 330 (2014).

54. Y. Ping, D. G. Hicks, B. Yaakobi, F. Coppari, J. Eggert, and G. W. Collins, Rev. Sci. Instrum. **84**, 123105 (2013).

55. J. Edwards *et al*., Phys. Rev. Lett. **92**, 075002 (2004).

56. P. K. Patel *et al*., Phys. Rev. Lett. **91**, 125004 (2003).

57. S. C. Wilks *et al*., Phys. Plasmas **8**, 542 (2001).

58. R. F. Heeter, S. B. Hansen, K. B. Fournier, M. E. Foord, D. H. Froula, A. J. Mackinnon, M. J. May, M. B. Schneider, and B. K. F. Young, Phys. Rev. Lett. **99**, 195001 (2007).

59. F. Pérez, G. E. Kemp, S. P. Regan, M. A. Barrios, J. Pino, H. Scott, S. Ayers, H. Chen, J. Emig, J. D. Colvin, M. Bedzyk, M. J. Shoup, A. Agliata, B. Yaakobi, F. J. Marshall, R. A. Hamilton, J. Jaquez, M. Farrell, A. Nikroo, and K. B. Fournier, Rev. Sci. Instrum. **85**, 11D613 (2014).

60. D. Besnard *et al*., Los Alamos National Laboratory, Los Alamos, NM, Report LA-12303-MS (1992).

61. K. Falk, C. A. McCoy, C. L. Fryer, C. W. Greeff, A. L. Hungerford, D. S. Montgomery, D. W. Schmidt, D. G. Sheppard, J. R. Williams, T. R. Boehly, and J. F. Benage, Phys. Rev. E **90**, 033107 (2014).

62. K. Falk *et al*., Phys. Rev. Lett. **112**, 155003 (2014); K. Falk *et al*., Phys. Plasmas **21**, 056309 (2014).

63. M. D. Knudson and R. W. Lemke, J. Appl. Phys. **114**, 053510 (2013).

64. L. Disdier, A. Rouyer, D. C. Wilson, A. Fedotoff, C. Stoeckl, J. L. Bourgade, V. Yu. Glebov, J.-P. Garçonnet, and W. Seka, Nucl. Instrum. Methods Phys. Res. A **489**, 496 (2002).

65. L. Disdier, A. Rouyer, A. Fedotoff, J.-L. Bourgade, F. J. Marshall, V. Yu. Glebov, and C. Stoeckl, Rev. Sci. Instrum. **74**, 1832 (2003).

66. L. Disdier, R. A. Lerche, J. L. Bourgade, and V. Yu. Glebov, Rev. Sci. Instrum. **75**, 2134 (2004).

67. A. Rouyer, Rev. Sci. Instrum. **74**, 1234 (2003).

68. L. Disdier, A. Rouyer, I. Lantuéjoul, O. Landoas, J. L. Bourgade, T. C. Sangster, V. Yu. Glebov, and R. A. Lerche, Phys. Plasmas **13**, 056317 (2006).

69. T. Caillaud, O. Landoas, M. Briat, B. Rosse, I. Thfoin, F. Philippe, A. Casner, J. L. Bourgade, L. Disdier, V. Yu. Glebov, F. J. Marshall, T. C. Sangster, H. S. Park, H. F. Robey, and P. Amendt, Rev. Sci. Instrum. **83**, 10E131 (2012).

70. T. Caillaud, O. Landoas, M. Briat, S. Kime, B. Rossé, I. Thfoin, J. L. Bourgade, L. Disdier, V. Yu. Glebov, F. J. Marshall, and T. C. Sangster, Rev. Sci. Instrum. **83**, 033502 (2012).

# Publications and Conference Presentations

## Publications


S.-W. Bahk, I. A. Begishev, and J. D. Zuegel, "Precompensation of Gain Nonuniformity in a Nd:Glass Amplifier Using a Programmable Beam-Shaping System," Opt. Comm. **333**, 45 (2014).

A. Davies, D. Haberberger, R. Boni, S. Ivancic, R. Brown, and D. H. Froula, "Polarimetry Diagnostic on OMEGA EP Using a 10-ps, 263-nm Probe Beam," Rev. Sci. Instrum. **85**, 11E611 (2014).

A. K. Davis, D. T. Michel, S. X. Hu, R. S. Craxton, R. Epstein, V. N. Goncharov, I. V. Igumenshchev, T. C. Sangster, and D. H. Froula, "Mass-Ablation-Rate Measurements in Direct-Drive Cryogenic Implosions Using X-Ray Self-Emission Images," Rev. Sci. Instrum. **85**, 11D616 (2014).

C. Dorrer, "Analysis of Nonlinear Optical Propagation in a Longitudinal Deuterated Potassium Dihydrogen Phosphate Pockels Cell," J. Opt. Soc. Am. B **31**, 1891 (2014).

C. Dorrer, R. G. Roides, J. Bromage, and J. D. Zuegel, "Self-Phase Modulation Compensation in a Regenerative Amplifier Using Cascaded Second-Order Nonlinearities," Opt. Lett. **39**, 4466 (2014).

D. Eimerl, E. M. Campbell, W. F. Krupke, J. Zweiback, W. L. Kruer, J. Marozas, J. Zuegel, J. Myatt, J. Kelly, D. Froula, and R. L. McCrory, "StarDriver: A Flexible Laser Driver for Inertial Confinement Fusion and High Energy Density Physics," J. Fusion Energ. **33**, 476 (2014).

G. Fiksel, W. Fox, A. Bhattacharjee, D. H. Barnak, P.-Y. Chang, K. Germaschewski, S. X. Hu, and P. M. Nilson, "Magnetic Reconnection Between Colliding Magnetized Laser-Produced Plasma Plumes," Phys. Rev. Lett. **113**, 105003 (2014).

V. Yu. Glebov, C. J. Forrest, K. L. Marshall, M. Romanofsky, T. C. Sangster, M. J. Shoup III, and C. Stoeckl, "A New Neutron Time-of-Flight Detector for Fuel-Areal-Density Measurements on OMEGA," Rev. Sci. Instrum. **85**, 11E102 (2014).

M. Hohenberger, F. Albert, N. E. Palmer, J. J. Lee, T. Döppner, L. Divol, E. L. Dewald, B. Bachmann, A. G. MacPhee, G. LaCaille, D. K. Bradley, and C. Stoeckl, "Time-Resolved Measurements of the Hot-Electron Population in Ignition-Scale Experiments on the National Ignition Facility," Rev. Sci. Instrum. **85**, 11D501 (2014) (invited).

S. X. Hu, L. A. Collins, V. N. Goncharov, T. R. Boehly, R. Epstein, R. L. McCrory, and S. Skupsky, "First-Principles Opacity Table of Warm Dense Deuterium for Inertial-Confinement-Fusion Applications," Phys. Rev. E **90**, 033111 (2014).

H. P. H. Liddell, J. C. Lambropoulos, and S. D. Jacobs, "Thermomechanical Model to Assess Stresses Developed During Elevated-Temperature Cleaning of Coated Optics," Appl. Opt. **53**, 5865 (2014).

F. J. Marshall and P. B. Radha, "Masked-Backlighter Technique Used to Simultaneously Image X-Ray Absorption and X-Ray Emission from an Inertial Confinement Fusion Plasma," Rev. Sci. Instrum. **85**, 11E615 (2014).

J. B. Oliver, T. J. Kessler, C. Smith, B. Taylor, V. Gruschow, J. Hettrick, and B. Charles, "Electron-Beam–Deposited Distributed Polarization Rotator for High-Power-Laser Applications," Opt. Express **22**, 23883 (2014).

F. Pérez, G. E. Kemp, S. P. Regan, M. A. Barrios, J. Pino, H. Scott, S. Ayers, H. Chen, J. Emig, J. D. Colvin, M. Bedzyk, M. J. Shoup III, A. Agliata, B. Yaakobi, F. J. Marshall, R. A. Hamilton, J. Jaquez, M. Farrell, A. Nikroo, and K. B. Fournier, "The NIF X-Ray Spectrometer Calibration Campaign at OMEGA," Rev. Sci. Instrum. **85**, 11D613 (2014).

F. Philippe, V. Tassin, S. Depierreux, P. Gauthier, P. E. Masson-Laborde, M. C. Monteil, P. Seytor, B. Villette, B. Lasinski, H. S. Park, J. S. Ross, P. Amendt, T. Döppner, D. E. Hinkel, R. Wallace, E. Williams, P. Michel, J. Frenje, M. Gatu-Johnson, C. K. Li, R. Petrasso, V. Glebov, C. Sorce, C. Stoeckl, A. Nikroo, and E. Giraldez, "Demonstrated High

Performance of Gas-Filled Rugby-Shaped Hohlraums on OMEGA," Phys. Plasmas **21**, 074504 (2014).

H. G. Rinderknecht, H. Sio, J. A. Frenje, J. Magoon, A. Agliata, M. Shoup, S. Ayers, C. G. Bailey, M. Gatu Johnson, A. B. Zylstra, N. Sinenian, M. J. Rosenberg, C. K. Li, F. H. Séguin, R. D. Petrasso, J. R. Rygg, J. R. Kimbrough, A. Mackinnon, P. Bell, R. Bionta, T. Clancy, R. Zacharias, A. House, T. Döppner, H. S. Park, S. LePape, O. Landen, N. Meezan, H. Robey, V. U. Glebov, M. Hohenberger, C. Stoeckl, T. C. Sangster, C. Li, J. Parat, R. Olson, J. Kline, and J. Kilkenny, "A Magnetic Particle Time-of-Flight (MagPTOF) Diagnostic for Measurements of Shock- and Compression-Bang Time at the NIF," Rev. Sci. Instrum. **85**, 11D901 (2014) (invited).

C. Stoeckl, M. Bedzyk, G. Brent, R. Epstein, G. Fiksel, D. Guy, V. N. Goncharov, S. X. Hu, S. Ingraham, D. W. Jacobs-Perkins, R. K. Jungquist, F. J. Marshall, C. Mileham, P. M. Nilson, T. C. Sangster, M. J. Shoup III, and W. Theobald, "Soft X-Ray Backlighting of Cryogenic Implosions Using a Narrowband Crystal Imaging System," Rev. Sci. Instrum. **85**, 11E501 (2014).

M. Storm, B. Eichman, C. Orban, S. Jiang, G. Fiksel, C. Stoeckl, G. Dyer, T. Ditmire, R. Stephens, W. Theobald, J. A. Delettrez, R. R. Freeman, and K. Akli "$K_\alpha$ X-Ray Imaging of Laser-Irradiated, Limited-Mass Zirconium Foils," Phys. Plasmas **21**, 072704 (2014).

J. Zhang, J. F. Myatt, R. W. Short, A. V. Maximov, H. X. Vu, D. F. DuBois, and D. A. Russell, "Multiple Beam Two-Plasmon Decay: Linear Threshold to Nonlinear Saturation in Three Dimensions," Phys. Rev. Lett. **113**, 105001 (2014).

## Forthcoming Publications

R. Epstein, S. P. Regan, B. A. Hammel, L. J. Suter, H. A. Scott, M. A. Barrios, D. K. Bradley, D. A. Callahan, C. Cerjan, G. W. Collins, S. N. Dixit, T. Doeppner, M. J. Edwards, D. R. Farley, K. B. Fournier, S. Glenn, S. H. Glenzer, I. E. Golovkin, A. Hamza, D. G. Hicks, N. Izumi, O. S. Jones, M. H. Key, J. D. Kilkenny, J. L. Kline, G. A. Kyrala, O. L. Landen, T. Ma, J. J. MacFarlane, A. J. Mackinnon, R. C. Mancini, R. L. McCrory, D. D. Meyerhofer, N. B. Meezan, A. Nikroo, H.-S. Park, P. K. Patel, J. E. Ralph, B. A. Remington, T. C. Sangster, V. A. Smalyuk, P. T. Springer, R. P. J. Town, and J. L. Tucker, "Applications and Results of X-Ray Spectroscopy in Implosion Experiments on the National Ignition Facility," to be published in Proceedings of Atomic Processes in Plasmas (invited).

D. T. Michel, R. S. Craxton, A. K. Davis, R. Epstein, V. Yu. Glebov, V. N. Goncharov, S. X. Hu, I. V. Igumenshchev, D. D. Meyerhofer, P. B. Radha, T. C. Sangster, W. Seka, C. Stoeckl, and D. H. Froula, "Implosion Dynamics in Direct-Drive Experiments," to be published in Plasma Physics and Controlled Fusion.

W. Theobald, A. A. Solodov, C. Stoeckl, K. S. Anderson, F. N. Beg, R. Epstein, G. Fiksel, E. M. Giraldez, V. Yu. Glebov, H. Habara, S. Ivancic, L. C. Jarrott, F. J. Marshall, G. McKiernan, H. S. McLean, C. Mileham, P. M. Nilson, P. K. Patel, F. Pérez, T. C. Sangster, J. J. Santos, H. Sawada, A. Shvydky, R. B. Stephens, and M. S. Wei, "Time-Resolved Compression of a Capsule with a Cone to High Density for Fast-Ignition Laser Fusion," to be published in Nature Communications.

## Conference Presentations

D. H. Froula, J. F. Myatt, A. Shvydky, S. H. Glenzer, L. Divol, O. L. Landen, O. S. Jones, C. H. Still, S. Langer, A. J. Mackinnon, J. S. Ross, B. B. Pollock, M. J. Edwards, R. P. J. Town, L. J. Suter, G. R. Tynan, and G. Gregori, "Effects of Thermal Transport and Laser-Beam Smoothing on Beam Propagation Through Long-Scale-Length Plasmas," Fundamental Science with Pulsed Power Workshop, Albuquerque, NM, 20–23 July 2014.

The following presentations were made at Turbulent Mixing and Beyond, Trieste, Italy, 4–9 August 2014:

I. V. Igumenshchev, L. Gao, and P. M. Nilson, "Self-Generated Magnetic Fields in Rayleigh–Taylor Unstable Laser-Produced Plasma."

S. P. Regan, R. Epstein, R. L. McCrory, D. D. Meyerhofer, T. C. Sangster, B. A. Hammel, L. J. Suter, H. A. Scott, M. A. Barrios,

D. K. Bradley, D. A. Callahan, C. Cerjan, G. W. Collins, T. Dittrich, S. N. Dixit, T. Doeppner, M. J. Edwards, K. B. Fournier, S. Glenn, S. W. Haan, A. Hamza, D. E. Hinkel, O. A. Hurricane, C. A. Iglesias, N. Izumi, O. S. Jones, O. L. Landen, T. Ma, A. J. Mackinnon, N. B. Meezan, A. Pak, H.-S. Park, P. K. Patel, J. Ralph, B. A. Remington, V. A. Smalyuk, P. T. Springer, R. P. J. Town, B. G. Wilson, S. H. Glenzer, I. E. Golovkin, J. J. MacFarlane, H. Huang, J. Jaquez, J. D. Kilkenny, A. Nikroo, J. L. Kline, G. A. Kyrala, and R. C. Mancini, "Diagnosing Hot-Spot Mix with X-Ray Spetroscopy."

---

The following presentations were made at Optics and Photonics, San Diego, CA, 17–21 August 2014:

K. L. Marshall, O. Didovets, and D. Saulnier, "Contact-Angle Measurements as a Means of Probing the Surface Alignment Characteristics of Liquid Crystal Materials on Photoalignment Layers."

S. P. Regan, M. Bedzyk, M. J. Shoup III, R. K. Jungquist, C. Abbott, A. Agliata, F. J. Marshall, R. A. Hamilton, B. Yaakobi, C. Sorce, R. E. Bahr, N. Whiting, E. Kowaluk, J. M. Schoen, W. Byrne, P. Mittermeyer, A. L. Rigatti, J. Hettrick, K. L. Marshall, T. Lewis, T. Clark, S. Lombardo, R. Callari, R. Fellows, S. Gross, C. DeBottis, S. Ross, G. Pien, J. DeWandel, T. C. Sangster, D. D. Meyerhofer, R. Epstein, J. Magoon, B. Staerker, J. Rodas, J. Church, M. Callahan, J. Kendrick, H. Beck, M. Schleigh, B. Ruth, T. Davlin, D. Neyland, D. Walker, S. Dent, C. Lucas, M. Rowland, S. Stagnitto, D. Mastrosimone, W. J. Armstrong, M. Labuzeta, T. Klingenberger, C. Kingsley, M. J. Bonino, J. Fooks, D. R. Harding, S. F. B. Morse, R. L. McCrory, K. B. Fournier, M. A. Barrios, H. Chen, F. Perez, S. Ayers, N. Izumi, A. G. MacPhee, P. Bell, J. D. Kilkenny, D. K. Bradley, J. Emig, B. Ehrlich, D. H. Kalantar, R. Wood, C. Bailey, G. E. Kemp, J. Pino, D. Larson, J. Celeste, B. W. Hatch, J. Jaquez, M. Farrell, A. Nikroo, C. Shipbaugh, S. C. Wilks, and A. Dalton, "Streaked X-Ray Spectrometer for the National Ignition Facility."

---

C. M. Sorce, R. Boni, S. Ingraham, C. Mileham, A. Sorce, and P. Jaanimagi, "Streak Camera Usage at the Laboratory for Laser Energetics: Past, Present, and Future," Streak Camera Workshop, Albuquerque, NM, 26–27 August 2014.

---

The following presentations were made at Laser Damage 2014, Boulder, CO, 14–17 September 2014:

K. Mikami, S. Papernov, S. Motokoshi, S. D. Jacobs, and T. Jitsuno, "Detection of the Laser-Damage Onset in Optical Coatings by the Photothermal-Deflection Method."

J. B. Oliver, J. Bromage, C. Smith, and D. Sadowski, "Large-Aperture Plasma-Ion–Assisted Coatings for Femtosecond-Pulsed Laser Systems" (invited).

J. B. Oliver, T. J. Kessler, S. Papernov, C. Smith, B. Taylor, V. Gruschow, J. Hettrick, and B. Charles, "Electron-Beam–Deposited Distributed-Polarization Rotator for High-Power Laser Applications."

S. Papernov, A. A. Kozlov, and J. B. Oliver, "Interface Absorption Versus Film Absorption in $HfO_2/SiO_2$ Thin-Film Pairs in the Near-Ultraviolet and Relation to Pulsed-Laser Damage."

---

A. A. Solodov, W. Theobald, K. S. Anderson, A. Shvydky, C. Stoeckl, R. Epstein, G. Fiksel, V. Yu. Glebov, S. Ivancic, F. J. Marshall, G. McKiernan, C. Mileham, P. M. Nilson, T. C. Sangster, L. C. Jarrott, C. McGuffey, B. Qiao, F. N. Beg, E. Giraldez, R. B. Stephens, M. S. Wei, H. Habara, K. Tanaka, H. McLean, H. Sawada, and J. Santos, "Hydrodynamics of Cone-in-Shell Implosions on OMEGA," 13th International Fast Ignition Workshop, Oxford, UK, 14–18 September 2014.


1850
MELIORA
UNIVERSITY of
ROCHESTER